ABSTRACT

Title of Dissertation:	EFFECTS OF PHYSICO-CHEMICAL CUES FROM THE BLOOD-BRAIN BARRIER MICROENVIRONMENT ON TUMOR CELL MIGRATION AND MORPHOLOGY
	Marina Alexandrovna Pranda, Doctor of Philosophy, 2019
Dissertation directed by:	Assistant Professor Kimberly M. Stroka Fischell Department of Bioengineering

Cancer metastasis is particularly deadly, leading to 90% of cancer deaths. During metastasis, tumor cells break off from a primary tumor and travel to distant sites. Metastasis to the brain results in a poor patient prognosis. However, several common cancers, such as breast cancer and melanoma, metastasize to the brain. In order to metastasize to the brain, tumor cells have been shown to cross the highly selective blood-brain barrier (BBB), which separates the brain parenchyma from the circulatory system. The BBB is highly impermeable, even for many chemotherapeutics, however, tumor cells are able to cross it by a poorly understood mechanism. The BBB consists of endothelial cells connected by tight junctions, and is supported by cells of the neurovascular unit, such as astrocytes. Furthermore, the composition of the extracellular matrix beyond the BBB is unique and contains hyaluronic acid (HA). In disease, HA organization or biophysical properties may become altered. The goal of this study was to investigate how specific physico-chemical interactions of tumor cells and the BBB microenvironment may impact tumor cell behavior at the BBB, as well as explore cold atmospheric plasma (CAP) as potential cancer treatment. This understanding could lead to better future therapeutics and a better prognosis for patients.

We hypothesized that biophysical and biochemical cues from the BBB microenvironment, as well as the tumor cell phenotype, can influence tumor cells' migration and morphology. In this dissertation, we investigated the interaction of tumor cells with astrocyte-secreted biochemical cues and the biophysical cues from a HA/gelatin extracellular matrix on tumor cell morphology, migration, and incorporation into an endothelium. Our results showed that tumor cell migration and morphology are significantly altered by astrocyte-secreted factors and the HA/gelatin extracellular matrix; however, the extracellular matrix is less significant during incorporation. We also showed that brain- and bone-seeking tumor cells display varied morphologies on matrices with niche-relevant mechanical properties. Finally, we demonstrated that CAP selectivity for reducing migration of tumor vs. normal cells is highly sensitive to cell culture media formulation. Together, these results provide new insights into tumor cell behavior at the BBB and inform future studies and therapeutic development.

EFFECTS OF PHYSICO-CHEMICAL CUES FROM THE BLOOD-BRAIN BARRIER MICROENVIRONMENT ON TUMOR CELL MIGRATION AND MORPHOLOGY

by

Marina Alexandrovna Pranda

Dissertation submitted to the Faculty of the Graduate School of the
University of Maryland, College Park, in partial fulfillment
of the requirements for the degree of
Doctor of Philosophy
2019

Advisory Committee:
Professor Kimberly M. Stroka, Chair
Professor Jose Helim Aranda-Espinoza
Professor Alisa Morss Clyne
Professor Gottlieb S. Oehrlein
Professor Ian White

Dedication

I would like to dedicate this dissertation to my husband and our growing family.

Scientific Acknowledgements

I would like to thank the following people for their help and support in completing my work:

- Dr. Kimberly Stroka, my adviser, for all the guidance in experimental design, experimentation, and data presentation throughout my PhD process.
- My committee for their valuable feedback and their time to review my dissertation and defense:
    - Dr. Gottlieb Oehrlein
    - Dr. Ian White
    - Dr. Jose Helim Aranda-Espinoza
    - Dr. Alisa Morss Clyne
    - As well as Dr. William Bentley and Dr. Ryan Sochol for their time and feedback on my proposal.

Chapter 3:

- Dr. Herbert Geller, NIH for his helpful feedback and discussion.
- Dr. Caitlin Mencio, NIH for providing astrocyte conditioned media for all experiments and conducting all animal work at the NIH.
- Jonathan Siglin for helping set-up some of the experiments and data analysis (Figure 3.2, 3.7 - 3.9).
- Rebecca Moriarty for assistance with both data analysis and experiments relating to varying cell lines and extracellular matrix proteins as well as ROCK inhibition and MMP addition (Figure 3.4, 3.5, 3.10, 3.11).
- Gregory Dawson for some assistance with overall data analysis.

- The UMD Biosciences Imaging Core:
    - Amy Beaven for her help in using the Zeiss LSM 710 confocal microscope.
- University of Maryland Micro and Nano Fabrication Laboratory (FabLab) for providing photolithography resources.
- Mary Doolin for programming help.

Chapter 4:

- Kelsey Gray for taking Atomic Force Microscopy measurements of HA/gelatin gels (Figure 4.1).
- Dr. William Luscinskas, Harvard Medical School, USA, for providing the VE-cadherin-GFP adenovirus.
- Kelsey Gray for conducting studies on endothelial monolayer integrity (data not shown).
- Gregory Dawson for data analysis of cell migration and morphology (Figure. 4.2).
- Ariana Joy DeCastro for helping set-up live-cell VE-cadherin-GFP experiments and imaging (Figure 4.5).
- Danielle Rossi for optimizing HA/gelatin film gelation times.
- The UMD Computer, Mathematical and Natural Sciences Imaging Incubator
    - Dr. Stephan Brenowitz for his help in using the PerkinElmer confocal spinning disk microscope.
- Mary Doolin for programming help.

Chapter 5:

- Dr. Toshiyuki Yoneda, Osaka University, Japan, for providing MDA-MB-231 cell clones.
- Nathaniel Girma, Research Experience for Undergraduates student, for conducting suspended cell imaging and analysis (Figure 5.1), making polyacrylamide gels, and analyzing some data (Figure 5.2, 5.3).
- Ariana Joy DeCastro for setting up experiments varying extracellular matrix proteins and performing a lot of the cell culture (Figure 5.2).
- John Merlo-Coyne for analyzing data of tumor cells on glass (Figure 5.3) and helping with cell culture.
- Kelsey Gray for taking Atomic Force Microscopy measurements of cells (Figure 5.4).

Chapter 6:

- Dr. Gottlieb Oehrlein for insightful discussion and feedback.
- Dr. Andrew Knoll for providing plasma sources and running the plasma treatments, providing the figure of the set-ups (Figure 6.1), and help in writing the resulting manuscript. Also, for taking image of plasma jet in Chapter 2 (Figure 2.3).
- Brittney Murugesan for analyzing the experimental data and helping make experimental diagram (Figure 6.2, 6.5, 6.6).
- Dr. Pingshan Luan for insightful discussion of experimental set-up.
- Mary Doolin for programming help.

Appendix C:

- Gregory Dawson for experimental help and data analysis (all figures).
- Mary Doolin for programming help.

I would like to thank my funding sources for their support:

- University of Maryland Graduate School
    - Ann G. Wylie Dissertation Fellowship
    - International Conference Student Support Award
    - Jacob K. Goldhaber Travel Award
- A. James Clark School of Engineering
    - Future Faculty Program
- Biomedical Engineering Society
    - Career Development Travel Award
- Fischell Department of Bioengineering
- A. James Clark School of Engineering
- University of Maryland, College Park
- Burroughs Wellcome Career Award at the Scientific Interface (to PI, Dr. Kimberly Stroka, for all work)
- DOE Grant #DE-SC0001939 (to PI, Dr. Gottlieb Oehrlein, for work in Chapter 6)
- National Institutes of Health, NHLBI Intramural Research Program (to PI, Dr. Herbert Geller, Dr. Caitlin Mencio, for work in Chapter 3)

Personal Acknowledgements

There are a lot of people I have to thank for their help and support during my graduate school career, without whom this dissertation would not have been possible. They have supported me both personally and professionally throughout my PhD journey and I am extremely grateful for everything they have done for me.

Firstly, I would like to thank my adviser and mentor, Dr. Kimberly M. Stroka, for her continued guidance and advice throughout my PhD as well as her full support for my personal and professional goals. I thank her for taking a chance on me, despite my lack of a cell biology background, and continuing to guide me through all the ups and downs of the PhD journey. Dr. Stroka always inspires me with her ability to turn a seemingly unsuccessful experiment or otherwise stressful situation into an opportunity for something even more interesting than the original plan.

I would also like to thank Kelsey Gray for being an amazing labmate as well as my support system in the early days of the Stroka Lab. Her hard work and dedication to both science and her peers are always an inspiration.

I also want to thank Ariana Joy DeCastro for her enthusiasm when joining the Stroka Lab this past year and jumping in with both feet into research projects. She has been a great help and great Stroka Lab member.

I also want to thank Mary Doolin and Rebecca Moriarty for the intellectual conversations, technical help, coding help, and general support in the lab as well as their positive attitude and encouragement in and outside the lab.

Additionally, my PhD would not have been possible without the support of several amazing friends who have kept me motivated as well as balanced, so I would

like to thank Alessandra Zimmerman, Kristina Stephens, Dr. Ajmeeta Sangtani, Dr. Svetlana Ikonomova, and Rachel Woods for support on all levels of going through graduate school.

Of course, I owe great gratitude to my family, my mother Irina, my father Alexander, and sister Victoria Shumakovich, for all their moral and emotional support before, during, and probably after my PhD. They helped me keep things in perspective.

I also owe a great deal to my parents and sister in-law, Katarina, Pavol, and Paula Pranda for their continued support and encouragement.

Finally, I need to give a huge thank you to Adam Pranda, who went from boyfriend, to fiancé, to husband, and soon-to-be father in the five years that we have been at the University of Maryland and he was and is naturally great at all of those roles as well as at providing constant support and encouragement in my successes and challenges throughout graduate school (and way before that). I could never have made it this far without his positivity, patience, emotional support, and of course, infallible computer skills.

Table of Contents

† These chapters were taken or adapted from Marina A. Pranda's published, submitted, or in-preparation work. All published work is used with permission from the publisher. Citations are included in the beginning of each chapter. Some work was published under Marina A. Pranda's maiden name: Marina A. Shumakovich.

List of Tables

List of Figures

List of Abbreviations

ACM: Astrocyte conditioned media

ADAM: A Disintegrin and Metalloprotease

AFM: Atomic force microscopy

AJ: Adherens junction

APPJ: Atmospheric pressure plasma discharge

AQP5: Aquaporin-5

AR: Aspect ratio

BBB: Blood-brain barrier

BL: Basal lamina

BO: Bone (seeking cells)

BR: Brain (seeking cells)

BSA: Bovine serum albumin

CAP: Cold atmospheric plasma

CD44: Cluster of differentiation 44

CSPG: Chondroitin sulfate proteoglycan

D: Diffusion coefficient

DMEM: Dulbecco's modified eagle's medium

DMSO: Dimethyl sulfoxide

DTT: Dithiothreitol

ECGS: Endothelial cell growth supplement

EV: Extracellular vehicle

F: Force

FBS: Fetal bovine serum

FGF: Fibroblast growth factor

GFAP: Glial fibrillary acidic protein

GFP: Green fluorescent protein

HA: Hyaluronic acid

HBMEC: Human brain microvascular endothelial cell

HBSS: Hank’s balanced salt solution

IAR: Inverse aspect ratio

IL-1β: Interleukin-1β

iPSC: Induced pluripotent stem cell

LOX: Lysyl oxidase

MMP: Matrix metalloproteinases

MSD: Mean square displacement

N: number of trials

n: number of cells

PA: Polyacrylamide

PBS: Phosphate buffered saline

PDL: Poly-D-Lysine hydrobromide

RNS: Reactive nitrogen species

ROCK: Rho-associated kinase

ROS: Reactive oxygen species

RPMI: Roswell Park Memorial Institute

SMD: Surface microdischarge

S1P3: Sphingosine-1 phosphate receptor 3

TC: Tumor cell

TEMED: Tetramethylethylenediamine

TGF-β: Tumor growth factor β

TJ: Tight junctions

VE-cadherin: Vascular endothelial cadherin

VEGF: Vascular endothelial growth factor

ZO: Zonula occluden

3D/2D: 3 or 2 dimensional

1 Introduction

Cancer metastasis is the process by which tumor cells break away from a primary tumor, travel through the circulatory system, and colonize a distant site, forming a secondary tumor [1]–[3]. Metastasis can occur at various sites, such as brain and bone [4]. Metastasis of tumor cells from a primary tumor to the brain is a particularly deadly aspect of cancer progression, with very short survival post-diagnosis [5], [6]. However, several common cancers, such as breast cancer and melanoma, preferentially metastasize to the brain [5]. In order to metastasize to the brain, tumor cells have to cross the blood-brain barrier (BBB), which lines brain capillaries and separates the brain parenchyma from the circulatory system [7], [8]. The BBB consists of brain endothelial cells connected by tight junctions, consisting of tight junction proteins such as Occludins, Zonula Occludens (ZO), and Claudins, and tight slightly less tight adherens junctions, consisting of adherens junction proteins such as VE-cadherin [7]. The BBB is supported by other cells of the neurovascular unit, such as astrocytes, pericytes, and neurons [7]. This creates a highly selective barrier between the brain and the circulatory system that is impermeable to most molecules, including many chemotherapeutic drugs [5], [6], [9]. However, despite the highly selective and protective properties of the BBB, metastatic tumor cells are able to cross the BBB by a not fully understood mechanism [5].

In addition to being a uniquely impermeable barrier, the BBB microenvironment has unique physical properties, such the very soft brain

extracellular matrix that lies beyond it [10] with an elastic modulus of 0.1 - 1 kPa [10] and is primarily made up of hyaluronic acid (HA) [11]. Additionally, brain capillaries are very narrow, ranging in average diameter from 7 µm to 10 µm [11]. These factors distinguish the BBB from many other organs in the body and create an important niche for cancer research.

The overall goal of this dissertation is to evaluate physico-chemical cues of the BBB microenvironment and metastatic breast tumor cells in order to begin to understand what leads tumor cells to cross the BBB and metastasize to the brain as well as investigate a novel therapeutic approach. We evaluate three tumor cell-BBB interactions: 1) Biochemical factors from the BBB microenvironment, 2) biophysical factors at the BBB, and 3) phenotypic properties of metastatic breast tumor cells that preferentially metastasize to brain and bone. Specifically, this dissertation addresses the effects of biochemical cues (e.g., from astrocytes), physical cues (e.g., HA), and organotropism of tumor cells on the

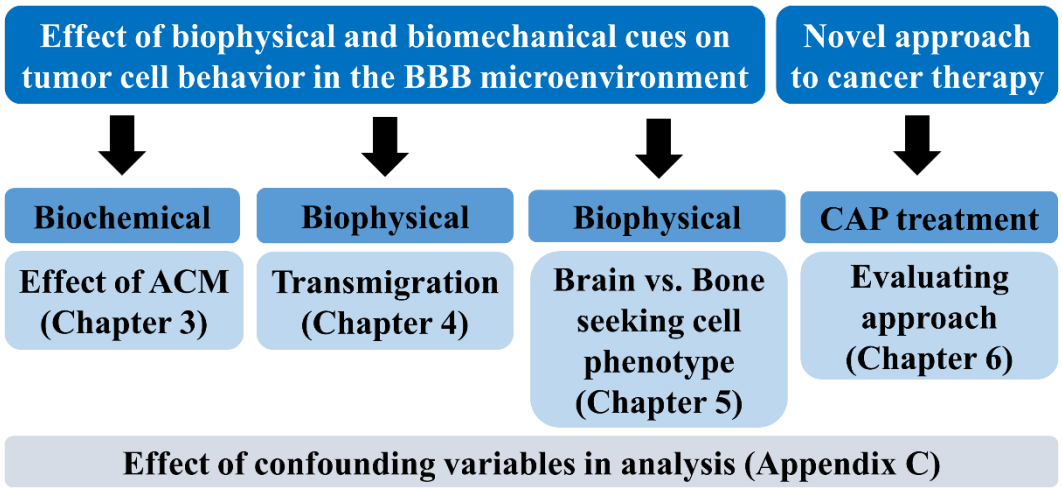

Figure 1.1: Dissertation outline. Biophysical and biomechanical cues from the brain microenvironment on the behavior of metastatic breast tumor cells were investigated. CAP-treated media was examined as a potential cancer therapeutic and the effect of confounding variables on data analysis was examined.

migration, morphology, and incorporation of metastatic breast tumor cells. Additionally, this dissertation addresses a potential therapeutic approach, Cold Atmospheric Plasma (CAP), which has the potential to selectively damage tumor cells while leaving normal cells intact (Figure 1.1).

In this dissertation, we examined the **biochemical** effect of astrocytes on metastatic breast tumor cells with the use of conditioned media (ACM) (Chapter 3). Prior literature showed that astrocytes play a key role both in BBB integrity as well as in BBB interaction with tumor cells [12]–[15], making them an important BBB component during tumor cell invasion. However, it was unknown whether astrocyte-secreted factors could alter tumor cell migration via the cell's extracellular matrix, and whether the effects of astrocyte secreted factors were dependent on the degree of metastatic potential of the tumor cells or specific extracellular matrix components. This dissertation directly addresses these topics. Here, we examined the effect of direct ACM treatment, or pre-treatment of the extracellular matrix with ACM, on the migration and morphology of MDA-MB-231 metastatic tumor cells (Chapter 3). We also examined the differences in the effect of ACM on tumor cells with different metastatic potentials and on tumor cells cultured on different extracellular matrix proteins (Chapter 3). We found that both direct ACM treatments of tumor cells and - pre-treatment of tumor cells' extracellular matrix increases tumor cell velocity; however, tumor cell area only increases with direct ACM treatment of the cells (Chapter 3). Interestingly, pre-treatment of the extracellular matrix with ACM resulted in even larger increases in cell velocity compared to direct treatment of cells with ACM, suggesting that astrocyte-secreted factors act on cells through the

extracellular matrix. Furthermore, we have shown that the effect of ACM can depend on both the cell type and extracellular matrix binding moieties, with potential integrin dependence (Chapter 3). We provide evidence that these effects occur through MMPs present in the ACM, and through a ROCK-mediated signaling pathway in tumor cells. However, ACM did not appear to be a tumor cell chemoattractant (Chapter 3). In summary, we have identified a novel mechanism by which biochemical factors secreted by astrocytes may act on tumor cells (e.g., through the extracellular matrix) to promote breast cancer metastasis to the brain (Chapter 3).

Because the brain extracellular matrix is rather unique in its composition and biophysical properties, we aimed to investigate the **biophysical** interactions of metastatic breast tumor cells with a brain-relevant extracellular matrix, along with a monolayer of brain endothelial cells (Chapter 4). Specifically, we investigated the migration, morphology, and incorporation mechanisms of metastatic breast tumor cells on HA/gelatin films and human brain microvascular endothelial cell (HBMEC) monolayers (Chapter 4). We discovered that while tumor cells respond differently to varying degrees of HA/gelatin crosslinking, the extracellular matrix crosslinking did not significantly affect tumor cell incorporation into HBMEC monolayers (Chapter 4). Additionally, we showed that tumor cells could be potentially incorporating not only paracellularly, but also transcellularly into HBMEC monolayers (Chapter 4).

Metastasizing tumor cells also undergo a non-random process known as "organotropism," where tumor cells are distributed preferentially to various distant sites [16]. This process can be regulated by various factors, ranging from cancer subtype, cross-talk with adjacent cells, to barrier properties and function of the host

tissue [16]. It is possible that phenotypical properties of the tumor cells or their interaction with the extracellular matrix result in tumor cells crossing the BBB (Chapter 5). Here, we examined the differences in morphology and stiffness of regular, brain-, and bone-seeking metastatic breast tumor cell clones as they respond to substrate stiffness. We aim towards an understanding of whether morphological differences in tumor cell phenotype and tumor cell-extracellular matrix interactions could allow us to differentiate between the tumor cell clones (Chapter 5). We showed that while the different breast tumor cell clones do not vary in stiffness, they do vary in morphology (Chapter 5).

Since one of the key issues with tumor cell metastasis to the brain is the lack of successful therapies, we also examined the novel potential cancer therapeutic known as CAP (Chapter 6). Upon careful review of literature, we found that there are some critical gaps in cell-related CAP experiment consistency (Chapter 6). Thus, we aimed to provide a systematic examination of the effect of various experimental parameters on the effectiveness and selectivity of CAP-treated media as a potential cancer therapeutic (Chapter 6). We found that some common experimental parameters, such as media formulation and plasma source, significantly affect outcome of CAP-based cancer treatments, indicating that more work should be done to optimize the conditions before the treatment could potentially be introduced *in vivo* (Chapter 6). However, with further development, CAP or CAP-treated liquids could become a new potential therapy that can be used to either destroy tumor cells in circulation, be applied directly to secondary tumors, or potentially even cross the BBB and target incorporating tumor cells, since CAP generates reactive oxygen and

nitrogen species (ROS/RNS) which could potentially cross the BBB via channel or member transport [11].

Together, our results show that physico-chemical cues from the BBB microenvironment and the phenotype of tumor cells could be playing a significant role in the progression of brain metastases. Additionally, show that the potential novel therapeutic, CAP, is highly dependent on experimental parameters.

2 Background

2.1 Motivation

2.1.1 Clinical presentation of brain metastases

Cancer is one of the deadliest diseases and the second most common cause of death in the United States [17]–[19]. It is characterized by the uncontrolled growth of cells and can occur at many different sites in the body [18]. It is not fully understood why and how cancer occurs, although various risk factors such as smoking, obesity, and alcohol consumptions can significantly increase ones changes of the disease [18], [19]. While cancer statistics are lagging 2 - 4 years behind in the US, it is projected that 1.7 million new cancer cases and 606,880 cancer deaths will occur in 2019 in the US, which is the equivalent of 1,660 deaths per day [18], [19]. Some cancer are particularly prevalent, such as breast cancer and prostate cancers which are expected to make up 30% of new cancer cases in women and 20% of new cancer cases in men, respectively in 2019 [18], [19]. These cancers are expected to lead to 15% and 10% of deaths among women and men respectively [18], [19]. On the other hand, primary brain cancer is relatively rare, leading to only 3% of expected cancer deaths among both men and women [18], [19]. This is despite the fact that brain and nervous system tumors are the leading cause of mortality in the US in men below the age of 40 and women below the age of 20, while breast cancer is the leading cause of death among women between ages 20 and 59 years [18], [19]. Since this dissertation focuses on breast cancer metastasis to the brain, it is noteworthy that for 2019 it is estimated that there will be 268,600 new cases of invasive breast cancer diagnosed in women in the

US, and 2,670 cases of invasive breast cancer are projected to be diagnosed in men in the US [18], [19]. In the US in 2019, 42,260 people are expected to die from breast cancer [18], [19].

When breast cancer is diagnosed prior to the spread of tumor cells to other parts of the body, it's 5-year survival rate is 99% [18]. However, the deadliest aspect of cancer is metastasis, where cells from a primary tumor intravasate into the circulatory or lymphatic systems, travel to distant organs, such as the brain, extravasate, and form secondary tumors (Figure 2.1) [20], [21]. Indeed, 90% of cancer deaths are due to metastasis [4]. Metastasis to the brain is one of the more deadly complications of primary tumors, with 10 - 35% of adult cancer cases resulting in brain metastasis [22],[23]. Various cancers, such as lung and breast cancers and melanoma, which account for 67% - 80% of all cancers [22], commonly

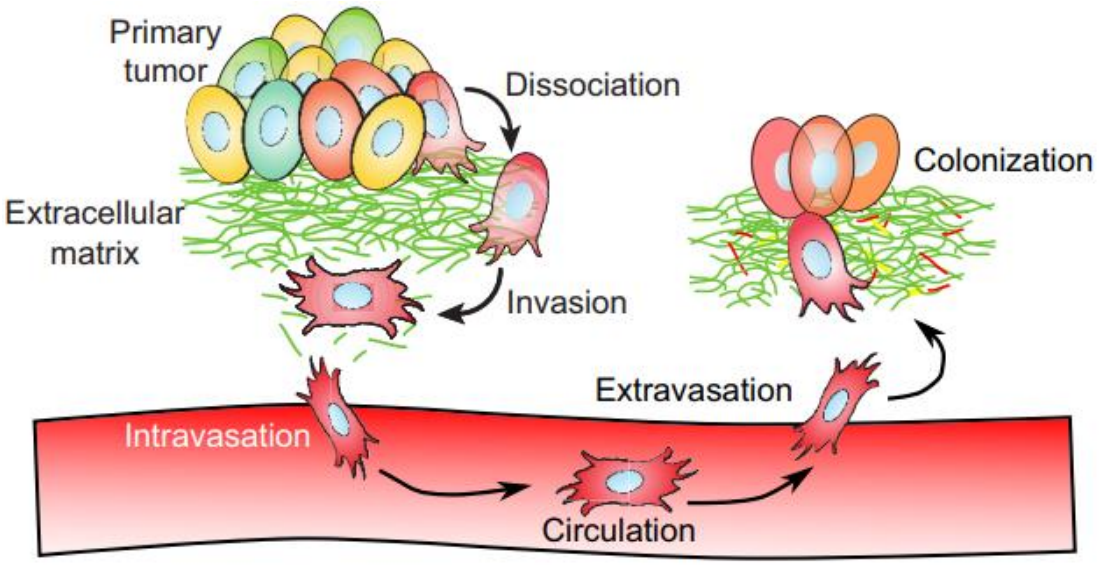

Figure 2.1: Metastatic cascade. Process of tumor cell dissemination from a primary tumor, into the blood stream, and to distant sites forming secondary tumors. Image used with permission from publisher (Open Access article distributed under the terms of the Creative Commons Attribution License (http://creativecommons.org/licenses/by/3.0)). J. L. Albritton and J. S. Miller, "3D bioprinting: improving in vitro models of metastasis with heterogeneous tumor microenvironments," *Dis. Model. Mech.*, vol. 10, pp. 3–14, 2017. [21]

and preferentially metastasize to the brain [22],[6]. While in the past five years treatment and subsequent survival of brain metastases patients has improved [23], it is still extremely deadly and there is no consistently effective treatment. Metastasis has been recognized as a tremendous hurdle to survivability for a long time. In fact, as early as 1889, Dr. Stephen Paget suggest an breakthrough new theory, suggesting that metastasis is governed not just by patterns of circulatory flow, but by cross-talk of tumor cells and surrounding tissue [24], [25]. In the case of brain metastasis, breast cancer is the second most common cancer to metastasize to the brain (after lung cancer), and this leads to a worse diagnosis, more difficult treatment, and more devastating prognosis [26].

2.1.2 Historic "seed and soil" hypothesis

In 1889, Dr. Stephen Paget proposed in a seminal paper that tumor cells follow a "seed and soil" theory when spreading through the body to distant organs [24], [25]. Specifically, Dr. Paget asked himself what are the determinants directing to which organ tumor cells will spread during metastasis [24], [25]. His clinical findings disproved the earlier theory that tumor cells spread simply by passive blood flow and settle in whichever tissue they passed [24], [25]. Dr. Paget suggested that based on his clinical data, primarily on breast cancer and melanoma, in order to metastasize the tumor cell "seed" and the secondary organ "soil" need to be compatible, which is likely determined by the specific properties of each [24], [25]. While this theory has been extensively studied and revised over the past over 100 years, it still remains widely accepted that tumor cells rely heavily on cross-talk, both biochemical and biophysical, with their microenvironment [25]. However, while

prior work has explored the effects of several microenvironment cues, such as tumor cell response to tissue stiffness and matrix composition [27]–[32], in many cancers they remain unknown or unclear. For example, in tumor metastasis to the brain it has still not been established what properties of tumor cells and the BBB or brain microenvironments result in metastasis across the BBB and to the brain. This dissertation seeks to shed light on a small subset of these cues, in the hopes of contributing to the understanding of the brain metastasis mechanisms and eventually the development of effective therapies to address those mechanisms.

2.1.3 Mechanism of metastasis

In order to colonize a secondary tissue, tumor cells have to extravasate from the blood vessels into surrounding tissue. If the "seed and soil" hypothesis, described in Section 2.1.2, holds true, then both the tumor cells ("seed") and the surrounding microenvironment ("soil") have to be favorable for metastasis to occur. In order to extravasate, tumor cells have to attach to the wall of the blood vessel, and in some cases incorporate into the vessel's endothelium prior to subsequent extravasation [33], [34]. In the very small vessels of the brain, the diameter of tumor cells is larger than that of the vessel, and thus tumor cells can become trapped in the vessels, leading to increased extravasation [34]. Certain biochemical and biophysical factors have been observed to be involved in tumor cell extravasation. For example, it is suspected that the presence of VEGF receptors on tumor cells contributes to metastasis. Furthermore, since tumor cells have to interact with diverse extracellular matrix proteins during metastasis, the presence of matrix metalloproteinase (MMPs) also is suggested to be involved in metastasis [35].

The physical aspects of the microenvironment can also influence tumor cells. Mechanical forces surrounding primary tumors, metastatic tumor cells, and secondary tumors are extremely important for understanding the underlying disease mechanisms. Two components are particularly important: the viscoelastic properties of the extracellular matrix and the cells themselves, as well as the physical composition of cells' microenviornment. Increased extracellular matrix stiffness alters the structure of tumor cells' cytoskeleton and their integrin clustering, resulting in increased invasiveness of tumor cells [36], [37]. For example, it has been shown that breast tumor cells become more invasive as their surrounding collagen matrix stiffens, promoting metastasis [38]. As the stiffness of cells' extracellular matrix changes, cells are also able to change their own viscoelastic properties [39]. It has been shown that increased metastatic potential correlates with increased compliance of single tumor cells, which correlate with their invasiveness [40]. For example, using ovarian cancer cells it was shown that cancer cells have a lower stiffness than non-malignant cells of the same type [41].

Interestingly, some tumor cells still readily metastasize to the brain, despite its unique microenvironment which does not share many characteristics with a typical tumor environment. For example, the brain microenvironment is very soft and is not made up of collagen and fibronectin proteins that are common in tumors and other parts of the body. In order to be able to effectively treat or event prevent devastating brain metastases, it is crucial to first understand what guides tumor cells to spread to the brain in the first place and how tumor cells are able to cross the BBB. **This dissertation addresses this gap in knowledge by exploring the biochemical and**

biophysical properties of the BBB as well as the intrinsic phenotypical properties of tumor cells in order to begin to understand which cell and microenvironmental properties direct brain metastasis.

2.2 Blood-brain barrier (BBB) and brain microenvironment

In order to understand how tumor cells cross the BBB, it is first crucial to understand what makes the BBB and brain microenvironments unique. Overall, the neurovascular unit includes the brain endothelium, astrocytes, pericytes, neurons, microglia, basal lamina, and extracellular matrix and space [11], [42]. Brain capillaries range in size, but are overall extremely small with an average diameter of 7 - 10 μm [11] and they are lined with the highly impermeable BBB. Despite the small capillary size, the BBB creates a very large surface area for transport between the brain and circulatory systems [7], with a total surface area of approximately 15 - 25 m^2 [11].

Structurally, the BBB consists of brain endothelial cells, connected by tight junctions with proteins such as zonula occludens (ZO), occludin, and claudin as well as adherens junctions with proteins such as vascular endothelial (VE)-cadherin, that line brain capillaries and are supported by other cells of the neurovascular unit, such as astrocytes, pericytes, and neurons (Figure 2.2) [7], [12]. There are two separate basal lamina supporting cells of the BBB: the endothelial basal lamina and the parenchymal basement membrane, separated by pericytes [43]. In a healthy BBB state, the two basal lamina layers cannot be told apart [43]. In general, the basal lamina is a sheet of organized proteins, and is only 50 – 100 nm thick. It consists primarily of collagen IV, laminin, nidogen, perlecan, and heparin sulfate and is

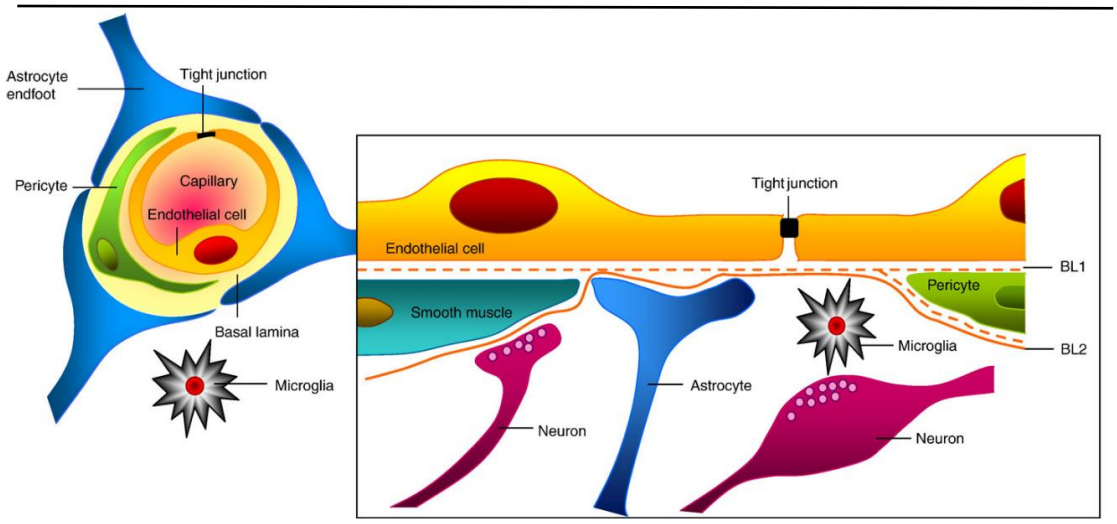

Figure 2.2: Blood-brain barrier physiology. Blood-brain barrier structure with main physical components from the brain microenvironment. BL: basal lamina. Image reprinted from *Neurobiol. Dis*, vol. 21, no. 4, N. J. Abbott, A. A. Patabendige, D. E. M. Dolman, S. R. Yusof, and D. J. Begley, Structure and function of the blood-brain barrier, pp. 13–25, 2010, with permission from Elsevier [7].

somewhat different from the structure and composition of the brain extracellular matrix, which is a dense network of glycoproteins such as tenascins, hyaluronic acid (HA), and chondroitin sulfate proteoglycans [43], [44].

Together with tight junctions and adherens junctions, all of these structural features create a barrier that separates the brain from the circulatory system and only transports select molecules, such as lipid soluble molecules, glucose, small peptides, and amino acids [7]. Tight junctions of brain endothelium regulate paracellular transport between the blood and the brain, while transporters, pumps, and receptors regulate the transcellular transport [11]. The BBB has an high electrical resistance between 1000 and 2000 Ω-cm^2, which might guard against polar and ionic molecules [9]. Some of the transport mechanisms across the BBB include passive diffusion (eg. lipid soluble non-polar molecules), active efflux carriers (eg. lipid soluble non-polar molecules and conjugates), carrier-mediated influx via solute carriers (eg. glucose,

amino acids, nucleosides, small peptides, organic anions and cations, monocarboxylates), receptor and adsorptive-mediated transcytosis (eg. lipoproteins, insulin, amyloid β), and mononuclear cell migration (eg. leukocytes) [7].

Beyond the BBB, the brain is extremely soft (0.1 kPa – 1 kPa) and has a unique extracellular matrix composition [45], [46]. It contains little collagen, fibronectin, vitronectin, and laminin, which are abundant in other organs, but is rich in heparan sulfate and chondroitin sulfate proteoglycans, tenascins, and HA [45], [46]. Since the stiffness of the extracellular matrix and its composition play a role in metastasis [29] and tumors are typically stiffer than normal tissue [36], especially the brain, and are made up of the more common extracellular matrix proteins such as collagen and fibronectin, it is surprising that tumor cells still preferentially metastasize to the brain, despite its unique environment. While it is known that the structure of the BBB can be altered in the presence of tumor cells [47], the exact mechanisms by which tumor cells interact with the BBB are still not known [6]. The open question that remains is: **which aspects of the BBB microenvironment or tumor cells motivate tumor cells to preferentially metastasize to the brain?** Chapters 3 – 5 of this dissertation address several biochemical, biophysical, and phenotypic aspects of tumor cell – BBB interaction in order to begin to answer this question.

2.3 Biochemical interactions of tumor cells with BBB via astrocytes and astrocytes secreted factors

While tumor cells can interact with their microenvironment both via direct physical contact, they can also do so via indirect biochemical signaling. It is important to consider the indirect biochemical interactions that take place between tumor cells and the BBB microenvironment, since biochemical cues could be some of the first factors encountered by the tumor cells during the metastatic cascade, especially if the BBB is already damaged. Astrocytes, in particular, have been implicated in affecting tumor cells at the BBB, especially due to their proximity to the brain vasculature (Figure 2.2) [15]. In healthy physiology, astrocytes and their perivascular end-feet play a crucial role in maintaining the brain's ionic, amino acid, neurotransmitter, and water homeostasis as well as supporting neuronal function [12]. Additionally, astrocytes upregulate various features of the BBB and help form and maintain tight junctions [12]. However, in the case of cancer, it has been shown that astrocytes can actually enhance cancer proliferation, chemoprotection, invasion, and immunoprotection [14]. More work has been necessary to fully understand the extent to which tumor cells and astrocytes interact, and which pathways are involved.

Prior research has implicated astrocyte-secreted serpins in tumor cell survival during metastasis across the BBB using *in vivo* assays [15], attributed an increased BBB invasiveness of tumor cells to astrocyte secreted matrix metalloproteinases (MMPs) [48], and shown that astrocytes and tumor cells can form gap-junctions [49]. It has been reported that extracellular vehicles (EVs) secreted by astrocytes carry fibroblast growth factor (bFGF or FGF-2) and vascular endothelial growth factor

(VEGF) [50], which have been shown to enhance tumor cell proliferation [51]. Furthermore, certain lipopolysaccharide (LPS)-activated microglia secrete chemical factors, such as tumor necrosis factor-α, that help destroy lung tumor cells in the brain [52]. However, astrocytes can also help tumor cells be resistant to chemotherapy [6] and microglia can increase the invasiveness of breast tumor cells via the Wnt and inflammatory signaling pathways [53]. In fact, astrocytes themselves can have different phenotypes *in vivo* which could affect their interaction with tumor cells.

An additional consideration is that while in healthy physiology, astrocytes provide support for the brain and the BBB [12], during traumatic brain injury, astrocytes become reactive, forming glial scars that primarily consist of chondroitin sulfate proteoglycan (CSPG) [54]. During this process, CSPG and the fibrillary acidic protein (GFAP) are upregulated in astrocytes and astrocytes show signs of hypertrophy [54], [55]. It has been shown *in vivo* that fibrinogen-bound TGFβ infiltrates the brain through a damaged BBB and TGFβ activates the astrocytes [54]. Since astrocytes become reactive in response to injury, reactive astrocytes have been implicated in neurodegenerative diseases, such as Alzheimer's disease, and some effect on tumor cells [55], [56]. Based on one study, during inflammation, astrocytic sphingosine-1 phosphate receptor 3 (S1P3) is upregulated and it helps tighten the blood-tumor barrier formed as a result of brain metastasis [57], [58]. Thus, it is evident that astrocytes and their different activation states could play a key role in the successful progression of brain metastasis. Two unanswered question that still remain is**: how do tumor cells interact directly and indirectly with astrocytes in combination with physical cues at the BBB?**; and **do astrocytes have to be**

reactive in order to influence tumor cells? Chapter 3 of this dissertation will address the biochemical interaction of astrocytes and tumor cells as well the effect of astrocytes on tumor cell extracellular matrix and touches upon the activation of astrocytes *in vitro*. The next step after investigating the effect of biochemical cues, is to explore the physical interactions of tumor cells and the BBB extracellular matrix and endothelial cells, since in order to invade the brain, tumor cells have to inevitably physically cross the endothelial barrier.

2.4 Transmigration and incorporation of tumor cells into endothelia

2.4.1 General transmigration and incorporation of tumor cells

Gaining a better understanding of tumor cell transmigration into the BBB endothelium will shed light on the most crucial step in the metastatic cascade which actually allows tumor cells to read their secondary tumor site. As described in Section 2.2, the brain is particularly soft, and is abundant in unusual extracellular matrix molecules, such as HA. Yet, it has been previously shown that stiffer extracellular matrix can alter a cell's migration, morphology, cytoskeletal arrangement, and focal adhesion and integrin density [36], [59], [60]. Thus, it remains to be understood how tumor cells interact with the brain's extremely soft extracellular matrix and why certain cells preferentially metastasize to the brain, despite this potentially less than favorable environment [10]. One factor that could begin to address this dilemma is the fact that while the brain is abundant in HA, both tumor cells and brain endothelial cells express a specific HA receptor, CD44, a cell-surface glycoprotein [61], [62]. In tumor cells, such as breast tumor cells, CD44 is implicated in greater attachment to

endothelia and increased metastatic phenotype [63]. Studies have also shown that HA availability and CD44 expression could mediate transmigration of neural precursor cells across endothelia [64], leukocytes, and likely cancer cells [61]. CD44 can also bind to collagen, laminin, and fibronectin [61].

Prior work comparing the transmigration of tumor cells across peripheral endothelia with the transmigration of the immune cells, leukocytes, showed that tumor cells implement an additional step in the process and displace endothelial cells [33]. However, the study also showed that there are significant differences in the mechanisms employed by tumor cells from different cancers and their reaction to different extracellular matrix [33].

2.4.2 Transmigration across BBB-relevant endothelia

Furthermore, some cancers, such as breast cancer, express genes that facilitate their adhesion to the BBB endothelium and further transmigration [65]. One study has shown, using a Transwell model of the BBB with porcine brain endothelial cells and astrocytes, that the metalloproteinase-disintegrin proteinase ADAM8 expression is related to higher brain metastasis incidence as well as an increased ability of tumor cells to transmigrate across a BBB model endothelium [66]. Furthermore, the study showed that blocking ADAM8, MMP-9 and β1 integrins reduced breast tumor cells' transmigration across a BBB-like endothelium [66]. An additional study has shown that breast cancer cells and melanoma cells interact differently with the brain endothelium [67]. Utilizing a microfluidic device and rat brain endothelial cells the study shows that melanoma cells have a greater ability to attach and transmigrate through a BBB-like endothelium [67]. Additionally, melanoma cells were more able

to disrupt tight junctions, as evidenced by claudin-5 localization [67]. The study also implicated the tumor cells' Rho/ROCK pathway in their ability to transmigrate effectively through a brain-like endothelium [67]. Similarly, a study has shown that ROCK inhibition in melanoma cells, but not brain endothelial cells, enhances transmigration [68]. Additional studies have shown that the adhesion of melanoma cells to a brain-like endothelium could also be cell-dependent based on the mechanical properties of the specific cell or cell type [69]. Interestingly, an additional study has shown that breast tumor cells are able to incorporate into brain-like endothelial via paracellular and transcellular pathways in an N-cadherin independent manner, while the transmigration of melanoma cells was limited to the paracellular pathway in an N-cadherin dependent manner [70]. These studies were carried out both *in vivo and in vitro* [70]. Furthermore, it has been suggested that endothelial-mesenchymal transition of brain endothelial cells induced by tumor cells via TGF-β could be an essential part of successful tumor cell transmigration [71].

2.4.3 Open questions in studying transmigration across the BBB

To complicate matters further, tumor cells are highly heterogeneous, making it difficult to find a mechanism that can be generalized to an entire cell line or cancer type [6]. While prior studies shed light on tumor cell extravasation through non-BBB endothelia [72] as well as several important aspects of melanoma and breast tumor cells transmigration across brain-like endothelia, the following open question remains**: how do various aspects of the microenvironment affect how tumor cells cross the BBB?** Chapter 4 of this dissertation address the incorporation of tumor cells in to a BBB model on an HA/gelatin extracellular matrix, in order to begin to

understand whether the process is different from peripheral endothelia. However, understanding the interactions of tumor cells with biochemical and biophysical cues at the BBB leaves the question as to whether the tumor cell phenotype plays a role in preferential metastasis across the BBB.

2.5 Brain- and bone-seeking clones of metastatic breast tumor cells

Sections 2.2 – 2.4 have addressed portions of the "soil" portion of the "seed and soil" hypothesis introduced in Section 2.2. However, the "seed" portion, or the tumor cells themselves, could prove to be similarly important in explaining tumor cell metastasis to the brain. In order to study the phenotype of the tumor cells in brain metastasis, different metastatic clones of the same cell lines have been generated. Specifically, to study the driving forces behind tumor cells from the same primary tumor type traveling to different distant metastatic sites, Yoneda *et al*. established two stable clones from the MDA-MB-231 parental metastatic tumor cell line [73]. The two established clones were repeatedly passaged through a mouse model until each clone metastasized solely to either the bone or the brain, creating the bone- and brain-seeking MDA-MB-231 clone lines [73]. The final clones metastasized with 100% efficiency to their respective metastatic sites [73]. While the three different cell clones (parental, brain- and bone-seeking) exhibited similar tumorigenicity at the orthotopic site, they showed various biological differences. For example, the brain-seeking cells produced more parathyroid hormone and their anchorage-independent growth was not dependent on TGF-β, unlike the brain-seeking and parental phenotypes [73]. The brain-seeking cells were also more sensitive to insulin-like growth factor I than the other two clones [73] and the bone-seeking cells showed a

much higher adhesion to bone matrix, than brain-seeking and parental clones [74]. Furthermore, it has been shown that exosomes from brain-, lung-, and liver-tropic tumor cells can actually be taken up by cells of the host tissue and thus the tumor cells in a way prepare a new niche [75].

These tumor cell clones created an opportunity for the understanding of what separates tumor cells of the same type that preferentially metastasize to very physiologically distinct sites, such as the brain and bone. One study has performed a genomic analysis of the brain-seeking clone and determined that there are substantial changes in protein expression between brain-seeking clones and parental MDA-MB-231 tumor cells, with the majority of the altered proteins being responsible for signaling and cell motility, cell cycle, metabolism, and transcription and translation [76]. Furthermore, it has been shown that brain-seeking MDA-MB-231 tumor cells show a higher migration and invasion potential in a transwell system and express a higher amount mRNA for MMP-1 and MMP-9 than bone-seeking and parental cells [77].

While some work has been done to understand what differentiates the various clones, an open question remains: **are there unique biophysical properties in brain-seeking clones that are absent in bone-seeking clones and the parental tumor cells which could be used to differentiate cell clones and determine the future metastatic destination of cells in a sample population**? Chapter 5 of this dissertation begins to address some of the phenotypic differences in the different tumor cell clones. Phenotypic differences could allow us, in the future, to determine which organotropic population a given tumor cell is from based on its response to

various engineered environments. Additionally, the phenotype of tumor cells can be crucial in the process of metastasis, including properties such as migration and morphology of tumor cells in different microenvironments. A better understanding of the physical response of these tumor cell clone to various components of a physiological microenvironment could be key to understanding more about what makes certain cells prefer metastasizing to the brain, despite it lacking many of the commonly preferred properties, such as high stiffness and collagen and fibronectin-based extracellular matrix. While Chapter 5 addresses exclusively morphological differences, future work will focus on addressing additional phenotypic parameters.

2.6 Therapeutic approaches

2.6.1 Current therapeutic challenges

Sections 2.1 – 2.5 have introduced some current gaps of knowledge in cancer research, while Chapters 3 – 4 of this dissertation seek to address a few of these gaps to improve the current understanding of the mechanisms behind tumor cell metastasis across the BBB. However, the ultimate goal of cancer research is to not only understand its mechanisms, but to cure the cancer or stop its progression. Thus, an essential part of cancer research is also to address potential therapies that could improve upon or provide an advantage in addition to current cancer treatment methods.

The most common anti-cancer therapies include surgery, radiation, chemotherapy, and some newer drugs such as biologics or targeted therapies [78]. However, despite there being a rapid development in the cancer therapy field, there

are still many downsides to most of the commonly used treatments. For example, surgery is commonly used in combination with other therapeutic methods and does not work effectively on cancer that has metastasized [78]. Additionally, some tumors are located in hard to access areas, such as some delicate parts of the brain, and surgery is not always an effective option and some cancers are chemoresistant [49]. Radiation and chemotherapy both have been very effective in treating certain cancers, however they result in significant and often long-term side effects due to damage to normal cells and organs [78]. While some novel therapies sometimes have fewer unpleasant side-effects, they often have to be administered in conjunction with more traditional methods leaving patients open to the same negative side effects [78]. Thus, novel therapies are always in high demand, especially for difficult to treat cancers and cancer complications, such as brain metastasis.

While the impermeability of the BBB is crucial for maintaining healthy brain physiology, it becomes an unwanted barrier to drugs and therapeutics during disease treatment [79]. Currently, the state-of-the-art treatments for secondary metastatic brain tumors include antibody-based and chemotherapy drugs [79]. Recently, those drugs have been coupled with stereotactic radiosurgery and whole-brain radiotherapy, which can also be used independently, in order to decrease the tumor burden and allow drugs to cross through the BBB [79]. Furthermore, magnetic resonance imaging and Raman spectroscopy have helped make significant advances in the accuracy of cancer therapies and thus minimized damage to surrounding brain tissue [79]. New studies have also shown that focused ultrasound can be used to temporarily disrupt the BBB and allow for drugs to enter the brain [80]. Yet, there is still a need for novel

therapies that would help stop tumor cells prior to invading the brain or target cells in the brain without damaging health cells. However, in order to use a promising therapy *in vivo* to target the complex process of metastasis, especially to the brain, it has to be fully understood and optimized. Thus, Chapter 6 of this dissertation addresses a new potential cancer therapy, cold-atmospheric plasma (CAP) and study its ability to selectively destroy tumor cells without damaging surrounding normal cells.

2.6.2 Cold-atmospheric plasma (CAP)

CAP has been proposed by several researchers as a potential selective treatment that can damage or destroy tumor cells while leaving normal cells unharmed [81]. CAP itself has been long used in the physics and materials engineering fields; however, its application in biomedicine is relatively recent. Plasma in general is formed during an increase in the energy of atoms [82], [83]. As the energy of atoms increases, matter transforms from a solid, to a liquid, to a gas, and subsequently to plasma, which is formed by a process known as ionization where the high energy results in an electron breaking away and creating a free electron and positively charged atom (Figure 2.3 A) [82], [83]. Thus, plasma is a high energy ionized gas, that is on average neutral, consisting of positively charged ions, electrons, and neutral particles [81]. As matter changes states, its temperature also changes [81]. Due to the frequent collisions of electrons and heavy particles in the plasma a thermal equilibrium is reached and most common plasma is of very high temperature [81]. However, CAP is a special category of plasma where the plasma discharge is very fast and does not reach thermal equilibrium, thus the temperature remains much lower [81]. The heavy particles in this plasma range in temperature

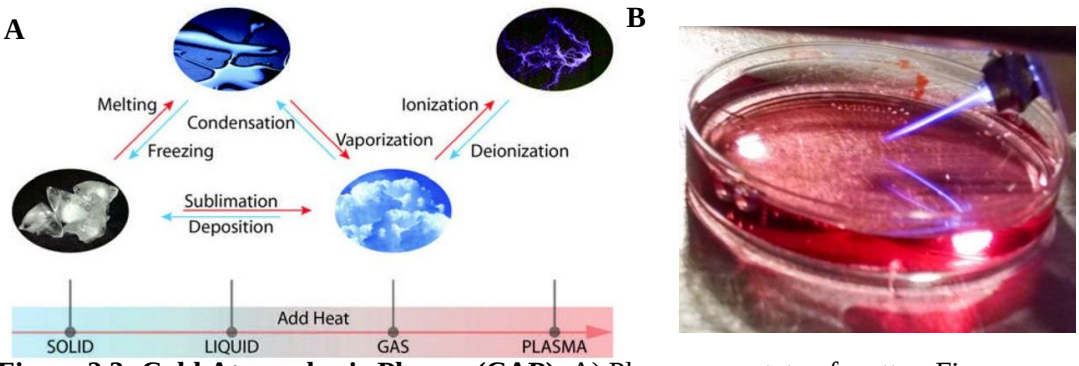

Figure 2.3: Cold Atmospheric Plasma (CAP). A) Plasma as a state of matter. Figure taken from [83] with permission from publisher (Creative Commons Attribution-NonCommercial-ShareAlike 4.0 License). B) Atmospheric pressure plasma jet (APPJ) CAP set-up in the process of CAP-treating cell culture medium. Image taken by Andrew Knoll.

from 25°C to 45°C and this type of plasma is preferred for use in biomedical applications, since the temperature range is physiologically appropriate [81]. CAP results in the formation of reactive oxygen and nitrogen species (ROS/RNS) which in turn then can become important for biological applications [81], [82]. It is important to note that while some of the reactive species have been identified, it is still not fully understood what specific combinations of reactive species are generated upon plasma treatment of various media, such as a liquid [84]. Thus, plasma treatments provide a unique modification of a surface or liquid which could not easily be replicated with other chemical or biological modifications. Furthermore, the species generated by plasma reactions are highly susceptible to modifications via changes in treatment type, time, gas types, and many other known and unknown parameters.

There exist various CAP devices which have become key for plasma medicine applications. They are generally separated into direct and indirect CAP categories [81], [82]. In a direct system, the sample being treated serves as one of the electrodes or is part of the dielectric and thus is a part of the discharge [81], [82]. In an indirect

system, a gas (air or added gas) is used to carry the plasma generated reactive species to the sample [81], [82]. One example of an indirect plasma source is as a plasma jet (Figure 2.3 B) where the plasma is formed between an anode and a cathode, one of which is covered by a dielectric material [81], [82]. In the jet system, gas, such as argon, can be introduced and the continuous flow of the gas results in a needle-like projection of plasma [81], [82]. Another example of an indirect plasma source is the surface micro discharge (SMD), where there is no carrying gas present just air and plasma is applied over a much larger area [85]. In a jet source, convection is the primary transport mechanism with a small degree of diffusion, while the SMD is entirely based on diffusion [85]. In an SMD source that uses room air as the working gas, the main reactive species produced are O_3, N_2O_5 , N_2O, and HNO_3 [86], while for a jet that uses argon as the working gas, the reactive species produced are also ROS/RNS but their exact composition is not fully known [84]. Other plasma sources fall into the hybrid category, where they incorporate some elements of direct and indirect sources [82].

Recently, CAP has been shown to selectively destroy tumor cells while preserving normal cells [82], [87]–[90]. While the process by which this occurs is still being investigated, one theory is that while a small amount of ROS/RNS might actually increase cell proliferation, once the levels cross a certain threshold, cell death occurs [91]. In tumor cells, the baseline amount of ROS/RNS is greater due to a lack of redox homeostasis, and thus when additional ROS/RNS are introduced, tumor cells are more likely to cross the threshold necessary for cell death (Figure 2.4) [91]. Thus, the same concentration of ROS/RNS introduced by CAP can be expected to damage

tumor cells and not harm normal cells (Figure 2.4) [91]. However, with some CAP treatment conditions, even healthy cells become damaged by CAP [84]. Furthermore, it has been suggested in prior studies that CAP affects tumor cells through aquaporin and integrin based mechanism [82], [92]. Additionally, a study has shown that CAP does not significantly damage astrocytes as compared to tumor cells [93] and increases or restores chemotherapy sensitivity in glioma cells [94], indicating that it could work as an additional therapy along with currently existing treatments brain-related applications. *In vivo* it is expected that direct CAP treatment could be effective for surface tumors, such as melanoma or other cancers that form closer to the surface of the skin. CAP-treated media, on the other hand, is proposed as a potential mechanism for treating tumor cells deeper in the body through administration into bodily fluid or catheterization. In fact, such a method could potentially be used to address circulating tumor cells in the circulatory and lymphatic systems, or could be adapted to be administered at or near the brain without significant damage to

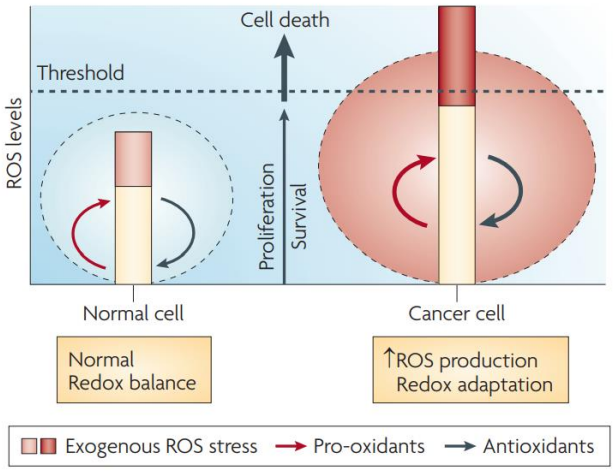

Figure 2.4: ROS and cell death. ROS from sources such as plasma can cause tumor cell death without destroying normal cells. Figure reprinted by permission from Springer Nature Customer Service Centre GmbH: Spring Nature, Nat. Rev. Drug Discov., Targeting cancer cells by ROS-mediated mechanisms: a radical therapeutic approach?, D. Trachootham, J. Alexandre, and P. Huang, 2009 [91].

surrounding sensitive tissue. CAP has been using for biomedical applications both directly, and through the use of CAP-treated media or buffer solution. Extensive literature exists discussing the biomedical implications of CAP in cancer therapy [82], angiogenesis [95]–[97], wound healing [98] and more. However, there is still a long road ahead to clinical translation of CAP in the cancer therapeutics field. In fact, in order to achieve successful translation and a potential future application in treating brain metastasis, the current *in vitro* methods for CAP cancer treatments have to be systematically optimized, which is still missing from plasma literature. Specifically, the generation of CAP-treated media has shown a lot of promise; however, since bodily fluids do not correspond exactly to any buffer or media condition, it is important to understand how CAP interactions with its *in vitro* culture environment affect CAP study outcomes, in order to understand how it will potentially be translated into a significantly less controlled and predictable *in vivo* setting. One of the important open questions in the plasma medicine, and specifically plasma cancer treatment field is: **which experimental parameters can alter the outcomes of CAP-based cancer treatment experiments and how does that relate to future *in vivo* applications?** Chapter 6 of this dissertation addresses some cell culture parameters that can affect the outcomes of CAP-based tumor cell treatment studies in order to establish some parameters that need to be considered when setting up CAP-based experiments.

2.7 Conclusion

Cancer metastasis is a devastating outcome of an already serious illness. Yet, despite huge progress in cancer therapeutics as well as understanding of cancer and

metastasis as a whole, a lot of the information necessary for developing successful therapies remains unknown. That is particularly true about metastasis to the brain, which can involve tumor cells crossing the highly impermeable BBB, and it remains a mystery how exactly that process occurs. Fortunately, there have been multiple successful studies that have shed light on some parts of the process, opening a path for further research into this field. This dissertation addresses some of the gaps in understanding of the physico-chemical interactions at the BBB during tumor metastasis. This dissertation focuses on biochemical cues from astrocytes (Chapter 3), biophysical interactions during incorporation (Chapter 4), and morphology of different metastatic clones (Chapter 5). Furthermore, this dissertation addresses the optimization of potential therapeutic approach, CAP, which has been tested for various cancer therapy applications, but optimization and validation is necessary before it can be translated *in vivo* (Chapter 6).

3 Astrocytes from the brain microenvironment alter migration and morphology of metastatic breast cancer cells†

3.1 Introduction

Metastasis to the brain is one of the most deadly aspects of breast cancer, leading to a particularly poor prognosis for patients [99]. As described inuring metastasis, breast tumor cells break away from the primary tumor, travel through the circulatory system, preferentially infiltrate the brain, and form secondary tumors, which are notoriously difficult to treat [99]. During metastasis, tumor cells encounter many heterogeneous microenvironments containing an array of biochemical and physical cues [100], both of which regulate the migration, mechanobiology, and signaling mechanisms used by tumor cells to navigate these environments [4]. In the case of brain metastasis, it has been shown that that astrocytes in the brain microenvironment promote brain metastasis and facilitate tumor cell invasion [15], [48], [49], [56], [101]. Here, we hypothesize that astrocyte-secreted biochemical cues regulate the morphology and migration of metastatic breast tumor cells, and that this effect depends on the astrocyte activation state, as well as the mechanical microenvironment of the tumor cells.

† This chapter is republished with permission of Fedn of Am Societies for Experimental Bio (FASEB) from M. A. Shumakovich, C. P. Mencio, J. S. Siglin, R. A. Moriarty, H. M. Geller, and K. M. Stroka, "Astrocytes from the Brain Microenvironment Alter Migration and Morphology of Metastatic Breast Cancer Cells," FASEB J., vol. 31, no. 11, pp. 5049–5067, 2017; permission conveyed through Copyright Clearance Center, Inc. C.P.M provided astrocyte conditioned media, J.S.S and R.A.M assisted with experiments and analysis.

In healthy physiology, astrocytes provide support for neurons by maintaining an ionic, neurotransmitter, amino acid, and water balance in the brain [12]. The end-feet of astrocytes support the blood-brain barrier (BBB) by assisting with the exchange of chemical signals between the circulatory system and the brain [12] and modulating the physiology of brain endothelial cells [12]. While astrocytes are important regulators of brain homeostasis, they also play a role in brain metastasis. Recently, it was reported that astrocyte-secreted serpins are involved in tumor cell survival during metastasis across the BBB *in vivo* [15]. Other reports have demonstrated an increased invasiveness of tumor cells in response to astrocyte-conditioned media (ACM), and they attributed this response to astrocyte-secreted matrix metalloproteinases (MMPs) [48]. Others yet have shown that astrocytes and tumor cells can form gap-junctions, which then transport molecular messages between the two cell types [49]. Furthermore, it has been reported that extracellular vesicles (EVs) secreted by astrocytes carry fibroblast growth factor-2 (FGF-2) and vascular endothelial growth factor (VEGF) [50], which have been shown to enhance tumor cell proliferation [51]. Together, these reports suggest that astrocytes interact with metastasizing tumor cells and thus influence brain metastasis.

While there exists evidence that astrocytes are involved in tumor cell metastasis across the BBB, it is unclear whether tumor cells react to signals from quiescent astrocytes or altered molecular signals from tumor cell-affected astrocytes. Interestingly, secretion of MMPs by astrocytes does not necessarily require two-way communication between tumor cells and astrocytes [48], and thus could be a part of the one-way paracrine signaling of astrocytes to tumor cells that we explore here.

MMPs are secreted by various cell types including both astrocytes and tumor cells, function to degrade the extracellular matrix, and are known to promote tumor cell splitting from a primary tumor, intravasation into the vasculature, and extravasation across capillary endothelial cells and the BBB [102]. Thus, MMPs secreted by astrocytes could act on breast cancer cells, or their extracellular matrix (ECM), to potentiate the metastatic phenotype.

Tumor metastasis across the BBB likely causes BBB damage, which may be similar to BBB damage following traumatic brain injury. A damaged BBB permits the infiltration of fibrinogen-bound TGF-β, which then activates astrocytes [54], leading to formation of glial scars that primarily consist of chondroitin sulfate proteoglycans (CSPGs) [54], and altering the astrocyte secretome [103]. The secretome of activated astrocytes is enriched in pro-inflammatory cytokines and other small molecules [104]. In the case of cancer, similar activation of fibroblasts supports cancer cell growth, motility and invasion [105], which suggests that astrocyte activation may also have a role in brain cancer metastases. Thus, we hypothesize that there would be differential effects of adding conditioned media from untreated astrocytes versus TGF-β-activated astrocytes to tumor cells.

In addition to biochemical cues, physical cues, such as physical confinement, also affect tumor cell migration. Metastasizing tumor cells encounter confined microenvironments when migrating through microtracks within tissues, through narrow brain capillaries which can be as small as 10 μm in diameter [106], through the brain endothelium, and along the blood vessel post extravasation across the endothelium [107]. Thus, understanding the effect of confinement on tumor cell

metastasis across the BBB is crucial. Prior studies by our lab demonstrated that an Aquaporin 5 (AQP5)-based mechanism drives the migration of metastatic breast tumor cells in confined channels [108], suggesting that tumor cell migration in 2D and in confinement utilizes different mechanisms. Thus, the effects of astrocyte-secreted factors on tumor cells could be different depending on the mode of migration employed by the tumor cells. Hence, we hypothesize that physical confinement alters the effects of ACM on tumor cell migration in a microfluidic model where ACM serves as a potential chemoattractant.

In order to test our aforementioned hypotheses regarding the effects of astrocyte-secreted factors on metastastic breast tumor cell migration and morphology, we applied ACM (from untreated or TGF-β-treated astrocytes) to tumor cells or their extracellular matrix and quantified cell migration and morphology parameters on 2D substrates or in confined microchannels. We show that ACM increases tumor cell migration and alters their morphology towards a more elongated and larger phenotype, with enhanced actin stress fiber organization. Furthermore, we show that pre-treating collagen substrates with ACM prior to seeding tumor cells results in significantly increased tumor cell velocity as compared to control cells, with increases in velocity that are more drastic than treating cells directly with ACM. Additionally, we show that ACM affects tumor cells differently depending on the relative activation state of the astrocytes, and that MMPs are likely to be at least partially responsible for the ACM-dependent increases in tumor cell migration. Interestingly, the effect of astrocyte-secreted factors is contingent on the physical microenvironment of the tumor cells.

3.2 Materials and Methods

3.2.1 Cell Culture

Human breast adenocarcinoma highly metastatic cells (MDA-MB-231), human breast adenocarcinoma metastatic cells (MDA-MB-468), human breast adenocarcinoma tumorigenic cells (MCF7), and human mammary gland non-cancerous epithelial cells (MCF10A) were purchased from American Type Culture Collection (Manassas, VA, USA). MDA-MB-231 and MCF7 cells were cultured in media consisting of Dulbecco's Modified Eagle's Medium (DMEM) with high glucose and pyruvate (ThermoFisher Scientific, Waltham, MA, USA), 10% Fetal Bovine Serum (FBS; HyClone Characterized GE Healthcare, Pittsburgh, PA, USA or ThermoFisher Scientific), and 1% Penicillin-Streptomycin 10,000 U/mL. MDA-MB-468 cells were cultured similarly, but with DMEM/F12, HEPES (ThermoFisher Scientific) instead of DMEM. MCF10A cells were cultured in media consisting of DMEM/F12, HEPES, 100 µg/ml endothelial growth factor (Sigma Aldrich, St. Louis, MO, USA) in 10 mM acetic acid, 1 mg/ml hydrocortisone (Sigma Aldrich) in 95% ethanol, 4 mg/ml insulin (ThermoFisher Scientific), 5% horse serum, New Zealand origin (ThermoFisher Scientific), and 1% Penicillin-Streptomycin 10,000 U/mL. Cells were washed with Phosphate-Buffered Saline (PBS) (VWR, Radnor, PA, USA), and detached with 0.25% Trypsin-EDTA (ThermoFisher Scientific). MDA-MB-231 and MCF7 cells were used up to a passage of 30 post-purchasing, and MDA-MB-468 and MCF10A cells were used up to passage 10 post-purchasing. All cells were cultured at 37˚C, 50% humidity, and 5% CO_2:95% air

3.2.2 Extracellular matrix Proteins and Coatings

In order to study the role of different extracellular matrix proteins on the effect of ACM on cells, several extracellular matrix conditions were examined. Cells were grown on glass coated with 300 μL of 20 μg/ml of the following extracellular matrix proteins: type I collagen from rat tail (Sigma Aldrich, St. Louis, MO, USA), type IV collagen from human cell culture (Sigma Aldrich), fibronectin from human plasma (Sigma Aldrich), laminin from human fibroblasts (Sigma Aldrich), or 20 μg/ml Poly-D-Lysine hydrobromide (PDL; stored at 1 mg/ml and dissolved in sterile MilliQ water) (Sigma Aldrich) for 1 hour at 37˚C, depending on the type of experiment. Following the incubation, wells with collagen type I or IV, fibronectin, or laminin, were washed three times with PBS, wells with laminin were washed with Hank's Balanced Salt Solution (HBSS) (ThermoFisher Scientific), and wells with PDL were washed with sterile MilliQ water.

3.2.3 Astrocyte Conditioned Media

Prepared by Dr. Caitlin Mencio, NIH.

All animal care and procedures were approved by the Institutional Animal Care and Use Committee at the National Heart, Lung, and Blood Institute and performed in accordance with their guidelines by Dr. Caitlin Mencio. None of the animal work was carried out by Marina Pranda or at the University of Maryland, College Park. Pregnant C57Bl/6 mice were procured from Charles River Laboratories (Wilmington, MA, USA). Primary cortical astrocyte cultures were prepared from neonatal (1–3 day old) C57BL/6 mouse brains as described previously [103]. In short,

the cerebral cortices were dissected out and dissociated into single cell suspension. Dissociated cells were seeded into T75 flasks and grown in DMEM with high glucose and pyruvate, 10% FBS, and 1% Penicillin-Streptomycin 10,000 U/mL, at 37°C and 5% CO_2:95% air atmosphere until cells grew to confluency (10–14 days later). Flasks were shaken for 20 hours (120 rpm, 37°C) to detach microglia, oligodendrocytes, and neurons from the more adherent astrocytes. After shaking, the medium was replaced with fresh media. This occurred again 24 hours after the end of shaking. After the second complete change of media, astrocyte conditioned media (ACM) was harvested every 48 hours and frozen until utilized. To harvest conditioned media from reactive astrocytes, the purified astrocytes were plated onto 6-well plates or T-25 flasks in serum containing medium. After once again reaching confluence, astrocytes were incubated in one of three conditions: 1) serum-free media overnight and then treated with 10 ng/mL TGF-β (Peprotech, Rocky Hill, NJ, USA) in serum-free media for 5 days before harvest; 2) serum-free media overnight and treated with 10 ng/mL TGF-β in serum-containing media for 5 days before harvest; 3) serum-containing media overnight and treated with 10 ng/mL TGF-β in serum-containing media for 5 days before harvest. Activation of astrocytes was confirmed (data not shown) in astrocytes cultured in serum-free media overnight and then treated with TGF-β (condition 1) by western blots for GFAP in astrocytes and CSPG in ACM performed as previously described [109]. The different conditioned medias collected from astrocytes were centrifuged at 300 g for 10 minutes and the supernatant was filtered using a 40 μm nylon cell strainer (VWR, Radnor, PA, USA) based on a published protocol [93]. The debris pellet was discarded.

3.2.4 MMP inhibition

To inhibit MMPs in ACM, the broad spectrum MMP inhibitor batimastat (BB94) (Sigma Aldrich, St. Louis, MO, USA) was used [110], [111]. Batimastat was diluted to 50 mM in Dimethyl Sulfoxide (DMSO) (Sigma Aldrich) and frozen in aliquots. For experiments, the 50 mM stock of batimastat was diluted to 0.1 μM, 1 μM, or 5 μM in ACM. DMSO was used as a vehicle control.

3.2.5 Addition of Exogenous MMP-2 and MMP-9

For some experiments, MMP-2 from humans (Sigma Aldrich, St. Louis, MO, USA) was diluted to 5 mg/ml in water and then diluted to 100 and 40 ng/ml in control media (25, 26). MMP-9 from humans (Sigma Aldrich) was diluted to 50 μg/ml in PBS and then diluted to 100 and 40 ng/ml in control media (25, 26). The extracellular matrix was pre-treated with MMP-2- or MMP-9-containing media. To increase cell numbers for the control condition (no MMPs), control data was pooled from both vehicle controls (water and PBS) since they were run on the same well plate and displayed no significant differences between them.

3.2.6 ROCK inhibition

For some experiments of the 10 μM Y27636 (Cayman Chemical, Ann Arbor, MI, USA) ROCK inhibitor was used. Y-27632 was added at the same time as ACM (for direct treatment of cells with ACM) and incubated with the cells for the duration of the time lapse experiment, or it was added when the cells were plated (for cells on ACM-treated collagen I) and incubated with the cells for the remainder of the time lapse experiment. DMSO was used as a vehicle control.

3.2.7 2D Migration Assays

Glass bottom 24-well cell culture plates (MatTek, Ashland, MA, USA**)** were coated with type I collagen, type IV collagen, fibronectin, laminin, or PDL, depending on the experiment**.** MDA-MB-231, MDA-MB-468, MCF7, or MCF10A cells (1×10^4 total) were plated in each well in experiments where cells were directly later treated with ACM, depending on the type of experiment. All experiments comparing cell morphology and migration on different extracellular matrix molecules were performed using MDA-MB-231 cells only. All experiments comparing the response of different cell lines to ACM were performed using type I collagen extracellular matrix. All other experiments were performed using MDA-MB-231 cells and a type I collagen extracellular matrix. Cells were incubated at 37˚C, 50% humidity, and 5% CO_2:95% air overnight. The next day, media was changed to ACM, control media, or control media or ACM with batimastat, TGF-β, DMSO, water, PBS, MMP-2, or MMP-9, depending on the type of experiment. In some experiments, 10 ng/ml of TGF-β was directly added to ACM, control media, and serum free media in order to compare results to the ACM from TGF-β-treated astrocytes. For ACM pre-treatment of extracellular matrix protein or PDL, ACM or control media with DMSO, water, PBS, MMP-2, or MMP-9, depending on the type of experiment, was added directly to the extracellular matrix and incubated overnight at 37˚C, 50% humidity, and 5% CO_2:95% air. On the following day, the extracellular matrix was washed three times with PBS, HBSS, or water, depending on the extracellular matrix, and 1×10^4 MDA-MB-231, MDA-MB-468, MCF7, or MCF10A cells were plated, depending on the type of experiment. Cells seeded on pre-treated extracellular matrix

were allowed to attach for three hours prior to imaging. MDA-MB-231, MDA-MB-468, MCF7, or MCF10A cells (5×10^4 total) were plated in the same conditions as discussed above on extracellular matrix-coated glass bottom dishes for staining with phalloidin, as discussed below.

3.2.8 Timelapse and Phase Imaging

Images were acquired on an Olympus IX83 microscope (Olympus, Center Valley, PA, USA) using a 10× objective. In order to maintain the cells alive during the imaging, a chamber calibrated to 37˚C, 50% humidity, and 5% CO_2:95% air was used on the microscope stage. Images were taken at 5 - 10 minute intervals (as described in detail in figure captions). On the following day, a collection of phase contrast images was taken using a 20× objective.

3.2.9 Microfabrication

We have previously reported the procedure to fabricate microfluidic devices containing channels of varying width [108],[112],[113]. All fabrication was carried out in the University of Maryland microfabrication facility using photolithographic methods. Briefly, a mask was designed in AutoCAD (AutoDesk, San Rafael, CA, USA). Four-inch diameter silicon wafers (University Wafer, Boston, MA, USA) were spin coated with SU-8 (negative photoresist) 3010 and 3025 in two layers (MicroChem, Westborough, MA, USA) for the cell seeding and confinement channels, respectively. For each layer, an EVG620 Mask Aligner (EVG Group, Albany, NY, USA) was used to crosslink the photoresist with ultraviolet light (UV) through the mask. The non-crosslinked photoresist was developed away. After

fabrication, the wafer surface was silanized with tridecafluoro 1,1,2,2,tetrahydrooctyl-1-trichlorosilane (97%) (Pfaltz & Bauer, Waterbury, CT, USA) overnight. This process resulted in a silicone wafer with raised channels of 50, 20, 10, 6, and 3 μm widths (data shown for 50, 10, and 3 μm widths), 200 μm length, and approximately 10 μm height. Polydimethylsioloxane (PDMS) was mixed to a 10:1 ratio of elastomer base and elastomer curing agent from a Silicon Elastomer Kit (Robert McKeown Company, Branchburg, NJ, USA), degassed in a vacuum chamber for approximately one hour, and baked at 80ºC until cured, approximately two hours. The PDMS devices, along with 35 mm by 75 mm #1.5 glass coverslips, were then cleaned with ethanol, reverse osmosis treated water, and then ethanol again. They were then treated by plasma using a plasma cleaner (Harrick Plasma, Ithaca, NY, USA) and pressed together for bonding. The fabrication process resulted in a chemotactic device with 4 inlet wells. Cells were seeded in the bottom-most well, and a chemoattractant was added to the top-most well, as described in the following section.

3.2.10 Microchannel Assay

Microfabricated devices containing microchannels were incubated with type I rat tail collagen (20 μg/mL) for one hour at 37˚C and then washed three times with PBS. MDA-MB-231 cells (1x105 cells suspended in 25 μL of either serum free media or full media, depending on the experimental condition) were then seeded into the inlet of the microfluidic device and incubated for 5-10 minutes to allow the cells to loosely attach. Then, the remaining media was taken out and replaced by 60-80 μL (per well) of either serum-containing media in all wells of the device, or serum-free media in all wells except the topmost one, which contained serum. In both cases, the

top channel contained either serum-containing control media or ACM. The following chemoattractant conditions were considered: serum alone (positive control since serum is a chemoattractant for MDA-MB-231 cells), serum-containing ACM alone, serum-containing ACM with serum as additional chemoattractant, and no chemoattractant (all wells with serum-containing control media as a negative control). Two general set-ups were used: 1) tumor cells were seeded in serum-free media, and serum-containing ACM or serum-containing control media was used as a chemoattractant in the topmost channel. In some cases, cells were pre-incubated in ACM for 1-4 days and seeded similarly with serum-containing ACM as the chemoattractant. 2) tumor cells were seeded in serum-containing control media and either serum-containing ACM or serum-containing control media was used as the chemoattractant or negative control, respectively, in the topmost channel. The cells were then imaged live using time lapse microscopy at 37˚C, 50% humidity, and 5% CO2:95% with 10 minute intervals.

3.2.11 Cell Staining

Cells were washed once with PBS and fixed with 3.7% formaldehyde (FisherScientific, Fair Lawn, NJ, USA) for 10 minutes. Following fixation, cells were washed three times with PBS. Cells were then permeabilized with 1% Triton X-100 (Sigma Aldrich) for 5 minutes at room temperature. Cells were washed again three times with PBS. Cells were then blocked for non-specific binding with 2.5% bovine serum albumin (BSA) (Sigma Aldrich) for at least an hour. Cells were then incubated with 1:500 Alexa Fluor 488 conjugated to phalloidin (ThermoFisher Scientific) and

1:2500 Hoechst 33342 (ThermoFisher Scientific) in PBS for one hour at room temperature. After staining, cells were washed three times with PBS.

3.2.12 Confocal Microscopy

Stained samples were imaged via either a Zeiss LSM 710 confocal microscope (Zeiss, Oberkochen, Germany) using a 60× oil immersion objective, or an Olympus FV3000 confocal microscope (Olympus) in resonance scanning mode with deconvolution using an appropriate filter and a 100× silicone immersion objective. Confocal images were reconstructed in ImageJ software (https://imagej.nih.gov) into a three-dimensional image using a maximum intensity projection. Intensities of corresponding control media-ACM image pairs were adjusted equally in ImageJ, as noted in the figure caption.

3.2.13 Data Analysis

Data were analyzed using the ImageJ software. Morphology of cells was measured by first manually tracing the outlines of cells imaged via phase contrast microscopy using a 20× objective, as we have previously described in Stroka et al, 2016[114]. Briefly, cell "inverse aspect ratio" was calculated by dividing the length of the minor axis of the cell by the length of the major axis of the cell. Cell circularity was defined $\frac{4\pi A}{P^2}$, where A is the area of the cell and P is the perimeter of the cell, both of the cell projections in phase contrast images. Cell solidity was defined as the ratio $\frac{A_{cell}}{A_{convex}}$, where A_{cell} is the area of the cell and A_{convex} is the convex area of the cell. These parameters are further described in Appendix A.

Positions of cells both in 2D and in confinement were evaluated by tracking cells using the "Manual Tracking" ImageJ plug-in. The approximate centroid of each cell was tracked over 300-670 minutes (for 2D assays, as stated in detail in figure captions) or 15 hours (for confinement assays). 5-10 minute time intervals were used between images, as stated in figure captions. Cells were not tracked if they divided, went out of the frame, or were significantly obstructed by an artifact or another cell. MCF7 and MCF10A cells that formed clusters were not analyzed and only single cells were selected for analysis. Migration analysis was started on the frames where cells appeared to have attached. A custom MATLAB (Mathworks, Natick, MA, USA) code was used to calculate velocities of the cells using output from the ImageJ tracking. The average velocity of cells in 2D was quantified by calculating the instantaneous velocities between every set of two points and then averaging the individual instantaneous velocities over all timepoints. The mean square displacement (MSD) was reported for 500 minutes and the diffusion coefficient was obtained from a Langevin-type fit [115] carried out in MATLAB to the mean square displacement curve over 200-268 minutes. MSD was calculated as the average of the square of the distance traveled using a sliding time average, and as described in Appendix B [115]. The sliding time average was obtained by averaging the MSD values for every time interval and thus obtaining the MSD at each time point [115]. The Langevin-type equation used was as follows: $r^2 = 4D\left(t - \tau\left(1 - e^{-1/\tau}\right)\right)$, where D is the diffusion (or random motility) coefficient, r^2 is the two-dimensional MSD, t is time, and τ is the persistence time, and as described in Appendix B [115]. In confinement, speed was calculated in the same way as 2D velocity, with no consideration for whether the cell

is moving toward or away from the chemoattractant. The chemotactic index (CI) was calculated by dividing the end-to-end distance of a cell from the beginning and end of tracking by the sum of the distances between all the points as follows:

$CI = \frac{\sqrt{(x_{end} - x_{start})^2 + (y_{end} - y_{start})^2}}{\sum\sqrt{(x_{j+1} - x_j)^2 + (y_{j+1} - y_j)^2}}$ and as described in Appendix B. The chemotactic index ranges from 0 to 1, where 1 indicates that the cell is moving completely straight (i.e., persistently). To compare the increase in velocities of ACM-treated conditions when cells were treated directly and when collagen was pre-treated with ACM, the percent change was calculated as by obtaining the difference between the velocities of cells in the ACM-treated conditions and the velocities of cells in the control media-treated conditions and dividing by the reference value, which is the control media-treated condition. These parameters are further described in Appendix B. This was carried out for each of three trials for the ACM-treated cells and collagen sets of data as follows: % change = $\frac{V_{ACM} - V_{Control}}{V_{Control}} x100\%$, where V is velocity.

3.2.14 Statistics

Three independent trials were conducted for each experiment unless otherwise stated in the caption. Cells from all three experiments were pooled. Normality was assumed due the large sample size, which allows for parametric statistical analyses. For comparison of more than two groups of data, a one-way Analysis of Variance (ANOVA) test was performed in GraphPad (GraphPad, San Diego, CA), with a Tukey post-hoc test for multiple comparisons. A two-sided Welch's t-test was used to compare means of two-category results in GraphPad. A frequency analysis in

GraphPad was used to generate histograms. A 95% confidence interval with $P<0.05$ was used as the significance cutoff for all statistical tests. Cumulative distribution functions were tested for statistical significance using the two-sample Kolmogorov-Smirnov test with $P<0.05$ indicating significantly different distributions.

3.3 Results

3.3.1 ACM alters metastatic breast tumor cell morphology and migration

Astrocyte-secreted factors can reportedly enhance tumor cell invasion and metastatic potential[48], though the details of these effects are poorly understood. In order to corroborate previous reports regarding ACM-induced cell migration and identify whether these effects are accompanied by changes in tumor cell morphology, MDA-MB-231 cells were seeded on type I collagen-coated glass, allowed to attach overnight, and on the following day, culture media was replaced with ACM and incubated overnight (~16 hours) (Figure 3.1 A). Type I collagen was chosen as a substrate for preliminary experiments due to the fact that cell migration and

---

Figure 3.1: **Morphology and migration of ACM-treated tumor cells**. For all images and plots: Black=Control Media; Red=ACM A) Diagram of experimental set-up, showing MDA-MB-231 cells plated on type I collagen on glass on day 1, and media replaced with ACM on day 2. B) Representative phase contrast images of MDA-MB-231 cells treated with control media (left) or ACM-treated cells (right). Scale bar represents 20 μm and applies to both images. C) Cell areas and D) circularities, inverse aspect ratios, and solidities of the MDA-MB-231 cells treated with control media or ACM. n(control)=1800 cells; n(ACM)=2045 cells. E) Trajectories of all the cells treated with control media or ACM (5-minute time intervals). F) Cumulative distribution function plot of cell velocities when treated with control media or ACM. n(control)=272 cells; n(ACM)=300 cells, G) Average cell velocities tracked for 500 minutes with a 5-minute time interval, H) mean square displacement over 500 minutes, and I) diffusion coefficients obtained from a Langevin-type fit to the mean square displacement plot over 200 minutes, of cells treated with control media or ACM. n(control)=272 cells; n(ACM)=300 cells. 5-minute time interval. Statistical analysis carried out using an unpaired t-test using a Welch's t-test with $p<0.05$ (* $p<0.05$; ** $p<0.01$; *** $p<0.001$; **** $p<0.0001$). In all plots, bars indicate mean of pooled data from $N\geq3$ independent experiments, and error bars represent standard error of the mean.

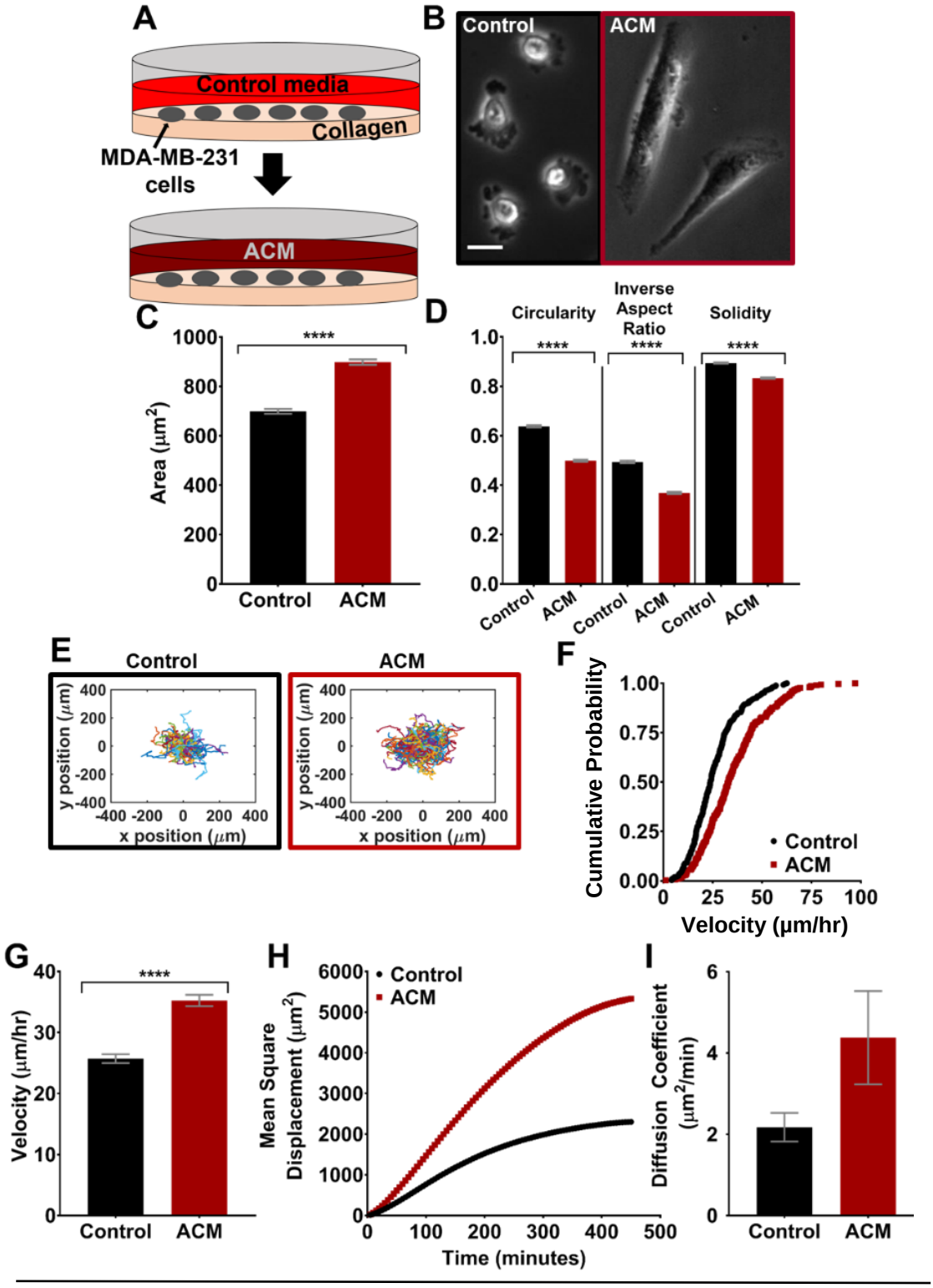
A
Control media
Collagen
MDA-MB-231 cells
ACM
B
Control
ACM
C
Area (μm²)
Control
ACM
****
D
Circularity
Inverse Aspect Ratio
Solidity
****
Control
ACM
E
Control
ACM
y position (μm)
x position (μm)
F
Cumulative Probability
Velocity (μm/hr)
Control
ACM
G
Velocity (μm/hr)
****
Control
ACM
H
Mean Square Displacement (μm²)
Time (minutes)
Control
ACM
I
Diffusion Coefficient (μm²/min)
Control
ACM

morphology on this extracellular matrix have been well characterized in the literature [116]–[119]. Phase contrast images revealed that ACM-treated cells were larger and more elongated than control cells (Figure 3.1 B); this observation was confirmed quantitatively, with ACM-treated cells having significantly larger cell areas (Figure 3.1C) and aspect ratios (Figure 3.1 D).

The trajectories of tumor cells treated with control media or ACM overnight on type I collagen-coated glass indicated that the population of ACM-treated cells migrated over a larger area than control media-treated cells (Figure 3.1 E). Cumulative distribution functions of velocities for control and ACM-treated cells were significantly different when tested with the two-sample Kolmogorov-Smirnov test, with a shift towards increased velocity for cells treated with ACM (Figure 3.1 F). Further, the average velocity of ACM-treated cells was significantly greater (Figure 3.1 G) than those of control media-treated cells, and the ACM-treated cells also had larger MSD versus time (Figure 3.1 H), and diffusion coefficient (Figure 3.1 I) in comparison with control cells.

Media conditioned by astrocytes could be depleted of nutrients, including serum, in addition to being enriched in other soluble factors produced by the astrocytes. To evaluate the possible effects of the concentration of soluble factors in ACM on tumor cell morphology and migration, ACM was diluted to 5, 10, 20, 50, and 75% using serum-containing control media. Serum-free media was included as a control in order to test a nutrient deficient condition. Tumor cells were seeded on type I collagen-coated glass, allowed to attach overnight, and on the following day, culture media was replaced with either ACM at varying dilutions, control media, or serum

free media, and incubated overnight. Tumor cell areas increased with increased ACM concentration (Figure 3.2 A), suggesting the presence of a soluble factor influencing tumor cell morphology. Areas (Figure 3.2 A), circularities, inverse aspect ratios, and solidities (Figure 3.2 B) were all significantly different from the control media at ACM concentrations above 20% ACM. The velocities of the tumor cells were higher in concentrations of 50% ACM and above compared to the control (Figure 3.2 C). The diffusion coefficient of ACM-treated cells also tended to increase with ACM concentration, though this relationship was not statistically significant (Figure 3.2 D). While tumor cells treated with serum-free media had similar morphologies to 100% ACM (Figure 3.2 B), they did not display increased migration potential, and further showed no differences in velocity or diffusion coefficient in comparison with cells treated with serum-containing control media (Figure 3.2 C, D). Hence, we conclude that the effect of ACM on cell migration is likely due to soluble factors present in ACM and not due to serum depletion.

3.3.2 ACM-induced changes in extracellular matrix alter metastatic breast tumor cell migration

Our results herein and the work of others indicate that ACM applied directly to MDA-MB-231 tumor cells can increase tumor cell migration potential. However, no studies have yet evaluated the effects of astrocyte-secreted factors on the extracellular matrix. Thus, type I collagen was pre-treated with ACM prior to seeding MDA-MB-231 cells (Figure 3.3 A). In these experiments, the area of the tumor cells did not increase on ACM-treated type I collagen as it did when cells were treated

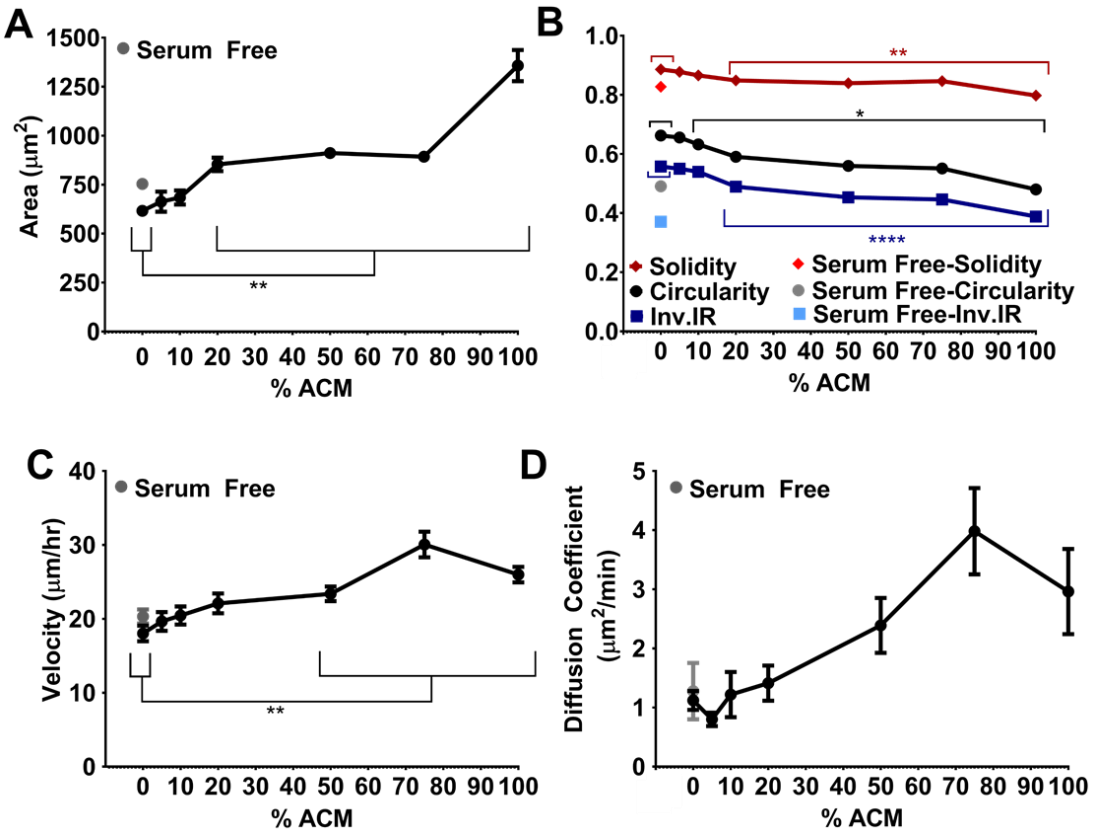

Figure 3.2: **Morphology and migration of ACM-treated tumor cells with different ACM dilutions.** A) Areas and B) circularity, inverse aspect ratio, and solidity (right) of the MDA-MB-231 cells (on type I collagen) treated with control media or 5-100% ACM. n(serum free) = 682; n(0% ACM)=1010; n(5% ACM)=689; n(10% ACM)=663; n(20% ACM)=634; n(50% ACM)=1025; n(75% ACM)=476; n(100% ACM)=896 cells. C) Velocities and D) diffusion coefficient (right), obtained from a Langevin-type fit to a mean square displacement curve over 200 minutes. n(serum free) = 96; n(0% ACM)=157; n(5% ACM)=102; n(10% ACM)=109; n(20% ACM)=83; n(50% ACM)=165; n(75% ACM)=54; n(100% ACM)=187 cells. 5-6.7 minute time intervals. Statistics carried out using a one-way ANOVA and Tukey's post-hoc analysis with $p<0.05$. (* $p<0.05$; ** $p<0.01$; *** $p<0.001$; ****$p<0.0001$). In all plots, individual points indicate mean of pooled data from $N\geq3$ independent experiments, and error bars represent standard error of the mean. Note that some error bars not visible because the size of the point marker is larger than the error bars. Jonathan Siglin assisted with some experiments and data analysis.

directly with ACM. Of additional morphology parameters, inverse aspect ratio significantly increased when the collagen was pre-treated with ACM (Figure 3.3 C), which was opposite the effect when cells were treated directly with ACM. Meanwhile, area (Figure 3.3 B) and other morphology parameters (Figure 3.3 C) did not change significantly. However, most notably, we observed a substantial increase in tumor cell migration on ACM-treated type I collagen substrates, with cell trajectories showing tumor cells on ACM-treated type I collagen migrating over a larger area than cells on control media-treated type I collagen (Figure 3.3 D). Cumulative distribution functions of velocities for cells migrating on control and ACM-treated extracellular matrix were significantly different when tested with the two-sample Kolmogorov-Smirnov test, with a shift towards increased velocity for cells on ACM-treated extracellular matrix (Figure 3.3 E). Quantitatively, there was a significant increase in tumor cell average velocity (Figure 3.3 F), MSD (Figure 3.7 G), and diffusion coefficient (Figure 3.7 H); this increase in migration was even greater than when cells were treated directly with ACM, as indicated by the comparison of a percent increase in velocity of 36% for ACM-treated cells versus 92% for ACM-treated type I collagen as compared to control-media treatments (Figure 3.7 I).

3.3.3 Cells of varying tumorigenic and metastatic potential respond uniquely to ACM

To determine whether cell response to ACM is conserved over multiple cell lines, we repeated migration and morphology experiments on several additional cell lines, including (1) the weakly metastatic human breast tumor cell line, MDA-MB-

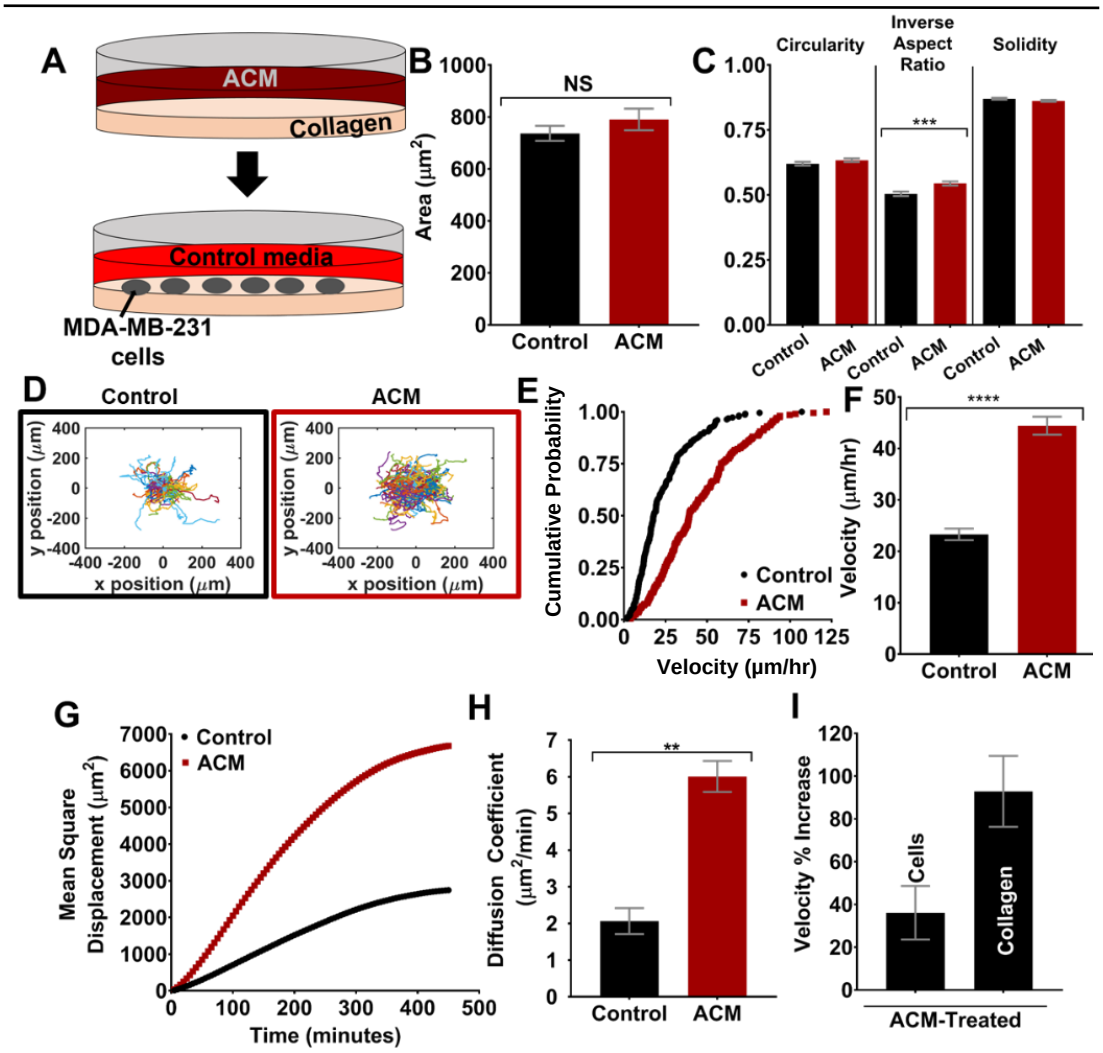

Figure 3.3: **Morphology and migration of tumor cells on ACM-treated extracellular matrix.** For all images and plots: Black=Control Media; Red=ACM A) Diagram of experimental set-up, showing type I collagen plated and treated with ACM on day 1, and on day 2 MDA-MB-231 cells plated in control media. B) Quantification of cell areas and C) circularity, inverse aspect ratio, and solidity of MDA-MB-231 cells plated on control media or ACM-treated type I collagen. n(control)=716 cells; n(ACM)=742 cells. D) Trajectories of all the cells on collagen treated with control media (left) or ACM (right). n(control)=223 cells; n(ACM)=201 cells. E) Cumulative distribution function plot of cell velocities on control- or ACM-treated type I collagen. Also shown is quantification of F) average cell velocities, G) mean square displacement with 5 minute intervals over 500 minutes, and H) diffusion coefficient, obtained from a Langevin-type fit to the mean square displacement curve over 200 minutes, of MDA-MB-231 cells on control media or ACM-treated type I collagen. I) Comparison of percent increase in velocity between ACM-treated and control media-treated conditions of the ACM-treated cells and ACM-treated type I collagen experiments. Statistical analysis carried out using an unpaired t-test using a Welch's correlation with $p<0.05$. (* $p<0.05$; ** $p<0.01$; *** $p<0.001$; ****$p<0.0001$). In all plots, bars indicate mean of pooled data from $N\geq3$ independent experiments, and error bars represent standard error of the mean.

468; (2) the tumorigenic but non-metastatic breast tumor cell line, MCF7; and (3) the normal breast epithelial cell line, MCF10A. We selected these additional cell lines to (a) evaluate the effects of ACM on an additional metastatic breast tumor cell line, and (b) evaluate whether ACM can alter the morphology and/or increase the migration of non-metastatic breast tumor cells, or even normal breast epithelial cells. Migration assays on both type I collagen (and also on fibronectin; data not shown) revealed that MCF7 and MDA-MB-468 cells were non-migratory (velocities less than 10 μm/hr, which is mostly due to small random displacements in place rather than true migration), and addition of ACM to either the cells or their extracellular matrix did not promote migration. Meanwhile, direct treatment of MCF10A cells with ACM led to a statistically significant increase in cell migration velocity (Figure 3.4 A), while

---

Figure 3.4: **Morphology and migration of cells of varying metastatic potential either treated with ACM or on ACM-treated extracellular matrix.** For all images and plots: Black=Control Media; Red=ACM. Velocities of MCF10A cells on type I collagen when the cells were A) treated with control media or ACM (n(control)=100 cells; n(ACM)=110 cells) and B) seeded on type I collagen pre-treated with control media or ACM (n(control)=118 cells; n(ACM)=118 cells). Statistical analysis carried out using an unpaired t-test using a Welch's correlation with $p<0.05$. (* $p<0.05$). C) Percent change in velocities of cells of MCF10A cells when treated with control media or ACM or seeded on type I collagen that was pre-treated with control media or ACM. Cell migration was analyzed over 5 hours with 10 minute intervals between frames. D) Areas and E) corresponding circularities, inverse aspect ratios, and solidities of MCF10A, MCF7, and MDA-MB-468 cells on type I collagen when the cells were treated with control media or ACM (n(control, MCF10A)=120 cells; n(ACM, MCF10A)=69 cells; n(control, MCF7)=206 cells; n(ACM, MCF7)=161; n(control, MDA-MB-468)=492 cells; n(ACM, MDA-MB-468)=380 cells). F) Areas and G) corresponding circularities, inverse aspect ratios, and solidities of MCF10A, MCF7, and MDA-MB-468 cells seeded on type I collagen that was pre-treated with control media or ACM (n(control, MCF10A)=158 cells; n(ACM, MCF10A)=139 cells; n(control, MCF7)=562 cells; n(ACM, MCF7)=389 cells; n(control, MDA-MB-468)=646 cells; n(ACM, MDA-MB-468)=700 cells). Note that for all experiments, only single cells were analyzed and cells that formed clusters were excluded. Statistical analysis was performed using a Tukey's multiple comparison post-hoc test with $p<0.05$. (* $p<0.05$; ** $p<0.01$; *** $p<0.001$; ****$p<0.0001$). In all plots, bars indicate mean of pooled data from N=2 independent experiments, and error bars represent standard error of the mean with $p<0.05$. (* $p<0.05$; ** $p<0.01$; *** $p<0.001$; ****$p<0.0001$). In all plots, bars indicate mean of pooled data from $N\geq3$ independent experiments, and error bars represent standard error of the mean. Rebecca Moriarty assisted with experiments and analysis.

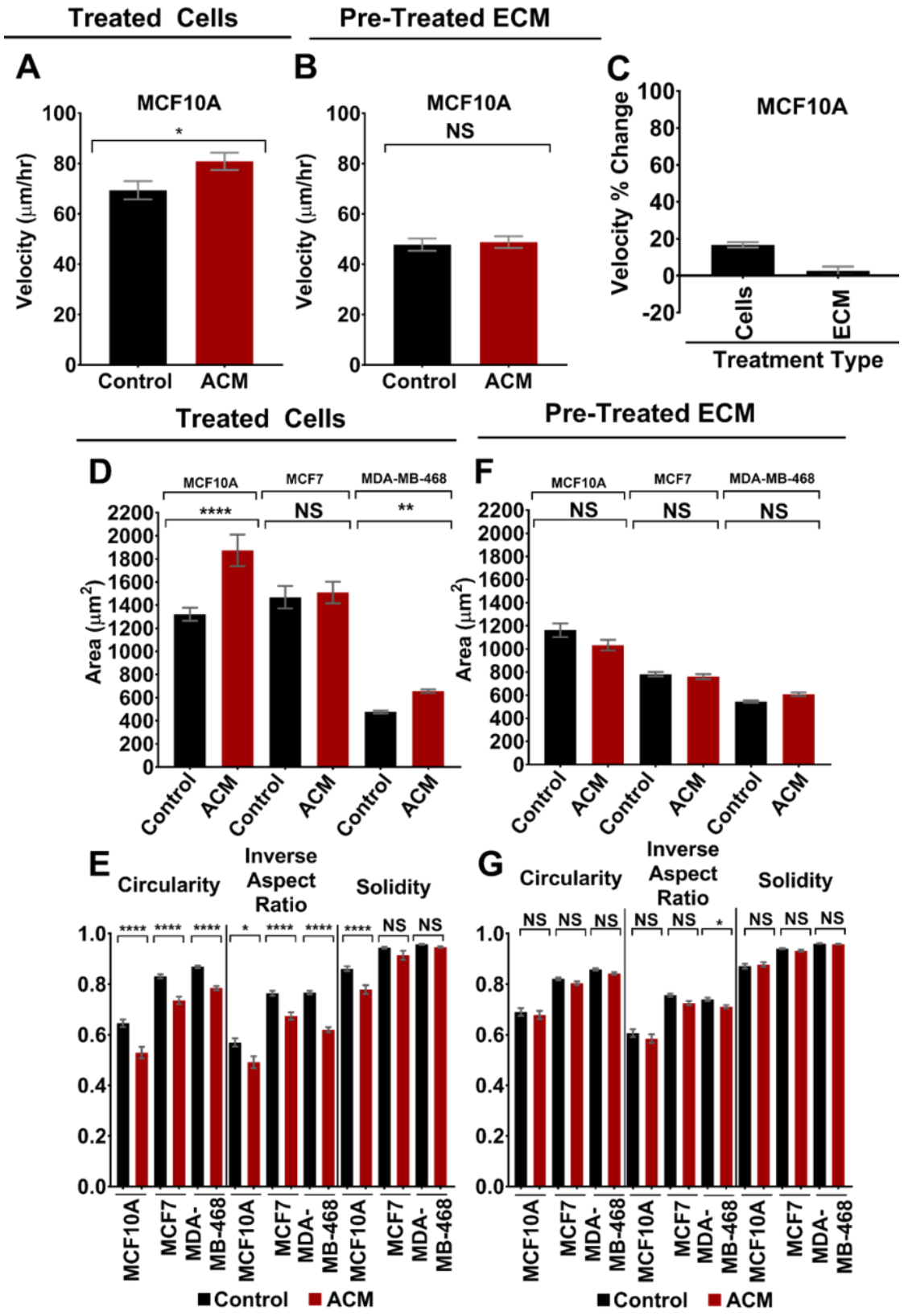
Treated Cells
Pre-Treated ECM
A
MCF10A
Velocity (μm/hr)
Control
ACM
B
MCF10A
NS
C
MCF10A
Velocity % Change
Cells
ECM
Treatment Type
Treated Cells
Pre-Treated ECM
D
MCF10A
MCF7
MDA-MB-468
****
NS
**
Area (μm²)
F
NS
E
Circularity
Inverse Aspect Ratio
Solidity
G
Control
ACM

MCF10A cells plated on ACM-treated type I collagen substrates demonstrated no change in cell migration velocity (Figure 3.4 B). Thus, for MCF10A cells, the percent change in velocity from control to ACM was significantly more positive for the condition in which cells were directly treated with ACM, in comparison with ACM-treated extracellular matrix (Figure 3.4 C). These results differ from MDA-MB-231 cells (Figure 3.3 I), suggesting that the effects of ACM (either directly on cells or treatment of extracellular matrix) on cell migration may be dependent on cell type and degree of tumorigenicity or metastatic potential.

Meanwhile, for all additional cell lines, we observed mostly similar trends in morphological changes (i.e. same trends as MDA-MB-231 cells on type I collagen in Figures 3.1 and 3.3) in cells treated directly with ACM, and also cells plated on ACM-treated type I collagen substrates (Figure 3.4 D, E, F, G). More specifically, direct treatment of cells with ACM resulted in statistically significant increases in cell area, along with decreases in inverse aspect ratio, circularity, and solidity for MCF10A and MDA-MB-468 cell lines (similar to MDA-MB-231 cells in Figure 1 B, C, D) (Figure 3.4 D, E). Meanwhile, direct treatment of MCF7 cells with ACM resulted in no difference in cell area or solidity, but decreased inverse aspect ratio and circularity (Figure 4 D, E). We also observed some minor (or no) changes in cell morphological parameters in cells plated on ACM-treated type I collagen substrates, but these were much less significant than in cells treated directly with ACM (Figure 3.4 F, G), which is also consistent with what we observed for MDA-MB-231 cells (Figure 3.3 B, C). Hence, the effects of ACM (either direct treatment of cells or

treatment of the collagen substrate) on cell morphology seem to be conserved across multiple breast cell lines and cell lines with varying tumorigenic and metastatic potential.

3.3.4 Cell response to ACM is conserved on multiple extracellular matrix proteins

In order to test whether the response of cells was unique to type I collagen, or whether it was conserved across multiple extracellular matrix proteins, we repeated the morphology and migration experiments using MDA-MB-231 cells plated on several additional extracellular matrix proteins that are present in the BBB microenvironment, including fibronectin, laminin, and type IV collagen. The migration assays demonstrated that there was no significant increase in MDA-MB-231 cell velocity when cells (on fibronectin, laminin, or collagen IV) were treated directly with ACM (Figure 3.5 A), unlike on type I collagen, where an increase in cell migration velocity was observed (Figure 3.1 G). However, for fibronectin and laminin, there was a statistically significant increase in cell migration velocity on substrates pre-treated with ACM (Figure 3.5 B). The more pronounced increase in migration on ACM-treated fibronectin and laminin substrates (in comparison with cells directly treated with ACM; Figure 3.5 C) is consistent with our migration results on type I collagen (Figure 3.3 I). Interestingly, we did not observe any statistically significant changes in migration velocity for any conditions on collagen IV (Figure 3.5 A, B), suggesting that there may be differential migration-induced effects of the ACM on various extracellular matrix or basement membrane proteins. Notably, MDA-MB-231 cells plated on each of fibronectin, laminin, and type IV collagen

and treated directly with ACM demonstrated significant morphological changes (similar to results on type I collagen), including increases in cell area and decreases in inverse aspect ratio, circularity, and solidity (Figure 3.5 D, E). Meanwhile, morphological changes in MDA-MB-231 cells plated on ACM-treated fibronectin, laminin, and type IV collagen substrates were either not significantly different, or less so than for the case of cells directly treated with ACM (e.g., p-value closer to 0.05) (Figure 3.5 F, G). These results are also consistent with our results for type I collagen (Figures 3.3 B, C).

Figure 3.5: **Morphology and migration of ACM-treated tumor cells and tumor cells on ACM-treated extracellular matrices with varying binding moieties.** For all images and plots: Black=Control Media; Red=ACM. Velocities of MDA-MB-231 cells on type IV collagen, fibronectin, laminin, and PDL when the cells were A) treated with control media or ACM (n(control, type IV collagen)=127 cells; n(ACM, , type IV collagen)=152 cells; n(control, fibronectin)=133 cells; n(ACM, fibronectin)=142 cells; n(control, laminin)=118 cells; n(ACM, laminin)=131 cells; n(control, PDL)=73 cells; n(ACM, PDL)=58 cells) and B) seeded on extracellular matrix pre-treated with control media or ACM (n(control, type IV collagen)=131 cells; n(ACM, , type IV collagen)=155 cells; n(control, fibronectin)=141 cells; n(ACM, fibronectin)=151; n(control, laminin)=116 cells; n(ACM, laminin)=129 cells; n(control, PDL)=62 cells; n(ACM, PDL)=83 cells). C) Percent change in velocities of cells of MDA-MB-231 cells when seeded on type IV collagen, fibronectin, laminin, or PDL and treated with control media or ACM or seeded on extracellular matrix that was pre-treated with control media or ACM. Cell migration was analyzed over 5 hours with 10 minute intervals between frames. D) Areas and E) corresponding circularities, inverse aspect ratios, and solidities of MDA-MB-231 cells on type IV collagen, fibronectin, laminin, and PDL when the cells were treated with control media or ACM (n(control, type IV collagen)=578 cells; n(ACM, type IV collagen)=578 cells; n(control, fibronectin)=704 cells; n(ACM, fibronectin)=559 cells; n(control, laminin)=436 cells; n(ACM, laminin)=363 cells; n(control, PDL)=220 cells; n(ACM, PDL)=208 cells). F) Areas and G) corresponding circularities, inverse aspect ratios, and solidities of MDA-MB-231 cells seeded on extracellular matrix pre-treated with control media or ACM (n(control, type IV collagen)=560 cells; n(ACM, type IV collagen)=642 cells; n(control, fibronectin)=526 cells; n(ACM, fibronectin)=733 cells; n(control, laminin)=556 cells; n(ACM, laminin)=585 cells; n(control, PDL)=162 cells; n(ACM, PDL)= 225 cells). Statistical analysis was performed using a Tukey's multiple comparison post-hoc test with $p<0.05$. (* $p<0.05$; ** $p<0.01$; *** $p<0.001$; **** $p<0.0001$). In plots for type IV collagen, fibronectin, and laminin, bars indicate mean of pooled data from $N\geq3$ independent experiments while in plots for PDL bars indicate mean of pooled data from $N\geq2$ independent experiments, and error bars represent standard error of the mean. Rebecca Moriarty assisted with experiments and analysis.

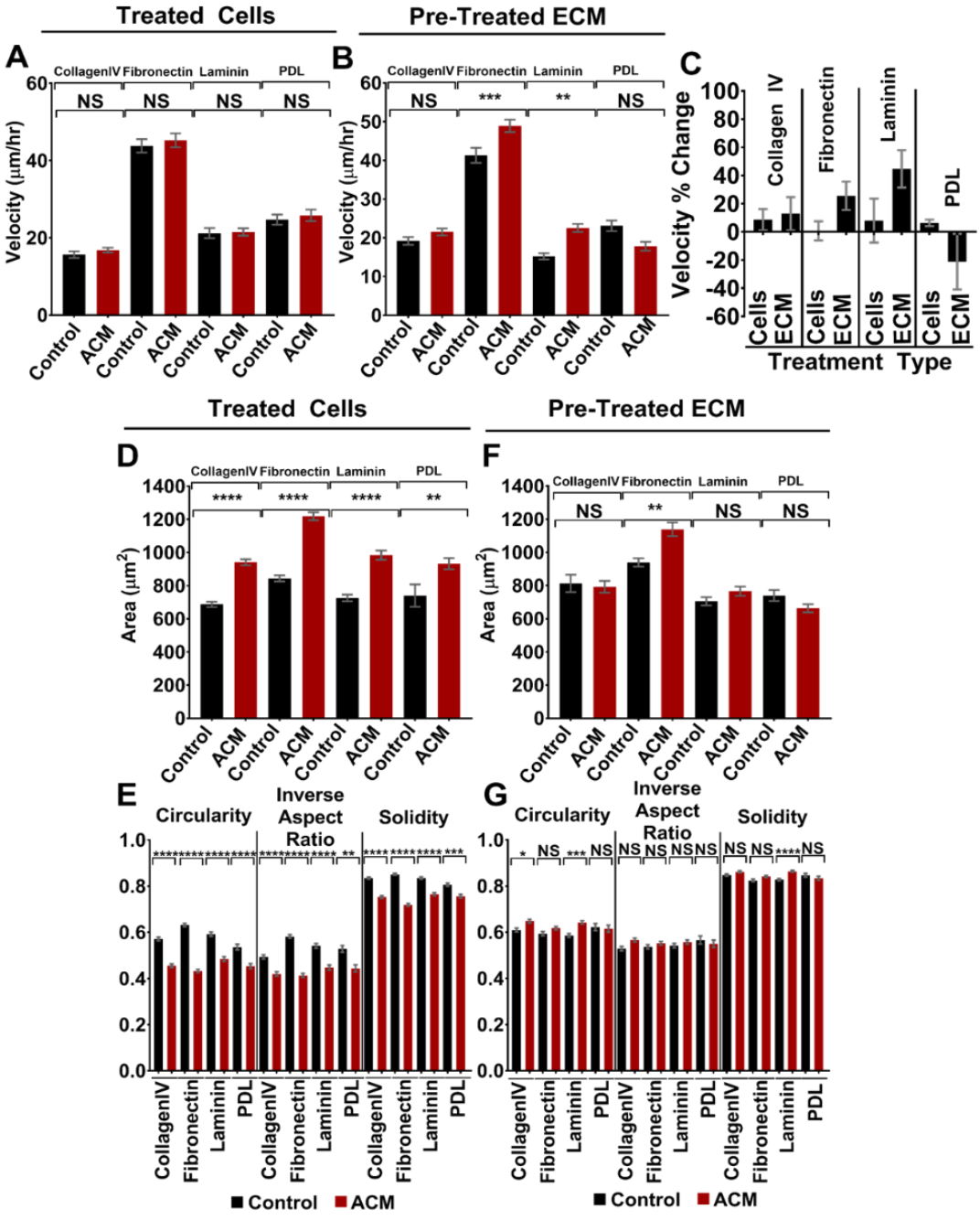
Treated Cells
Pre-Treated ECM
A
B
C
CollagenIV Fibronectin Laminin PDL
NS NS NS NS
NS *** ** NS
Velocity (μm/hr)
Control ACM Control ACM Control ACM Control ACM
Velocity % Change
Collagen IV
Fibronectin
Laminin
PDL
Cells ECM Cells ECM Cells ECM Cells ECM
Treatment Type
Treated Cells
Pre-Treated ECM
D
F
CollagenIV Fibronectin Laminin PDL
**** **** **** **
NS ** NS NS
Area (μm2)
E
G
Circularity
Inverse Aspect Ratio
Solidity
CollagenIV Fibronectin Laminin PDL
Control ACM

We also performed morphology and migration experiments on substrates coated with poly-D-lysine (PDL), which enhances electrostatic interactions between cells and the surface but does not promote integrin binding. We added this coating into the experimental setup to (indirectly) test the hypothesis that ACM treatment of the extracellular matrix or basement membrane alters integrin binding to the substrate. MDA-MB-231 cells plated on PDL and treated with ACM demonstrated statistically significant changes in morphological parameters, including increased area and decreased inverse aspect ratio, circularity, and solidity (Figure 3.5 D, E). Meanwhile, cells plated on ACM-treated PDL demonstrated no changes in any morphological parameter (Figure 3.5 F, G). Therefore, we speculate that ACM-induced changes in cell morphology are not integrin-dependent. Intriguingly, MDA-MB-231 cells plated on PDL and treated directly with ACM demonstrated no change in cell migration velocity (Figure 3.5 A), and trended towards *decreased* velocities (though not statistically significant) on ACM-treated PDL (in contrast with the increased velocities observed on other ACM-treated extracellular matrix substrates) (Figure 3.5 B, C). Hence, we speculate that the migratory response of cells to ACM treatment of the extracellular matrix may be dependent on integrin binding, though further work will be needed to confirm this hypothesis.

3.3.5 Direct treatment of cells with ACM alters actin cytoskeleton organization

Given the significant alterations in cell morphology observed in response to direct treatment with ACM, we hypothesized that the actin cytoskeleton would also demonstrate concomitant changes in organization in response to ACM. Hence, cells were plated on extracellular matrix-coated glass substrates, fixed, permeabilized, stained for actin, and imaged via laser scanning confocal microscopy. Indeed, ACM-treated MDA-MB-231 cells displayed more prominent actin stress fibers in comparison with control media-treated cells on type I collagen (Figure 3.6 A, B) and also on collagen IV, fibronectin, and laminin substrates (Figure 3.6 C). Meanwhile, ACM did not alter cell for both control and ACM-treated cells (Figure 3.6 C). There was also a (visual) actin organization on PDL, where only a diffuse actin network was observed for both control and ACM-treated cells (Figure 3.6 C). There was also a (visual) increase in actin stress fiber alignment in ACM-treated MCF10A cells and a minimal (visual) increase in stress fiber content in MCF7 cells (Figure 3.6 D). ACM did not appear to alter the actin organization of MDA-MB-468 cells (Figure 3.6 D).

Figure 3.6: **Cytoskeletal arrangement of ACM-treated cells of different metastatic phenotypes and tumor cells on ACM-treated extracellular matrix.** A) Stitched images of a large area of MDA-MB-231 cells treated with control media or ACM and stained for actin (green) and the nucleus (blue) on type I collagen. B) Images of control media-treated (top) and ACM-treated MDA-MB-231 cells (bottom) stained for actin (green) and the nucleus (blue) on type I collagen. Images in panels (A) and (B) were taken using a 100x objective of an Olympus FV3000 confocal microscope. C) Images of control media-treated (left) and ACM-treated (right) MDA-MB-231 cells on type IV collagen, fibronectin, laminin, or PDL and stained for actin (green) and the nucleus (blue). D) Images of MCF10A, MCF7, and MDA-MB-468 on type I collagen, stained for actin (green) and the nucleus (blue). Images in panels (C) and (D) were taken using a 60x objective of a Zeiss LSM 710 confocal microscope. The intensity of the images was adjusted equally between each set of conditions in order to best view the actin arrangement. Scale bars = 20μm and apply to all images within each sub-panel.

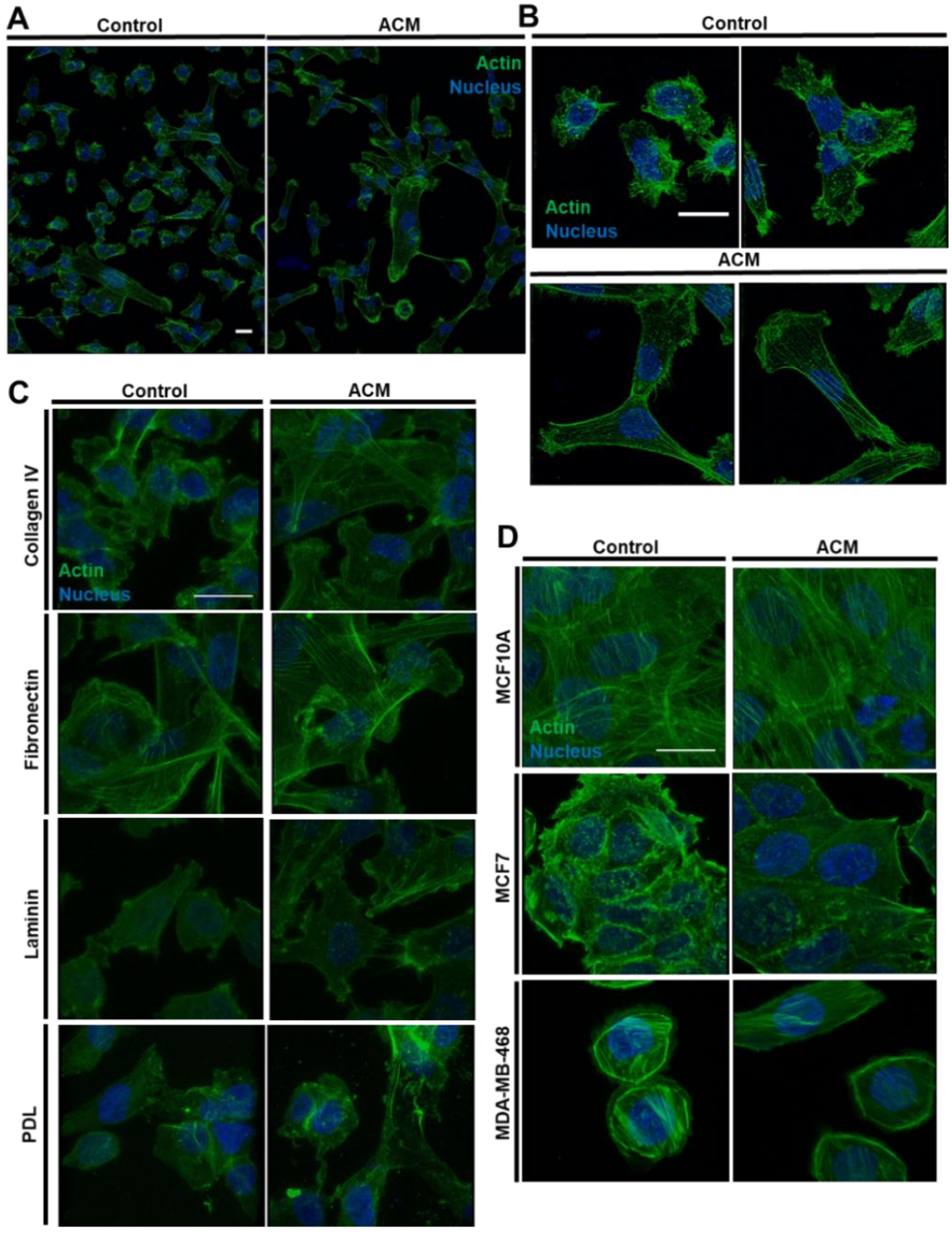
A
Control
ACM
Actin
Nucleus
B
Control
Actin
Nucleus
ACM
C
Control
ACM
Collagen IV
Actin
Nucleus
Fibronectin
Laminin
PDL
D
Control
ACM
MCF10A
Actin
Nucleus
MCF7
MDA-MB-468

3.3.6 Astrocyte activation via TGF-β does not enhance the effect of ACM

As discussed above, the astrocyte secretome changes when astrocytes become reactive, which occurs in response to injury or insult, such as cancer or stroke [120]. To date, no studies have systematically evaluated the effects of soluble factors from quiescent and activated astrocytes on tumor cell morphology and migration. We and others have previously shown that different serum conditions in conjunction with TGF-β treatment can be used to alter the activation state of astrocytes [103], [121], [122]. Specifically, we have shown that TGF-ß in combination with serum starvation induces a time-dependent increase in $K_{Ca}3.1$ protein expression, and at 5 days, induces expression of the glial fibrillary acidic protein (GFAP; marker protein of reactive astrogliosis) and the production of chondroitin sulfate proteoglycans (CSPGs). Thus, three ACM regimens were used with or without TGF-β treatment: 1) astrocytes were cultured in serum-free media overnight and then treated with TGF-β in serum-free media for 5 days; 2) astrocytes were cultured in serum-free media overnight and then treated with TGF-β in serum-containing media for 5 days; 3) astrocytes were cultured in serum-containing media overnight and then treated with TGF-β in serum-containing media for 5 days before harvest. The addition of serum was necessary since the ACM used for other experiments contained serum. We note that in each of the experiments, astrocytes remained attached to the substrate, maintained confluency, and appeared viable. Astrocytes demonstrate strong contact-inhibition and thus stop dividing once they reach confluency, and hence total astrocyte numbers were comparable between all experiments. MDA-MB-231 tumor

cells were cultured on type I collagen-coated glass overnight, and on the following day, culture media was replaced with ACM from TGF-β-treated astrocytes, ACM from untreated astrocytes, or control media, and incubated overnight. Tumor cell morphology was not significantly different after treatment with ACM from a five-day culture of TGF-β-activated astrocytes, in comparison with ACM from untreated astrocytes (Figure 3.7 A, B). However, ACM from TGF-β-treated serum-starved astrocytes resulted in significantly decreased tumor cell velocities in comparison with ACM from untreated serum-starved astrocytes (Figure 3.7 C). Without astrocyte serum starvation, TGF-β treatment in astrocytes had no effect on tumor cell velocity (Figure 3.7 C). Meanwhile, there was no significant difference in tumor cell diffusion coefficient after tumor cells were treated with ACM from TGF-β-treated versus untreated astrocytes for any of the serum conditions (Figure 3.7 D).

However, TGF-β itself can promote epithelial-mesenchymal transition and induce directional migration in breast cancer cells [123]. Thus, to confirm that the observed effects on tumor cell morphology and migration were not simply due to free TGF-β in the ACM, 10 ng/ml TGF-β was added to serum free media, control media, and two-day ACM, and migration experiments were performed on MDA-MB-231 tumor cells cultured on type I collagen-coated glass. TGF-β addition resulted in increased circularity and inverse aspect ratio for tumor cells in serum free media and two-day ACM, and increased area for tumor cells in control media (Figure 3.8 A, B); however, the relative trends between TGF-β-treated and untreated tumor cells did not correspond to the changes seen in tumor cells treated with ACM from TGF-β -treated and untreated astrocytes, where there was no significant change in any morphology

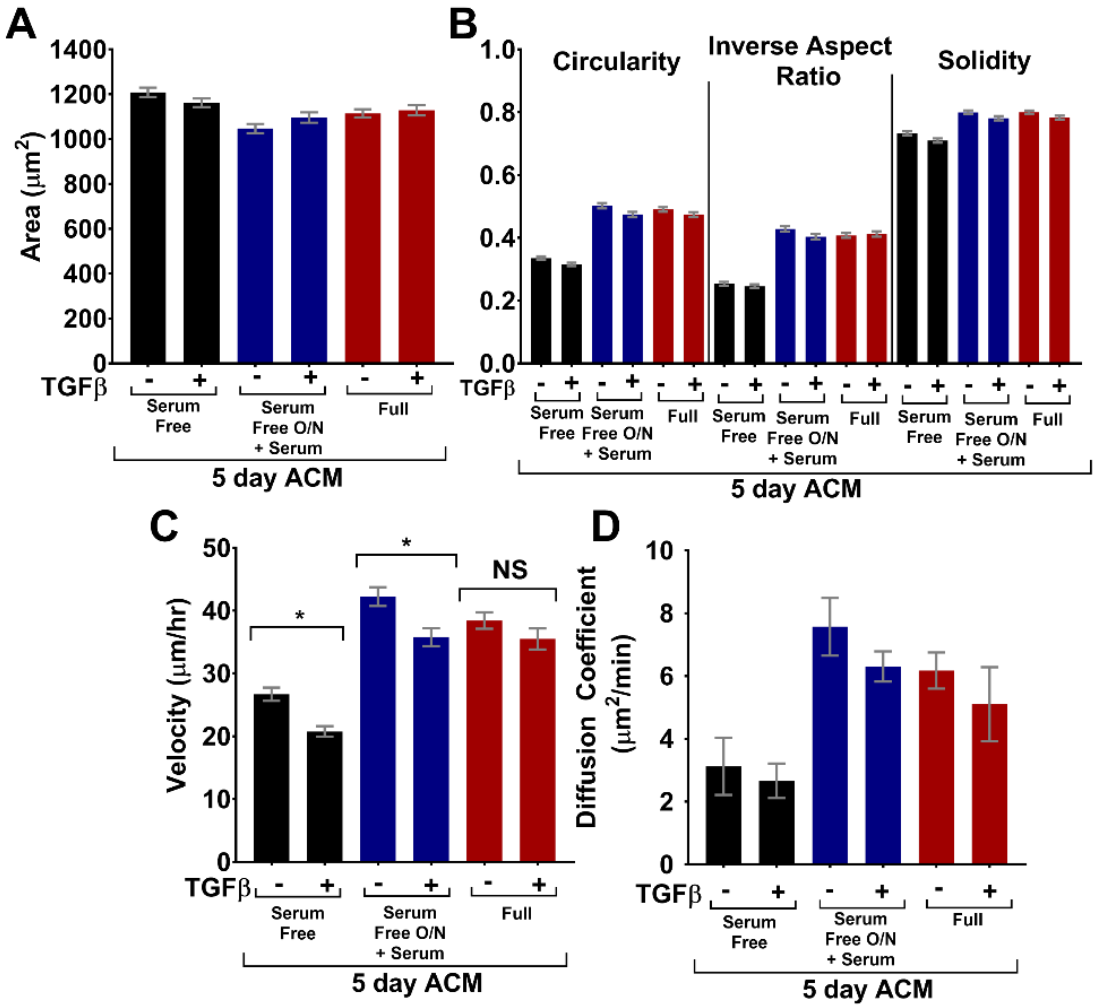

Figure 3.7: **Tumor cells treated with ACM from TGF-β-treated astrocytes.** Key: Serum Free: astrocytes were cultured without serum with or without TGF-β; Serum Free O/N+Serum: astrocytes were cultured without serum overnight and media was changed to media with serum with or without TGF-β; Full: astrocytes cultured in full media (with serum) with or without TGF-β. All ACM was conditioned for five days. A) Areas and B) circularity, inverse aspect ratio, and solidity of the MDA-MB-231 cells treated with control media or ACM. n(Serum Free – TGF-β)=626; n(Serum Free + TGF-β)=634; n(Serum Free O/N+Serum – TGF-β)=531; n(Serum Free O/N+Serum + TGF-β)=569; n(Full – TGF-β)=728; n(Full + TGF-β)=638 cells. C) Velocities (cells tracked for 670 minutes with 6.7 minute intervals) and D) diffusion coefficient, obtained from a Langevin-type fit to a mean square displacement curve over 268 minutes. n(Serum Free – TGF-β)=96; n(Serum Free + TGF-β)=93; n(Serum Free O/N+Serum – TGF-β)=73; n(Serum Free O/N+Serum + TGF-β)=69; n(Full – TGF-β)=102; n(Full + TGF-β)=93 cells. Statistics carried out using a one-way ANOVA and Tukey's post-hoc analysis with $p<0.05$. (* $p<0.05$; ** $p<0.01$; *** $p<0.001$; ****$p<0.0001$). In all plots, bars indicate mean of pooled data from N independent experiments, and error bars represent standard error of the mean ($N\geq3$ for all conditions, except Serum Free O/N+Serum condition where N=2). Jonathan Siglin assisted with experiments and analysis.

parameter for any condition (Figure 3.7 A, B). Furthermore, addition of TGF-β resulted in no changes in velocities (Figure 3.8 C) or diffusion coefficients (Figure 3.8 D) of tumor cells in serum-free media, control media, or ACM. Thus, we conclude that free TGF-β did not cause the decrease in tumor cell velocity measured when tumor cells were treated with ACM from TGF-β-activated astrocytes (Figure 3.7 C, D). Instead, changes in cell migration in response to ACM from TGF-β-activated astrocytes are likely a result of the altered astrocyte secretome in response to TGF-β.

3.3.7 Inhibiting MMPs in ACM reverses its effect on metastatic breast tumor cells

Previous studies have implicated MMPs in tumor cell migration changes [124] and also in the astrocyte secretome [48], [125]. Thus, MMPs could be one astrocyte-secreted factor that might potentiate the observed phenotypic changes in tumor cells in response to ACM. In order to test this hypothesis, a broad-spectrum MMP inhibitor, batimastat, was used to inhibit all types of MMPs present in ACM. MDA-MB-231 tumor cells were cultured on type I collagen-coated glass overnight, and on the following day, culture media was replaced with control media with vehicle control, ACM with vehicle control, or ACM with varying concentrations of batimastat, and incubated overnight. In these experiments, as the concentration of batimastat in the ACM increased from 0.1 - 5 μM, the areas of tumor cells decreased to a similar size as the areas of cells treated with control media (Figure 3.9 A). Similarly, as batimastat concentration increased, tumor cells also returned to control-like values of circularity, inverse aspect ratio, and solidity (Figure 3.9 B). Notably,

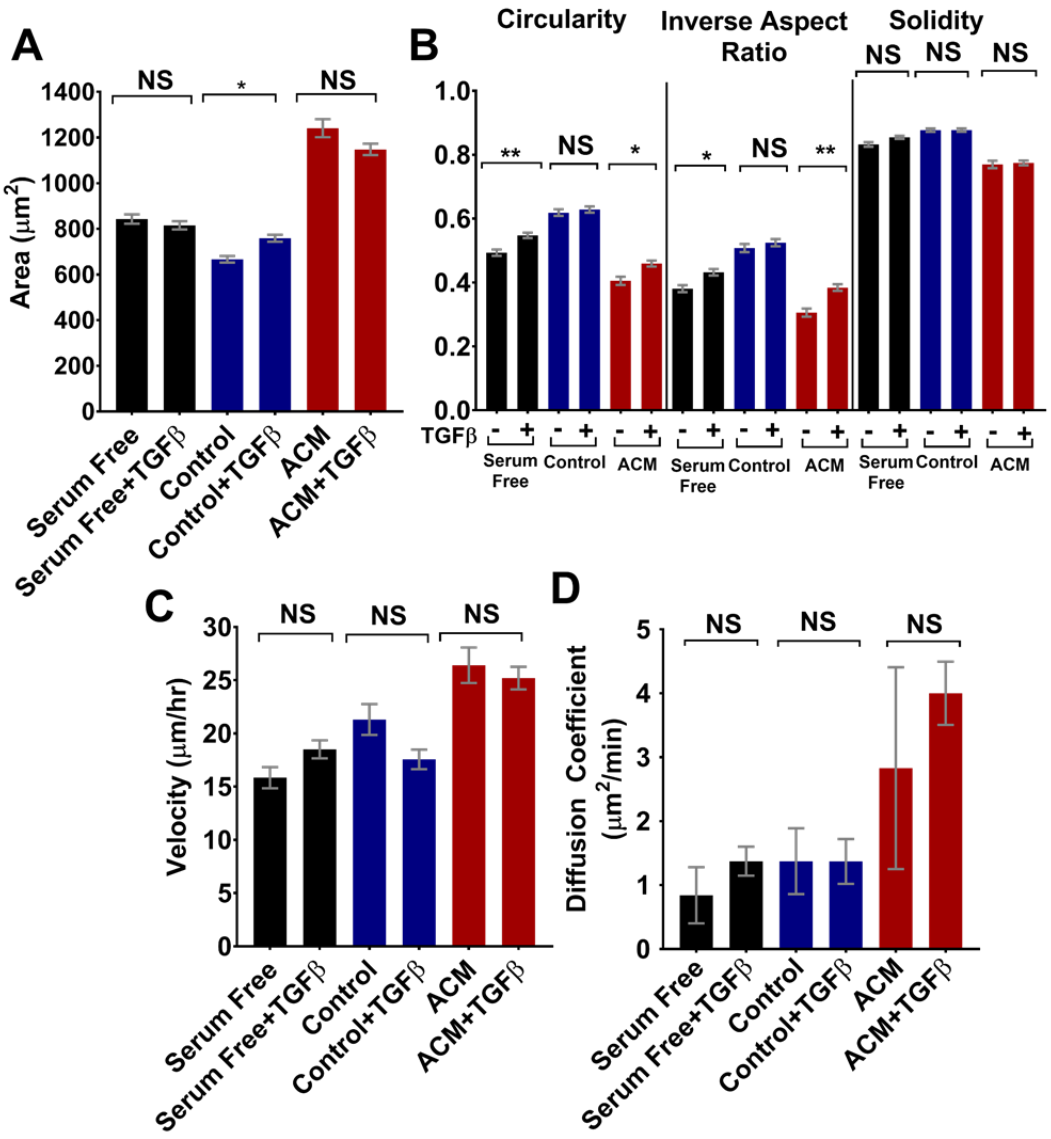

Figure 3.8: Effect of exogenous TGF-β on ACM morphology and migration of ACM-treated tumor cells. A) Areas B) circularity, inverse aspect ratio, and solidity of MDA-MB-231 cells treated with control media, serum free media, or ACM with and without 10 ng/ml TGF-β. n(Serum Free – TGF-β)=264; n(Serum Free + TGF-β)=466; n(Control – TGF-β)=284; n(Control + TGF-β)=408; n(ACM – TGF-β)=159; n(ACM + TGF-β)=383 cells. C) Velocities and D) diffusion coefficient, obtained from a Langevin-type fit to a mean square displacement curve over 200 minutes. n(Serum Free – TGF-β)=54; n(Serum Free + TGF-β)=66; n(Control – TGF-β)=49; n(Control + TGF-β)=71; n(ACM – TGF-β)=33; n(ACM + TGF-β)=74 cells. 5-6.7 minute time intervals for 500-670 minutes. Statistics carried out using a one-way ANOVA and Tukey's post-hoc analysis with $p<0.05$. (* $p<0.05$; ** $p<0.01$; *** $p<0.001$; ****$p<0.0001$). In all plots, bars indicate mean of pooled data from N independent experiments, and error bars represent standard error of the mean (N≥3 for all conditions, except ACM condition where N=2). Jonathan Siglin assisted with experiments and analysis.

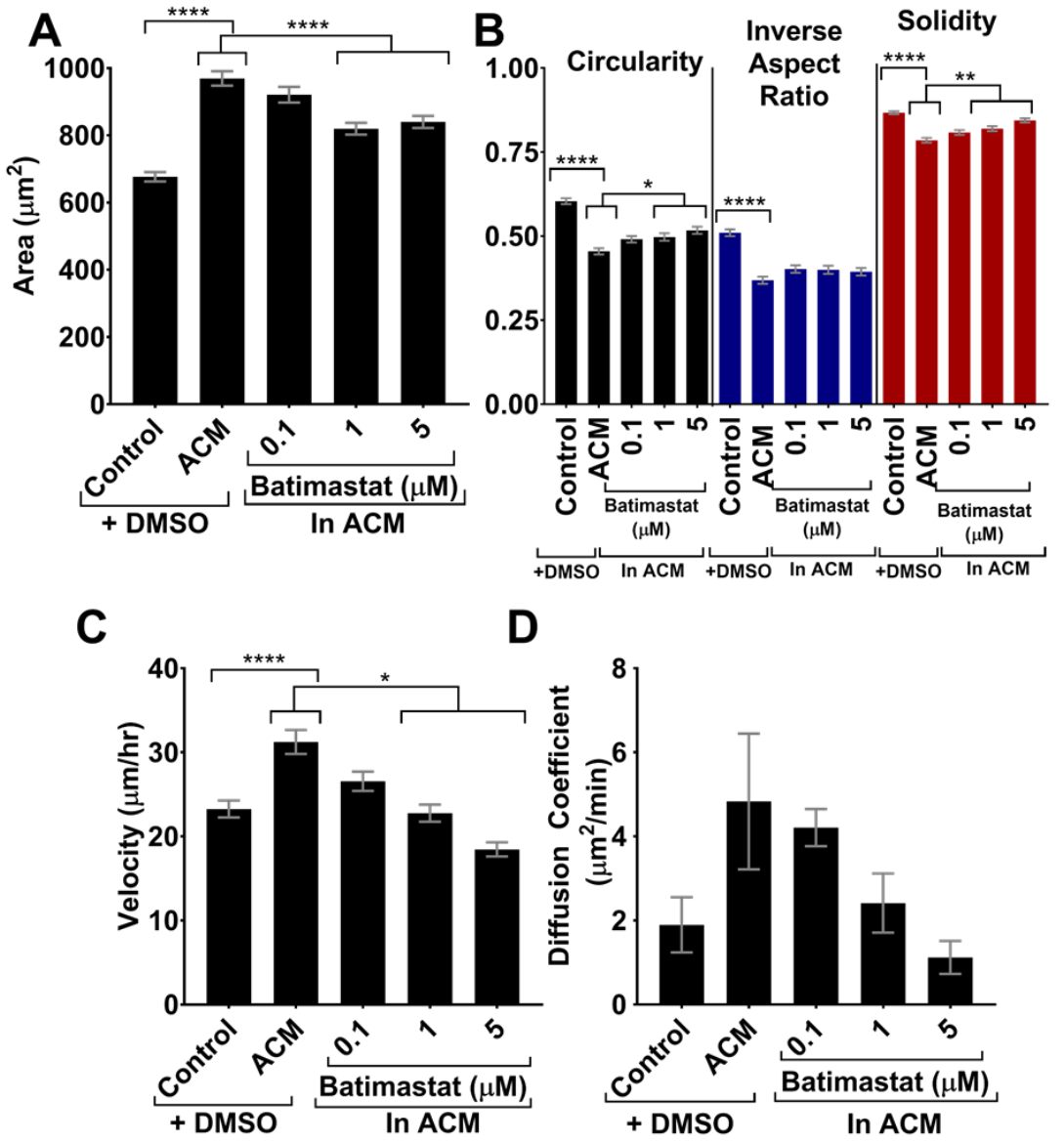

Figure 3.9: **Effect of MMP inhibition on morphology and migration of ACM-treated tumor cells.** A) Areas and B) circularity, inverse aspect ratio, and solidity for MDA-MB-231 cells treated with control media or ACM with DMSO as well as with ACM with 0.1, 1, and 5 μM Batimastat. n(Control+DMSO)=445; n(ACM+DMSO)=343; n(ACM+0.1μM Batimastat)=328; n(ACM+1μM Batimastat)=325; n(ACM+5μM Batimastat)=360 cells. C) Velocities (cells tracked every 5 minutes for 500 minutes) and D) diffusion coefficients obtained from a Langevin-type fit to a mean square displacement curve over 200 minutes. n(Control+DMSO)=64; n(ACM+DMSO)=71; n(ACM+0.1μM Batimastat)=73; n(ACM+1μM Batimastat)=71; n(ACM+5μM Batimastat)=73 cells. Statistics carried out using a one-way ANOVA and Tukey's post-hoc analysis with $p<0.05$. (* $p<0.05$; ** $p<0.01$; *** $p<0.001$; ****$p<0.0001$). In all plots, bars indicate mean of pooled data from $N\geq3$ independent experiments, and error bars represent standard error of the mean. Jonathan Siglin assisted with experiments and analysis.

batimastat treatment also dose-dependently decreased the migration parameters of velocity (Figure 3.9 C) and diffusion coefficient (Figure 3.9 D) of cells treated with ACM. The results of MMP inhibition studies in ACM suggest that MMPs are implicated in the phenotypic changes of tumor cells treated with ACM.

There exists evidence in the literature that MMP-2 and MMP-9 both can both cleave type I collagen [126], [127] and both of these MMPs are reportedly contained within ACM [48]. Thus, we added MDA-MB-231 cells to type I collagen-treated substrates that were pre-treated with exogenous MMP-2 or MMP-9 at 40 ng/ml or 100 ng/ml. These concentrations were chosen based on previously published MMP-2 and MMP-9 activity assay against gelatin [128] as well as previously published studies with exogenous MMP-2 and MMP-9 [129]. Treatment of cells on MMP-2- or MMP-9-treated extracellular matrix substrates resulted in similar increased (but not statistically significant) migration velocities as ACM (e.g., for 40 and 100 ng/mL MMP-2 and 40 ng/mL MMP-9) (Figure 3.10 A), while morphology was mostly unaffected by either MMP-2 or MMP-9 (Figure 3.10 B-C). These results suggest that MMP-2 and/or MMP-9 in ACM might be at least partially responsible for the ACM-

Figure 3.10: **Effect of exogenous MMP -2 and -9 on migration and morphology of tumor cells on ACM-treated extracellular matrix.** A) Velocities of MDA-MB-231 cells on type I collagen that was pre-treated with control media, ACM, or control media with exogenous MMP-2 or MMP-9. (n(control)=80 cells; n(ACM)=120 cells; n(control+40 ng/ml MMP-2)= 120 cells; n(control+100 ng/ml MMP-2)= 120 cells; n(control+40 ng/ml MMP-9)=80 cells; n(control+100 ng/ml MMP-9)=120 cells). Cell migration was analyzed over 5 hours with 10 minute intervals between frames. B) Areas and C) corresponding circularities, inverse aspect ratios, and solidities of MDA-MB-231 cells seeded on type I collagen that was pre-treated with control media, ACM, or control media with exogenous MMP-2 or MMP-9 (n(control)=321 cells; n(ACM)=449 cells; n(control+40 ng/ml MMP-2)=379 cells; n(control+100 ng/ml MMP-2)=366 cells; n(control+40 ng/ml MMP-9)=256 cells; n(control+100 ng/ml MMP-9)=317 cells). Statistical analysis was performed using a Tukey's multiple comparison post-hoc test with $p<0.05$. (* $p<0.05$; ** $p<0.01$; *** $p<0.001$; ****$p<0.0001$). In all plots, bars indicate mean of pooled data from $N\geq2$ independent experiments, and error bars represent standard error of the mean. Rebecca Moriarty assisted with experiments and analysis.

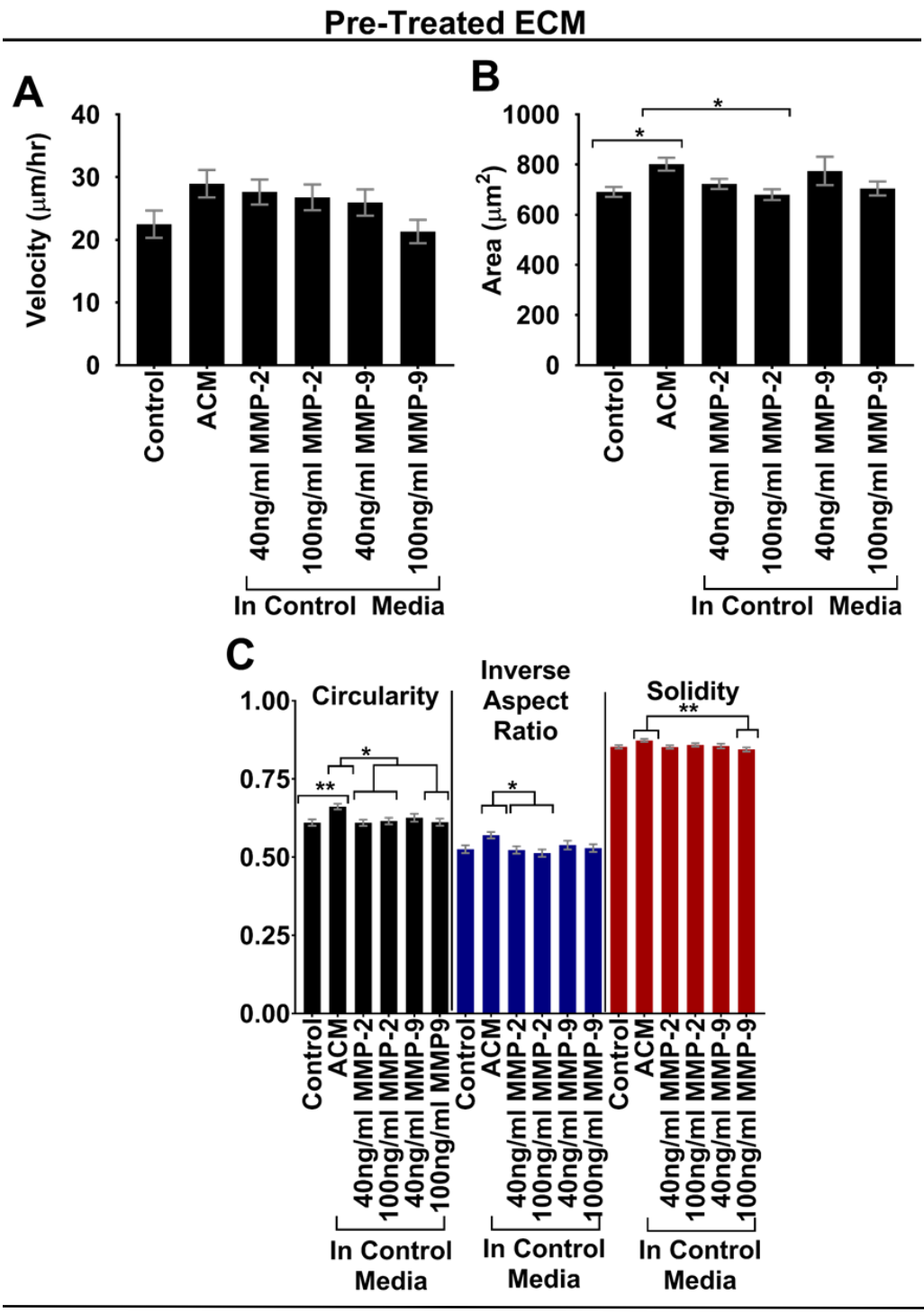
Pre-Treated ECM
A
Velocity (μm/hr)
40
30
20
10
0
Control
ACM
40ng/ml MMP-2
100ng/ml MMP-2
40ng/ml MMP-9
100ng/ml MMP-9
In Control Media
B
Area (μm²)
1000
800
600
400
200
0
*
*
Control
ACM
40ng/ml MMP-2
100ng/ml MMP-2
40ng/ml MMP-9
100ng/ml MMP-9
In Control Media
C
Circularity
Inverse Aspect Ratio
Solidity
1.00
0.75
0.50
0.25
0.00
**
*
*
**
Control
ACM
40ng/ml MMP-2
100ng/ml MMP-2
40ng/ml MMP-9
100ng/ml MMP9
In Control Media
In Control Media
In Control Media

induced effects on cell migration, for cells plated on ACM-treated type I collagen substrates, though the lack of statistical significance in velocity data (Figure 3.10 A) suggests other mechanisms are likely also at play.

3.3.8 ROCK inhibition

To begin to address the role of Rho/ROCK, we treated MDA-MB-231 tumor cells plated on collagen I with Y27632, a pharmacological ROCK inhibitor, and repeated morphology and migration experiments. We hypothesized that if ACM led to ROCK activation in either cells treated directly with ACM, or the cells on ACM-treated extracellular matrix, then parallel treatment with Y27632 would attenuate the effects of ACM. We found that the addition of Y27632 enhanced migration overall, and negated the effect of ACM on velocity for both ACM-treated cells and extracellular matrix (Figure 3.11 A, B). However, morphological trends remained consistent between ROCK inhibited and control conditions, except for the inverse aspect ratio, where the effect of ACM was no longer apparent after ROCK inhibition (Figure 3.11 C, D, E, F). Thus, these preliminary results seem to suggest that ROCK could be a player in the cross-talk between astrocytes and tumor cells, at least for the purposes of tumor cell migration.

3.3.9 ACM does not serve as a chemoattractant for metastatic breast tumor cells in confined microchannels

During metastasis across the BBB, tumor cells are exposed not only to biochemical cues, but also to physical cues such as confinement, since tumor cells have to travel through very narrow capillaries and then cross the BBB. Our previous

work has suggested that tumor cells in confinement migrate via an alternate mechanism based on water permeation [108], as compared to cell migration in 2D which is drive by actin polymerization. Other recent work has continued to explore potential mechanisms guiding tumor cell migration in 3D matrices [130], [131]. Thus, an open question is whether ACM alters tumor cell migration differently in confinement versus 2D. In addition, it was also important to address whether ACM acts as a chemoattractant for tumor cells. Hence, here we used microfluidic devices containing microchannels of varying width to expose tumor cells to varying degrees of physical confinement and to a chemoattractant (e.g., serum or ACM). Two different conditions were used: (A) cells were seeded in serum-containing control media with no chemotactic gradient or with ACM as the sole chemoattractant (Figure 3.12 A); or (B) cells were seeded in serum-free media with serum-containing control

Figure 3.11: **Effect of ROCK inhibition on tumor cells' response to ACM.** Velocities of MDA-MB-231 cells on type I collagen when A) treated with control media with DMSO, ACM with DMSO, control media with Y27632 (ROCK inhibitor), or ACM with Y27632 (n(control+DMSO)=120 cells; n(ACM+DMSO)=75 cells; n(control+Y27632)=120 cells; n(ACM+ Y27632)=120 cells); and B) seeded on type I collagen pre-treated with control media or ACM and seeded in media containing DMSO or Y27632 (n(control+DMSO)=40 cells; n(ACM+DMSO)=80 cells; n(control+ Y27632)=80 cells; n(ACM +Y27632)=80 cells). Cell migration was analyzed over 5 hours with 10 minute intervals between frames. Areas of MDA-MB-231 cells on type I collagen when C) treated with control media with DMSO, ACM with DMSO, control media with Y27632, or ACM with Y27632 (n(control+DMSO)=414 cells; n(ACM+ DMSO)=429 cells; n(control+Y27632)=198 cells; n(ACM +Y27632)=240 cells); and D) seeded on type I collagen pre-treated with control media or ACM and seeded in media with DMSO or Y27632 (n(control+ DMSO)=113 cells; n(ACM+DMSO)=257 cells; n(control+Y27632)=109 cells; n(ACM +Y27632)=134 cells). Corresponding circularities, inverse aspect ratios, and solidities of MDA-MB-231 cells on type I collagen when cells are E) treated with control media with DMSO, ACM with DMSO, control media with Y27632, and ACM with Y27632 and F) seeded on type I collagen pre-treated with control media or ACM and seeded in media with DMSO or Y27632. Statistical analysis was performed using a Tukey's multiple comparison post-hoc test with $p<0.05$. (* $p<0.05$; ** $p<0.01$; *** $p<0.001$; ****$p<0.0001$). In all plots, bars indicate mean of pooled data from $N\geq2$ independent experiments with just one replicate of the control+DMSO in the pre-treated collagen condition, and error bars represent standard error of the mean. Note, this figure was not included as part of the original paper. Rebecca Moriarty assisted with experiments and analysis.

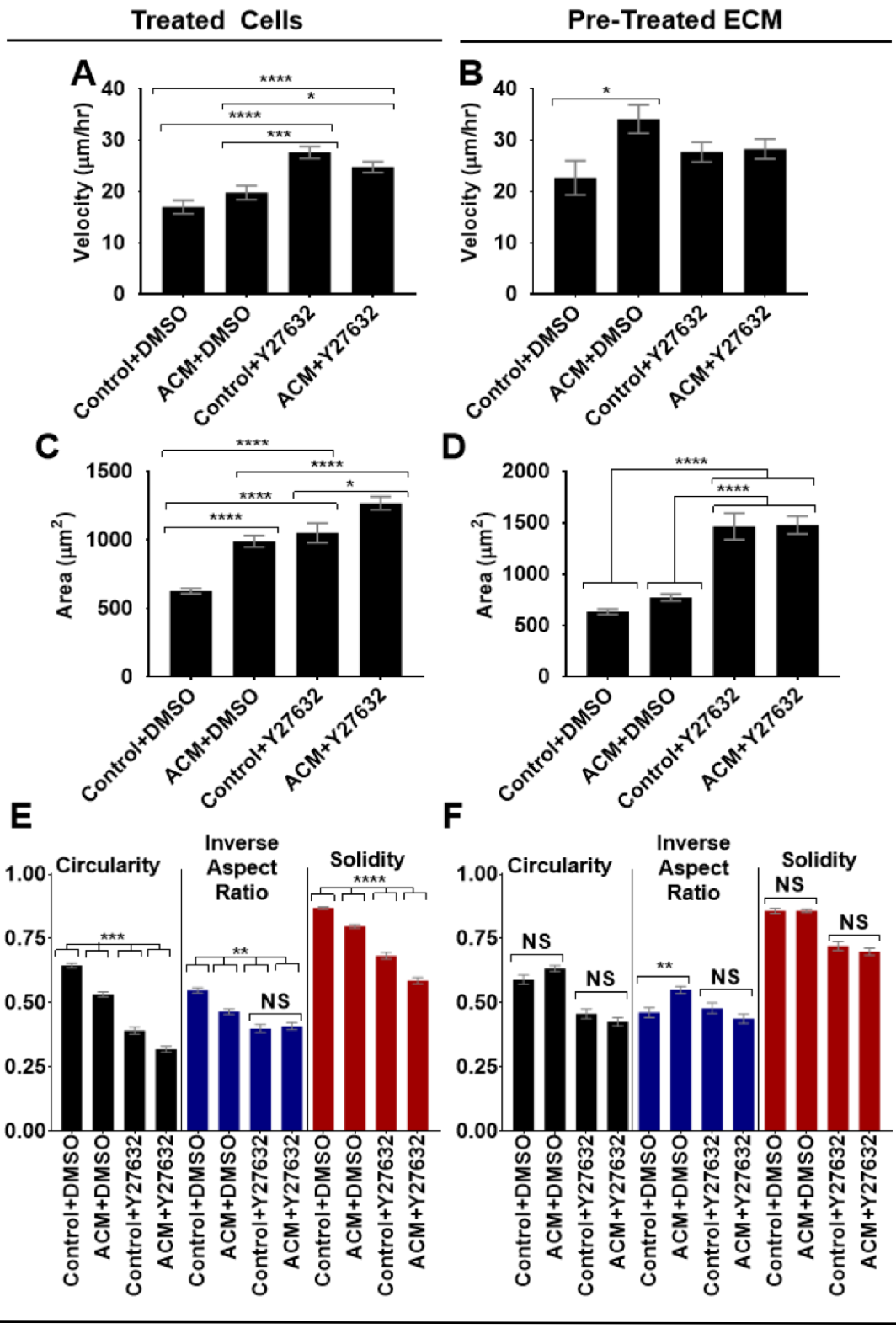
Treated Cells
Pre-Treated ECM
A
B
C
D
E
F
Velocity (µm/hr)
Area (µm²)
Control+DMSO
ACM+DMSO
Control+Y27632
ACM+Y27632
Circularity
Inverse Aspect Ratio
Solidity
NS

media or serum containing ACM on the other side of the channels, such that either serum or serum and ACM-containing soluble factors were the chemoattractants (Figure 3.12 B). Condition (A) was used to determine whether ACM by itself acted as a chemoattractant. Condition (B) was used to determine whether ACM enhanced the effects of serum as a chemoattractant. In both conditions, cells were seeded in the collagen-coated devices and media was changed to one of the conditions described above. Cells migrated through the narrow channels towards the opposite side (Figure 3.12 C), and cell velocity and chemotactic index were calculated as described in the Materials and Methods section, Appendix B, and in Figure 12 D. In both cases, tumor cells' speed showed a biphasic relationship with channel width, with cells having

---

Figure 3.12: **Effect of ACM as a chemoattractant of tumor cells in microfluidic channels.** A) Diagram of experimental set-up where ACM is serving as the sole chemoattractant (condition A). B) Diagram of experimental set-up where ACM and serum are chemoattractants (condition B). Cells cultured in control media or ACM. C) Example image sequence taken with 10 minute intervals of a single cell (indicated by arrow) traveling through a 6 μm channel with serum as a chemoattractant. The time step is labeled every 30 minutes and the arrows indicate the same cell and are re-located from the leading to the trailing edge of cell due to space constraints at the end of the channel. D) Chemotactic index calculation. E) Speed and F) chemotactic index of cells traveling through microchannels with 3, 10, 50 μm widths from control media towards ACM or control media (condition A). n(50μm channels with Control media everywhere)=152; n(50μm channels with ACM as chemoattractant)=212; n(10μm channels with Control media everywhere)=97; n(10μm channels with ACM as chemoattractant)=233; n(3μm channels with Control media everywhere)=18; n(3μm channels with ACM as chemoattractant)=57 cells. G) Speed and H) chemotactic index of cells traveling through microchannels with 3, 10, 50 μm widths from serum free media towards ACM or control media (condition B). n(50μm channels with Control chemoattractant)=200; n(50μm channels with ACM as chemoattractant)=158; n(50μm channels with ACM as chemoattractant and cells pretreated in ACM)=205; n(10μm channels with Control chemoattractant)=183; n(10μm channels with ACM as chemoattractant)=126; n(10μm channels with ACM as chemoattractant and cells pretreated in ACM)=122; n(3μm channels with Control chemoattractant)=18; n(3μm channels with ACM as chemoattractant)=23; n(3μm channels with ACM as chemoattractant and cells pretreated in ACM)=63 cells. The tracking time interval was 10 minutes for up to 15 hours. Statistical analysis was performed using a Tukey's multiple comparison post-hoc test with $p<0.05$. (* $p<0.05$; ** $p<0.01$; *** $p<0.001$; ****$p<0.0001$). In all plots, bars indicate mean of pooled data from $N\geq3$ independent experiments, and error bars represent standard error of the mean. For some conditions, cells migrated into 3μm channels in only 2/3 trials.

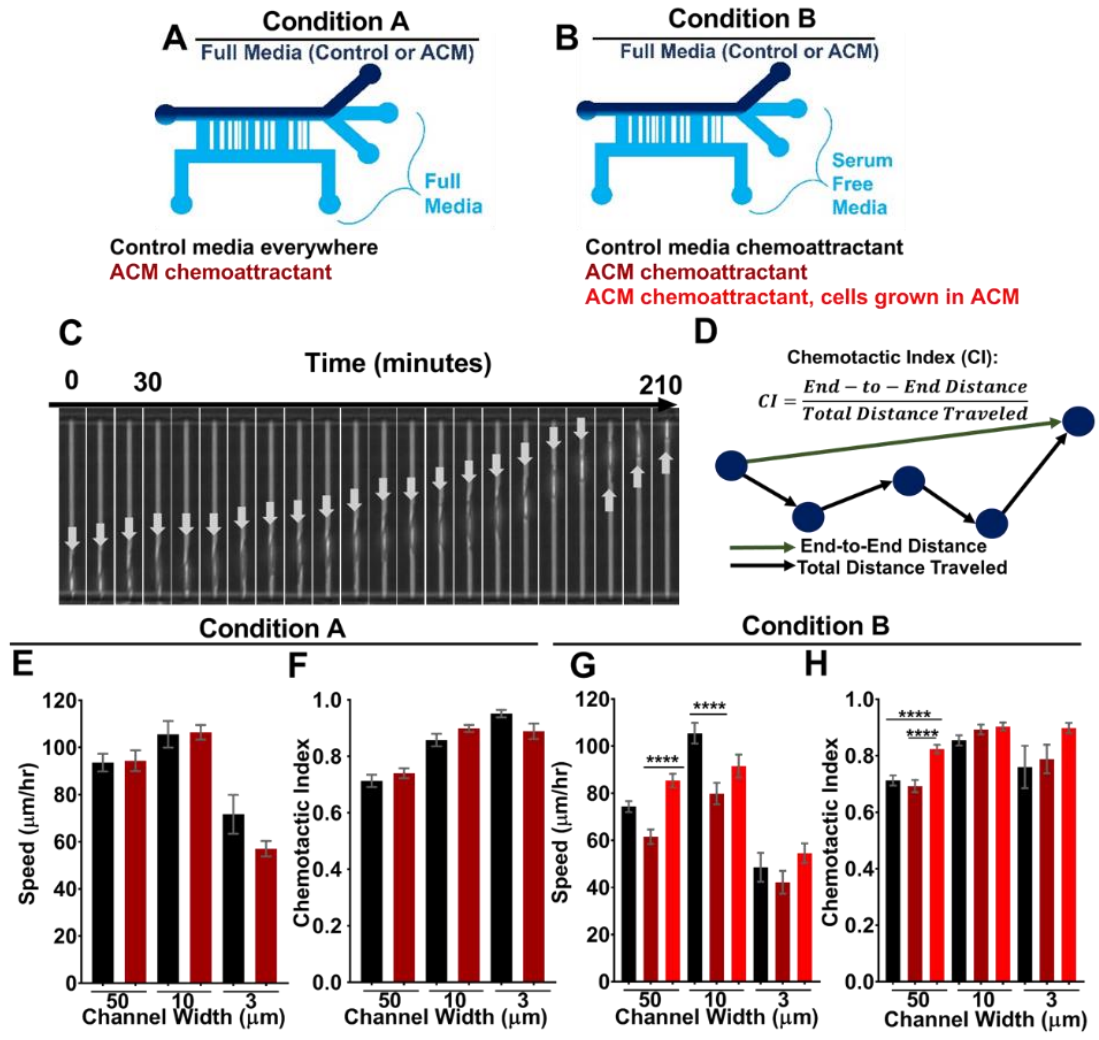
A
Condition A
Full Media (Control or ACM)
Full Media
B
Condition B
Full Media (Control or ACM)
Serum Free Media
Control media everywhere
ACM chemoattractant
Control media chemoattractant
ACM chemoattractant
ACM chemoattractant, cells grown in ACM
C
Time (minutes)
0
30
210
D
Chemotactic Index (CI):
$CI = \frac{End - to - End\ Distance}{Total\ Distance\ Traveled}$
End-to-End Distance
Total Distance Traveled
Condition A
Condition B
E
F
G
H
Speed (μm/hr)
Chemotactic Index
Channel Width (μm)
50
10
3
****

smallest speeds in 50 and 3 μm channels and largest speeds in the 10 μm channels. However, when ACM was the sole chemoattractant (condition A), there was no significant difference in cell speed (Figure 3.12 E) or their chemotactic index (Figure 3.12 F). On the other hand, when the ACM was used as a chemoattractant in conjunction with serum (condition B), tumor cells were significantly slower in 10 μm when migrating towards the serum-containing ACM from serum-free media (Figure 3.12 G) but had similar chemotactic indices in all channels (Figure 3.12 H). Interestingly, when tumor cells were first cultured in ACM, they were no longer affected by the ACM and serum gradient and migrated from serum-free media at almost the same speed towards serum-containing ACM as towards serum-containing control media gradient (Figure 3.12 G). Together, these results suggest that ACM does not serve as a chemoattractant for the tumor cells, either with or without serum in the seeding media, since using ACM as a chemotactic source did not enhance the speed of the tumor cells in confinement, as it did in 2D. Furthermore, these results could suggest that the different migration modes utilized by tumor cells in 2D and in confinement are affected differently by astrocyte-secreted factors, which is important for understanding these interactions in physiological microenvironments.

3.4 Discussion

Mounting evidence suggests that astrocytes are implicated in increasing metastatic tumor cell invasiveness at the BBB [15], [48], [49], [56], [101]. Here, we investigated whether the one-way biochemical communication from astrocytes to tumor cells (and/or their extracellular matrix) influences tumor cell migration, and whether these effects are accompanied by alterations in tumor cell morphology and

cytoskeletal organization. An additional goal was to probe the role of MMPs in the resulting phenotypic and behavioral changes of tumor cells.

We found that (1) application of ACM directly to MDA-MB-231 metastatic breast tumor cells or MCF10A normal breast epithelial cells increased cell velocity and induced an enlarged, elongated morphology; (2) pre-treating type I collagen, fibronectin, or laminin extracellular matrix substrates with ACM prior to seeding MDA-MB-231 tumor cells resulted in significantly increased tumor cell velocity as compared to control cells, with increases in velocity that were more drastic than treating cells directly with ACM; (3) a broad spectrum MMP inhibitor added to ACM reversed the effect of ACM on MDA-MB-231 tumor cell migration and morphology; (4) applying conditioned media from TGF-β-activated astrocytes reduced MDA-MB-231 tumor cell migration velocity in comparison with media from untreated astrocytes; and (5) applying ACM as a sole chemoattractant did not affect MDA-MB-231 tumor cell migration speed, but ACM in combination with serum as a chemoattractant reduced tumor cell migration speed in the 10 μm wide channels.

Our results suggest that astrocytes have a significant effect on MDA-MB-231 metastatic breast tumor cells prior to any potential signaling from tumor cells to astrocytes and reactive gliosis, indicating that astrocytes might play an important role in tumor cell recruitment and not just extravasation. Previous reports [132] have shown that changes in cell morphology on a 2D surface are correlated with metastatic potential. The specific trends seem to depend on tumor cell type, but they suggest that quantitative cell shape parameters can provide useful information about other aspects of cell phenotype. Here, astrocyte-secreted factors in ACM increased MDA-MB-231

and MCF10A cell migration velocity and altered their morphology to be larger and more elongated, with enhanced stress fiber formation on 2D extracellular matrix-coated substrates, all suggesting a more mesenchymal and metastatic phenotype[133]. Thus, ACM can enhance the migratory potential of (already) migratory metastatic breast tumor cells and also normal breast epithelial cells. Our migration results are in agreement with past studies where ACM increased tumor cell migration in wound healing and transwell assays [48]. Furthermore, we show that tumor cell morphology and actin cytoskeleton organization are also modulated by ACM, which could contribute to facilitation of migration in ACM-treated cells. We confirmed that serum depletion was not the cause of these results, since dilution of ACM with fresh serum-containing media, down to 50%, also led to changes that were significantly different from control media. Thus, we conclude that there exist soluble factors secreted by astrocytes that increase tumor cell velocity and alter their morphology. The altered morphology and migration potential of tumor cells during exposure to ACM indicates that secreted factors by astrocytes could affect tumor cell phenotype, even without any exposure of the astrocytes to the tumor cell or injury.

We found that ACM from astrocytes activated by TGF-β resulted in slower migration of tumor cells in comparison with untreated astrocytes, which is consistent with prior literature showing that ACM from interferon γ- and tumor necrosis factor α-activated astrocytes decreases the proliferation of tumor cells as compared to ACM from unreactive astrocytes [101]. Since astrocytes generally become reactive in response to injury and their secretome changes as a result, it is significant to note that this astrocyte phenotype appears to be less conducive to tumor cell invasion, even

though tumor cells are likely to cause injury and activate surrounding astrocytes. Since astrocytes need serum starvation in order for TGF-β to increase reactivity, as confirmed via western blot, and Wang *et al.* show no significant difference in tumor cell invasion and metastasis in ACM with and without serum [48], the fact that the most significant results occurred in the serum free activation conditions is still indicative of TGF-β-induced reactivity playing a role in astrocytes' effect on tumor cells. We speculate that once astrocytes become reactive, they also become increasingly protective of the brain microenvironment by producing biochemical cues to reduce tumor cell migration. However, in other studies, activation of astrocytes via recombinant interleukin-1β (IL-1β) and subsequent co-culture with MDA-MB-231 cells led to an enriched population of cancer stem cells in the culture. It is possible that the specific signaling leading to astrocyte activation, whether it is through injury-modulated TGF-β stimulation, or through tumor cell-modulated activation of Notch signaling in astrocytes [56], leads to different effects on tumor cells, and future work could elucidate this relationship.

The astrocyte secretome contains an array of biochemical factors [134], many of which can influence cell migration. Previous studies have implicated astrocyte-secreted MMPs in ACM-mediated effects on tumor cells [48]. In order to further explore the mechanisms that alter tumor cell phenotype when exposed to ACM, we used a broad-spectrum MMP inhibitor, batimastat, to inhibit MMP activity in ACM. In these experiments, we observed a dose-dependent decrease in cell velocity with increased batimastat treatment, with the highest dose nearly reverting ACM-treated tumor cells back to their velocity and morphology from the control condition. These

results are consistent with previous reports, where inhibition of MMPs using another broad spectrum inhibitor, ONO-4817, reduced cell invasion in a transwell assay in a dose-dependent manner [48]. Thus, we provide further evidence that MMPs produced by astrocytes could be at least partly responsible for the ACM-induced alterations in tumor cell migration and morphology. Furthermore, we provide preliminary evidence that addition of exogenous MMP-2 or MMP-9 to extracellular matrix substrates can produce similar effects to ACM on cell migration. However, since tumor cells also secrete MMPs, application of an MMP inhibitor to the ACM may also inhibit MMPs produced by the tumor cells, thus confounding interpretation of the results. It has been found that TGF-β1 increases MMP production by astrocytes [135], however the TGF-β treatment of astrocytes actually decreased the velocity of the subsequent ACM-treated tumor cells as compared to vehicle control-treated ACM. This suggests that MMPs are not the only, and potentially not the dominant, molecular mechanism at play in astrocyte-induced increased cell migration. Future analysis should be aimed at exploring the molecular interplay of the astrocyte-tumor cell signaling and the role of MMPs. Perhaps most notably, we discovered that pre-treating the extracellular matrix with ACM resulted in a significant increase in MDA-MB-231 tumor cell migration velocity in comparison with untreated extracellular matrix, which was even greater for type I collagen, laminin, and fibronectin substrates than the velocity increase when tumor cells were treated with ACM directly. Because the ACM was removed from the extracellular matrix prior to seeding cells, it seems that astrocyte-secreted factors in the ACM in some way alter the extracellular matrix, leading to enhanced migration. It is likely that the MMPs produced by astrocytes and contained

in the ACM degrade and/or reorganize the extracellular matrix, since MMPs have collagenase and gelatinase activity. However, minimal change in morphology was observed when the extracellular matrix substrates were pre-treated with ACM, suggesting that morphological changes alone are not responsible for the increased migration. This also suggests that there are different mechanisms involved in the ACM-induced phenotypical changes in tumor cell morphology and migration, respectively. Alternatively, it is possible that other biochemical factors, such as IL-6, tumor necrosis factor-α and IL-1β [136], within the ACM bind to the extracellular matrix and subsequently enhance tumor cell migration through adhesion-based signaling mechanisms. However, if this were the case, we would have expected to observe increased cell velocity over time during the overnight migration assays, since at later timepoints the extracellular matrix would have been coated in the same ACM factors. Instead, cell velocity was mostly consistent during the entire time lapse sequence (data not shown), suggesting this latter mechanism was not the case. Meanwhile, the fact that cells plated on PDL (which promotes adhesion through electrostatic interactions between cells and the substrate rather than through integrin binding) do not exhibit increased migration in response to ACM, in comparison with cells plated on extracellular matrix proteins (i.e., type I collagen, fibronectin, and laminin) suggests that integrin-based adhesions may be altered by ACM treatment. While it is unclear by which mechanisms the ACM alters the extracellular matrix to enhance migration, these findings do suggest that tumor cell-extracellular matrix interactions are critical to the effect that ACM has on tumor cells and provide a

logical link to the MMP pathways since MMPs are known to degrade extracellular matrix proteins.

While MMPs are more commonly implicated in 3D migration, they also have several important effects in 2D. It is known that MMPs are primarily involved in proteolysis of extracellular matrix; however, it appears that MMPs also result in the rearrangement of extracellular matrix structure, in a MMP- extracellular matrix protein-dependent manner [137], [138]. This rearrangement could be responsible for ACM-induced changes in the 2D protein extracellular matrix that lead to changes in tumor cell migration and morphology. For example, MMP2 has been shown to induce epithelial migration on laminin by cleaving the laminin and exposing a pro-migratory site, even though MMP2 is not specifically known to degrade laminin [137], [139]. Thus, the specific interactions of different MMPs and extracellular matrix proteins could help explain the differences in the effect of ACM on tumor cells when seeded on different matrices. Furthermore, MMPs have been shown to interact with integrins [137] and since integrins are crucial in 2D migration, it is possible that this interaction could be involved in the effect of MMP-containing ACM on tumor cells and their extracellular matrix. Furthermore, it has been shown that the overexpression of some MMPs in epithelial cells activates other MMPs and also leads to reduced cell-cell contacts [137]. While this is primarily relevant to epithelial cells with strong cell-cell contacts, it could also speak to increased epithelial-to-mesenchymal transition and as a result a potential further enhancement of metastatic potential of ACM treated tumor cells.

While the studies observing the effect of MMPs in 2D show several interesting pathways by which MMP-containing ACM could be affecting tumor cells and their extracellular matrix, further experiments are necessary in order to fully understand how the presence of MMPs in ACM is affecting tumor cells. One way to achieve that would be to culture tumor cells in 3D collagen I or collagen IV gels and either pre-treat the scaffold with ACM or treat the tumor cells within the scaffold directly. Observing the migration and morphology of ACM-treated tumor cells in 3D would shed further light on the potential significance of MMPs in the effect of ACM. Furthermore, the MMP inhibition and addition experiments should be repeated in 3D. Future work will focus on delineating this relationship and also evaluate whether ACM can affect the extracellular matrix in a 3D matrix.

Both in 2D and 3D it would be very interesting to study the structure of the extracellular matrix before and after ACM treatment. This could be achieved by scanning electron microscopy, simple harmonic generation imaging, or immunostaining for the appropriate extracellular matrix protein. Additionally, since it appears that MMPs are tied to the expression of integrins, immunostaining ACM-treated tumor cells and tumor cells on ACM-treated extracellular matrix for the expression of paxillin or several different integrins could help shed light on further ACM-mediated mechanisms. This can also be carried out with MMP addition and inhibition in order to understand what the role of MMPs specifically is in the process.

Additionally, we also inhibited ROCK in cells treated directly with ACM and cells cultured on ACM-treated collagen I. While we found that ROCK inhibition attenuates the effect of ACM on tumor cell migration, the mechanism still needs to be

further examined. In the future, a more carefully investigation of the roles of the Rho family GTPases would help shed more light on the significance of the Rho/ROCK pathway in tumor cell – ACM interactions.

Furthermore, we have previously shown that tumor cells can utilize an alternate, water permeation-based migration mechanism in confinement in comparison with 2D where migration is actin-driven [108]. Thus, we found it important to observe the interplay between effects of ACM and the physical cue of confinement. As discussed above, metastatic tumor cells experience confinement at the BBB when traveling through microtracks of the basement membrane in the brain, as well as when migrating through narrow brain capillaries which can be as small as 10μm in diameter [106], through the brain endothelium, and along the blood vessel post extravasation across the endothelium [107]. The biphasic trend of tumor cell migration velocity with respect to channel width could be due to an optimal balance between effects of contact guidance and nuclear deformation in intermediate width channels. That is, in wide channels, no nuclear deformation is necessary, but cells are not completely contact guided by both walls of the channels. In narrow channels, cells are able to receive contact guidance from channel wall on both sides, but the nucleus must significantly deform in order for cells to squeeze through the channels. Interestingly, our work suggests that physical confinement and introduction of ACM as a chemoattractant contrasts the effects that ACM has in 2D, since cells exposed to ACM as a chemoattractant in confined microchannels were not preferentially attracted to the ACM over control media. Additionally, when the ACM gradient was combined with a serum gradient tumor cells actually moved significantly slower

towards the ACM in comparison with control media. Furthermore, pre-culturing cells in ACM resulted in them migrating towards ACM at a similar speed as towards control media. Future work will focus on which mechanisms (i.e. chemotaxis, confinement, contact guidance by edges of the channels) are responsible for the altered behavior of the tumor cells in the microchannels, since literature has shown that tumor cells can be attracted towards astrocytes in a Boyden chamber coculture assays [101]. Indeed, new assays are necessary to understand the physiologically relevant interaction of tumor cells and astrocytes and how cells respond to the complex interplay of biochemical and physical cues at the BBB.

Overall, the observed changes in tumor cell migration and morphology as a result of ACM treatment of tumor cells and their matrix could potentially reflect on their ability to metastasize. Recent studies have shown that morphology and velocity of tumor cells are correlated with the cells' metastatic potential [140]. Specifically, cells with a greater potential to metastasize tend be more migratory [140]. Those cells are also generally larger, more elongated, and with more protrusions and have a greater ability to form distant metastases *in vivo* [140]. Together, this suggests that the observed increase in speed and area of tumor cells treated with ACM and seeded on ACM-treated matrix could be potentially correspond to an increase in their metastatic potential and enhancing their ability to invade the brain.

3.5 Conclusions

This work demonstrates that astrocyte-secreted factors affect the migration, morphology, and actin cytoskeleton organization of metastatic breast tumor cells and also normal breast epithelial cells. This suggests that paracrine signaling between

astrocytes that have not been exposed to metastatic breast tumor cells could enhance metastasis at the BBB, although this effect could be abrogated if tumor cells experience physical confinement. When exposed to ACM, tumor cells become more elongated, larger, and faster, which suggests an increase in metastatic phenotype. Secretion of MMPs by astrocytes could be at least partially responsible for the changes observed in the tumor cell phenotype, and future work will continue to explore this hypothesis. Our work also found that ACM from TGF-β-activated astrocytes results in a lower tumor cell velocity than tumor cells treated with ACM from unreactive astrocytes, without significant changes in tumor cell morphology. Perhaps most notably, we found that treating the extracellular matrix substrate with ACM prior to seeding tumor cells has a greater effect on MDA-MB-231 tumor cell velocity than treating tumor cells directly with ACM, indicating that astrocyte-secreted factors can alter the cells' extracellular matrix. Finally, we showed that ACM may not serve as a chemoattractant to tumor cells in unconfined or confined microenvironments that also subject tumor cells to chemotaxis and contact guidance, suggesting that astrocytes may not attract tumor cells to the brain or help them move through confined spaces, but simply alter general morphology and migration properties. Regardless, our work provides support that astrocytes have a clear effect on tumor cell migration, morphology, and actin cytoskeleton arrangement in one way paracrine communication, and we show that astrocyte-secreted factors can also act indirectly on cells through their extracellular matrix to induce changes in morphology and migration. Further work should continue to examine the specific astrocyte-secreted factors influencing tumor cells and their extracellular matrix, and also the

molecular mechanisms and pathways by which astrocyte secreted factors act on tumor cells.

4 Tumor cell mechanosensing during incorporation into the brain microvascular endothelium†

4.1 Introduction

Evidence in the literature, including *in vivo* imaging, has shown that tumor cells are capable of metastasizing to the brain via the circulatory and lymphatic systems [141], and that metastasis occurring through the circulatory system requires the tumor cells to traverse the BBB in order to reach the brain parenchyma [142]. However, the mechanisms governing how tumor cells cross the blood-brain barrier (BBB) are not well understood.

In one study, close physical contact with the abluminal surface of the blood vessel was crucial for the spread of tumor cells, which actively transmigrated through gaps in the wall of the vasculature but also engaged in vascular remodeling during extravasation [143]. Unique to the BBB, tight junctions proteins (e.g., claudins, occludins) are overexpressed, and act in conjunction with adherens junctions (e.g., vascular endothelial cadherin, VE-cadherin) to regulate barrier integrity and permeability [144]. These junctional proteins link to the actin cytoskeleton through zonula occludens (e.g., ZO-1), which has been shown to regulate cell and junctional tension, cellular migration, barrier formation, and angiogenesis [145]. Disruption of these junctions is linked with increased permeability of the BBB to cells and

† This chapter has been accepted for publication as M.A. Pranda*, K.M. Gray*, A J. L. DeCastro, G.M. Dawson, J.W. Jung, K.M. Stroka. “Tumor cell mechanosensing during incorporation into the brain microvascular endothelium”, CMBE Journal, 2019. Atomic force microscopy carried out by K.M.G. AJ.L.D and G.M.D helped out with experiments and analysis respectively.

molecules and is implicated in several diseases [146], including cancer metastasis [147]. Metastatic breast tum or cells reportedly secrete factors that promote increased tumor cell-BBB adhesion and disrupt or rearrange junctions, weakening the barrier and leading to tumor cells transmigration [148], [149].

tumor cells-derived biochemical cues and physical interaction with brain endothelial cells can alter brain endothelial cell-cell junctions in such a way that directs the mode of trans-endothelial migration. For instance, melanoma cells are reported to disrupt junctions, presumably through protease secretion, and induce endothelial cell apoptosis leading to paracellular transmigration [150]. Other studies have shown that breast tumor cells can cross endothelial barriers utilizing both transcellular and paracellular pathways [151]. Tumor cells also secrete endothelial-altering substances that can lead to an influx of calcium [152], glycocalyx degradation [151], and increased contractility [153], [154], of the targeted endothelial cells, all of which are associated with enhanced tumor cells transmigration at cell-cell junctions [151]–[154]. Furthermore, we and others have demonstrated that tumor cells can even physically displace endothelial cells and “incorporate” or “intercalate” into the endothelium [33], [155], [156], and we hypothesized that this process may also represent a distinct step in the extravasation of tumor cells through the brain endothelium. Hence, here we aimed to quantify how breast tumor cells biochemical factors and physical contact with the brain endothelium affect endothelial cell-cell junction organization, and ultimately, tumor cells incorporation into a biomimetic BBB microenvironment.

In addition to cell-secreted factors, cell functionality is profoundly influenced by its surrounding extracellular matrix [157]. However, it is not yet well understood which aspects of the brain microenvironment play a role in cancer progression [158]. Hyaluronic acid (HA) is a glycosaminoglycan that serves as a major building block of the brain extracellular matrix, which, unlike other parts of the body, is not highly organized and consists mainly of loosely crosslinked networks [159]. HA in the brain is linked with small glycoproteins, as well as tenasins, the density of which plays a large role in the function of various neural processes. Thus, the disruption of these linkages [159] as well as extracellular matrix rearrangement [160] could play a large role in disease progression. Indeed, for other extracellular matrix models such as collagen gels, crosslinking (e.g., via lysyl oxidase) has been shown to increase extracellular matrix stiffness, making it more conducive to the progression of tumors and other diseases [31], [38], [161], [162]. While HA has important biological functions related to joint lubrication and wound healing, it also plays a role in the invasion of tumor cells, and, in the case of primary glioma tumors, HA is highly upregulated in the surrounding extracellular matrix [157].

Because extracellular matrix structure (e.g., arrangement, stiffness, etc.) is known to play a significant role in healthy and diseased states of the brain, here we have investigated how the crosslinking of a brain-like extracellular matrix affects brain endothelial cells, tumor cells, and the interaction between the two cell types. We have used an HA/gelatin-based system with varying degrees of crosslinking to mimic the brain extracellular matrix and used live-cell microscopy and immunofluorescence imaging to quantify cellular migration, morphology, cell-cell junction presentation,

and tumor cells incorporation into brain endothelial cell monolayers, thus providing insight into the interplay of extracellular matrix crosslinking and bi-cellular systems on breast cancer metastasis across the BBB.

4.2 Materials and Methods

4.2.1 Cell Culture

Human breast adenocarcinoma cells, MDA-MB-231s (American Type Culture Collection, Manassas, VA, USA), were cultured, similarly to Chapter 3, in Dulbecco's Modified Eagle's Medium (DMEM) with high glucose and L-glutamine supplemented with 1% Penicillin/Streptomycin 10,000 U ml^{-1} (Pen/Strep) and 10% Fetal Bovine Serum (FBS) (Thermo Fisher Scientific, Waltham, MA, USA) and used below passage 20 after purchase. Human brain microvascular endothelial cells, HBMECs (Cell Systems, Kirkland, WA, USA), were cultured under static conditions in flasks coated with 0.1% gelatin (VWR, Radnor, PA, USA) in RPMI-1640 supplemented with 20% FBS, 1% Pen/Strep, 2mM L-Glutamine (Thermo Fisher Scientific), 30 μg ml^{-1} endothelial cell growth supplement (ECGS) (Millipore Sigma), and 100μg/ml heparin (Millipore Sigma) and used below passage 12. For VE-cadherin-GFP adenovirus amplification, 293A cells (Thermo Fisher Scientific) were cultured in medium composed of high glucose DMEM, 10% FBS, 0.1 mM MEM Non-Essential Amino Acids (NEAA) (Thermo Fisher Scientific), 2 mM L-glutamine, and 1% Pen/Strep. All cells were cultured in a climate-controlled incubator at 37°C, with 5% CO_2:95% air and 50% humidity.

4.2.2 HA/gelatin film formation

HA/gelatin films were formed using the HyStem-C kit (ESIBIO, Alameda, CA, USA). The kit contained four components: DG water, Glycosil (thiolated HA), Gelin (thiolated Gelatin), and Extralink (thiol-reactive PEGDA crosslinker). Instructions from the kit were followed and were also described previously by Prestwich [163] . Briefly, all components were thawed for 30 - 60 minutes. Glycosil, Gelin, and DG water were then briefly heated at 37°C in a water bath to increase solubility. Glycosil and Gelin were then dissolved in 1 mL DG water, rocked for 1 hour at room temperature, then briefly re-heated in the water bath. Extralink was dissolved in DG water to 10%, then was further diluted into aliquots of 6, 4, and 1%. 24-well glass bottom plates (13 mm glass diameter) or 35 mm glass bottom dishes (14 mm glass diameter) (MatTek, Ashland, MA, USA) were plasma treated using a plasma cleaner with a 5 minute pumping step to create a vacuum and a 2.5 minute treatment on the “High” RF power setting (Harrick Plasma, Ithaca, NY, USA, PDC-001-HP (115 V)) to increase hydrophilicity. The plates were then treated with ultraviolet light for 5 - 10 minutes for sterilization. Gelin and Glycosil were mixed in a 1:1 ratio and then the Glycosil/Gelin solution was combined in a 4:1 ratio with the appropriate concentration of Extralink. The final concentration of Extralink within the films were 0.2, 0.8, 1.2, and 2%. Twenty microliters of solution were plated in each well, spread, and covered for gelation, the time of which varied by Extralink concentration (2%: 2 - 5 minutes, 1.2%: 3-6 minutes, 0.8%: 4 - 7 minutes, 0.2%: 6 - 9 minutes). Once crosslinked, medium was added, and the films were incubated at 37°C for at least 30 minutes or until cells were ready to plate.

4.2.3 Atomic force microscopy (AFM)

Written, analyzed, and carried out by Kelsey Gray.

To measure the stiffness of the HA/gelatin, films were formed on 50 x 9 mm petri dishes. After the films had polymerized, the dishes were filled with PBS and an Asylum MFP-3D-BIO Atomic Force Microscope was used to perform AFM. The "Get Real" approach provided by Asylum Research was used to calculate the inverse optical lever sensitivity and the cantilever spring constant of the TR400PB(L) probes used for measurement. The cantilever spring constants were within the nominal range of 0.01 to 0.05 N m^{-1} (measured range: 0.026 to 0.028 N m^{-1}) and within a factor of 1.37 to Asylum's nominal value of 0.02 N m^{-1}. Four film samples of each composition were measured via five 100-curve force maps each (20 force maps in total). The force map specifications were as follows: 10 μm x 10 μm area, 2 μm force distance, 1 V trigger point (~1.57 nN), and a 0.99 Hz scan rate. The Hertz models was used to fit the data within Asylum's Igor Pro-based software using the equation $F = \frac{4}{3} \cdot (\frac{E}{1-\nu 2}) \cdot \sqrt{r} \cdot \delta^{3/2}$ where the fitting parameter, E, is the Young's modulus, and δ, is the measured indentation of the sample. The Poisson's ratio, ν, and tip radius of curvature, r, were assumed to be 0.45 and 30 nm, respectively. The results are shown in Figure 4.1 and indicate that all HA/gelatin films are in the physiological brain stiffness range.

4.2.4 Tumor cell morphology and migration assays

HA/gelatin films were prepared as described above in 24-well glass bottom plates. After soaking with medium in the incubator, $5x10^4$ MDA-MB-231 cells were

plated on top of the films and set-up to image as soon as the cells settled to the bottom of the plate. Images were collected via time-lapse phase-contrast microscopy and analyzed as described below in the data analysis section.

4.2.5 Tumor cell immunofluorescence staining

For CD44 staining, $2x10^4$ MDA-MB-231 cells were plated on HA/gelatin films formed with 0.2, 0.8, 1.2, and 2% Extralink in glass bottom dishes, or on dishes incubated with 20 μg ml^{-1} type I collagen for at least 1 hour at 37°C and washed three times with PBS. The next day, the cells were fixed in 3.7% formaldehyde (Millipore Sigma) for 10 minutes at room temperature, washed three times with PBS for 5 minutes each on a rocker, and permeabilized with 0.5% Triton-X 100 (Millipore Sigma) for 5 minutes. The samples were then washed again three times in PBS for 5 minutes each and blocked in 2% Bovine Serum Albumin (BSA) (Millipore Sigma) for one hour at room temperature. Cells were then incubated at 4°C overnight with CD44 antibody (monoclonal CD44 antibody (156 3C11) Mouse mAb #3570, Cell

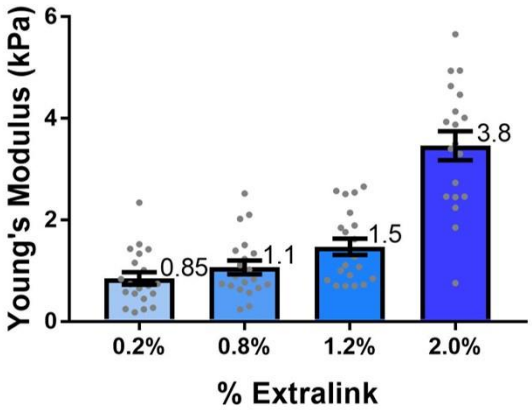

Figure 4.1: **AFM measurements of HA/gelatin gel stiffness.** Young's modulus measurements of HA/gelatin films as a function of HA/gelatin film crosslinking. Each point represents the average Young's modulus of a 100-curve force map covering a 10 μm x 10 μm area. Five measurements were taken across 4 different samples for each film composition. The ROUT method (Q=1%) was used to identify and remove 1 outlier. The numbers next to each bar represent the average modulus for that film composition. Data obtained, analyzed, and figure generated by Kelsey Gray.

Signaling Technologies, Danvers, MA, USA), which was dissolved in 2% BSA at a 1:100 ratio. Next, cells were rinsed with PBS and again blocked with 2% BSA for one hour at room temperature and washed with PBS. Cells were then incubated with 1:500 Phalloidin - Alexa Fluor 488 (Thermo Fisher Scientific), 1:100 of secondary antibody (Goat anti-Mouse IgG (H+L) Cross-Adsorbed Secondary Antibody Alexa Fluor 568, Thermo Fisher Scientific, A-11004), and 1:2500 of Hoechst 33342 (Thermo Fisher Scientific) diluted in PBS for 1 hour at room temperature. HBMECs transfected with the VE-cadherin-GFP adenovirus and tumor cells stained with Cell Tracker (described below) were also fixed for 10 minutes in 3.7% formaldehyde, washed with PBS, and stained with 1:2500 of Hoechst 33342 for one hour at room temperature. Finally, all samples were washed with PBS and stored at 4°C until imaging via confocal microscopy.

4.2.6 Adenovirus amplification

The VE-cadherin-GFP adenovirus was a generous gift from Dr. William Luscinskas (Harvard Medical School), whose lab has previously described the construction of this vector [164]. For amplification of VE-cadherin-GFP adenovirus, 293A cells cultured to ~80% confluency in 100 mm dishes. The 293A cells were then infected with the adenovirus and cultured until ~80-90% of all cells lifted off the dish. The cells were then collected and centrifuged at 1000 rpm. The resultant pellet was frozen at -80°C for 30 minutes and then thawed at 37°C for 15 minutes. The freeze-thaw was repeated a total of three times. The lysed cells were centrifuged at 3000 rpm and the supernatant was saved and frozen at -80°C. This supernatant was then used to transfect HBMECs.

4.2.7 Tumor cell incorporation assay

HA/gelatin films were prepared as described above in 24-well, glass bottom plates with 0.2, 0.8, 1.2, and 2% Extralink as well as a 1:1 mixture of gelatin and HA without Extralink (0%). $5x10^4$ - $1x10^5$ HBMECs were plated on the HA/gelatin films. For experiments fluorescently visualizing live VE-cadherin-GFP-expressing HBMECs' cell-cell junctions, freshly plated and barely-attached HBMECs were transfected with 10 μL of the VE-cadherin-GFP adenovirus, as previously described by Hamilla *et al.* [33], and incubated for two days. To investigate the percent incorporation of MDA-MB-231 cells into HBMEC monolayers, live MDA-MB-231 cells were first stained with CellTracker Orange CMRA Dye (Thermo Fisher Scientific) per the manufacturer's instructions. CellTracker Orange CMRA Dye is stated in product specifications to only transfer from parent cell to daughter cell and not in between neighboring cells. Since staining was carried out in the complete absence of HBMECs, transfer of dye between the two cell types is highly unlikely. Briefly, MDA-MB-231 cells were cultured in 6 well plates and equilibrated in HBMEC medium for two hours. The cells were washed with PBS and then incubated with 2 mL of 0.5 μM CellTracker Orange dye in RPMI-1640 and 1% Pen/Strep for 15 minutes. Cells were then washed again with PBS and incubated for 30 minutes in full HBMEC medium. The stained cells were then trypsinized and $1x10^4$ - $2.5x10^4$ MDA-MB-231 cells were plated on top of HBMECs that had been cultured on HA/gelatin films and allowed to form monolayers for two days prior to MDA-MB-231 cell seeding. These samples were imaged using time-lapse phase-contrast and fluorescence microscopy as described below.

4.2.8 Time-lapse microscopy

Similarly to Chapter 3, live-cell phase contrast and fluorescence images were captured using an IX83 microscope (Olympus, Center Valley, PA, USA) with a 10x objective (tumor cell migration assays on bare films), 20x objective (tumor cell morphology assays on bare films, incorporation assays with non-transfected HBMECs and CellTracker-stained tumor cells), and 60x oil objective (incorporation assays with VE-cadherin-GFP-expressing HBMECs and CellTracker-stained tumor cells). The Olympus cellSens Software (Olympus) was used to acquire the images. Phase contrast images of tumor cells on bare films were collected every 5 to 15 minutes for migration analysis, and additional images were captured at the end of the time-lapse on the second day for morphological analysis. The imaging regions for transmigration experiments were selected based on best monolayer coverage and the presence of MDA-MB-231 cells. The live-cell imaging chamber was maintained at 37°C, 50% humidity, and 5% CO_2:95% air surrounding the microscope stage.

4.2.9 Confocal microscopy

A PerkinElmer confocal spinning disk microscope (PerkinElmer, Waltham, MA) was used to obtain 3D images of fixed cells using a 40x water immersion objective. Vertical z-stacks were taken using appropriate filters using the Volocity 3D Image Analysis software. All acquisition settings were kept consistent between images within each experiment for CD44 imaging and slightly adjusted for best visualization for transmigration imaging. The ImageJ software (NIH; https://imagej.nih.gov) was used to reconstruct individual z-stack images into 3D,

maximum-intensity and interpolated projections. Brightness of each channel in images of tumor cells stained for CD44 was adjusted separately but identically between each image to ensure that intensities could be compared. Brightness of each channel in images of tumor cells incorporating into HBMEC monolayers were adjusted separately for best visibility of appropriate parts of the cells; thus, intensities cannot be directly compared for these images.

4.2.10 Data analysis

Tumor cell morphology and migration: tumor cell morphology was analyzed using ImageJ by manually tracing phase contrast images of live cells captured during or after time-lapse experiments in ImageJ. Cell circularity, solidity, and inverse aspect ratio were calculated as described in Appendix A. To track tumor cell migration on bare films, phase-contrast time-lapse images were acquired in 5-minute intervals. The ImageJ Manual Tracking plugin was used to track the approximate centroid of each cell starting with frame 60 (when cells appeared to have attached) and continuing up to 100 frames. Cells were not tracked if they went out of frame, divided during the tracking time, or were otherwise obstructed or hard to track. A custom Matlab (MathWorks, Natick, MA, USA) code was used to calculate cell speed, mean square displacement, and diffusion coefficient of the migrating cells, as described in detail in Appendix B. One hundred frames (495 minutes) were used for speed calculation, 90 frames (445 minutes) were used for MSD calculation, and 40 frames (195 minutes) were used for diffusion coefficient calculations. Analysis commenced once cells appeared attached (frames 60-70).

Tumor cell incorporation: To quantify the time that tumor cells take to incorporate into HBMEC monolayers, and the percent of the tumor cells that incorporate into the monolayers, CellTracker-stained tumor cells were tracked on HMBEC monolayers by capturing images in 15-minute intervals. First, the total number of tumor cells per frame was recorded at the start of each time-lapse sequence. Tracking was carried out for 40 frames (585 minutes). Cells that went out of frame before frame 40 were excluded from analysis, as well as cells deemed "untrackable" due to clumping, visual obstructions, or migration to areas of large gaps in the monolayer. An incorporating cell was subjectively identified based on the disappearance of a white halo surrounding the cell and transition to a 2D-flattened morphology in phase contrast images. If a cell was spread, but retained a halo and 3D appearance, it was counted as not incorporating and instead was likely spreading on top of the monolayer. Percent incorporation was calculated by dividing the total cells that incorporated into the monolayer by the total number of cells tracked in each frame. The start time for a cell to incorporate was marked as the first frame where the cell appeared to be spreading into the monolayer, or the very first frame if it was already spread. If cells incorporated and then exited the monolayer, only the first instance of incorporation was counted. If a cell divided before incorporating or before frame 40, it was counted as two separate cells. If cells divided after incorporation, it was counted as one cell. Cumulative percent incorporation was calculated by averaging the total percent of cells that had incorporated at each 15 minute timepoint out of the total number of analyzable cells.

For migration analysis pre- and post-incorporation, select cells were manually traced in ImageJ. If cells remained completely rounded for 40 frames, they were tracked for 20 frames (285 minutes) and characterized as “non-incorporating.” Cells that incorporated were tracked for 6 frames (75 minutes) prior to spreading (i.e. “pre-incorporation”) and 6 frames (75 minutes) after they had fully incorporated (i.e. “post-incorporation”). If a cell started to incorporate within the first 6 frames (i.e., did not have a sufficient pre-incorporation phase to track) or rounded up again post-incorporation in less than 6 frames, the cell was omitted. Tumor cells that appeared to be spread-out but maintained a white halo, indicating a higher focal plane, and did not incorporate within 40 frames were interpreted as cells adhered to, and migrating on, the surface of the monolayer, and were entirely excluded from analysis. Three randomly selected HBMECs per frame were also traced for up to 8 frames (105 minutes) for three experiments (36-66 cells total). The average absolute value of the change in area or speed between each time point was calculated for a given cell by subtracting the area or speed at the previous time point from the area or speed at the current time point and taking the absolute value of the difference. These differences were then averaged for the time points analyzed for each cell.

4.2.12 Statistical Analysis

GraphPad Prism 8 (GraphPad, La Jolla, CA, USA) was used for all statistical analysis and graph preparation. Data was tested for normality using a D'Agostino-Pearson normality test, and it was found that the majority data within the same set did not follow a normal distribution. Thus, non-parametric tests were used for statistical analysis. A non-parametric Kruskal-Wallis ANOVA test with a Dunn’s multiple

comparison post-hoc test was used with $P > 0.05$ indicating not statistically different, * $P \leq 0.05$, ** $P \leq 0.01$, *** $P \leq 0.001$, **** $P \leq 0.0001$. A linear regression was used to compare the number of tumor cells at the start versus monolayer quality. Errors bars represent standard error of the mean. All data represents pooled values from three independent trials unless otherwise noted in the figure captions.

4.3 Results

4.3.1 MDA-MB-231 cells become smaller and slower with increased HA/gelatin crosslinking

Extracellular matrix crosslinking has been shown to alter tumor cell phenotype and invasiveness, and HA is known to be one of the primary components of the brain's extracellular matrix [38], [159], [161], [162]. Hence, we aimed to evaluate the migration and morphology response of MDA-MB-231 tumor cells to varying degrees of HA/gelatin film crosslinking by altering the concentration of Extralink, a PEGDA-based crosslinker, during film formation [165]. We found that with increased Extralink concentration from 0.2% to 2%, tumor cells became significantly smaller (Figure 4.2 A, B) and more circular (Figure 4.2 A, C) and increased in inverse aspect ratio, circularity, and solidity (Figure 4.2 A, C). Furthermore, cells plated on HA/gelatin films with increased Extralink concentrations demonstrated more homogeneous morphologies as evidenced by a decreased spread of the data with higher Extralink concentrations (Figure 4.2 B, C). Additionally, tumor cell speed decreased with increased crosslinking of HA/gelatin films (Figure 4.2 D). Plots of mean squared displacement vs. time indicated that tumor cells

explored smaller areas with increased crosslinking of HA/gelatin films (Figure 4.2 E), with a non-statistically significant decrease in diffusion coefficient with increased crosslinking of HA/gelatin films (Figure 4.2 F). Because a mesenchymal, metastatic phenotype is typically associated with highly migratory, elongated cells [166], these changes in cell morphology and migration could be relevant to the cells' functionality.

Cell attachment to HA is mediated by CD44, which also has been implicated in transducing HA stiffness cues and associated with brain tumor progression and invasion [157], [167]–[169]. For breast tumor cells, CD44 increases tumor cell adhesion to and invasion of the endothelium, increasing the efficiency of distant metastasis [170]. Hence, we explored whether the morphological and migratory behavior with altered HA/gelatin film crosslinking were also associated with differences in CD44 binding. Interestingly, MDA-MB-231 cells immunostained for CD44 on HA/gelatin films with varying degrees of crosslinking, as well as type I collagen-coated glass, did not present observable differences in CD44 expression (Figure 4.2 G).

Figure 4.2: **MDA-MB-231 morphology and migration parameters on HA/gelatin films with varying degrees of crosslinking.** A) Phase contrast images of MDA-MB-231 cells on HA/gelatin films with 0.2, 0.8, 1.2, and 2% Extralink. Scale bar is 50 μm and applies to all images. B) Areas, C) inverse aspect ratio, circularity, and solidity, D) speed, E) mean square displacement, and F) diffusion coefficient of MDA-MB-231 cells on HA/gelatin films with 0.2, 0.8, 1.2, and 2% Extralink. Means of columns that do not share a lower-case letter are significantly different with $P < 0.05$ via a non-parametric Kruskal-Wallis ANOVA test with a Dunn's multiple comparison post-hoc test. B,C: $529 \leq N \leq 582$, D,F: $142 \leq N \leq 228$ where N is the number of cells. E: $N = 3$, where N is the number of trials. All error bars represent standard error of the mean. All values are pooled from three independent trials. G) Reconstructed confocal z-stacks of MDA-MB-231 cells immunostained for CD44 (red) and stained for actin (green) on HA/gelatin films with 0.2, 0.8, 1.2, and 2% Extralink, as well as on glass coated with type I collagen. Scale bar on first image is 50 μm and applies to all images. Scale bar in the zoomed in inserts is 25 μm. Green: actin; red: CD44, blue: DNA. All images were reconstructed from a z-stack in ImageJ and intensities were adjusted equally for each channel and image. Gregory Dawson assisted with analysis of cell migration and speed.

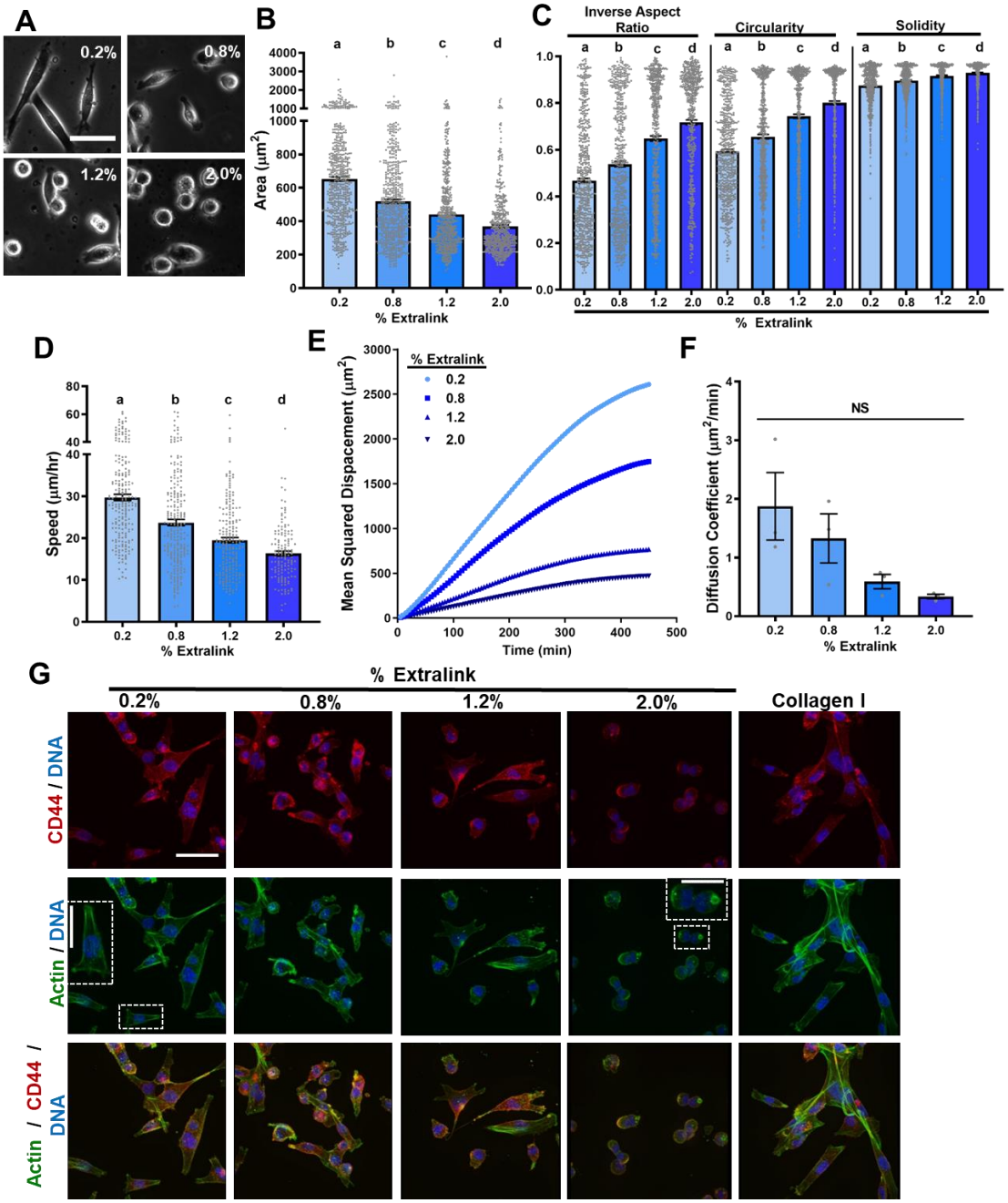
A
0.2%
0.8%
1.2%
2.0%
B
Area (µm²)
% Extralink
C
Inverse Aspect Ratio
Circularity
Solidity
% Extralink
D
Speed (µm/hr)
% Extralink
E
Mean Squared Dispacement (µm²)
% Extralink
0.2
0.8
1.2
2.0
Time (min)
F
Diffusion Coefficient (µm²/min)
NS
% Extralink
G
% Extralink
0.2%
0.8%
1.2%
2.0%
Collagen I
CD44 / DNA
Actin / DNA
Actin / CD44 / DNA

Meanwhile, actin arrangement was altered, with tumor cells on type I collagen and HA/gelatin films with 0.2% Extralink displaying a somewhat fibrous actin arrangement (Figure 4.2 G) which became more diffuse with increased film crosslinking, especially on the films with 2% Extralink (Figure 4.2 G). Increased cell spreading and mesenchymal migration are typically correlated with a more stress fiber-rich actin arrangement [171], which is indeed in line with our observations. A stress fiber-rich actin cytoskeleton is also often linked with a high degree of cellular contractility, which also correlates with the stiffness of the underlying cellular matrix [172]. Since increased crosslinking typically results in increased material stiffness, changes in film stiffness could drive alterations in tumor cell contractility and actin filament arrangement. Hence, we used atomic force microscopy to probe the effect of Extralink concentration on the Young's modulus of HA/gelatin films. The average modulus of the films formed with 0.2, 0.8, 1.2, and 2% Extralink were measured to be 0.85, 1.1, 1.5, and 3.8 kPa, respectively (Figure 4.1). Interestingly, only the Young's modulus of the film formed using 2% Extralink was statistically significantly different from the Young's modulus of the other film compositions. Despite this, we still found significant differences in tumor cell phenotype and behavior on those film compositions (Figure 4.2 A).

4.3.2 MDA-MB-231s incorporate into HBMEC monolayers, independent of HA/gelatin film crosslinking

Because other work in our lab observed that tumor cell-derived biochemical cues can alter HBMEC junction morphology (data not shown), we next examined the effect of HA/gelatin film crosslinking on tumor cell incorporation into HBMEC

monolayers. Phase contrast and fluorescence microscopy were used to evaluate CellTracker-stained MDA-MB-231 incorporation into HBMEC monolayers (Figure 4.3 A). We found no statistically significant difference in the percent incorporation of tumor cells into HBMECs (Figure 4.3 B) or in the time from the start of the timelapse to complete incorporation (Figure 4.3 C) as a function of Extralink concentration under static conditions. The cumulative percent of tumor cell incorporation, or percent of incorporation at each time point, was generally similar for all films, regardless of Extralink concentration under static conditions (Figure 4.3 D). Furthermore, we found that the plot of percent tumor cell incorporation at ~10 hours versus the average number of tumor cells at the start of the time-lapse had a slope that was not significantly non-zero (Figure 4.3 E).

Tumor cells can utilize multiple modes of extravasation across endothelial cell barriers, and hence we used confocal and live-cell microscopy to image CellTracker-stained tumor cells interacting with VE-cadherin-GFP-expressing HBMECs. We found that some tumor cells remained on top of or found their way underneath the HBMECs (Figure 4.4 A). As expected, many tumor cells simply squeezed paracellularly into gaps between HBMECs, with protrusions going above and/or underneath the monolayer (Figure 4.4 B, C (left insert)). We also found several interesting and unexpected interactions. In some cases, an HMBEC, identified by its VE-cadherin-GFP expression, contained an extra nucleus and internal CellTracker stain that should have exclusively stained the tumor cells (Figure 4.4 C (right insert), E, F). We note that CellTracker Orange CMRA is transformed into a cell-impermeant dye once inside the cell and is activated via enzymatic cleavage and thus can spread

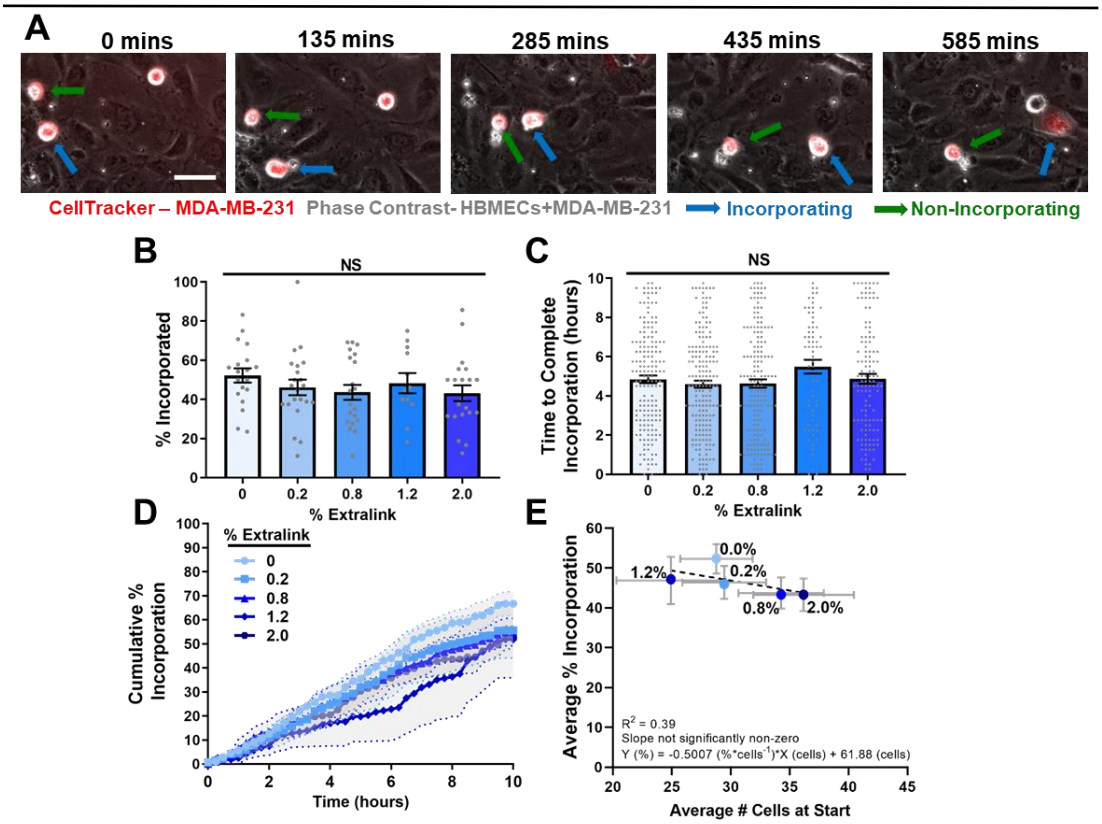

Figure 4.3: **MDA-MB-231 cell incorporation into HBMEC monolayers on HA/gelatin films with varying degrees of crosslinking.** A) Phase contrast images of an incorporating (blue arrow) and a non-incorporating (green arrow) CellTracker-stained MDA-MB-231 cell (red) on an HBMEC monolayer. B) Percent of tumor cells that incorporate ($12 \leq N \leq 22$, where N is the number of time-lapse sequences analyzed), C) time from start of time-lapse to full incorporation, and D) the cumulative percent incorporation of tumor cells over time ($65 \leq N \leq 184$, where N is the number of incorporating cells) into HBMEC monolayers on HA/gelatin films with 0, 0.2, 0.8, 1.2, and 2% Extralink in a total time of 9.75 hours. For panels B and C, $P > 0.05$ via a non-parametric Kruskal-Wallis ANOVA test with a Dunn's multiple comparison post-hoc test between all groups. E) Average percent incorporation as a function of the number of tumor cells in frame at the start of the time-lapse. All error bars represent standard error of the mean. All data is pooled from three independent trials.

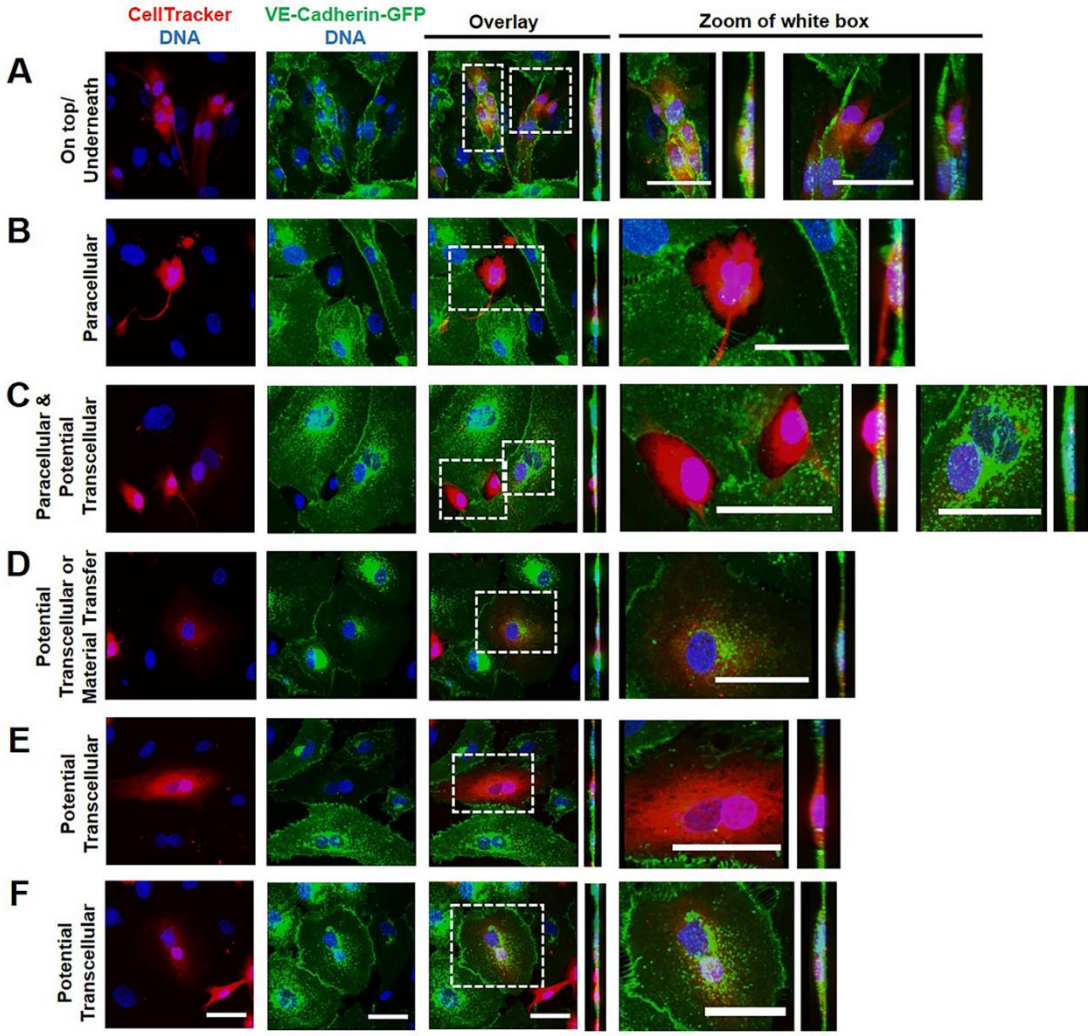

Figure 4.4: **Confocal images of various modes of tumor cell incorporation into HBMEC monolayers.** Confocal z-stacks reconstructed in ImageJ into a 3D stack showing evidence of A) MDA-MB-231 cells on top of or underneath HBMECs, B) paracellular incorporation of MDA-MB-231 with long cell tail above HBMEC monolayer, C) paracellular and potentially transcellular incorporation, D) potentially transcellular incorporation or spread of MDA-MB-231 cell material into HBMEC, E) and F) potentially transcellular incorporation of MDA-MB-231 cells into HBMEC monolayer. Intensity of each channel in each image were separately adjusted for better visualization; thus, relative intensities should not be compared. Scale bars from bottom row (panel F) apply to all images above except for the zoomed images. Each zoomed image is scaled individually, and all scale bars on zoomed images are 50 μm. All images were taken on HA/gelatin films with 0% Extralink. Green: VECadGFP (HBMEC); red: CellTracker (MDA-MB-231), blue: DNA (HBMEC and MDA-MB-231).

to daughter cells but not neighboring cells, and thus we do not expect for HBMECs to be nonspecifically labeled with CellTracker. By observing the 3D and cross-sectional view as well as the orthogonal view of the cells, it appeared that a tumor cell had transcellularly incorporated into the HBMEC monolayer, becoming a part of the HBMEC (Figure 4.4 C (right insert), E, F). A different mode of tumor cell-HBMEC interaction was observed in HBMECs that appeared to contain CellTracker stain but retained solely one nucleus (Figure 4.4 D). The punctate nature of the CellTracker stain in these HBMEC leads us to speculate that there could be extracellular vesicles or other cellular material shed by tumor cells and internalized by HBMECs (Figure 4.4 D).

4.3.3 MDA-MB-231 tumor cells dynamically interact with HBMEC junctions

To quantitatively capture the dynamics of tumor cell incorporation into HBMECs, we collected time-lapse images of GFP-VE-cadherin-expressing HBMECs and CellTracker-stained MDA-MB-231 tumor cells. We found that some tumor cells were able to migrate on top of HBMEC adherens junction and appear to morphologically “unzip” them (Figure 4.5 A, white arrow), such that the adherens junctions opened and then closed behind the tumor cell (Figure 4.5 A, yellow arrow). Additionally, we found that tumor cells could squeeze in between HBMECs, resulting in complete disruption of the surrounding adherens junctions (Figure 4.5 B, magenta and purple arrows). Similar to Figure 3 D, some image sequences suggested that HBMECs internalized cellular material shed by tumor cells, without damaging surrounding adherens junctions (Figure 4.5 B, blue arrow). These time-lapse sequences allowed us to dynamically confirm our static, confocal microscopy

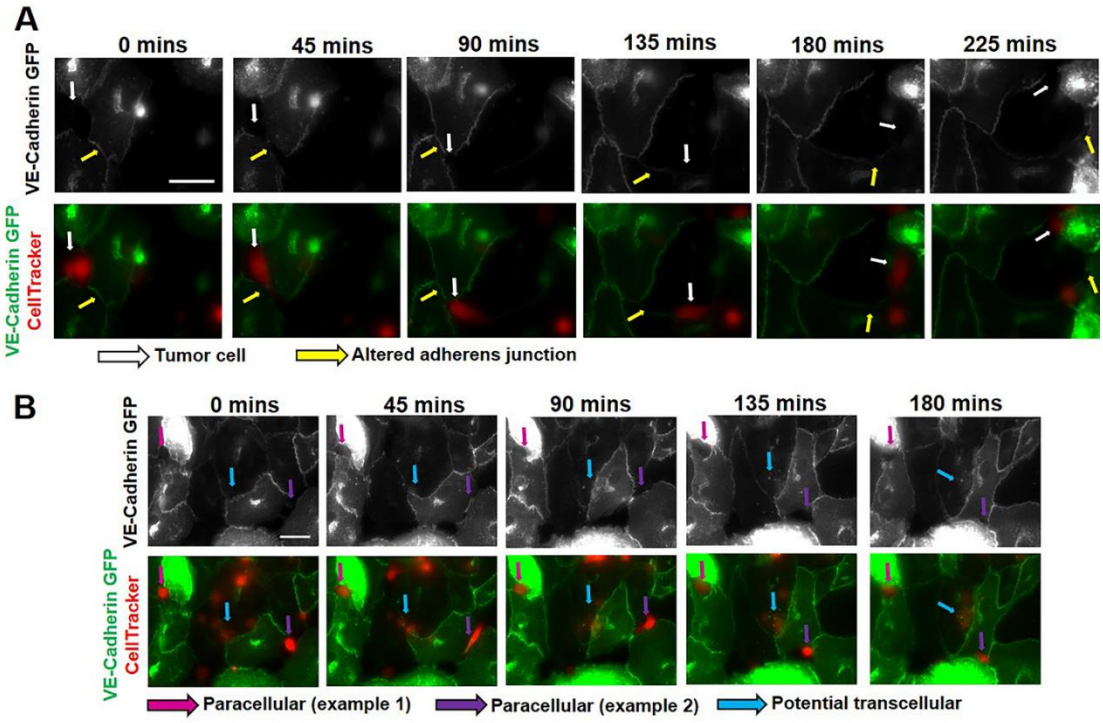

Figure 4.5: **Fluorescent live-cell imaging of VE-cadherin-GFP-expressing HBMECs and CellTracker-stained MDA-MB-231 cells.** A) Example of MDA-MB-231 cell (white arrow) altering VE-cadherin-GFP (yellow arrow) between HBMECs as the tumor cell passes over the HBMEC junction. B) Examples of tumor cells squeezing between HBMECs (pink and purple arrows) and possible material transfer from tumor cell to HBMEC, or potential transcellular incorporation (blue arrow). Intensity of each channel in each image was separately adjusted for better visualization, thus, relative intensities should not be compared. Scale bars from top row apply to all images in its series and are 50 μm. Starting time was selected for best visualization. All images were taken on HA/gelatin films with 0% Extralink. Green: VE-cadherin-GFP (HBMEC); red: CellTracker (MDA-MB-231). Ariana Joy DeCastro assisted with experiments.

findings, while simultaneously enabling us to observe tumor cell-adherens junction interactions.

4.3.4 MDA-MB-231 tumor cell morphology and migration speed are altered during incorporation into HBMECs

Tumor cell morphology and migration were clearly affected by the concentration of Extralink during migration on the bare HA/gelatin films (Figure 4.2); therefore, we explored the dynamics of tumor cell incorporation into HBMECs and whether this process depended on crosslinking of the HA/gelatin films. In some cases, tumor cells either remained rounded on top of the HBMEC monolayer and did not incorporate, or they spread into the monolayer (Figure 4.3 A). However, many tumor cells also spread and migrated on top of the HBMEC monolayer without incorporating. Therefore, we studied three specific cases over time: (1) MDA-MB-231 cells that incorporated into the monolayer, separated into a pre-incorporation (i.e., exclusively rounded) and a post-incorporation (i.e., spread out) regime; (2) MDA-MB-231 cells that did not incorporate and remained rounded for the entire study; and (3) three representative HBMECs from each monolayer. First, we observed that the area (Figure 4.6 A) and speed (Figure 4.6 B) of HBMECs remained mostly constant over time at each Extralink concentration. There was no statistical difference between the absolute value of the average changes in HBMEC area or speed across all timepoints as a function of Extralink concentration (Figure 4.6 C). A similar trend was observed for non-incorporating tumor cells, where both their area (Figure 4.6 D) and speed (Figure 4.6 E) did not change significantly over time (Figure 4.6 F). In general, though, the greatest variability across timepoints in non-

incorporating tumor cell area and speed occurred with the 1.2% Extralink concentration (Figure 4.6 F). However, the area of incorporating tumor cells increased during incorporation (Figure 4.6 G), while their speed decreased during incorporation (Figure 4.6 H). This increase in tumor cell size after incorporation is in line with a previous study that reported melanoma cells becoming more spread and elongated as they incorporated into endothelial monolayers [150]. For tumor cells pre- and post-incorporation, there were no significant differences between Extralink concentrations in the absolute value of the change in area or speed across timepoints; however, it was evident that area was generally more consistent between the different Extralink concentrations prior to incorporation and speed was generally more consistent post-incorporation (Figure 4.6 I).

To understand the statistical significance of this dynamic data, we calculated the area and speed of the cells averaged across multiple time points pre- or post-incorporation. First, we found that there were no differences in HBMEC or MDA-

---

Figure 4.6: **MDA-MB-231 tumor cell area and speed profiles over time during incorporation into HBMEC monolayers.** A) HBMEC area and B) HBMEC speed over time during incorporation experiments on HA/gelatin films with 0, 0.2, 0.8, 1.2, and 2% Extralink. $36 \leq N \leq 66$ where N is number of cells. C) Absolute value of the average change in area and speed between each time point from panels A and B, respectively. D) Area and E) speed over time of non-incorporating MDA-MB-231 cells on HBMEC monolayers on HA/gelatin films with 0, 0.2, 0.8, 1.2, and 2% Extralink. $14 \leq N \leq 89$, where N is the number of cells. F) Absolute value of the average change in area and speed between each time point from panels D and E, respectively. G) Area and H) speed over time for MDA-MB-231 cells pre-incorporation (while rounded) and post-incorporation (while spread out) into HBMEC monolayers. $30 \leq N \leq 78$ where N is the number of cells. I) Absolute values of the average change in area and speed between each time point from panels G and H, respectively. Average J) area and K) speed of HBMECs, non-incorporating MDA-MB-231 cells, and incorporating MDA-MB-231 cells (pre- and post-incorporation) on HA/gelatin films with 0, 0.2, 0.8, 1.2, and 2% Extralink. For panels J and K, each dot represents one cell. All data is pooled from three independent trials. Statistical significance was determined using a non-parametric Kruskal-Wallis ANOVA test with a Dunn's multiple comparison post-hoc test as follows: * $P \leq 0.05$, ** $P \leq 0.01$, *** $P \leq 0.001$, **** $P \leq 0.0001$. For all figures, error signifies standard error of the mean.

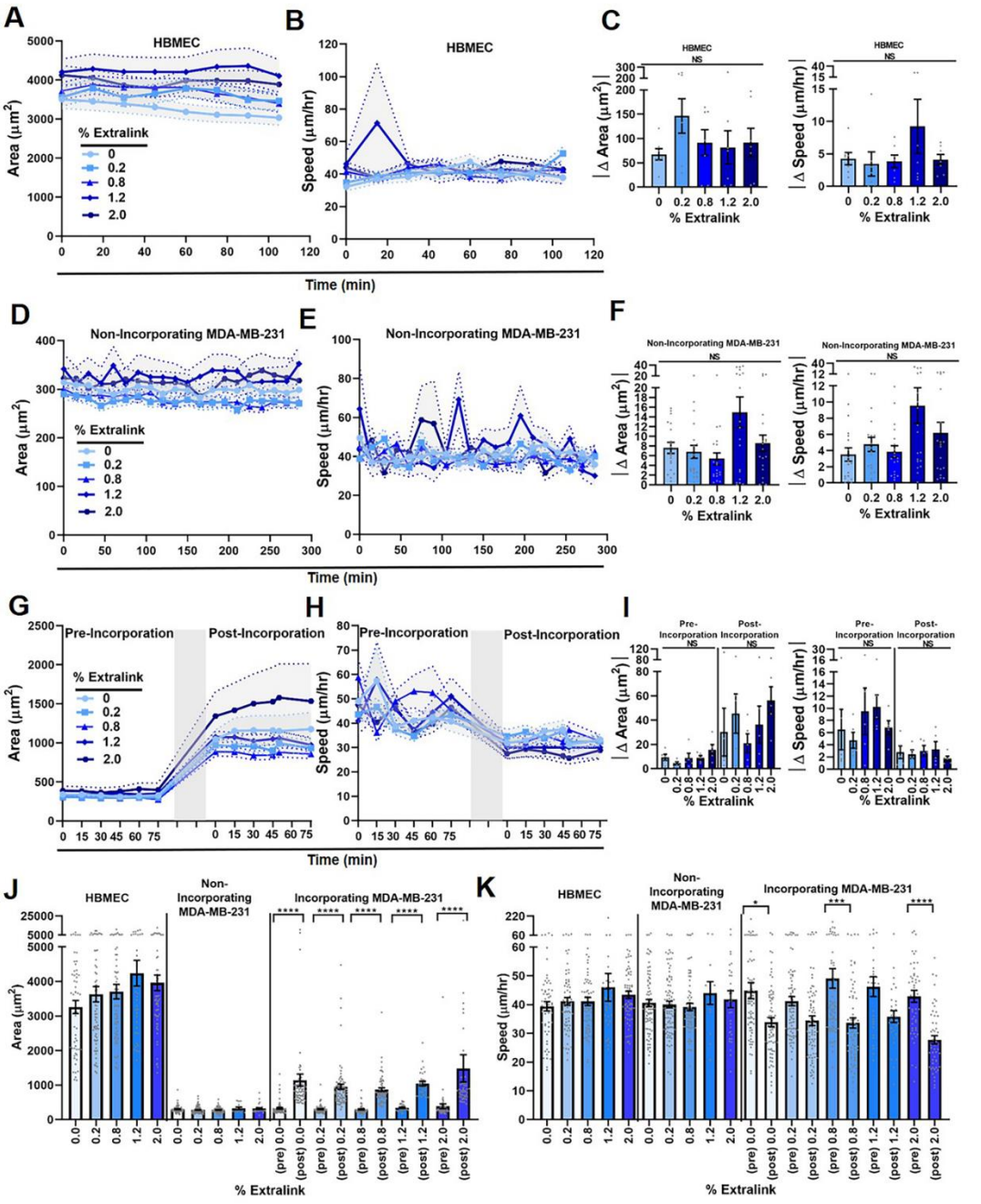
A
HBMEC
Area (μm²)
% Extralink
0
0.2
0.8
1.2
2.0
B
HBMEC
Speed (μm/hr)
Time (min)
C
HBMEC
NS
| Δ Area (μm²) |
| Δ Speed (μm/hr) |
% Extralink
D
Non-Incorporating MDA-MB-231
Area (μm²)
% Extralink
E
Non-Incorporating MDA-MB-231
Speed (μm/hr)
Time (min)
F
Non-Incorporating MDA-MB-231
NS
| Δ Area (μm²) |
| Δ Speed (μm/hr) |
% Extralink
G
Pre-Incorporation
Post-Incorporation
Area (μm²)
% Extralink
H
Pre-Incorporation
Post-Incorporation
Speed (μm/hr)
Time (min)
I
Pre-Incorporation
Post-Incorporation
NS
| Δ Area (μm²) |
| Δ Speed (μm/hr) |
% Extralink
J
HBMEC
Non-Incorporating MDA-MB-231
Incorporating MDA-MB-231
****
Area (μm²)
% Extralink
K
HBMEC
Non-Incorporating MDA-MB-231
Incorporating MDA-MB-231
*
***
****
Speed (μm/hr)
% Extralink

MB-231 tumor cell (incorporating and non-incorporating) area (Figure 4.6 J) or speed (Figure 4.6 K) as a function of HA/gelatin film crosslinking under static conditions. However, the area of the tumor cells was significantly larger pre-incorporation compared to post-incorporation on HA/gelatin films for all concentrations of Extralink (Figure 4.6 J), as was also observed in the plots over time (Figure 4.6 G). Meanwhile, there was a significant decrease in speed between pre- and post-incorporation phases of the tumor cells on HA/gelatin films with 0, 0.8, and 2% Extralink (Figure 4.6 K). These results suggest that the process of incorporation into HBMECs changes the morphology and migratory behavior of the tumor cells and also abrogates the mechanosensitivity of tumor cells to the crosslinking density of the HA/gelatin films.

We also note that for HA/gelatin films with 0.2% Extralink, the area of incorporating tumor cells (Figure 4.6 J) became similar to the area of tumor cells on bare films (Figure 4.6 B). However, due to the loss of a mechanosensation effect in the presence of HBMECs, tumor cells had much larger spreading areas and migration speeds during incorporation into HBMECs on the HA/gelatin films with 2.0% Extralink in comparison with tumor cells on the bare films.

4.4 Discussion

Extracellular matrix crosslinking and stiffness are known regulators of many cellular functions in the context of physiologic and pathologic conditions. In this work, we explored the effects of HA crosslinking on metastatic breast tumor cell migration and incorporation into the human brain endothelium. Interestingly, our results show reduced spreading area and more diffuse stress fibers for cells on more

crosslinked, and thus stiffer, HA/gelatin films is contradictory to frequent reports in literature, including our own, where cells spread more on stiffer extracellular matrix-coated polyacrylamide gels [60], [114], [173]. Similarly, previous studies have shown that when utilizing HA-methacrylate gels crosslinked with dithiothreitol (DTT) and functionalized with Arg-Gly-Asp (RGD) peptides for cell adhesion, increasing HA weight percent and crosslinking density, thus increasing stiffness, increased the spreading area and speed of glioblastoma cells [45]. Varying the concentration of DTT crosslinker in the same HA system was also found to alter the phenotype of brain-seeking clones of MDA-MB-231 cells, where they observed increased tumor cell area and speed with increased crosslinking and film stiffness [174]. Notably, the previous studies were performed on HA gels crosslinked using a different mechanism and with various coatings for cell adhesion, rather than gelatin incorporation as was used here. On the other hand, through chemical rather than mechanical signaling, soft HA gels can produce identical cellular responses to those on stiffer substrates [175]. Hence, mechanosensitivity in this context likely involves a delicate balance between sensing of multiple parameters of the extracellular matrix, including stiffness, method and degree of crosslinking, method of adhesion molecule incorporation, and the specific composition of the matrix.

One aspect of the HA/gelatin films that could have affected the response of tumor cells to changes in crosslinking is film porosity. Several studies in the past have observed that various different formulations of HA gels are structured as a mesh folded sheet which became dense with increased methacrylated HA polymer weight fraction [45]. Other studies have shown porous meshes in HA-chitosan gels where the

size of the pores gradually decreased with increased crosslinking [176]. The size of the pores was in the tens of microns range [176]. However, since the structure of the gels could be a result of either one of the two components in the gel, another study compared the structures of collagen gels, methacrylated HA gels, and gels that were a combination of both gels and found that while collagen itself had a fibrous structure, the HA gels had a sheet or flake-like structure, and the composite gels had elements from both types of gel and were highly porous [177]. Since in the case of this study the gelatin used can be expected to act similarly to collagen and form a tighter structure with increased crosslinking [178] it is expected that our films were comprised of both fibrous or sheet-like components as well as porous ones and increasing crosslinking decreases pore size and makes the mesh more dense. Based on literature, the pores of the films are likely of micron size and thus highly relevant to cell behavior since their size is of similar order of magnitude. This aspect of the HA/gelatin film structure could potentially play a role in the mechanosensitive response of the tumor cells.

For example, the presence of larger pores and a more diffuse network could be facilitating tumor cell-matrix degradation via invadopodia. Invadopodia are a type of actin rich protrusion of carcinoma cells, similarly to podosomes on endothelial and other cells [179]. Invadopodia are able to not only help cells attach to a matrix, but also degrade it with greater efficiency than podosomes and invadopodia are also larger than podosomes, with a maximum size of 8 μm x 5 μm [179]. It is possible that the larger pores and the more diffuse network of HA and gelatin allows for deeper invadopodia penetration of the matrix and thus increased matrix degradation by

MMPs [179]. Invadopodia have been shown to be involved in cell migration and transmigration [179], which could explain some of the differences observed on the differently crosslinked HA/gelatin films. As the matrix becomes more crosslinked and the pore size decreases, it is possible that fewer invadopodia invade the matrix resulting in decreased matrix degradation, and cell migration. Increased involvement of invadopodia could also correspond to an increased integrin expression [179], which could explain the increased spreading of cells on less crosslinked HA/gelatin matrices.

Our results suggest MDA-MB-231 are highly sensitive to HA/gelatin crosslinking despite the fact that the measured Young's modulus of the films was in the relatively small range of 0.85 to 3.8 kPa. This could indicate that extracellular matrix crosslinking could actually have a greater effect on tumor cells than extracellular matrix stiffness. The observed changes in migration and morphology of tumor cells on bare HA/gelatin films could be indicative of mechanosensitive changes in metastatic potential of the cells. For example, tumor cells have been shown to be more migratory during pre-micrometastasis (when they first cross an endothelium but prior to formation of tumor cell-tumor cell contacts) as compared in micrometastasis (once tumor cells form contacts and begin to form secondary tumors) [180]. In fact, the migratory pre-micrometastsis regime has been suggested as a therapeutic target [180]. Studies have also shown, as discussed in Chapter 3, that more cells with higher metastatic potential tend to also be more migratory [140]. This suggests that the mechanosensitivity of tumor cells to HA/gelatin crosslinking could also be tied to the metastatic potential of the tumor cells, where the cells are more likely to form new

secondary tumors when they are initially more migratory, as they are on less-crosslinked HA/gelatin films.

Furthermore, our results suggest a lack of correlation between the number of tumor cells in the area of observation and propensity to incorporate. We note that if a tumor cell interacted directly with a gap between HBMECs in the monolayer, it was not included in the analysis. Therefore, once a monolayer of HBMECs was present in the system, tumor cells appeared to be significantly less sensitive to HA/gelatin matrix crosslinking than when they were on bare films. These results suggest that HA/gelatin crosslinking does not significantly affect tumor cell incorporation into HMBEC monolayers, and that matrix mechanics might become more important post-extravasation, since tumor cells on the bare gels without HBMECs showed such dramatic differences in morphology and migration. Our observations are also consistent with our previous results, where percent tumor cell incorporation into HUVECs was independent of polyacrylamide gel stiffness [181].

Our observations suggest that breast tumor cells have multiple mechanisms by which they can interact with and incorporate into HBMEC monolayers. This is consistent with our prior studies in non-brain extracellular matrix, where tumor cells incorporated into and physically displaced endothelial cells in monolayers [33]. Other studies have found that tumor cells can utilize cytoplasmic protrusions (i.e., invadopodia) to assist in extravasation across endothelial barriers and degrade the basement membrane [182]–[185], which has been previously thoroughly reviewed [186], [187]. It is possible that similar interactions are occurring here during paracellular incorporation as tumor cells squeeze in between brain endothelial cells.

Furthermore, the dynamic nature by which we observed HBMEC adherens junctions open and close due to tumor cell interaction is of particular interest, and suggest that HBMECs have a potential for self-repair. Indeed, our results are supported by prior reports where endothelial cells were able to rearrange their cytoskeleton to repair themselves post para- and trans-cellular invasion of tumor cells [188].

Despite the interaction of tumor cells with the HA matrix when squeezing in between brain endothelial cells, the degree of HA/gelatin film crosslinking did not play a significant role in the ability of tumor cells to incorporate. It is also possible that brain endothelial cells deposit their own extracellular matrix to an extent that masks the mechanical properties of the original HA/gelatin films to the tumor cells. Indeed, previous studies have demonstrated that endothelial cells are capable of low levels of extracellular matrix deposition after just one day of culture in favorable conditions [189], and thus HBMEC-matrix remodeling is plausible during the three-day culture period.

Interestingly, other studies have reported enhanced transmigration of MDA-MB-231 cells in the presence of human brain endothelial cells, suggesting that the endothelial cells facilitate transmigration [190]. This could potentially explain the increase in tumor cell area and migration post-incorporation, where HBMECs are present, compared to their respective values on bare HA/gelatin films. Notably, though, this response was influenced by the extent of matrix crosslinking, since only minimal changes were observed on the films with 0.2% Extralink. Alternatively, as discussed above, HBMECs may be remodeling the underlying matrix and/or depositing new extracellular matrix, hence masking the original mechanical

properties of the HA/gelatin films to the incorporating tumor cells and altering their interactions with the matrix post-incorporation. It is also possible that junctional proteins, which may potentially be linking tumor cells and HBMECs, could physically alter the migratory capacity of tumor cells within an HBMEC monolayer.While our experiments have provided interesting insights into the biochemical and physical interactions between tumor cells, the HA matrix, and the brain endothelium, we acknowledge several important limitations of our system. First, our models lack other cell types present at the *in vivo* BBB, including astrocytes and pericytes. There is a growing body of literature [191], [192] to support the hypothesis that the presence of these cells, and/or their secreted biochemical factors, would likely influence tumor cell migration and incorporation into the brain endothelium, cell-cell junctions in the HBMECs, and possibly also the extracellular matrix. Indeed, our own previous work has shown that astrocyte conditioned media applied to tumor cells directly, or to their extracellular matrix only, can result in increased tumor cell migration, as described in Chapter 3. Secondly, our models lack physiologic flow conditions. Shear stresses in the brain capillaries of rodent models have been measured to be in the range of 20-40 dyne cm^{-2} [193], which can influence endothelial barrier function, cell migration, tumor cell adhesion, and tumor cell proliferation [194]–[198]. Another limitation of our model is the lack of cylindrical geometry, which can influence endothelial cell elongation in the presence of shear stress [199]. Incorporation of these additional cells and mechanical cues will continue to be important as the field develops benchmarks for BBB models.

4.5 Conclusion

We have shown that MDA-MB-231 morphology and migration parameters were sensitive to the crosslinking density of HA/gelatin films, with a trend that was opposite of that typically observed for varying stiffness of extracellular matrix-coated polyacrylamide gels. HA/gelatin crosslinking, however, did not seem to affect MDA-MB-231 tumor cell incorporation into the HBMEC monolayers. We also showed that MDA-MB-231 tumor cells were able to utilize multiple modes of incorporation into HBMECs, in addition to the commonly reported paracellular pathway, and that tumor cells dynamically modified their morphology and migration behavior, as well as HBMEC junctions, during incorporation into a biomimetic BBB. Overall, our quantitative results suggest that a combination of biochemical and physical factors promote tumor cell migration through the BBB, and suggest that extracellular matrix mechanics may become most significant once incorporation or transmigration is complete. Future work will continue to build upon these results by incorporating more cellular components and mechanical cues into the experimental *in vitro* models.

5 Morphological phenotyping of organotropic brain- and bone-seeking clones of metastatic breast tumor cells

5.1 Introduction

Yoneda *et al*. established organotropic brain- and bone-seeking clones from the MDA-MB-231 parental metastatic breast tumor cell line [73] which now can be used to study the different properties of the clones. Organotropic metastatic tumor cells have been shown to have several distinguishing properties, such as exosome secretion and molecular expression [16]. Breast cancer in particular is known to exhibit a significant level of organotropism [16]. A better understanding of the properties that make tumor cells organotropic, can inform further steps in targeting these specific cell phenotypes in the blood stream prior to transmigration, during transmigration, or as secondary tumors as well as could allow for earlier cancer detection [16]. Some, primarily biochemical, differences in the breast cancer cell clones have already been established. For example, brain-seeking tumor cells have been shown to produce more parathyroid hormone with TGF-β-independent growth while the bone-seeking and parental tumor cells did not have these properties [73]. Brain seeking tumor cell clones were also more sensitive to insulin-like growth factor I [73] and the bone-seeking tumor cells adhered more strongly osteoblast generated bone matrix, than brain-seeking and parental clones [74]. In fact, one study showed that adhesion properties of brain- and bone-seeking cells can be used to sort them based on their adhesion to brain and bone like extracellular matrix, as established via different combinations of extracellular matrix proteins [200]. An additional study

performed a proteomic analysis of the brain-seeking clones and compared them to the parental tumor cells, showing some major protein expression differences, and pathway analysis that revealed alterations in pathways related to cell signaling, division, movement, survival, protein synthesis, molecular transport, and cell-cell interaction, to name a few [76].

Here, we seek to understand any morphological differences that differentiate brain- and bone-seeking tumor cells from parental tumor cells on niche-relevant substrates in order to determine whether the use of niche-relevant substrates could be used to differentiate the cell clones based on morphology. This understanding would begin the process to learning how one could distinguish the cell clones and predict tumor cells' metastatic destination prior to colonization with the help of additional parameters. Since tumor cells are highly heterogenous, in addition to morphology, many additional parameters will need to be characterized such that a combination of various parameters can allow us to make an early determination of the metastatic destination of a population of metastatic tumor cells.

5.2 Materials and Methods

5.2.1 Cell Culture

Human breast adenocarcinoma highly metastatic cells (MDA-MB-231) and their brain-seeking and brain-seeking clones were generously provided by Dr. Toshiyuki Yoneda's laboratory in Osaka, Japan. Dr. Yoneda's lab developed the brain- and bone-seeking clones based on a published protocol where the parental cell line was injected into mice and allowed to metastasize to the brain and bone from

where the cells were collected and the process was repeated until a heterogenous population was obtained [73]. The cells were cultured in media consisting of Dulbecco's Modified Eagle's Medium (DMEM) with high glucose (ThermoFisher Scientific, Waltham, MA, USA), 10% Fetal Bovine Serum (FBS; HyClone Characterized GE Healthcare, Pittsburgh, PA, USA or ThermoFisher Scientific), and 1% Penicillin-Streptomycin 10,000 U/mL, similarly to previous chapters. Cells were washed with Phosphate-Buffered Saline (PBS) (VWR, Radnor, PA, USA), and detached with 0.25% Trypsin-EDTA (ThermoFisher Scientific). All cells were cultured at 37˚C, 50% humidity, and 5% CO_2:95% air.

5.2.2 Polyacrylamide (PA) gel formation and collagen coated glass

PA gels were formed as previously described [173], [201]. Briefly, 22 x 22 mm coverslips (Thermo Fisher Scientific) were activated using sodium hydroxide (Sigma Aldrich, St. Louis, MO), 3-aminopropyltrimethoxy silane (Sigma Aldrich) to, and glutaraldehyde (Sigma Aldrich). To form 280 kPa and 1 kPa PA gels (as measured previously by Dr. Kimberly M. Stroka and Dr. Leann Norman via AFM), acrylamide and bisacrylamide (bis) (Bio-Rad Laboratories, Hercules, CA) were combined as follows: 15% acrylamide + 1.2% bis, and 3% acrylamide + 0.2% bis and mixed with 1 M HEPES buffer (Thermo Fisher Scientific) and water and then crosslinked with tetramethylethylenediamine (TEMED) (Bio-Rad Laboratories) and ammonium persulfate (Sigma-Aldrich). The gels were then activated with sulfo-SANPAH (ThermoFisher Scientific) and treated with ultraviolet light (UV) for sterilization. They were then coated with 300 µl of 50 µg/mL collagen I (Sigma-Aldrich) for 4 hours at room temperature. 1 x 10^5 cells per gel were plated. For

experiments with 50 µg/mL collagen I coated glass, cells were plated in 50 mm AFM grade glass bottom dishes (VWR) without activation. They were coated with 780 µl of collagen I for 1 hour at 37 ˚C and 2.6 x 10^5 cells were plated on top. The difference in collagen volume and cell number was used to account for the difference in culture area.

5.2.3 Varying extracellular matrix binding moieties on glass

Experiments on varying extracellular matrix binding moieties were carried out the way as described in Section 3.2.2. However, only the following extracellular matrix moieties were used: type I collagen from rat tail (Sigma Aldrich, St. Louis, MO, USA), fibronectin from human plasma (Sigma Aldrich), laminin from human fibroblasts (Sigma Aldrich), or Poly-D-Lysine hydrobromide (Sigma Aldrich). As described in Section 3.2.7, 24-well glass bottom plates (MatTek, Ashland, MA) were coated in the varying binding moieties and incubated as described in Section 3.2.2. 1 x 10^4 cells (parental, brain- and bone-seeking) were plated on each substrate.

5.2.4 Cells in suspension

4 x 10^5 cells were plated in 6 well non-tissue culture treated plates (VWR) and imaged immediately. 10 µm diameter (9.94 µm exactly as per manufacturer for specific batch) Envy Green fluorescent beads (Bangs Laboratories, Inc, Fishers, IN, USA) were suspended in the same plates in order to validate imaging and analysis based on a known diameter.

5.2.5 Live cell phase imaging

Cells in suspension and beads were imaged immediately following seeding using an Olympus I.X83 microscope (Olympus, Center Valley, PA, USA) using a phase-contrast 20× objective, similarly to Section 3.2.8. Images of attached cells were taken following an overnight incubation of cells on all substrates. Imaging was carried out using a phase-contrast 10× objective. A climate-controlled chamber was calibrated to 37˚C, 50% humidity, and 5% CO_2:95% air on the microscope stage for all experiments.

5.2.6 Atomic force microscopy (AFM)

Carried out and analyzed by Kelsey Gray.

Stiffness of tumor cells on PA gels and on glass was measured using AFM. AFM was performed using an Asylum MFP-3D-BIO Atomic Force Microscope with TR400PB(L) probes (Asylum Research) as previously described [201]. All AFM measurements were carried out by Kelsey Gray. Briefly, the coverslip with tumor cells on glass or PA gels was adhered to the bottom of a 50 x 9 mm petri dish. After 1 day in culture, AFM was performed on live cells with the stage heated to 37 °C. Asylum's "Get Real" approach was used to measure the spring constant and inverse optical lever sensitivity of TR400PB(L) probes via the Sader method and thermal noise method, respectively. The average spring constant of the cantilevers was within a factor of 1.33 to Asylum's nominal value of 0.02 N/m and all within the nominal range of 0.1-0.5 N/m. One 100-curve force map covering a 5 μm^2 area was collected for each cell using a 2 μm force distance, a 1 V trigger point (approximately 1.35 nN),

and a scan rate of 0.99 Hz. The Hertz model was used to fit the force curves within Asylum's Igor Pro-based software using the equation $= \frac{4}{3} \cdot \frac{E}{1-\upsilon^2} \cdot \sqrt{r} \cdot \delta^{3/2}$, where δ is the measured indentation of the sample and the Young's modulus E was the fitting parameter. The Poisson's ratio υ of the sample was assumed to be 0.45 and the tip radius of curvature r was approximately 30 nm. Three biological replicates were performed in which three cells per condition per trial were measured (n = 9 cells total).

5.2.7 Data analysis

For cells in suspension and beads, images were modified in ImageJ for maximum brightness and contrast in order to get the sharpest contours. The image was then made black and white and binary. The ImageJ function to fill holes was used and the ImageJ built in particle analyzer was used with a cut off for size for area of 300 - 1250 pixels^2, and a cutoff circularity of 0.65 - 1. This was done in order to eliminate any aggregates from analysis. ImageJ then generated a spread sheet with the necessary parameters, such as area for all cells in a given frame. This was repeated for all frames. Data analysis for attached cells was carried out similarly to Sections 3.2.9 and 4.2.9. ImageJ was used to manually trace cells and calculate cell area, aspect ratio, circularity, and solidity (Appendix A).

5.2.8 Statistical analysis

Statistical analysis was carried out similarly to Section 3.2.10 and 4.2.10. GraphPad Prism (GraphPad, San Diego, CA) was used for all statistical analysis. The D'Agostino-Pearson test was used to test data for normality. Since the majority of

data was not normally distributed, the Kruskal-Wallis non-parametric test with a post-hoc Dunn's test was used to determine statistical significance. Between two and three independent trials were carried out for each experiment type, as indicated in figure caption). Histograms were generated using a frequency analysis in GraphPad. A Gaussian curve was fitted to a frequency distribution of cell and bead area and diameter in GraphPad as well. Statistical significance was determined with a 95% confidence interval with $P < 0.05$. Detailed statistical significance is indicated in figure captions.

5.3 Results

5.3.1 MDA-MB-231 metastatic tumor cell clone areas in suspension

In order to determine whether the different MDA-MB-231 cell clones would vary in morphology while still in circulation, we studied their projected area and diameter in suspension (prior to attachment to a surface). In suspension, the analysis methods were validated by analyzing beads with known diameters and found consistent results within approximately 1.86 μm of the dimeter and 32.4 μm^2 of the area (Figure 5.1 A, B). Thus, we proceeded to analyze cells in suspension. While based on images, there does not appear to be a great difference between the cells (Figure 5.1 C), upon quantification we determined that there were significant differences within the groups. The largest differences were in area and diameter between parental and bone-seeking cells as well as brain- and bone-seeking cells (Figure 5.1 D, E, F, G). A significant difference was also observed between parental and brain-seeking cells (Figure 5.1 D, E, F, G). However, despite these differences, it

is important to note that the populations are still highly heterogenous, even in suspension (Figure 5.1). Next, we chose to investigate whether these trends change once tumor cells become attached to an extracellular matrix.

5.3.2 MDA-MB-231 metastatic tumor cell clone areas on different substrates

Because some phenotypic differences were observed in suspension between the tumor cell clones, we decided to also examine them attached to extracellular matrix. Since tumor cells attach to different extracellular matrix molecules during metastasis to various distant sites, it is important to examine the tumor cell phenotypes on various extracellular matrix. Here, we considered two common extracellular matrix proteins, collagen I and fibronectin, as well as PDL, which unlike proteins, does not engage integrins and relies on electrostatic interactions for cell adhesion. When MDA-MB-231 metastatic breast parental tumor cells and brain- and bone-seeking clones were plated on collagen I, fibronectin, and PDL, some visual morphological differences became apparent (Figure 5.2 A). Specifically, bone-seeking clones were distinct from the parental and brain-seeking clones on collagen I, since they had more protrusions, and on fibronectin, where the cells are more spread (Figure 5.2 A). However, on PDL there were minimal observable differences between the three tumor cell clones (Figure 5.2 A). Because that all the cells appeared to attach to both extracellular matrix proteins and spread readily in an integrin-dependent fashion, further experiments were carried out to on collagen I.

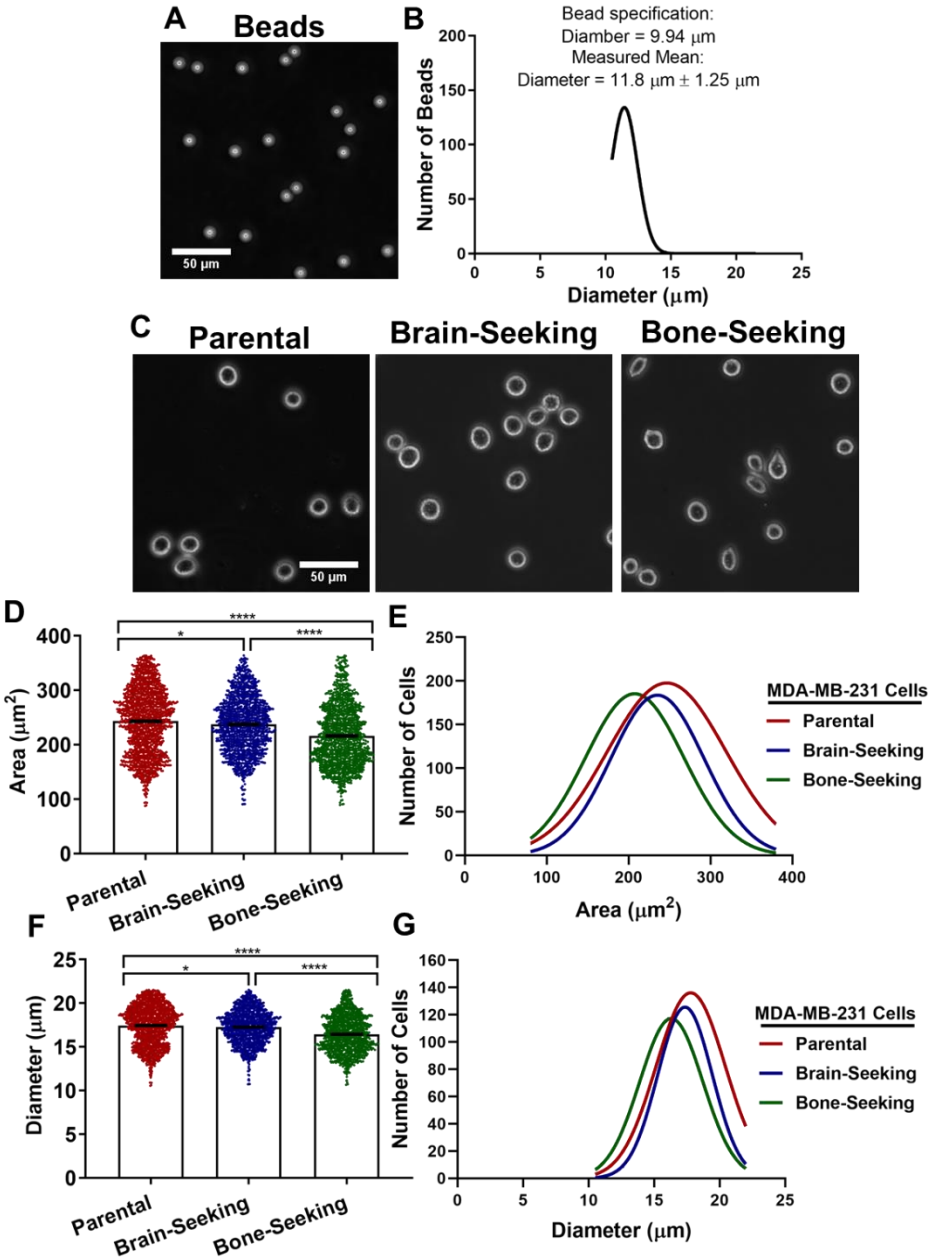

Figure 5.1: **Images of MDA-MB-231 parental cells and brain- and bone-seeking clones in suspension.** A), B) Proof of concept 9.94 µm beads in suspension. 606 beads analyzed. C) Images of MDA-MB-231 parental cells and their brain- and bone-seeking clones in suspension. Scale bar applies to all images. All images taken via 20x phase contrast imaging. D) Area and E) Gaussian distribution of MDA-MB-231 parental cells and their brain- and bone-seeking clones in suspension. F) Diameter and G) Gaussian distribution of MDA-MB-231 parental cells and their brain- and bone-seeking clones in suspension. All cell numbers are: $1277 \leq n \leq 1695$ cells. All data is pooled from three independent trials. (* $p < 0.05$; ** $p < 0.01$; *** $p < 0.001$, **** $p < 0.0001$). This data was collected and analyzed by Nathaniel Girma.

Furthermore, the three tumor cell clones were seeded on surfaces coated with collagen I but of different stiffness, glass (~50 GPa), 280 kPa (similar to bone), and 1 kPa (similar to brain) in order to further mimic biomechanical properties of the local extracellular matrix at various metastatic sites. With decreasing stiffness, all tumor cell clones became less spread (Figure 5.2 B). However, once again the bone-seeking clones stood out in morphology by having more protrusions and longer protrusions on all extracellular matrix stiffness than any of the other clones (Figure 5.1 B).

Upon quantification, significant differences in morphology parameters were observed among the different cell clones on collagen I coated glass and 280 kPa and 1 kPa stiffness PA gels. Within each extracellular matrix stiffness, all cell clones had statistically different areas from each other, except on glass and the 1 kPa gels, where parental and brain-seeking cells' areas were not different (Figure 5.3 A, B). On PA gels, bone-seeking cells had the largest area while on glass the brain-seeking cells were actually larger (Figure 5.3 A). The inverse aspect ratios were not significantly different between the three cell clones on 280 kPa gels, however, within glass and 1 kPa stiffness gels all cell groups were significantly different (Figure 5.3 C, D). Similarly, for circularity parental and brain-seeking cells were not different on the 280 kPa gels, while all other cells within each stiffness were statistically different (Figure 5.3 E, F). On the other hand, within each stiffness group all solidities were significantly different between the three different clones (Figure 5.3 G, H). Notably, the cell populations were all highly heterogeneous (Figure 5.3 B, D, F, H).

These results suggest that altering the extracellular matrix stiffness and composition can have a significant impact on the phenotype of parental, brain- and

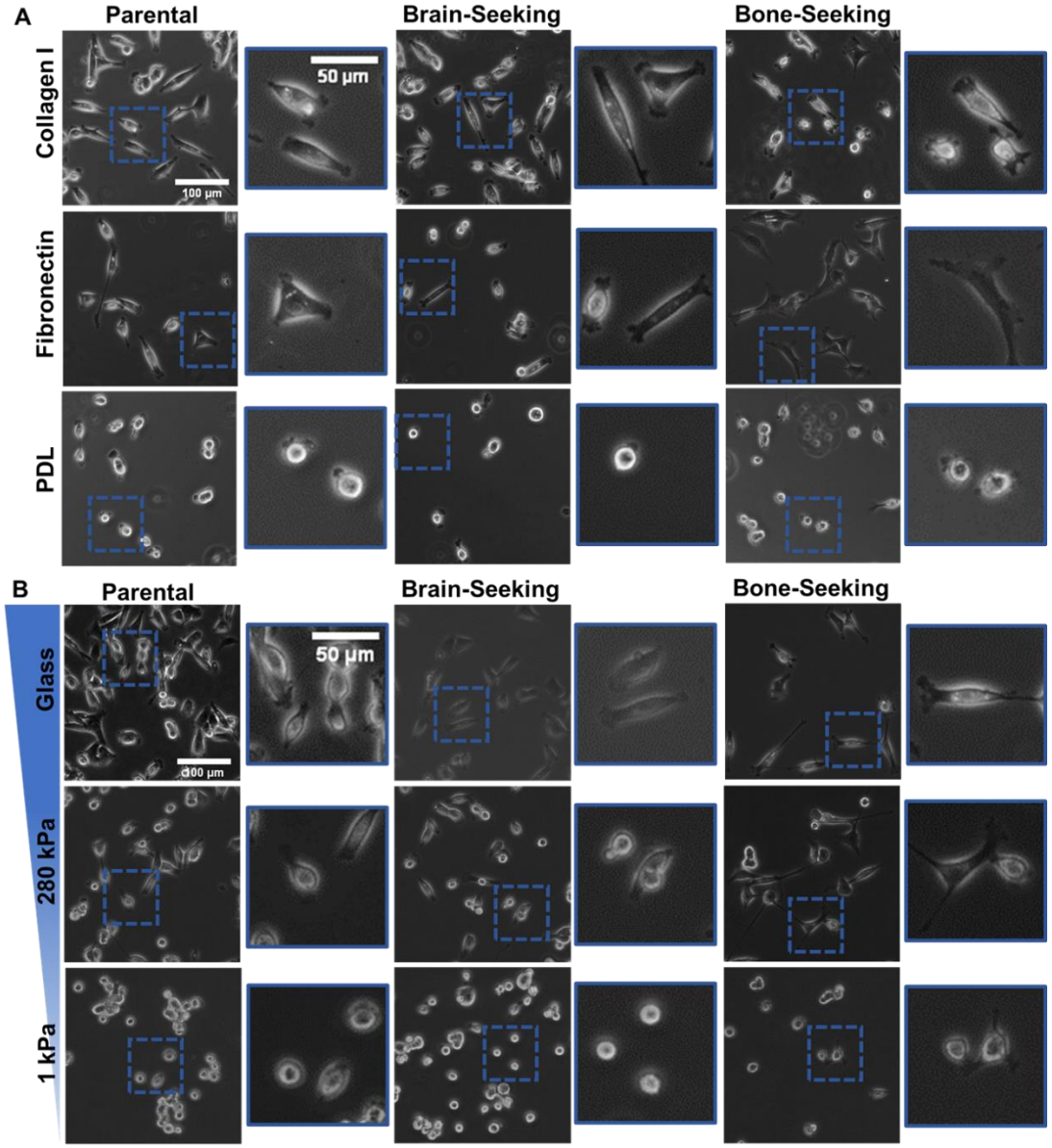

Figure 5.2: **Images of MDA-MB-231 parental cells and brain- and bone-seeking clones on various substrates.** MDA-MB-231 parental cells and their brain- and bone-seeking clones on 20 µg/ml A) collagen I, fibronectin, and PDL coated glass, and 50 µg/ml collagen I coated B) glass, 280 kPa (bone-like), and 1 kPa (brain-like) stiffness PA gels. Scale bars on first zoomed out image apply to all images in the sequence. Scale bar on first zoomed in image applies to all images in sequence. Images taken at 10x via phase contrast imaging with the help of Ariana Joy DeCastro.

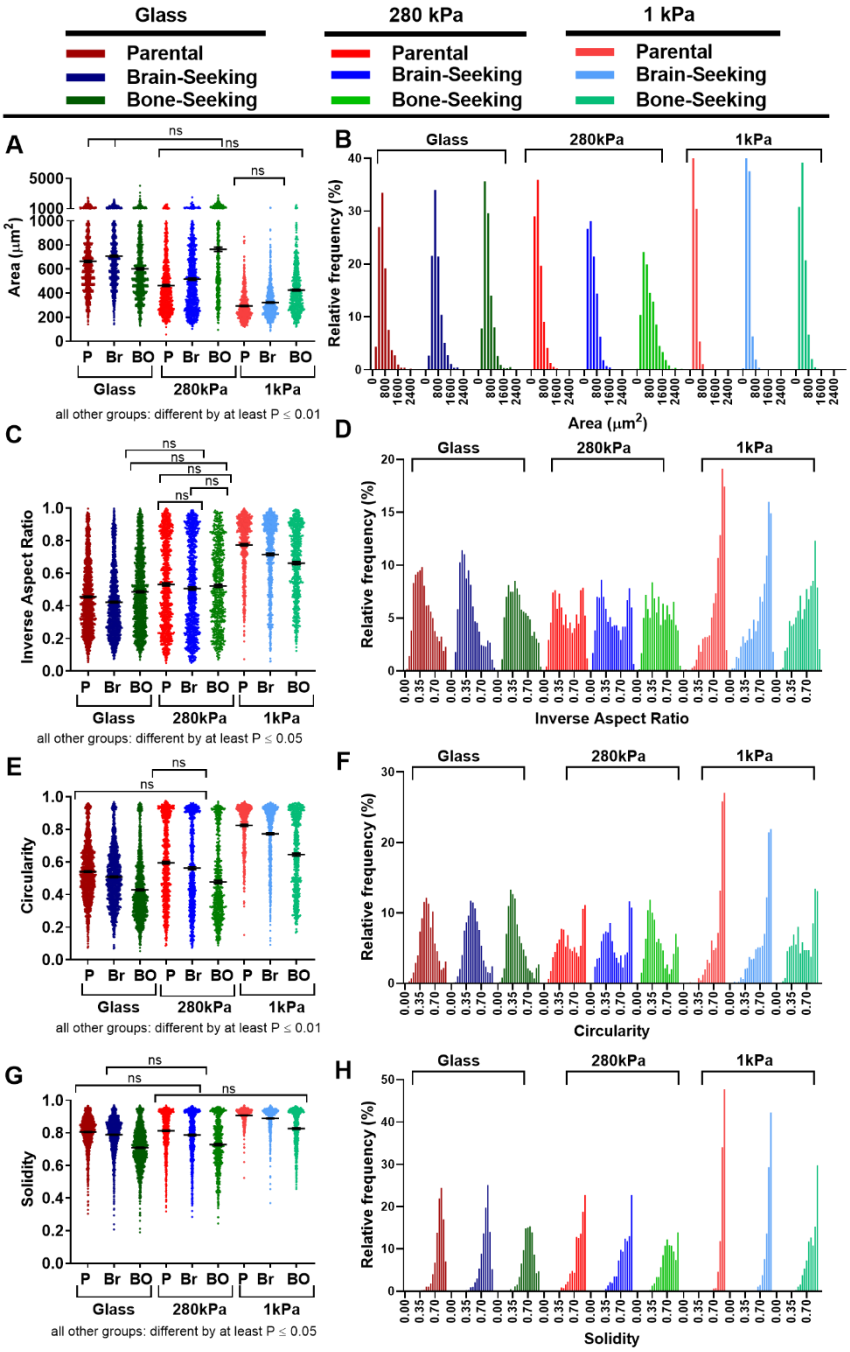

Figure 5.3: **Morphology of MDA-MB-231 parental cells and brain- and bone-seeking clones on collagen I coated glass.** MDA-MB-231 parental cells' (P) and their brain (Br) and bone-seeking (BO) clones' A), B) areas, C), D) inverse aspect ratios, E), F) circularities, and G), H) solidities. If no lack of significance is indicated, the groups are significantly different by P value indicated in plot. Legends apply to all plots. Data pooled from three independent trials. All substrates are coated with collagen I. All cell numbers are: $597 \leq n \leq 1532$ cells. ns: not statistically significant, $P > 0.05$. Label and legend apply to all figures. Nathaniel Girma assisted with experiments and data analysis and John Merlo-Coyne assisted with data analysis.

bone-seeking cells, however it does not appear that by using different substrate stiffnesses one could easily identify the various cell populations. It does appear possible that the 1 kPa substrate could be used as a starting point to start separating the cell populations, since the greatest number of differences were observed there for all parameter and the bone-seeking cells appearing most distinct on that surface. This could have important functional implications as they undergo metastasis from the breast to brain or bone.

5.3.3 MDA-MB-231 metastatic tumor cell clone stiffness on different substrates

As TCs metastasize, they have to travel through various porous physiological structures, and thus have to be able to get through very narrow spaces and the softer a cell is, the more likely it is be able to get through differently shaped spaces. Thus, we evaluated the stiffness of each cell clone type on collagen I coated glass and 280 and 1 kPa PA gels. Our data showed that all three cell clones do not have statistically different stiffness within each substrate (Figure 5.4). However, there are general differences between cells on different substrates, brain-seeking and bone-seeking cells on 1 kPa PA gels being the softest and parental and brain-seeking cells being stiffest on 280 kPa PA gels (Figure 5.4). This data suggests that cell stiffness is unlikely to be a primary determining factor in the preferential metastasis of the different cell clones.

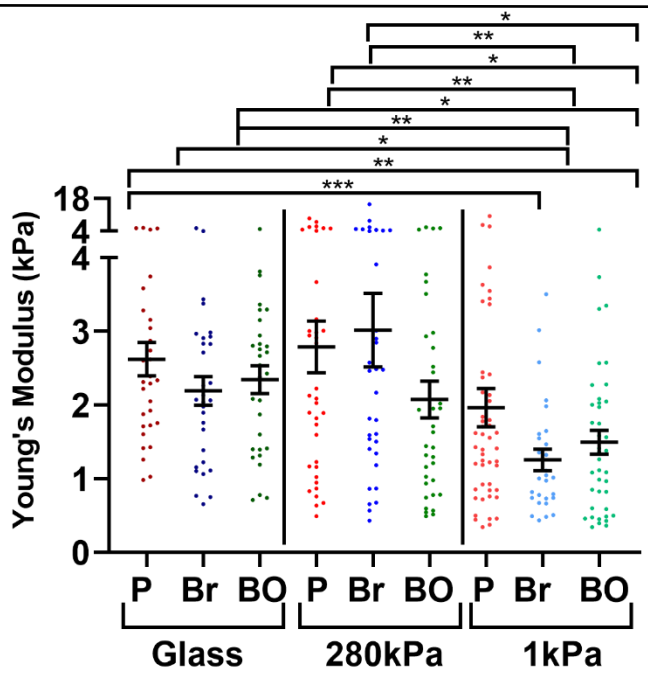

Figure 5.4: **Stiffness of MDA-MB-231 parental cells and brain- and bone-seeking clones' collagen I coated glass and PA gels.** MDA-MB-231 parental cells' (P) and their brain- (Br) and bone-seeking (BO) clones' Young's Modulus on 50 µg/ml collagen I coated glass, and 50 µg/ml collagen I coated 280 kPa and 1 kPa PA gels. All cell numbers are: $28 \leq n \leq 49$. Data was pooled from at least three independent trials. Statistical analysis was performed using a Kruskal-Wallis multiple comparison test with a Dunn's post-hoc test. (* $p < 0.05$; ** $p < 0.01$; *** $p < 0.001$). AFM measurements taken and analyzed by Kelsey Grey.

5.4 Discussion

This study begins to address the "seed" portion of the "seed and soil" hypothesis, focusing on the tumor cells themselves and not just the microenvironment. While the Chapter 3 and 4 examine cues exerted by the BBB microenvironment and surrounding cells on metastatic tumor cells, it is also crucial to study the tumor cells themselves in order to begin to understand whether there are some underlying driving forces within the cells themselves that result in preferential metastasis to the brain, versus other organs. As such, it is important to examine how brain-seeking tumor cells compare in their phenotype to parental or bone-seeking tumor cells and how all the cells respond to their microenvironments in order to begin

to discover differences that would allow us to predict the metastatic destination of a given tumor cell.

While it is still unknown whether tumor cells' metastatic site is controlled more by their intrinsic phenotypic and genotypic properties, or whether the properties of the tumor cells are altered as a result of metastasis to a particular organ, it is likely that the interaction of tumor cells with their microenvironment results in tumor cells that have different properties [76], [77], [202]. However, it is also important to note that the phenotype of tumor cells varies on surface versus traveling through the blood stream. Here, we seek to determine whether culturing tumor cell clones in different conditions could yield significant enough morphological differences to distinguish the three phenotypes.

We showed that parental and brain- and bone-seeking tumor cells exhibit different morphological properties both in suspension (Figure 5.1) and when attached to extracellular matrix (Figures 5.2 and 5.3). Visually, the bone-seeking cells are morphologically unique even when attached by showing greater protrusions (Figure 5.2). Interestingly, there does not appear to be a direct correlation between cells with different organotrophic destinations having distinct morphologies between soft and stiff substrate that vary clone to clone. Overall, our data shows that seeding cells on substrates with different stiffness would not allow us to differentiate the different cells based on morphology alone. This is more promising within each stiffness, especially on 1 kPa, however the cell populations are too heterogenous for morphology to be a sufficient parameter for distinction even for statistically significantly different groups. Tumor cell stiffness remained unchanged (Figure 5.4)

on all extracellular matrix substrates, suggesting that while morphology could be a potential future indicator of functional differences in the tumor cell clones when combined with additional factors such as migration or traction force generation, cell stiffness is unlikely to play a significant role. While the phenomena has to be further examined, this is consistent with prior studies showing distinct differences in the tumor cell clones, especially in response to different extracellular matrix [32], [200]. Prior studies have shown that larger tumor cells with more protrusions are more often more metastatic and have a greater ability to migrate through blood vessels to distant sites [140], [203], suggesting that phenotypic differences between different cell clones can also be indicative of changes in their metastatic potential and ability to metastasize to particular distant sites.

5.5 Conclusion

Based on this data we concluded that all tumor cells examined are more spread on stiffer substrates and less spread on the soft PA gels. However, there are distinct phenotypical differences between the different cell clones on all surfaces, suggesting that cell morphology could be one of the distinguishing characteristics of the different clones and could be either a result of functional changes or lead to functional changes in tumor cell metastasis. However, due to the heterogeneity of the tumor cell population on all surfaces, multiple additional characterization approaches need to be taken into account before the tumor clone populations can be effectively sorted based on phenotypical characteristics. Furthermore, tumor cell stiffness was not significantly different between clones on PA gels and glass, suggesting that this parameter is unlikely to be responsible for any functional differences and will not be

helpful in differentiating the cell clones. Future work will determine additional factors, such as migration, traction forces, or confined migration that can, together with morphology on various substrates, help distinguish the tumor cell populations. Additionally, functional significance of these any phenotypic differences and further investigate mechanobiological changes between brain- and bone-seeking phenotypes should be addressed in the future.

6 Sensitivity of tumor vs. normal cell migration and morphology to cold atmospheric plasma-treated media in varying culture conditions[†]

6.1 Introduction

Cancer is known to be an extremely devastating diagnosis. Most cancer deaths are due to metastasis, or the spread of cancer cells from a primary tumor to distant sites, where they then form more aggressive secondary tumors [35]. Currently, the most common cancer therapies, such as surgery, chemotherapy, and radiation, often leave patients with severe side effects such as anemia, bleeding, bowel dysfunction, bone density loss, infertility, and immune suppression [204]. This is often a result of significant damage to normal cells during the cancer treatment. While new and improved cancer therapeutics are constantly being developed [205]–[207], there remains a need for therapies that cause minimal damage to normal cells in the body.

One potential novel therapy that has been recently proposed is the use of cold atmospheric pressure plasma (CAP), which produces reactive oxygen and nitrogen species (ROS, RNS) with the capacity to selectively kill cancer cells [82], [208], [209]. While CAP has already been shown as a promising therapeutic for external wounds [98], [210], [211] and destroying certain cells while leaving others intact [82], [91], it remains unclear how CAP would be used *in vivo* in the presence of bodily fluids with highly variable compositions [212], [213]. In order to facilitate

† This chapter is modified from manuscript submitted for publication as M.A Pranda, B.J. Murugesan, A.J. Knoll, G.S. Oehrlein, K.M. Stroka, "Sensitivity of tumor vs. normal cell migration and morphology to cold atmospheric plasma-treated media in varying culture conditions." Data analyzed by BJM. Plasma treatment by A.J.K.

potential future CAP delivery *in vivo* [212], [213], many *in vitro* studies that assess the effectiveness of CAP as a cancer therapy are conducted in cell culture media, water, or buffer solutions [209], [214]. Hence, it is critical to understand what effect various cell culture parameters have on the outcome of CAP-treated media-based cancer treatment studies. Otherwise, there is a risk that the data will be a function of cell culture condition, instead of a function of the effectiveness of the actual treatment.

A thorough review of CAP-based cancer therapy literature (condensed version, Table 6.1) revealed that very different experimental conditions have been used between different laboratories, and even between different experiments in the same laboratory [212], [214]–[218]. While some studies solely examined the effect of CAP on one cell line [212], [217] [212], [217] others investigated CAP selectivity between normal and disease cells [90], [216], [219]. Many studies that utilized more than one cell line for CAP-based experiments used the same fluid for both cell lines (Table 6.1) [84], [90], [209], [214], [216], [218], [220], [221], while others used different media across different cell lines (Table 6.1) [213], [222]–[225]. Additionally, many studies that compared normal and tumor cells used cells from unmatched tissue samples [216], [220]. Furthermore, a majority of previous studies used cells grown on tissue culture plastic (Table 6.1) [84], [90], [213]–[218], [224] where cells primarily rely on polar interactions for adhesion [226]; however, this microenvironment is not representative of the *in vivo* situation, where cells typically adhere to extracellular matrix proteins via integrins [227]. Finally, most studies utilized jet-based CAP

Table 6.1: Literature review of CAP usage in biomedical research. Summary chart of several recent studies utilizing plasma for cancer cell treatment. This chart provides an overview of which treatment parameters and experimental conditions are commonly used in the field. References that discuss the effect of varying medias are highlighted in gray. Brittney Murugesan assisted with literature review.

Ref.	Plasma Source	Treatment	Cell Type	Media/Buffer Composition	Known Scavenger	Surface Coating
[212]	Jet: argon, helium, nitrogen	CAP treated DI water	Breast adenocarcinoma**:** **MDA-MB-231**	DMEM, Pen/Strep, FBS	---	Tissue culture plastic
[209]	Jet: helium	CAP treated media & buffer solution	Glioblastoma: **U87MG**: Adenocarcinoma**:** **PA-TU-8988T**: pancreas; **MDA-MB-231**: breast	DMEM, Pen/Strep (FBS for culture), PBS	---	Tissue culture plastic
[216]	Jet: helium + magnetic field	CAP treated media & cells	Breast adenocarcinoma**:** **MDA-MB-231**; **wild type mouse dermal fibroblasts**	DMEM, Pen/Strep, FBS, PBS	---	Tissue culture plastic
[217]	Jet: helium	CAP treated media	Normal epithelial cells from canine kidney: **MDCK**	Eagle's Minimum Essential Medium, Bovine Calf Serum, Pen/Strep, Glutamine	Sodium Pyruvate	Tissue culture plastic
[214]	Jet	CAP treated media & DI water	Breast adenocarcinoma**:** **MDA-MB-231**; Glioblastoma: **U87**	DMEM, Pen/Strep, FBS	---	Tissue culture plastic
[218]	Jet: helium	CAP treated media	Lymphoblastic lymphoma: **MWCL-1** & **RPCI-WM1**	Iscove's Modified Dulbecco's Medium, GlutaMAX-I (FBS for culture)	Sodium Pyruvate	Tissue culture plastic
[222]	Jet: argon (kINPen Med)	CAP treated media & cells	Ovarian cancer: **OVCAR-3**, **SKOV-3**, **TOV-21G**, **TOV-112D**	OVCAR-3: RPMI-1640, 10% FBS, gentamicin, insulin; SKOV-3: DMEM /F12, 5% FBS, gentamicin; TOV-21G, TOV-112G: MCDB105/medium 199, 15% FBS, gentamicin	Glutathione (RPMI), Sodium Pyruvate (DMEM/F12)	Tissue culture plastic
[220]	Jet, coagulator pen: argon, helium	CAP treated cells	Osteosarcoma: **U2-OS**; connective tissue: **3T3-fibroblasts**	DMEM, 1.0 g/l (4.5 g/l for fibroblast) glucose, FBS, sodium pyruvate, Pen/Strep	Sodium Pyruvate	Suspension, then transferred to poly-l-lysine surface

Ref.	Plasma Source	Treatment	Cell Type	Media/Buffer Composition	Known Scavenger	Surface Coating
[213]	Jet: helium	CAP treated DI water mixed with media	Breast adenocarcinoma: **MDA-MB-231**; gastric cancer: **NCI-N87**	NCI-N87: RPMI-1640, FBS; MDA-MB-231: DMEM, FBS, Pen/Strep	Glutathione (RPMI)	Tissue culture plastic
[223]	Dielectric barrier discharge: argon	CAP treated cells in various media	Normal breast: **MCF-10A**, **MCF-12A**; Breast adenocarcinoma: **MCF-7, MDA-MB-231**; Colon cancer: **HCT-15**; lung cancer; **NCI-H1299**	MCF-10A, MCF-12A: MEBM, MEGM Single Quots, cholera toxin; all others: RPMI-1640, FBS	Glutathione (PRMI); MEBM: proprietary	Tissue culture plastic
[224]	Source unclear: argon	CAP treated media	Glioblastoma: **U251SP**; astrocyt**es: ACBRI-371**	U251SP: DMEM, FBS, Pen/Strep; ACBRI-371: CSC complete recombinant medium, Culture Boost	CSC: proprietary	Tissue culture plastic + attachment factors, glass
[225]	Jet: helium	CAP treated cells	Fibroblasts: **WTDF 3**; human corneal limbal epithelial: **HCLE**	WTDF 3: DMEM, serum, L-glutamine , Pen/Strep; HECLE: Keratinocyte Serum Free Medium, Bovine Pituitary Supplement, Epidermal Growth Factor, $CaCl_2$, Pen/Strep	---	Tissue culture plastic and coated glass (fibronectin, collagen I, vitronectin)
[219]	Jet: helium	CAP treated cells	**fibroblasts**; skin cancer: **PAM**	not discussed	---	Tissue culture plastic coated with collagen I and fibronectin
[90]	Jet: helium	CAP treated media	Breast cancer: luminal: **MCF7**; Her2+: **SKBR3**, **SUM159PT**, triple negative: **SUM149PT**, **MDA-MB-231**, **MDA-MB-436**. Normal breast: **MCF10A**	Different medias used to grow but RMPI-1640 media used for treatment	Glutathione (RPMI)	Tissue culture plastic
[84]	RF Jet & Kinpen: argon, oxygen, air	CAP treated media & buffer	Eukaryotic epithelial: **CRFK;** Human keratinocytes: **HaCaT**	RPMI-1640, FBS Pen/Strep, sodium deoxycholate; PBS with $Mg^{2+/}Ca^{2+}$	Glutathione (RPMI), others tested as part of experiments	Tissue culture plastic

sources (Table 6.1), though other CAP sources exist. While these experiments have produced interesting and significant results, the translatability of future CAP treatments will rely on careful, systematic studies that optimize cell culture and CAP treatment conditions to ensure that reported tumor cell selectivity is not simply a function of cell culture conditions.

Here, our goal was to gain an understanding of the effects of cell culture conditions (e.g., media type and cell-matrix binding moieties) on the effectiveness of CAP-treated media as a selective treatment that can damage tumor cells while leaving normal cells unaffected. We chose two complimentary cell lines from the breast tissue, including a normal breast epithelial cell (MCF10A) and a metastatic breast tumor cell (MDA-MB-231) line. CAP-treated media was selected over direct CAP treatment of cells because *in vivo* metastatic cells are generally deeper in tissue and thus it would be very difficult to reach them directly with a plasma source. We varied cell culture media because different cell lines generally have different recommended media compositions, and thus when one is comparing the selectivity of a potential therapy, it is essential to ensure that conditions are standardized. We also compared the complimentary cells' response to CAP-treated media in the presence of different cell-matrix binding moieties, because CAP may affect cellular integrin expression and therefore could potentially act on cells via an integrin-dependent pathway [219]. Thus, here we show how varying CAP parameters, culture media, and cell-matrix binding moieties affects the ability of CAP-treated media to be selective in damaging tumor cells while leaving normal cells unharmed.

6.2 Materials and Methods

6.2.1 Cell culture

Human metastatic breast adenocarcinoma cells, MDA-MB-231 (American Type Culture Collection, Manassas, VA, USA), were cultured in Dulbecco's Modified Eagle's Medium (DMEM) with high glucose and L-glutamine (ThermoFisher Scientific, Waltham, MA, USA) supplemented with 1% Penicillin/Streptomycin 10,000 U ml^{-1} (Pen/Strep) (ThermoFisher Scientific) and 10% Fetal Bovine Serum (FBS) (ThermoFisher Scientific or HyClone Characterized GE Healthcare, Pittsburgh, PA, USA). Human mammary gland normal epithelial cells, MCF10A (American Tissue Type Culture Collection), were cultured in DMEM/F12, HEPES (ThermoFisher Scientific) with 0.02 µg/ml epidermal growth factor (Millipore Sigma, Burlington, MA, USA; E-9644, in 10 mM acetic acid), 0.5 µg/ml hydrocortisone (Millipore Sigma; H-0888, in 95% ethanol), 0.02 mg/ml insulin (ThermoFisher Scientific; 12585-014), and 5% horse serum of New Zealand origin, ThermoFisher Scientific), and 1% Pen/Strep. Cells were washed with Phosphate-Buffered Saline (PBS) (VWR, Radnor, PA, USA), and detached with 0.25% Trypsin-EDTA (ThermoFisher Scientific). All cells were used at or below passage 12 post-purchase. All cells were cultured in a climate-controlled incubator at 37°C, with 5% CO_2:95% air and 50% humidity. This was done similarly to Chapter 3.

6.2.2 Cold atmospheric plasma (CAP) set-up

Plasma treatments carried out by Andrew Knoll.

Two different CAP sources were used to introduce reactive species into media liquid used for cell culture. First, we utilized an atmospheric pressure plasma jet (APPJ) (Figure 6.1 A). This source has been well characterized in terms of plasma behavior and production of reactive species densities under various operating conditions [80], [215] and interactions with polymer materials [230]–[232]. The source utilizes a 1 mm diameter high voltage tungsten pin electrode sharpened to a point mounted inside a quartz tube, which has a 1.5 mm inner diameter and 3 mm

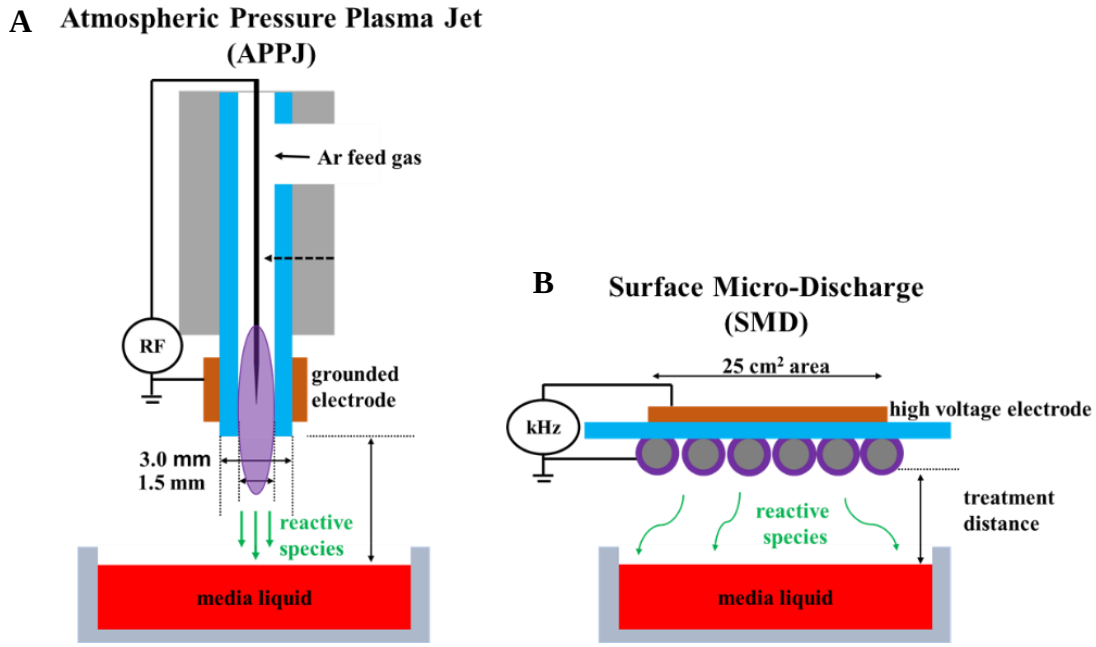

Figure 6.1: **Plasma source diagrams.** Schematic of A) a 13.56 MHz driven pin style APPJ source that operates using Argon gas fed through a quartz tube and produces an ionized plasma discharge extending several mm toward the treated area. The distance used for this source was 1 cm, with a plasma dissipated power of 1.5 W, and the reactive species are driven by convection to the sample surface. Also shown is a schematic of B) a 42 kHz driven SMD plasma source that operates in ambient air where the plasma forms around the grounded mesh below a quartz dielectric barrier. The distance used for this source is 3 mm, with a dissipated power of 0.25 $W \cdot cm^{-2}$, and there is no gas flow and the reactive species are primarily transported by diffusion to the sample surface. Figure created by A.J. Knoll. Plasma treatments carried out by A.J. Knoll.

outer diameter. There is also a grounded electrode made of copper on the outside of the quartz tube which has a 5.3 mm length and fits snug around the quartz tube. The standard operating conditions for the plasma jet are 20 kHz modulated 13.5 MHz sinusoidal wave with a 20% on, 80% off cycle. The dissipated power is 1.2 W with a gas flow of 1.5 slm of Argon (Ar), which corresponds to an average gas velocity of 14.15 $m \cdot s^{-1}$. The jet nozzle was set to a standard distance of 1 cm above the media. Details of how this power is calculated can be found in previous work characterizing this plasma source [233]. Secondly, our work utilized a surface microdischarge (SMD) style plasma source (Figure 6.1 B). This source is based on a design by Morfill as previously described [234], [235]. The powered copper electrode on the top of the source has an area of 25 cm^2, and a quartz plate with thickness 1.6 mm separates the high voltage electrode from the grounded stainless-steel mesh with a 50% opening. The source operates at 42 kHz sinusoidal wave, 6 kV_{p-p} voltage from a PVM500 power supply, at a total plasma dissipated power approximately 6.5 W over the 25 cm^2 area, or a specific power of 0.25 $W \cdot cm^{-2}$. The operating conditions for this source are in open ambient air with no active gas flow set 3 mm above the media.

6. 2.3 Experimental set-up (Figure 6.2 A)

This study compared two cell types (Figure 6.2 B), three different adhesion molecules (Figure 6.2 C), four different media conditions (Figure 6.2 D), and a control and CAP-treated condition. The following adhesion molecules were compared: type I collagen from rat tail (Millipore Sigma), fibronectin from human

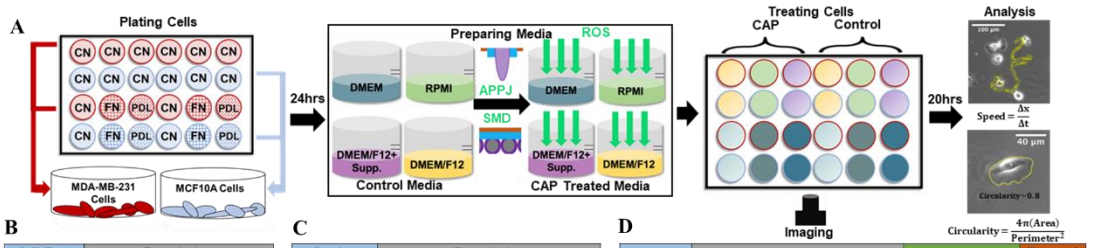

Cell Type	Description
MDA-MB-231	Breast adenocarcinoma. Highly metastatic and tumorigenic. Triple negative.
MCF10A	Non-tumorigenic breast epithelial cell line.

Coating	Description
Collagen I (CN)	Abundant proteins in extracellular matrix, engages cells' integrins for attachment and migration.
Fibronectin (FN)	
Poly-D-Lysine (PDL)	Synthetic molecule, does not engage integrins, instead enhances cells' electrostatic interactions with surface for attachment and migration.

Media	Composition	ROS Scavanger	Targeted ROS
RPMI	RPMI 1640, Penicillin/Streptomycin (Pen/Strep), Fetal Bovine Serum (FBS), Glutamine	Glutathione in RPMI	?
DMEM	Dulbecco's Modified Eagle Medium (DMEM), Pen/Strep, FBS	---	---
DMEM/F12	DMEM/F12 HEPES, Pen/Strep, FBS	Sodium Pyruvate in DMEM/F12	H_2O_2
DMEM/F12 + Supp.	DMEM/F12 HEPES, Pen/Strep, Horse Serum , Insulin, Hydrocortisone, Human epidermal growth factor	Sodium Pyruvate in DMEM/F12	H_2O_2

Figure 6.2: Experimental set-up. A) Experimental layout starting with culturing cells, preparing plasma treated media, treating cells, and imaging and analyzing cell speed and circularity. Descriptions of B) the complimentary cancer and normal cells used in experiment, C) the surface coatings varied in experiments (when surface coatings were varied, DMEM was used), and D) the media varied in experiments (when media were varied, a collagen I surface coating was used). Brittney Murugesan helped generate the figure.

plasma (Millipore Sigma), and Poly-D-Lysine hydrobromide (PDL) (Millipore Sigma) (Figure 6.2 C). The following media were compared: (1) native MDA-MB-231 medium, which consisted of DMEM + 10% FBS + 1% Pen/Strep; (2) native MCF10A medium, which consisted of DMEM/F12 + all supplements (DMEM + Supp.) (described in Figure 6.2 D and Cell Culture section); (3) DMEM/F12 + 10% FBS + 1% Pen/Strep (to verify the effect of the base media versus supplements); and (4) RPMI-1640 (ThermoFisher Scientific) + 10% FBS + 1% Pen/Strep + 3.56 mM L-glutamine (ThermoFisher Scientific) (Figure 6.2 d), since RPMI is a very common base medium used in many CAP studies [90]. Cells that were seeded on fibronectin and PDL were treated only with DMEM, while experiments evaluating the effects of the four different media compositions were performed only on type I collagen (Figure 6.2). This experimental set-up enabled a systematic evaluation of the effects of each individual cell culture parameter. Prior to cell-seeding, 24-well glass bottom plates

with 13 mm diameter glass (MatTek, Ashland, MA, USA) were coated with 300 μL of 20 μg/ml type I collagen in PBS, 20 μg/ml fibronectin from human plasma in PBS, or 20 μg/ml PDL in MilliQ water for at least 1 hour at 37˚C. In each plate, 16 wells were coated with type I collagen, 4 wells were coated with fibronectin, and 4 wells were coated with PDL (Figure 6.2 A). Wells with type I collagen and fibronectin were washed three times with PBS and wells with PDL were washed with sterile MilliQ water. MDA-MB-231 or MCF10A cells (1x104 total per well), were seeded per well such that each cell type was cultured under the same conditions (Figure 6.2 A). After plating, cells were grown in their native media overnight. On the second day, the experimental media were treated with CAP (described in "CAP-treated media preparation"), the cells were washed with PBS, and either 1 mL of CAP-treated media or the corresponding untreated control media was added. The layout is shown in Figure 6.2.

6.2.4 CAP-treated media preparation

CAP-treated media was prepared in the lids of Falcon Disposable Petri Dishes, Corning (VWR) for the SMD and in Corning tumor cell-Treated Culture Dishes (ThermoFisher Scientific) dishes for the APPJ. 4 mL of media were pipetted into each lid or dish. The lids used for SMD treatment were 4 mm tall and filled to 3 mm, and the inner radius was approximately 20 mm. The dishes used for APPJ treatment were 10 mm tall and filled to approximately 4.4 mm, and the inner radius was approximately 17 mm. Different lids/dishes were used for SMD and APPJ treatments due to the necessary distance of the plasma source from the surface of the fluid. The lid/dish was placed underneath the plasma source and treated at the

conditions described in “CAP set-up” for 1 or 7 minutes. The media was then collected into clean tubes. Within approximately 1.5 hours of each treatment, the media was heated for 10 minutes to 37°C and then applied to cells as described in “Experimental set-up” and Figure 6.2.

6.2.5 Live-cell imaging

Imaging of cells was started immediately after the media change to either CAP-treated or control media. Live-cell, time-lapse, phase contrast images were taken overnight every 10 minutes using an IX83 inverted microscope (Olympus, Center Valley, PA, USA) with a 10x objective. At the end of the time-lapse (approximately 15- 20 hours after switching to control or CAP-treated media), phase contrast images were taken of the live cells using a 20x objective. Images were acquired using cellSens Software (Olympus). The live-cell imaging chamber was maintained at 37°C, 50% humidity, and 5% CO_2:95% air surrounding the microscope stage.

6.2.6 Data analysis

Image analysis was completed using ImageJ software (https://imagej.nih.gov/ij/). Cell centroids were manually tracked in the time-lapse sequences using the Manual Tracking plugin in ImageJ. Cells were excluded from analysis if they divided, went out of frame, or were otherwise obstructed during the sequence. Cells imaged with a 20x objective after the time-lapse were analyzed for morphology by manually tracing the cell outline using ImageJ. ImageJ then calculated cell morphology parameters, including cell circularity according to the

following definition: $Circularity = 4*\pi*(Area / Perimeter^2)$ as described in Appendix A. With this definition, circularity can span the range 0 to 1, with a value of 1 corresponding to a cell with a very circular shape. A custom Matlab (MathWorks, Natick, MA, USA) code was used to calculate cell speed during cell migration by reading in the x and y coordinates of each cell centroid obtained through ImageJ tracking. For each individual cell, the instantaneous speed between every set of two points was calculated based on the x and y positions over time, and the instantaneous speeds were then averaged across all sets of two points to produce an instantaneous speed for that cell, as described in Appendix B.

2.7 Statistical analysis

All statistical analysis and graph preparation was carried out in GraphPad Prism 8 (GraphPad, La Jolla, CA, USA). A D'Agostino-Pearson normality test indicated that most data in each data set did not follow a normal distribution. Hence, non-parametric tests were used for subsequent statistical analysis. For all statistical analysis, a non-parametric Kruskal-Wallis test with a Dunn's multiple comparison post-hoc test was used. Statistical significance was indicated as follows: NS $P > 0.05$, * $P \leq 0.05$, ** $P \leq 0.01$, *** $P \leq 0.001$, **** $P \leq 0.0001$. Errors bars represent standard error of the mean. All data represent pooled values from two independent trials.

6.3 Results

6.3.1 Selective and non-selective treatments

To investigate tumor and normal cells' response to different CAP-treated media utilizing different CAP sources, we examined the cells' migration and circularity parameters as proxies for cell viability and functionality. Highly metastatic cells rely on their migration potential, as well as mesenchymal, elongated morphology for maximum invasion and thus metastasis, similarly to results shown in Chapter 3 [166]; therefore, more elongated cells (i.e., circularity <<1) with higher migration speed could be considered more viable or "functional." Normal MCF10A cells are also highly migratory and highly spread as single cells in 2D assays, as shown in Chapter 3, and thus these parameters could similarly be used as proxies for cell viability. Upon cell death, cell circularity approaches a value of 1 as the cell rounds and detaches from the substrate. Cell migration speed, which assesses a critical cellular function, along with cell circularity, can provide useful information towards assessing cell viability. Here, we defined the term "selective" in reference to a CAP treatment that reduced tumor cell migration (possibly coupled with an increase in tumor cell circularity), while having minimal effect on normal cells.

We determined that our treatments each had one of three outcomes: (1) the treatment was selective; (2) the treatment was not selective because both cell types migration (possibly coupled with an increase in tumor cell circularity), while having minimal effect on normal cells. showed reduced migration speed or increased circularity; and (3) the treatment was not selective because neither cell type was significantly

affected. Figure 6.3 provides several representative examples of these outcomes. One observed selective condition was the 1 minute APPJ treatment with DMEM-based medium (Figure 6.3 A). Based on cell morphology over time and cell trajectories, it was evident that when exposed to CAP-treated media, tumor cells became less migratory, rounder, and smaller, while the normal cells remained unaffected in terms of these parameters (Figure 6.3 A). However, when DMEM/F12-based medium with supplements was used with a 1 minute APPJ treatment, neither cell line changed visibility in migration or morphology post-exposure to CAP-treated media (Figure 6.3 B), suggesting a non-selective treatment. On the contrary, in DMEM-based medium with a 7 minute APPJ treatment, both the normal and tumor cells were smaller, rounder, and less migratory (Figure 6.3 C), again suggesting a non-selective treatment. When these results were compared to the 7 minute SMD treatment, we found that the 7 minute SMD treatment was still selective in DMEM-based medium (Figure 6.3 D); however, when RPMI-based medium was used, both cell types were affected by CAP-treated media (Figure 6.3 E), while neither cell line was affected when the DMEM/F12+Supp.-based medium was used (Figure 6.3 D). Figure 6.4

Figure 6.3: Images of CAP-treated cells over time. Phase contrast image sequences of representative MDA-MB-231 and MCF10A cells over time, along with trajectories of all cells analyzed for the corresponding condition. Shown are a) selective APPJ treatment condition: 1 minute APPJ treatment in DMEM, b) non-selective APPJ treatment condition where both cell types cells were unaffected by CAP: 1 minute APPJ treatment in DMEM/F12 + Supp. medium, c) non-selective APPJ treatment condition where both tumor and normal cells were affected by CAP: 7 minute APPJ in DMEM, d) selective SMD treatment condition: 7 minute SMD treatment in DMEM, e) non-selective SMD treatment condition where both cell types cells were unaffected by CAP: 7 minute SMD treatment in DMEM/F12 + Supp. medium, f) non-selective SMD treatment condition where both tumor and normal cells were affected by CAP: 7 minute SMD in RPMI medium. Scale bar applies to all images in the sequence and x-scale of last trajectory in sequence applies to all previous ones on that panel. Images were taken via phase contrast microscopy using a 10x objective. “0 min” corresponds to the time just after the media was changed to control or CAP-treated.

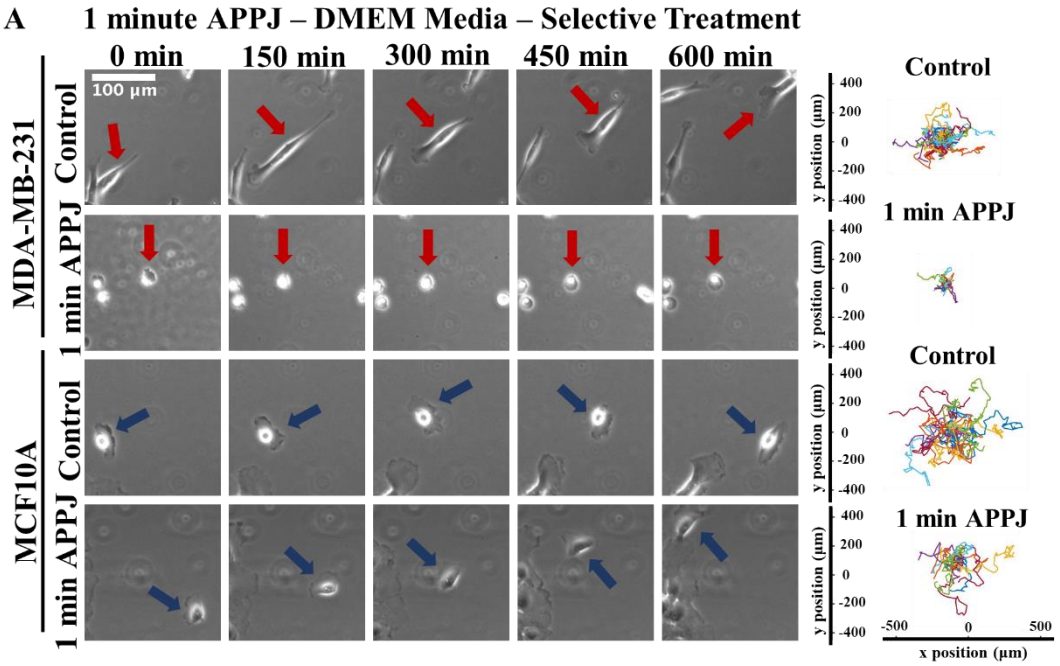
A
1 minute APPJ – DMEM Media – Selective Treatment
0 min
150 min
300 min
450 min
600 min
100 µm
MDA-MB-231
Control
1 min APPJ
MCF10A
Control
1 min APPJ
y position (µm)
x position (µm)
Control
1 min APPJ
Control
1 min APPJ

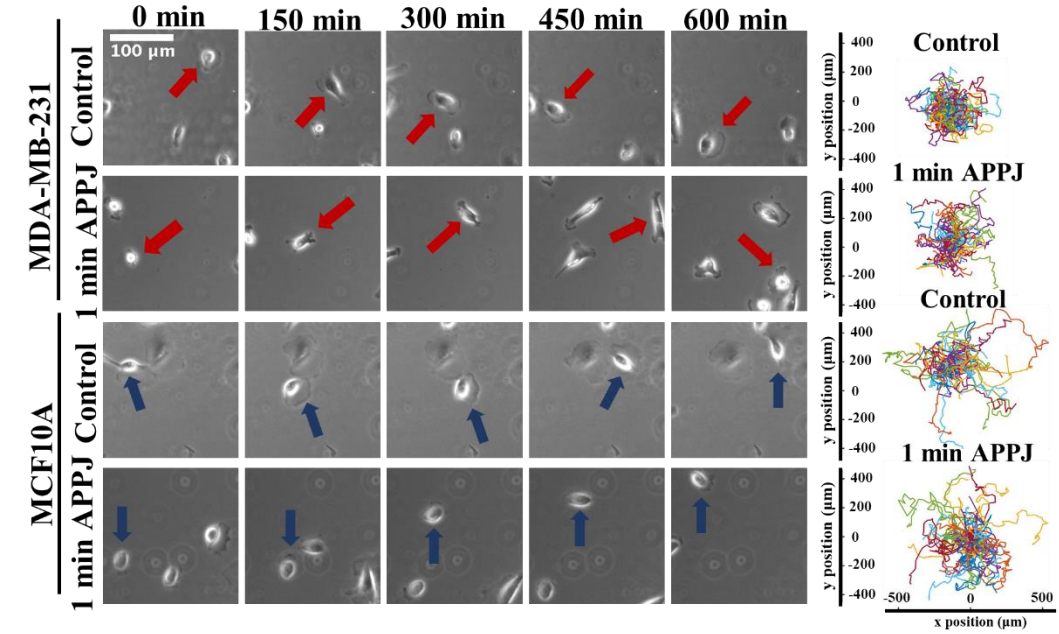
B 1 minute APPJ – DMEM/F12 + Supp. Media – Treatment Non-Selective
0 min
150 min
300 min
450 min
600 min
100 µm
MDA-MB-231
Control
1 min APPJ
MCF10A
Control
1 min APPJ
y position (µm)
x position (µm)
Control
1 min APPJ
Control
1 min APPJ

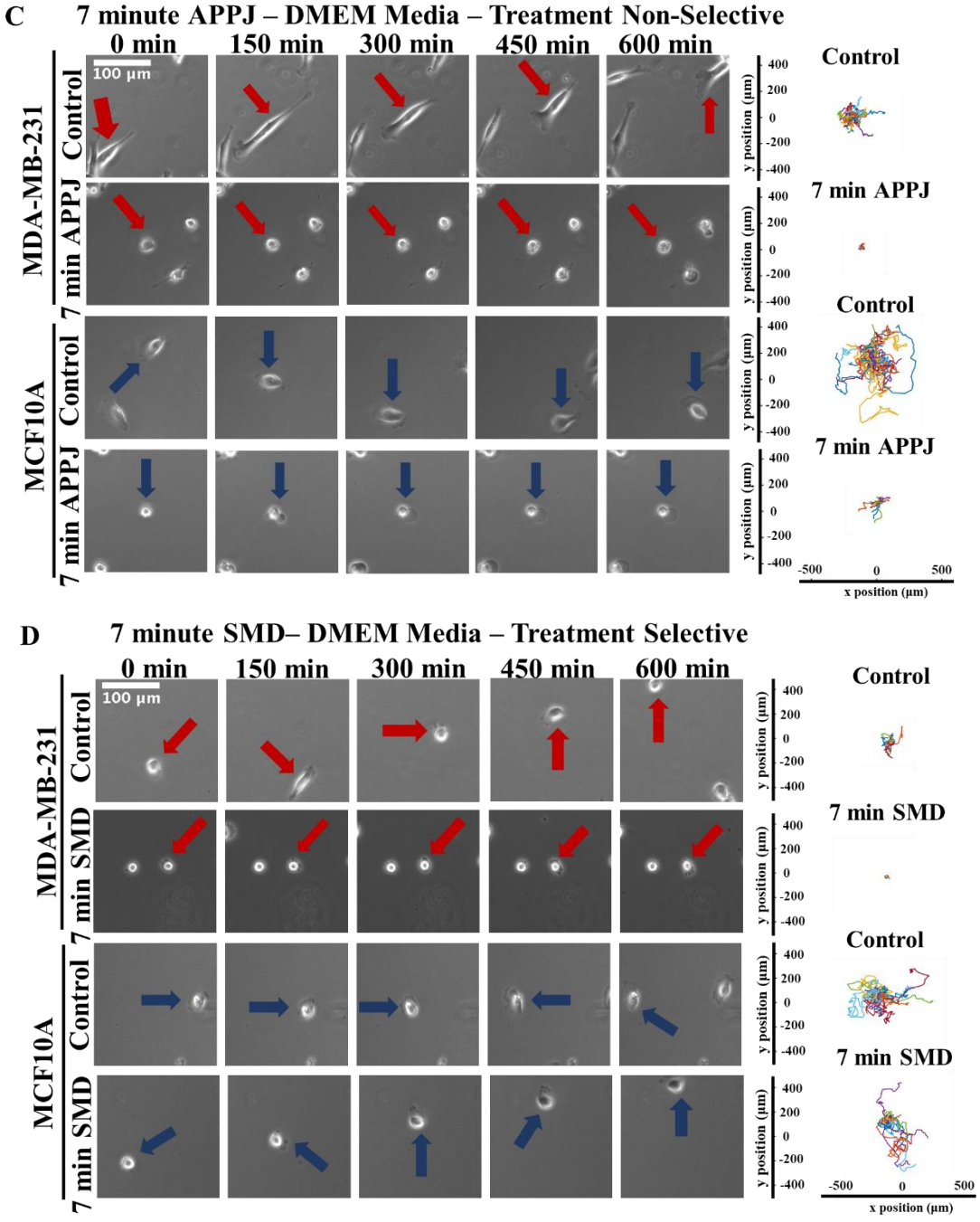
C
7 minute APPJ – DMEM Media – Treatment Non-Selective
0 min
150 min
300 min
450 min
600 min
100 µm
MDA-MB-231
Control
7 min APPJ
MCF10A
Control
7 min APPJ
y position (µm)
x position (µm)
Control
7 min APPJ
Control
7 min APPJ
D
7 minute SMD– DMEM Media – Treatment Selective
0 min
150 min
300 min
450 min
600 min
100 µm
MDA-MB-231
Control
7 min SMD
MCF10A
Control
7 min SMD
y position (µm)
x position (µm)
Control
7 min SMD
Control
7 min SMD

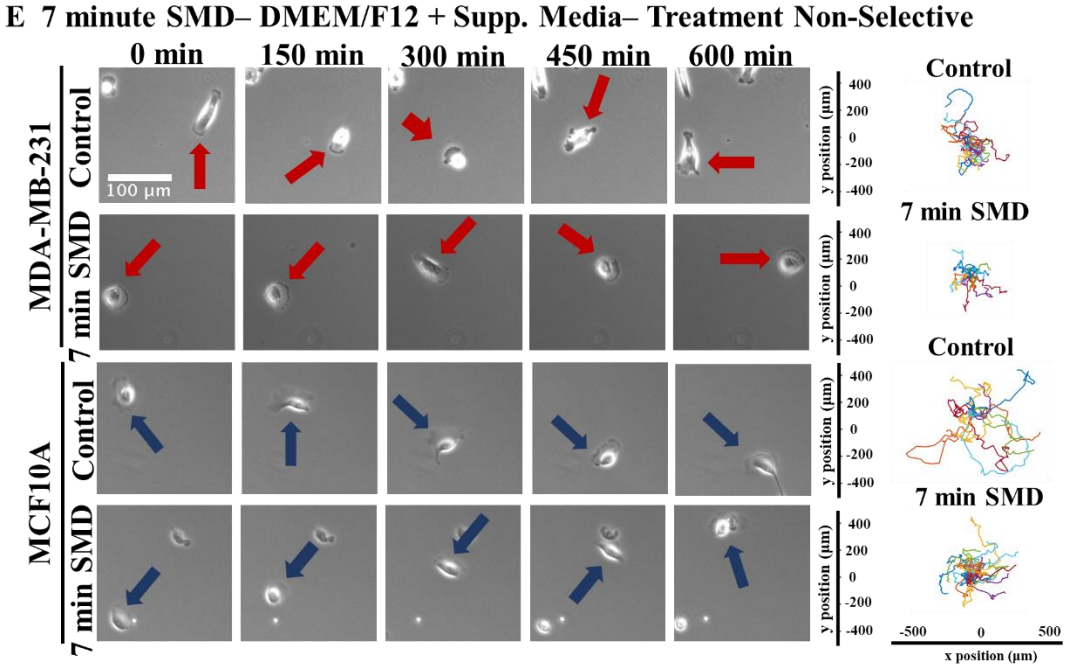
E 7 minute SMD– DMEM/F12 + Supp. Media– Treatment Non-Selective
0 min
150 min
300 min
450 min
600 min
MDA-MB-231
Control
7 min SMD
MCF10A
Control
7 min SMD
100 µm
y position (µm)
400
200
0
-200
-400
Control
7 min SMD
Control
7 min SMD
-500
0
500
x position (µm)

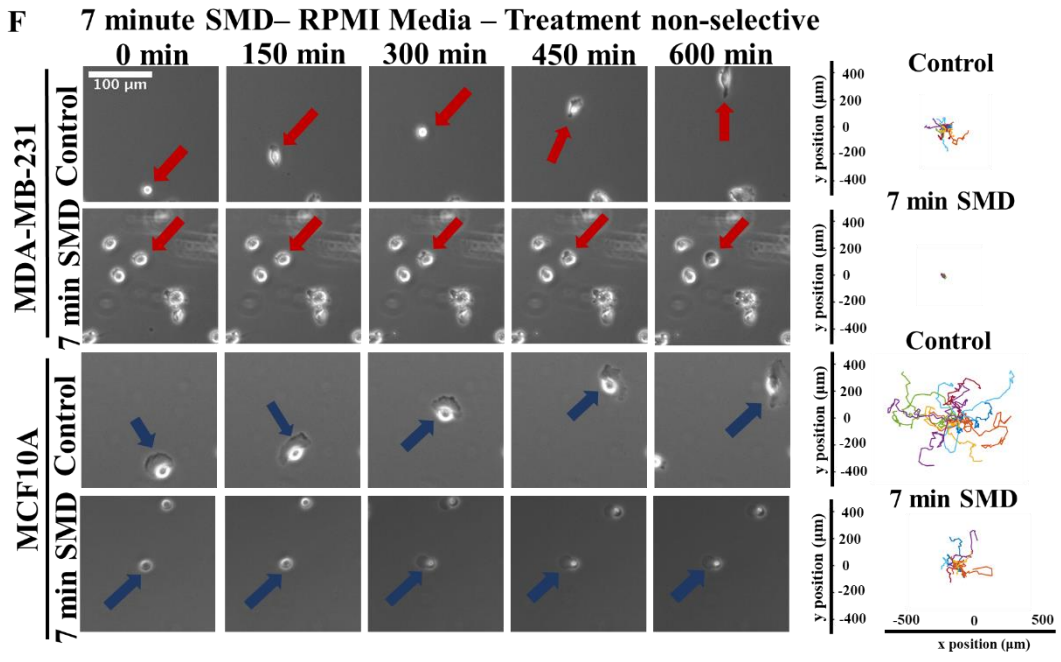
F 7 minute SMD– RPMI Media – Treatment non-selective
0 min
150 min
300 min
450 min
600 min
MDA-MB-231
Control
7 min SMD
MCF10A
Control
7 min SMD
100 µm
y position (µm)
400
200
0
-200
-400
Control
7 min SMD
Control
7 min SMD
-500
0
500
x position (µm)

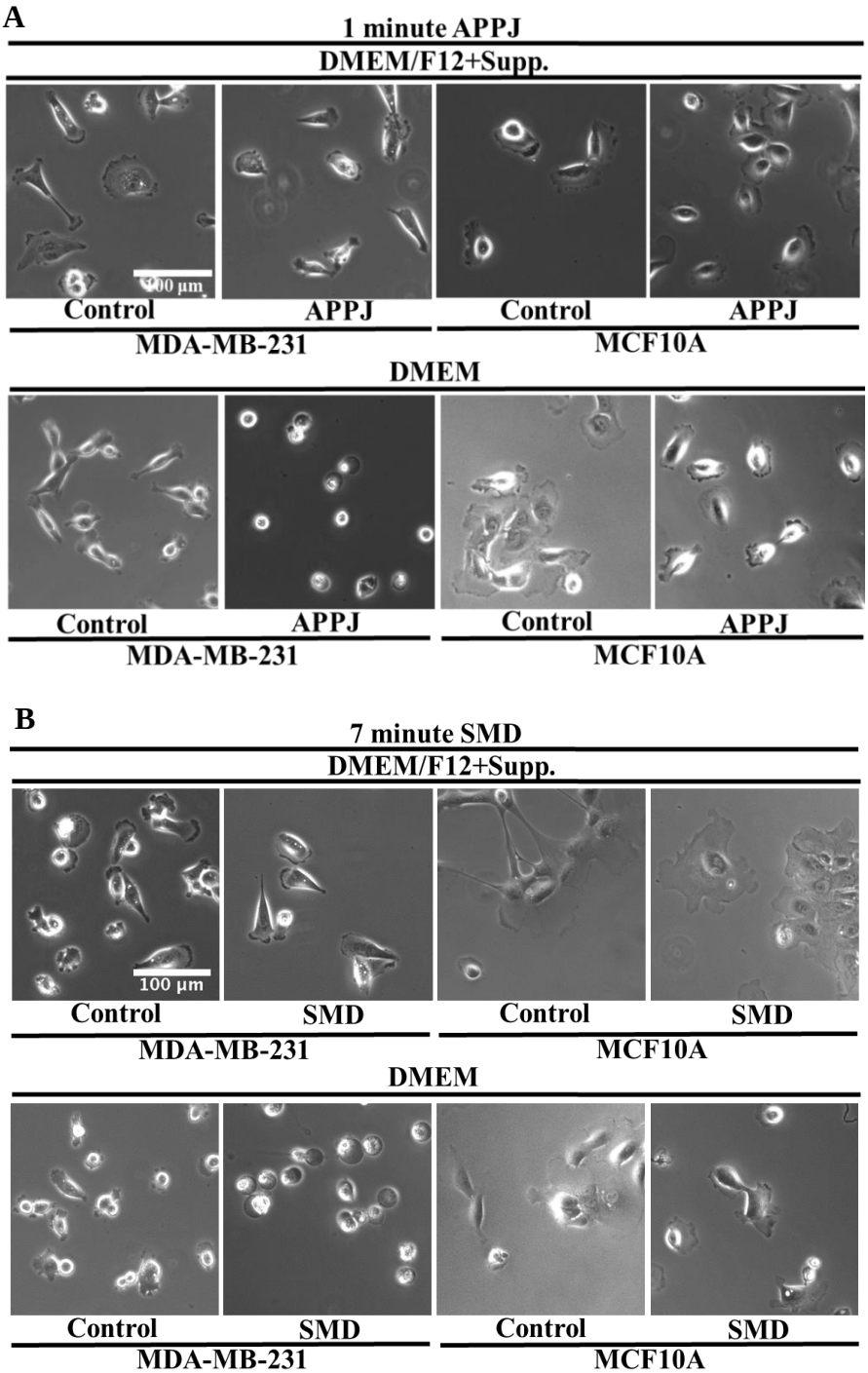

Figure 6.4: **Images of CAP-treated cells.** Phase contrast images of MDA-MB-231 and MCF10A cells when exposed to DMEM/F12 + Supp. or DMEM treated with A) 1 minute APPJ or B) 7 minute SMD. Scale bar applies to all images in the panel. Images were taken via phase contrast microscopy using a 20x objective approximately 15-20 hours after switching to control or CAP-treated media.

provides a side-by-side comparison of cells at higher magnification and shows the typical morphologies of both cell types after approximately 15-20 hours in various CAP-treated media. Together, these results show that the type of medium is critical in understanding CAP-tumor cell interactions. Although these media compositions have been routinely used in other studies, when they are compared side-by-side, the resulting conclusions about CAP-treatment selectivity could be completely different.

6.3.2 Quantification of CAP-treated media selectivity with varying medium

Next, we quantified the morphology and migration parameters and performed statistical analysis in order to understand which experimental parameters affected the interaction of CAP-treated media and tumor and normal cells to a statically significant degree. By analyzing cells treated with different CAP-treated and control media, we determined that the 7 minute APPJ treatment resulted in no selective conditions (Figure 6.5 A, B). In DMEM and RPMI-based media, the 7 minute APPJ

Figure 6.5: Effect of varying cell media. Plots of speed (panels A, C, E) and circularity (panels B, D, F) and selectivity summary tables of MDA-MB-231 (red) and MCF10A (blue) cells on collagen I-coated glass when cells were exposed to different media treated with A, B) 7 minute APPJ, C, D) 1 minute APPJ, and E, F) 7 minute SMD generated plasma. Speed was calculated from live-cell image sequences during exposure to control or CAP-treated media, taken with a 10 minute time-step, and tracked over 10 hours. Circularity was quantified from phase contrast images taken 15-20 hours after switching media to control or CAP-treated. Selectivity was determined via a non-parametric Kruskal-Wallis ANOVA test comparing all the data using a Dunn's multiple comparison post-hoc test with ns $P > 0.05$, * $P \leq 0.05$, ** $P \leq 0.01$, *** $P \leq 0.001$, **** $P \leq 0.0001$. (+) or (-) following statistical stars on summary tables indicates a trend opposite to that expected for a selective treatment. Appropriate pairs were picked out from test results for selectivity comparison. Each dot indicates the measurement for one cell, while the bar indicates the mean across all pooled cells. Errors bars represent standard error of the mean. Brittney Murugesan conducted the data analysis.

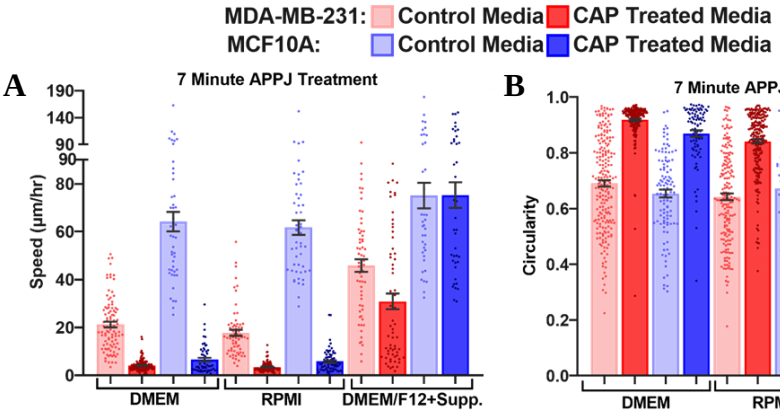

7 minute APPJ			
Media	Statistical Significance		
	MDA-MB-231	MCF10A	Selective?
DMEM	****	****	no
RPMI	****	****	no
DMEM/F12+Supp.	ns	ns	no

7 minute APPJ			
Media	Statistical Significance		
	MDA-MB-231	MCF10A	Selective?
DMEM	****	****	no
RPMI	****	****	no
DMEM/F12+Supp.	** (-)	ns	opposite

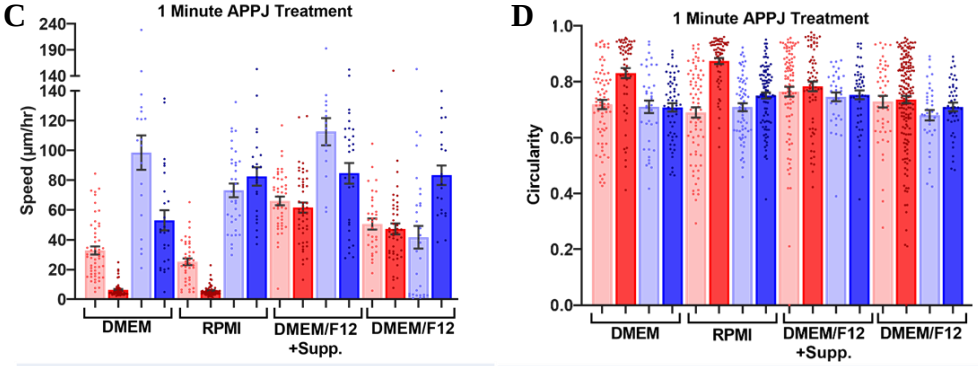

1 minute APPJ			
Media	Statistical Significance		
	MDA-MB-231	MCF10A	Selective?
DMEM	***	ns	yes
RPMI	ns	ns	no
DMEM/F12+Supp.	ns	ns	no
DMEM/F12	ns	** (+)	opposite

1 minute APPJ			
Media	Statistical Significance		
	MDA-MB-231	MCF10A	Selective?
DMEM	****	ns	yes
RPMI	****	ns	yes
DMEM/F12+Supp.	ns	ns	no
DMEM/F12	ns	ns	no

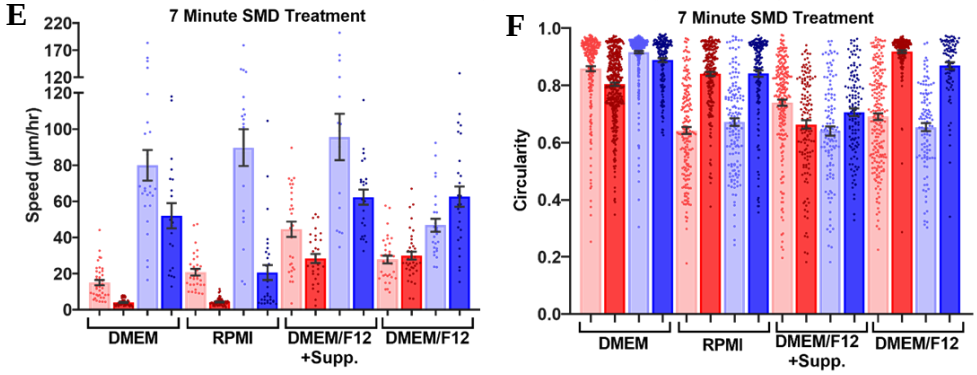

7 minute SMD			
Media	Statistical Significance		
	MDA-MB-231	MCF10A	Selective?
DMEM	*	ns	yes
RPMI	***	****	no
DMEM/F12+Supp.	ns	ns	no
DMEM/F12	ns	ns	no

7 minute SMD			
Media	Statistical Significance		
	MDA-MB-231	MCF10A	Selective?
DMEM	**** (-)	ns	opposite
RPMI	****	****	no
DMEM/F12+Supp.	ns	ns	no
DMEM/F12	****	****	no

treatment was so strong that both normal and tumor cells became significantly slower and rounder, while in the DMEM/F12 + Supp. medium, the speed remained unchanged while the circularity decreased, indicating an opposite trend of that expected in the case of cellular damage (Figure 6.5 A, B). With the 1 minute APPJ treatment, the DMEM-based medium treatments produced the sole, consistently-selective result in terms of both migration speed and circularity, where the speed decreased and circularity increased for tumor cells but not normal cells (Figure 6.5 C, D). Interestingly, for the DMEM/F12-based medium condition, the speed increased after CAP-treated media treatment of normal cells (Figure 6.5 C). Additionally, when looking at circularity, there was evidence of selectivity for both DMEM and RPMI-based media (Figure 6.5 D); however, only the DMEM-based medium condition had matching selectivity results for speed and circularity (Figure 6.5 C, D). Finally, with the 7 minute SMD treatment, the DMEM-based medium was the only treatment that was selective in terms of cell speed, where speed decreased for tumor cells in CAP-treated medium, while normal cells retained their speed (Figure 6.5 E). However, tumor cells unexpectedly became less circular with CAP-treated DMEM-based medium, while normal cells remained the same (Figure 5 F). Since only an *increase* in circularity is indicative of CAP-induced cell damage, this metric is not indicative of selectively for the 7 minute SMD treatment. Furthermore, in the RPMI-based medium, both the tumor and normal cells became significantly slower and more circular (Figure 6.5 E, F), suggesting that the effectiveness of CAP-treated media is highly dependent on the cell culture conditions. Overall, an important observation from these data is that, when experimentally analyzing CAP-based cell treatments,

not using matched media between different cell lines could significantly skew selectivity results, thus reducing translatability of experimental interpretations to clinical use.

6.3.3 Quantification of CAP-treated media selectivity with varying cell-matrix binding moieties

As previously discussed above, CAP may affect cellular integrin expression and therefore could potentially act on cells via an integrin-dependent pathway [219]. Hence, we evaluated the selectivity of CAP when cells were plated on several different substrate coatings, including collagen I, fibronectin, or PDL. We note that these experiments were all performed in DMEM, which showed the greatest number of selective conditions (Figure 6.5) and thus was most promising to further evaluate variation of cell-matrix binding moiety. Results for cells plated on collagen I and treated with control or CAP-treated DMEM were already presented in Figure 6.5, but are repeated on Figure 6.6 for easy comparison. First, we found that normal and tumor cells exposed to DMEM with 7 minute APPJ treatment had reduced migration

---

Figure 6.6: Effect of varying cell binding moieties. Plots of speed (panels A, C, E) and circularity (panels B, D, F) and selectivity summary tables of MDA-MB-231 (red) and MCF10A (blue) cells on collagen I, fibronectin, and PDL-coated glass when cells were exposed to DMEM treated with A, B) 7 minute APPJ, C, D) 1 minute APPJ, and E, F) 7 minute SMD generated plasma. Speed was calculated from live-cell image sequences during exposure to control or CAP-treated media, taken with a 10 minute time-step, and tracked over 10 hours. Circularity was quantified from phase contrast images taken 15-20 hours after switching media to control or CAP-treated. Selectivity was determined via a non-parametric Kruskal-Wallis ANOVA test comparing all the data using a Dunn's multiple comparison post-hoc test with ns $P > 0.05$, * $P \leq 0.05$, ** $P \leq 0.01$, *** $P \leq 0.001$, **** $P \leq 0.0001$. (+) or (-) following statistical stars on summary tables indicates a trend opposite to that expected for a selective treatment. Appropriate pairs were picked out from test results for selectivity comparison. Each dot indicates the measurement for one cell, while the bar indicates the mean across all pooled cells. Errors bars represent standard error of the mean. Brittney Murugesan conducted data analysis.

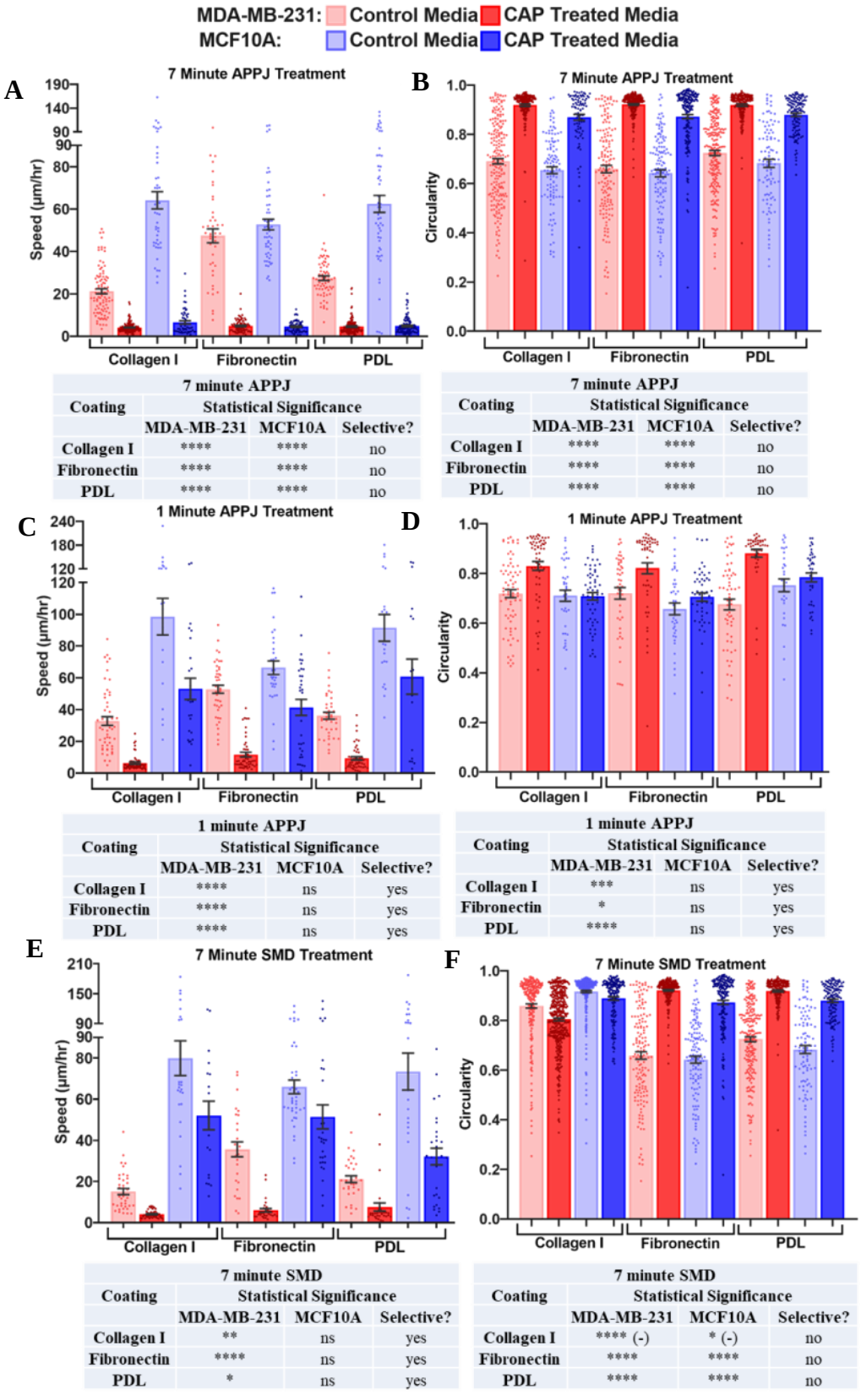

7 minute APPJ			
Coating	Statistical Significance		
	MDA-MB-231	MCF10A	Selective?
Collagen I	****	****	no
Fibronectin	****	****	no
PDL	****	****	no

7 minute APPJ			
Coating	Statistical Significance		
	MDA-MB-231	MCF10A	Selective?
Collagen I	****	****	no
Fibronectin	****	****	no
PDL	****	****	no

1 minute APPJ			
Coating	Statistical Significance		
	MDA-MB-231	MCF10A	Selective?
Collagen I	****	ns	yes
Fibronectin	****	ns	yes
PDL	****	ns	yes

1 minute APPJ			
Coating	Statistical Significance		
	MDA-MB-231	MCF10A	Selective?
Collagen I	***	ns	yes
Fibronectin	*	ns	yes
PDL	****	ns	yes

7 minute SMD			
Coating	Statistical Significance		
	MDA-MB-231	MCF10A	Selective?
Collagen I	**	ns	yes
Fibronectin	****	ns	yes
PDL	*	ns	yes

7 minute SMD			
Coating	Statistical Significance		
	MDA-MB-231	MCF10A	Selective?
Collagen I	**** (-)	* (-)	no
Fibronectin	****	****	no
PDL	****	****	no

speeds along with increased circularity on all binding moieties (Figure 6.6 A, B), which was consistent with experiments where medium was varied (Figure 6.5 A, B). For media with 1 minute APPJ treatment, cell speed and circularity both showed selectivity when cells were plated on collagen, fibronectin, or PDL (Figure 6.6 C, D). For the 7 minute SMD treatment, all substrate coatings yielded a selective result based on speed, but not based on circularity (Figure 6.6 E, F). Based on these results, we conclude that the condition with DMEM-based medium with a 1 minute APPJ treatment on any surface, yielded the most consistently selective result (Figure 6.6). If only migration speed was considered as a significant cell viability predictor, then the 7 minute SMD would also be an effective selective treatment for all coating types (Figure 6.6 E). Hence, the selection of the cell-matrix binding moieties may be less crucial to a consistent CAP-treatment outcome than the selection of the treatment media.

6.4 Discussion

Overall, our results show that media compositions are crucial in the outcome of studies involving CAP-treated media on tumor versus normal cells, and media selection should be carefully considered when designing experiments. In fact, changing the type of media could entirely change the selectivity outcomes. Meanwhile, binding moieties seem to play a less significant role.

Previous studies have investigated the effect of various culture conditions such as cell number, treatment time, medium volume, and treatment well size on the RNS/ROS concentration in CAP-treated media, as well as their effects on cells [236]. However, in those studies only tumor cells were used (not normal cells) and thus

treatment selectivity was not considered, yet there was a difference in outcomes even between different types of tumor cells [236]. Another study has shown that the effect of CAP-treated liquid on cell viability is dependent on both the cell type and the type of liquid, such as medium versus buffer [209]. Yet another study has shown that higher FBS concentrations in media can reduce CAP treatment's effects on glioblastoma cell viability [92]. However, that study did not address the selectivity of the treatment between normal and tumor cells. A few studies have found that altering media composition can alter the effects of CAP on cell viability (Table 6.1, shaded) [84], [90], [222]; however, no systematic assessment of selectivity has been carried out to the best of our knowledge. Furthermore, these studies showed that RPMI-based medium generally provides the best conditions to effectively reduce tumor cell viability; however, it does not address how the results might change for normal cells, and in fact one study shows that a decrease in normal cell viability when treated with RPMI-based CAP treated media [84], [90], [222]. It is also important to note that when considering therapeutics intended for *in vivo* use, the media do not fully recapitulate any particular body fluid. Thus, if a therapy is effective in one medium but not in another, it remains uncertain whether it will be effective in the presence of blood or another bodily fluid. Thus, in our work, we aimed to systematically evaluate the effects of CAP-treated media (produced by two different CAP sources) on the migration and morphology of metastatic breast tumor cells and their normal breast epithelial cell counterparts, while varying several common cell culture media and cell-matrix binding moiety conditions.

Our work not only demonstrates that the treatment and medium type affect how CAP-treated media impacts cells, but perhaps more importantly, it also shows that these parameters can change the conclusions made about the selectivity of the treatment. Since cancer therapy toxicity remains a challenging and important aspect of drug development [237], treatment selectivity for tumor cells (versus normal cells) is an important outcome to achieve. Here, we show that, of the media tested, CAP treatment of DMEM-based medium appears to most consistently result in damage to tumor cells while not significantly affecting normal cells. Overall, the 1 minute APPJ treatment and the 7 minute SMD treatment of DMEM resulted in selective reduction of tumor cell migration speed, with the 1 minute APPJ treatment of DMEM also resulting in a selective increase of tumor cell circularity.

Furthermore, the majority of previous reports involving CAP treatment of cells and media utilize tissue culture plastic surfaces, which bind cells via electrostatic forces. For our study, these surfaces are most similar to the PDL-coated glass, since that binding moiety also engages cells via electrostatic forces and does not activate integrins [238]. However, our results on PDL were mostly consistent with our results on collagen and fibronectin. These data suggest that cell-matrix binding moiety, whether via electrostatic interactions or integrin-extracellular matrix binding, has a negligible effect on the outcome of a CAP-treated media experiment; furthermore, our results do not support the hypothesis that CAP-treated media acts on cells through via integrin-mediated pathways.

Finally, we found that the type of CAP treatment is an important factor. “Over-treatment” of cell culture media can result in disappearance of treatment

selectivity, with *both* normal and tumor cells being damaged by the CAP-treated media, as seen for the 7 minute APPJ treatment. Consideration of these results are important because they provide guidelines for future CAP-treated media-based studies, as CAP-therapy cancer technology progresses towards becoming more ubiquitous and suitable for human use.

In this work we specifically observe tumor cell migration and morphology without evaluating cell death directly. This is motivated by the fact that tumor cells' ability to migrate and their morphology are tied to both their health [239] and their metastatic potential [140], [180], [203]. When tumor cells are smaller, rounder, and appear to be blebbing they tend to be less healthy [239]. Similarly, healthy MDA-MB-231 and MCF10A cells are highly migratory and thus a decrease in migration suggests some damage to the normal functioning of the cell [240]. When it comes to tumor cells' ability to metastasize, tumor cells with a higher metastatic potential tend to be larger, more elongated, with more protrusions, and more migratory [140]. Thus, the observation of decreased cell speed and increased circularity corresponds to potentially decreased cell health as well as a decrease in metastatic potential. While we do not show whether tumor cells are destroyed by CAP, the selective decrease in tumor cell speed relative to normal health and the selective increase in tumor cell circularity relative to normal cells under certain treatment conditions suggests that the tumor cells become less metastatic and less able to spread to distant sites. Alternatively, the selective CAP treatments also could return the tumor cells to a state where they are less aggressive and more localized to a specific area and thus more vulnerable to more traditional cancer therapeutics.

This work contributes to the discussion of how plasma treatment of liquids leads to effects on biological systems. There has been a wealth of research on plasma-liquid interactions for many purposes, from medical to waste water treatment, which has been summarized recently in work by Bruggeman *et al.*[241]. Specifically, the area of plasma medicine is interested in plasma-liquid interactions, as there is typically a liquid medium between the plasma species and the biological system, whether it could be bacteria or other cells [242]. RNS and ROS in the gas phase tend to cause reactions with the water which form different liquid-based reactive species. Some studies have investigated how different additives to the water or media influence the effect of plasma on biological systems. Wende *et al*. used the exact plasma source used in this work and investigated how buffered water impacts the species in the liquid, and how this liquid kills bacteria [84]. Specifically, they used catalase as a ROS scavenger to show that the plasma jet has no effect on cells when it is present through a liquid barrier, but has a significant effect on cells through water that is not buffered. In our experiments, it is possible that some compounds in the media solution, such as sodium pyruvate [243] or glutathione [244]. act similarly as reactive species scavengers which reduce the effectiveness of the plasma treatment on the cells. However, the simple presence of the ROS/RNS scavenger in media is not enough to explain the difference in results, since DMEM/F12 and RMPI contain sodium pyruvate and glutathione respectively (Figure 6.2), and yet yield very different results.

6.5 Conclusion

We have found that the type of plasma source and media in which CAP-treated media experiments are conducted are key parameters in achieving selective CAP-based treatments. As CAP technology is developed further and adapted for *in vivo* use, it is important to carefully consider the *in vitro* experimental parameters to ensure that the interpretation of results is based on CAP's effects and not simple interactions with arbitrary media. In the future, it would be key to determine what method of CAP delivery will be used *in vivo*, and then the appropriate bodily fluid should be tested similarly to our comprehensive study, in order to properly account for the presence of proteins, cells, minerals, and other components in the fluid.

7 Summary and Conclusions, Contributions to the Field

Metastatic tumor cells are able to cross the BBB and form devastating secondary tumors in the brain. However, the mechanism by which that occurs is not well understood and thus it is difficult to develop successful therapeutics, since many chemotherapeutic drugs cannot cross the BBB [245]. Thus, determining how tumor cells cross the highly impermeable BBB remains an important medically relevant problem, so that these mechanisms can either be targeted by therapies or the therapeutics could leverage the pathways to cross the BBB as well. This dissertation addresses this topic by looking at the physico-chemical interactions of tumor cells with the BBB microenvironment while also touching upon the optimization of a novel cancer therapeutic strategy.

7.1 Tumor cells become more elongated and migratory when exposed to astrocyte-secreted biochemical cues.

In Chapter 3, this dissertation shows that when tumor cells are exposed to astrocyte-secreted factors, they became more elongated and faster, which could indicate a more mesenchymal, and thus more invasive phenotype. Most interestingly, we showed that astrocyte-secreted factors not only directly affected the behavior of tumor cells, but they actually interacted with the tumor cell's extracellular matrix leading to an increase in tumor cell velocity. One of the potential biochemical cues that astrocytes secrete to alter tumor cell migration and morphology, could be MMPs, especially MMP-2 and -9. Specifically, the inhibition of MMPs in ACM led to a decrease in ACM-induced migration changes while adding exogenous MMPs into

control media appeared to enhance tumor cell migration similarly to ACM. Since MMPs are known to degrade the extracellular matrix, the presence of MMPs in ACM could partially explain why ACM alters tumor cell behavior even when they are not treated directly but seeded on extracellular matrix treated with ACM. Similarly, we found that inhibiting ROCK in tumor cells somewhat attenuated their response to ACM, indicating a likely involvement of the ROCK-mediated contractility pathway in the tumor cell response to astrocyte secreted factors.

Another surprising finding was that astrocyte activation via TGF-β led to a decrease in tumor cell changes when treated with ACM, compared to ACM from untreated astrocytes. This finding is interesting since reactive astrocytes are more likely to be found in a diseased state, such as brain metastasis, and thus it would have been unsurprising if astrocytes from a diseased state were enhancing tumor cell migratory behavior. However, due to the opposite trend, it is possible that astrocytes actually develop a more protective phenotype in disease. Moreover, while we have observed an increase in tumor cell speed when treated with ACM, this does not necessarily correspond to increased metastatic potential [180]. It is possible that metastatic tumor cells are slower at a secondary site and actually slow down as part of the process of proliferating into a secondary tumor [180]. However, more motile cells prior to extravasation could serve as a potential therapeutic target since they are more likely to form micrometastases that then form secondary tumors [180]. Since tumor cells could be exposed to astrocyte-secreted factors on either side of the vasculature, depending on factors such as BBB integrity, both of these cases should be considered.

It is important to note that these results were relatively consistent across cell lines of varying metastatic potential but from the same tissue source for cells treated with ACM, however the effect of ACM was less evident when cells of lower metastatic potential were plated on ACM-treated extracellular matrix. The results were also consistent across multiple extracellular matrix molecules, including collagen I, fibronectin, and laminin, for certain parameters. However, the effects of ACM on cell migration did not hold on PDL, suggesting that in addition to MMPs, integrins are likely to play a role in tumor cell-ACM response.

Together, Chapter 3 of this dissertation sheds light on some key pathways involved in the biochemical interaction of tumor cells with the BBB microenvironment. This work elucidates one potential cell type within the BBB microenvironment that could actually be resulting in tumor cells' enhanced invasiveness at the BBB, instead of serving in its protective role.

7.2 Tumor cells become slower on more crosslinked HA-gelatin films; however, the effect is diminished during incorporation into HBMEC monolayers.

Following an understanding of some of the biochemical interactions of tumor cells with the BBB microenvironment in Chapter 3, Chapter 4 addressed the biophysical interactions of tumor cells with a BBB-like extracellular matrix made of HA-gelatin films. Both types of interactions are essential to understand in order to start to form a more complete picture of the process of BBB metastasis. Chapter 4 addresses tumor cells both independently and during incorporation into HBMEC

monolayers as they interact with an HA-gelatin matrix that more accurately mimics the extracellular matrix structure and composition at the BBB, just outside the blood vessels, than does collagen or fibronectin. The HA-gelatin films are differently crosslinked, since during different physiological conditions the density of extracellular matrix molecules and their crosslinking can change significantly. Here, we established that while tumor cells are extremely sensitive to HA-gelatin crosslinking on bare films (tumor cell speed and area decrease significantly with increased crosslinking), this effect is diminished once HBMECs are introduced. This suggests that the underlying extracellular matrix might not be as significant during incorporation as the direct interaction of tumor cells and endothelial cells, and the extracellular matrix only begins to play a large role once tumor cells have crossed the endothelium. Alternatively, HBMECs could be depositing their own extracellular matrix that has a greater influence than the original HA/gelatin films. Fascinatingly, we have also shown that tumor cells might be crossing the BBB transcellularly, not only paracellularly as previously shown. These findings suggest that the underlying extracellular matrix is unlikely to be responsible for motivating tumor cells to cross the BBB, suggesting that other forces – biochemical or biophysical – are likely at play.

7.3 Tumor cell morphology varies based on the preferred metastatic site.

Another potential driving force for selective brain metastasis could be the tumor cell phenotype itself. In order to examine that, in Chapter 5, we utilized brain- and bone-seeking tumor cell clones from the same cell line in order to determine if there are distinct differences in their phenotypes. While prior studies have looked at

the proteomics of the clones and certain other parameters, here we were particularly interested in morphological differences. We found that parental and brain- and bone-seeking tumor cells all varied in their morphology on all substrates, with the bone-seeking tumor cells showing the greatest differences from the other two clones. However, the differences in morphology did not suggest that substrate stiffness alone can be used to distinguish between the cell types, especially given the heterogeneity of the cell population. The differences in morphology within each substrate stiffness, however, could indicate that with the addition of other biophysical and phenotypic parameters a system could be developed to distinguish between the different cell clones. Furthermore, it is possible that there is some functional significance to the differences in morphology.

7.4 CAP selectivity is highly dependent on culture conditions.

This dissertation addresses several physico-chemical factors that influence tumor cell's in a BBB microenvironment. However, the ultimate goal of understanding how tumor cells cross the BBB is to inform therapeutic design. In Chapter 6 we chose to further study CAP, which has been proposed as a novel cancer therapeutic. While CAP is not currently applied as treatments of brain metastasis or brain cancer, effective new cancer treatments are still gravely needed and could in the future be adapted for brain applications. Here, we focused on understanding which cell culture and treatment parameters would render CAP most and least effective in selectively destroying tumor cells without harming normal cells. In fact, we found that cell culture medium makes a dramatic difference in the selectivity of CAP, while extracellular matrix molecules have a much lesser effect. Additionally, we established

that certain treatments can be too long or too strong to be effective, while a reduction in dose or a change in CAP source actually renders it successful. Chapter 6 establishes a baseline understanding on what needs to be considered as CAP is further developed into a therapeutic and underscores the fact that any molecules in the body or bodily fluid that CAP is expected to interact with has to be thoroughly vetted since even small changes can greatly affect the outcome of a treatment.

7.5 Concluding remarks

The results presented in this dissertation suggest that the physico-chemical interactions of tumor cells with the BBB microenvironment could be responsible for phenotypical changes in tumor cells, making them potentially more migratory and invasive. This dissertation evaluates multiple steps in the metastatic cascade, from the phenotype of the tumor cells themselves, to the biochemical cues potentially outside the BBB, to the physical interactions of tumor cells with a BBB model. Together, these findings present a clearer picture of the tumor cell-BBB microenvironment than what was previously available and understood. This dissertation shows that metastasis across the BBB is a delicate balance of biochemical and physical cues from the endothelium, the extracellular matrix, cells inside the brain, and the tumor cells themselves, as predicted by the “seed and soil” hypothesis. While some of the pathways discussed in this dissertation have previously been studied in models of peripheral vasculature, the unique structure of brain vasculature and the BBB results in different outcomes and thus has to be studied independently. Thus, this dissertation addresses some key biological and medical gaps in the understanding of brain metastasis and opens up pathways for potential future therapies.

7.7 Contributions to the field

7.7.1 Scientific contributions

This dissertation makes the following contributions to the understanding of tumor cell metastasis across the BBB and novel therapeutics:

- Establishes that astrocyte secreted factors enhance migration potential and alter morphology of tumor cells (Chapter 3);
- Establishes that astrocyte secreted factors are able to alter the tumor cells' extracellular matrix, leading to further alterations in tumor cell migration and morphology (Chapter 3);
- Effect of ACM can be affected by the type of extracellular matrix and tumor cell line (Chapter 3);
- Establishes that tumor cell migration is significantly affected by the crosslinking of a brain-liked, HA-based, extracellular matrix (Chapter 4);
- Establishes that underlying extracellular matrix plays little role in the ability of tumor cells to incorporate into a brain-like endothelium (Chapter 4);
- Establishes that tumor cells might be using a transcellular mechanism to cross a brain-like endothelium (Chapter 4);
- Establishes that brain- and bone-seeking tumor cells do not show distinct morphological differences in response to substrate stiffness, however they do vary in morphology within each substrate stiffness (Chapter 5).
- CAP treatment selectivity is highly dependent on favorable cell culture conditions *in vitro* (Chapter 6).

7.7.2 Contributions to laboratory and field

My work contributed the following additional tools to Dr. Stroka's laboratory and my field:

- As one of two first graduate students in Dr. Stroka's laboratory, helped set-up most of the initial equipment and standard operating procedures. Adapted all protocols for use in the new lab and established sterile cell culture protocols.
- Established protocol for work with conditioned media.
- Optimized live-cell and timelapse imaging protocols specifically for studying cell morphology, migration, and transmigration with various staining and magnifications. (Appendix C)
- Established experimental protocol for studying tumor cell incorporation into endothelial monolayers at both high and low resolution with both tumor cell staining and live VE-cadherin staining.
- Developed systematic protocol for analysis of tumor cell incorporation into endothelial monolayers.
- Developed HA/gelatin film extracellular matrix system with varying degrees of crosslinking specifically for timelapse imaging applications.
- Created microfluidic device for HA gel incorporation and cell culture (see Section 8.1, Figure 8.2).
- Started a collaborative effort between materials' science and engineering and bioengineering labs to pursue plasma-based cancer therapeutics.
- Determined procedural flaws in plasma-based cancer therapeutics research and came up with project to address them.

- Established collaboration with Dr. Geller's lab at the National Institutes of Health.
- Trained 6 undergraduates, 1 Research Experience for Undergraduates student, and 3 rotation PhD students.

7.7.3 Publications

- **Pranda, M.A.***, Gray, K.M.*, Dawson, G.M., Decastro, A.J., Jung, J, Stroka, K.M. *Tumor cell mechanosensing during incorporation into the brain microvascular endothelium, (2019).* (accepted, *CMBE Journal*)
- **Pranda, M.A.*,** Dawson, G.M.*, Ornstein, T.S., Murugesan, B.J., Stroka, K.M**.** *Effects of confounding variables on the statistical analysis of the migration and morphology of metastatic tumor cells**,** (2019).* (in preparation)
- **Pranda, M.A.,** Murugesan, B.J., Knoll, A.J., Oehrlein, G.S., Stroka, K.M. *Sensitivity of tumor vs. normal cell migration and morphology to cold atmospheric plasma-treated media in varying culture conditions., (2019).* (under review, *Plasma Processes and Polymers*)
- **Shumakovich, M.A.**, Mencio, C.P., Siglin, J.S., Moriarty, R.A., Geller, H., Stroka, K.M. *Astrocytes from the brain microenvironment alter migration and morphology of metastatic breast cancer cells*, (2017). *FASEB J.* 31(11), 5049-5067.

7.7.4 Conference Presentations

* indicates presenting author (Pranda: married name; Shumakovich: maiden name)

- **Pranda, M.A.*,** Gray, K.M., Girma, N., Stroka, K.M. *Phenotyping of Metastatic Breast Tumor Cell Clones Based on Metastatic Site* (poster, 2019

American Association for the Advancement of Science Annual Meeting, February 2019, Washington, DC)

- **Shumakovich Pranda, M.*,** Gray, K.M., Dawson, G.M., DeCastro, A.J, Stroka, K.M. *Effect of Extracellular Matrix Crosslinking on Tumor Cell Migration and Transmigration* (talk, Biomedical Engineering Annual Meeting, October 2018, Atlanta, GA)
- **Shumakovich, M.A.***, Dawson, G.M, Gray, K.M., Stroka, K.M. *Engineered Hyaluronic Acid Matrices for Studying Unique Mechanobiology of Tumor Metastasis Across the Blood-Brain Barrier* (poster, Cellular and Molecular Bioengineering Conference, January 2018, Key Largo, FL).
- **Shumakovich, M.A.***, Siglin, J., Moriarty R.A., Dawson G.M., Stroka, K.M. *Metastatic Tumor Cell Migration in Engineered Blood-Brain Barrier Microenvironments* (talk, Biomedical Engineering Annual Meeting, October 2017, Phoenix, AZ) (travel award).
- Gray, K.M.*, **Shumakovich, M.A**., Brown, E.G., Stroka, K.M., *Human Brain Endothelial Cells on Biomimetic Substrates: Mechanobiological Response to Tumor Cells* (poster & talk, American Society for Matrix Biology Biennial Meeting, November 2016, St. Petersburg, FL).
- Gray, K.M., **Shumakovich, M.A**, Katz D., Stroka, K.M*. *Biomimetic Models to Study Cell Mechanobiology at the Blood-Brain Barrier* (talk, Biomedical Engineering Society Annual Meeting, October 2016, Minneapolis, MN).
- **Shumakovich, M.A.***, Siglin, J., Stroka, K.M. *Microfluidic Models to Understand Tumor Cell Mechanobiology at the Blood-Brain Barrier* (poster,

19th International Signal Transduction at the Blood-Brain Barriers Symposium, September 2016, Copenhagen, Denmark) (travel award).

- **Shumakovich, M.A.***, Siglin, J., Stroka, K.M. *Microfluidic Models to Understand Tumor Cell Interactions with the Brain Microenvironment at the Blood-Brain Barrie*r (talk & poster, Gordon Research Seminar and Conference, "Signal Transduction by Engineered Extracellular Matrices," June 2016, Biddeford, ME) (travel award).
- **Shumakovich, M.A.***, Bryant, K.W., Stroka, K.M. *Effects of Astrocytes from Brain Microenvironments on Motility and Morphology of Tumor Cells* (poster, Biomedical Engineering Society Annual Meeting, October 2015, Tampa, FL).

8 Future Work and Outlook

8.1 Further examination of biochemical cues and pathways

This dissertation examines the effect of biochemical cues from astrocytes on migration and morphology of metastatic breast tumor cells (Chapter 3). It also discusses the role of reactive versus non-reactive astrocytes, the potential role of MMPs, and the Rho/ROCK pathway in the cross talk of tumor cells and astrocytes (Chapter 3). However, this dissertation only addresses the one-way cross talk where biochemical cues from astrocytes are applied to tumor cells. In the future, it is important to look at the effect of tumor cell secreted cues on astrocytes and determine whether they change phenotype (eg. from non-reactive to reactive) upon exposure to cues from tumor cells. Another important consideration is the fact that here we did not consider a co-culture system where the tumor cells and astrocytes interact directly. This is another area that should be addressed in the future. If these studies are performed systematically, they can lead to a more physiologically relevant interaction model of tumor cells and astrocytes and could shed light on the phenotypes of both cell types.

Additionally, while astrocytes are highly important during tumor cell metastasis to the brain, in part due to their location in the direct proximity to the BBB, there are other cells in the neurovascular unit, such as pericytes and neurons, that could also play a biochemical role in tumor cells being able to cross the BBB. However, while there is some information available about the role of pericytes in peripheral metastasis and their support of blood vessels [246], there is little

information available on the mechanisms by which pericytes or neurons interact with metastasizing tumor cells at the BBB. Thus, in the future similar studies can be carried out with pericytes and neurons as have been with astrocytes.

8.2 Understanding incorporation in different disease states of the BBB

This dissertation examined the interaction of tumor cells and HBMEC monolayers on HA-gelatin films in order to shed light on the incorporation mechanisms involved in metastasis across the BBB (Chapter 4). However, in addition to understanding the tumor cell and HBMEC dynamics, the overall integrity of the monolayer during transmigration is also of interest. We have also shown from the data collected in Chapter 4, that the initial number of tumor cells does not consistently alter the monolayer quality at the end of analysis, suggesting that the tumor cell number does not necessarily control any tumor cell induced monolayer damage (Figure 8.1 A). We have also shown that when the data from Chapter 4 is qualitatively sorted by apparent monolayer quality, except for in one case (0.2% Extralink), poorer monolayer quality does not correspond to higher percent incorporation (Figure 8.1 B) (which could in part be due to the fact that cells that simply spread into monolayer gaps were excluded from analysis), however, overall monolayer integrity did decrease over time for all Extralink concentrations (Figure 8.1 C). Our data, combined with the fact that in a diseased state (such as during cancer), the BBB becomes disrupted and frequently exhibits weaker tight junctions, change in transport, and increased leukocyte infiltration and various biochemical cues have been implicated in damage of the BBB, such as VEGF, ROS, inflammatory cytokines, MMP-2 and -9 and well as leukocyte adhesion molecules [247], raises

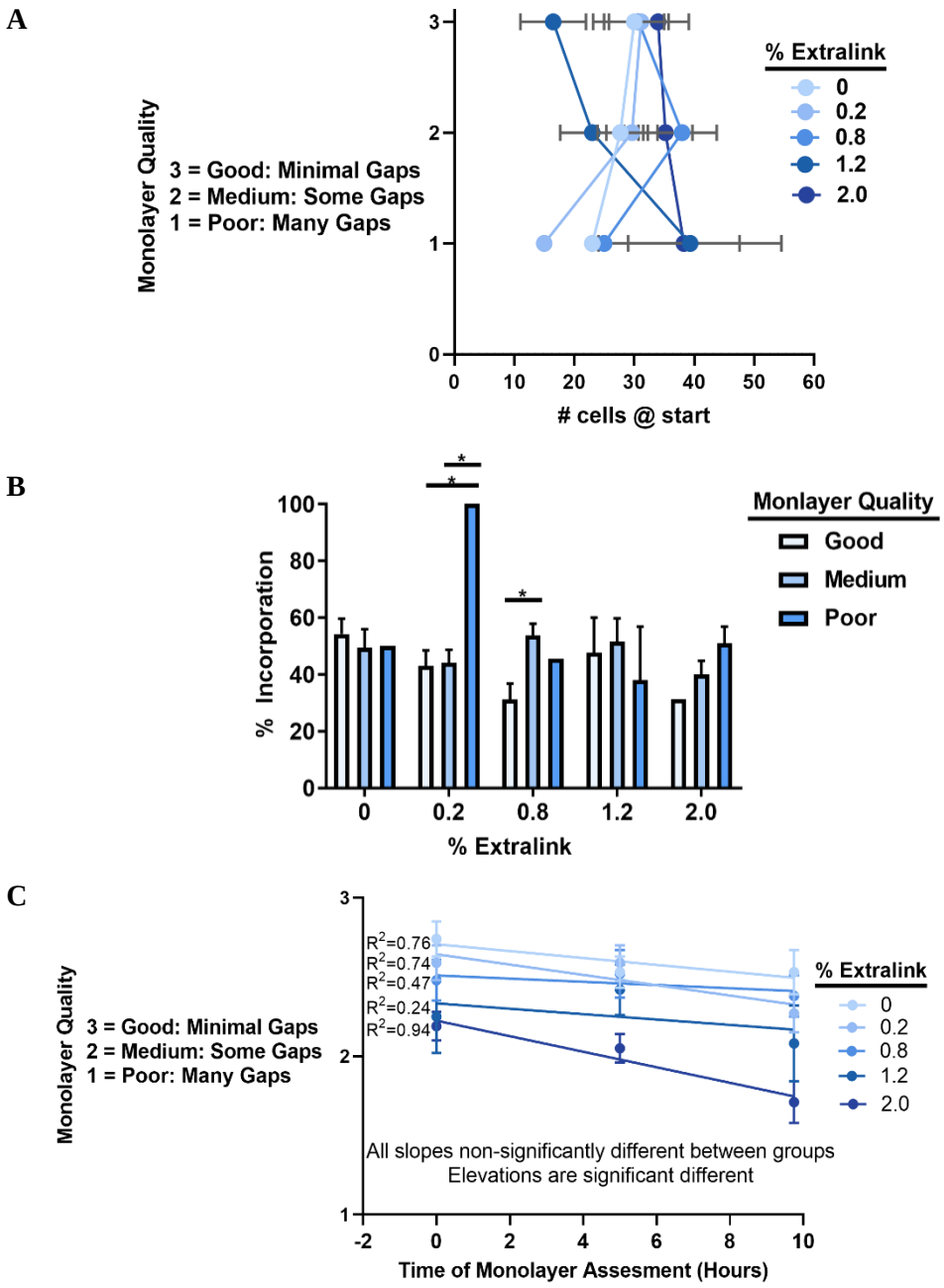

Figure 8.1: **HBMEC monolayer quality during tumor cell incorporation.** A) Monolayer quality at 9.75 hours as a function of number of tumor cells at the start. B) Percent incorporation separated by tumor cells of good, medium, and poor quality of HBMEC monolayers. C) Change in HBMEC monolayer quality during the course of incorporation as assessed at time = 0 hours, 4 hours, and 9.75 hours. The monolayer quality is assigned the following values: 3 = good, 2 = medium, 1 = poor, and for each percent Extralink, the monolayer quality for all frames is averaged. Error bars represent standard error of the mean. Statistics carried out using a non-parametric Kruskal-Wallis test with a Dunn's post-hoc analysis with $p<0.05$. (* $p<0.05$). Data is pooled from 3 independent trials.

questions regarding the HBMEC barrier dynamics during tumor cell incorporation. While this dissertation studied the behavior of individual HMBECs, a next step is to dynamically study the tight junction and adherens junction formation and disruption during incorporation.

8.3 More physiologically relevant 3D models of tumor cell-BBB interactions

This dissertation sheds light on crucial components of the metastatic cascade during tumor cell interaction with the BBB both during tumor cell incorporation into HBMEC monolayers and in the tumor cell response to astrocyte secreted factors. Additionally, in Chapter 4, a physiologically relevant extracellular matrix component, HA, is introduced in order to help understand the interaction of tumor cells not only with HBMEC monolayers but also with a more physiologically relevant extracellular matrix. The next will be to scale the system presented in Chapter 4 to a full 3D system that allows for better modeling. In fact, we have already shown that HA/gelatin gels have a physiologically relevant stiffness for the brain microenvironment (Figure 4.1). Furthermore, we have also shown that this gel can be incorporated into a microfluidic device that can be used to model the BBB in a co-culture system and even physiological shear stress can be incorporated (Figure 8.2). Thus, this is a natural next step to further develop the results obtained in Chapter 4.

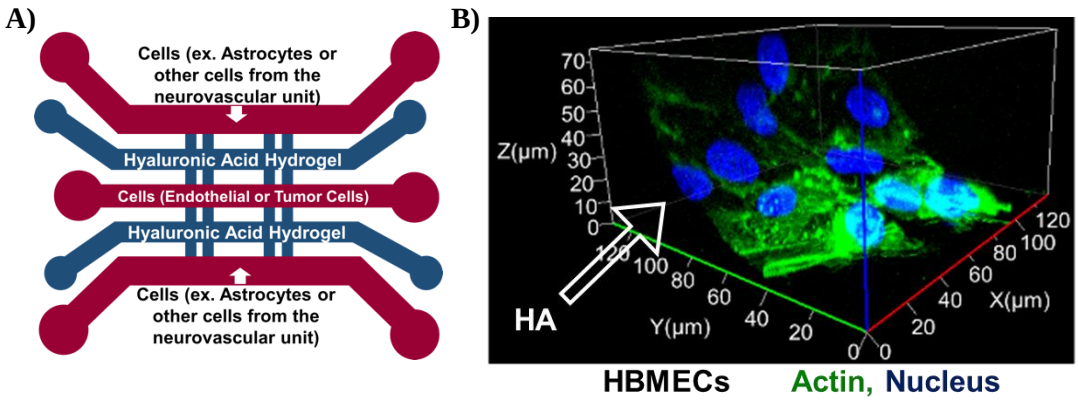

Figure 8.2: **3D microfluidic systems for BBB modeling.** A) Diagram of a microfluidic device providing a starting point for a potential system where multiple cells from the BBB microenvironment can be co-cultured along with tumor cells and their dynamic interaction can be observed in a physiologically relevant HA-based 3D microenvironment. B) Proof of concept image showing an HBMEC monolayer on a vertical HA gel in microfluidic device from A).

8.4 Further examination of the different interactions of the BBB and brain- versus bone-seeking tumor cells

In Chapter 5, this dissertation begins to show some distinct physiological differences between brain and bone-seeking metastatic breast tumor cells. The next important step will be to begin to characterize not only the morphology, but also the traction forces and migration speed of the different tumor cell clones and their migration in confinement. These parameters could shed further light on biophysical differences among the tumor cells as well as well the functional significance of observed morphological changes. Furthermore, morphology combined with other biophysical parameters could allow us to determine the organotropic destination of a tumor cell prior to colonization of a secondary organ. Thus, factors such as migration, response to confinement, and traction force generation should be examined.

Furthermore, ass more differences between the clones are established, one of the factors to consider will be whether the brain- and bone-seeking tumor cells will

have the same response to ACM and other biochemical factors from the BBB and whether their transmigration mechanisms vary. Thus, a potential next step will be to repeat the studies from Chapters 3 and 4 with the metastasis specific tumor cell clones.

Additionally, a novel concept in the field of detached tumor cells has recently been introduced, known as microtentacles (McTNs). McTNs are tubulin-based cytoskeletal projections in suspended tumor cells have been shown to help tumor cells attach to epithelium and thus play a large role in metastasis [248], [249]. McTNs have been introduced relatively recently, and thus a lot remains to be studied in this field. In Chapter 5, we showed that tumor cell clones in suspension vary in area, however it would be fascinating to explore the formation of McTNs in the different tumor cell clones that preferentially metastasize to the brain or bone, in order to determine whether McTNs could play a role in the preferential metastasis.

8.5 Induced pluripotent stem cell (iPSC) derived cells of the neurovascular unit for BBB modeling

Chapter 4 examines a BBB model composed of HBMECs on HA/gelatin films and Chapter 3 looks at biochemical cues from mouse astrocytes. These model systems allowed us to conduct studies on tumor cell response to astrocyte secreted cues and incorporation into monolayers successfully and allowed others to examine HMBEC junction formation. However, a novel method for establishing the cell lines for modeling the BBB have recently been established by Lippmann *et al* [250], [251]. This model proposes deriving all BBB cells from induced iPSCs such that all the cells

are from a common, human source [250], [251]. These models have been highly successful in attaching physiologically relevant barrier properties as measured by transendothelial electrical resistance, permeability, and tight junction staining [250], [251]. Thus, future work would include introducing novel BBB models using iPSCs.

8.6 Further investigation of the feasibility of CAP

This dissertation demonstrated that while CAP treated media has the potential to be a selective cancer therapeutic, it is highly sensitive to experimental conditions and thus further work should examine its feasibility *in vivo.* Some *in vivo* studies on subcutaneous murine tumors have shown selective CAP treatment success [252]. However, that involved using direct CAP treatments of tumors close to a mouse's skin surface, without the need for penetrating deep tissue. In order to achieve treatment of cancer beyond the surface of the skin, it is important to understand how CAP will behave in bodily fluids (both directly and through mixing with CAP treated media). In fact, it has been shown that CAP can coagulate blood for would healing purposes [253]. In addition, it has been shown that CAP can destroy some blood cells, such as leukocytes more readily than monocytes, and respective cell lines are more viable post CAP treatment than the same cell types from a human donor [254], in fact in general lymphocytes showed lower CAP tolerability than monocytes [254], [255]. This suggests that before CAP can be in used to treat tumor cells deep in the body, further optimization has to be carried out not only on the CAP treatments themselves, but also on the tolerability of CAP by different cell types along the way within the blood and surrounding tissue. Furthermore, the work in this dissertation shows that

this has to be done with optimized conditions such that the composition of the fluids involved in the treatment are considered.

8.7 Outlook

The work presented in this dissertation sheds light on crucial processes involved in tumor cell interaction with physico-chemical cues at the BBB. Here, we showed important pathways of interaction between tumor cells and astrocytes as well as elucidated the process of tumor cell incorporation specifically into a BBB-like endothelium on a physiologically relevant extracellular matrix. Additionally, we showed some morphological differences between metastatic tumor cells from the same original cell line, but selected to preferentially metastasize to the brain and bone. These findings show novel biophysical and biochemical factors that could influence brain metastasis, and that in the future could be utilized for the development of appropriate therapeutics. Furthermore, this dissertation touches on the subject of therapeutics by examining the effect of treatment conditions of the effectiveness of CAP as potential therapeutics. To the best of our knowledge, this is the first systematic study examining multiple culture parameters and treatment conditions and will allow for further investigation of the successful utilization of CAP *in vivo*. Together, this dissertation makes advances in the understanding of tumor cell metastasis to the brain as well as a novel therapeutic approach. It opens up doors for further investigation of these pathways, potentially in more physiologically relevant systems, and hopefully will in future inform therapeutic design.

9 Appendices

Appendix A: Shape parameter equations

All shape parameters were calculated in ImageJ.

Area

Increase: Larger cell

Decreases: Smaller cell

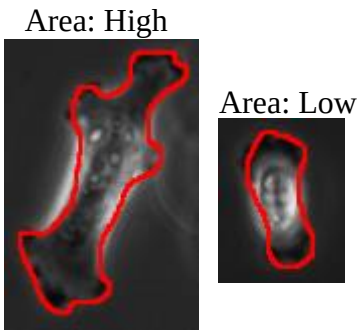

Figure A.1: Area. Area calculation in Image J.

$$\textbf{Aspect Ratio (AR)} = \frac{L_a}{L_b}$$

L_a = major axis length; L_b = minor axis length

Greater than 1: More elongated

Closer to 1: Less elongated

$$\textbf{Inverse Aspect Ratio (Inv. AR)} = \frac{1}{AR} = \frac{L_b}{L_a}$$

Closer to 1: Less elongated

Closer to 0: More elongated

Aspect Ratio ~ 5
Inverse Aspect Ratio ~ 0.2

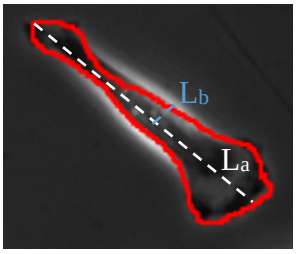

Aspect Ratio ~ 1
Inverse Aspect Ratio ~ 1

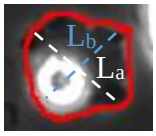

Figure A.2: Aspect ratio. Aspect ratio calculation in Image J.

$$\textbf{Solidity} = \frac{\boldsymbol{A_{cell}}}{\boldsymbol{A_{convex}}}$$

A_{cell} = cell area; A_{convex} = convect hull area

Closer to 1: Fewer protrusions

Closer to 0: More protrusions

Solidity ~ 0.5

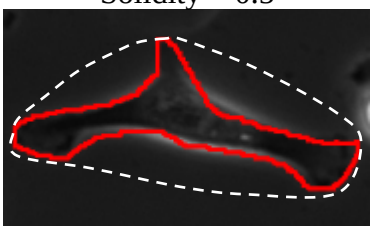

Solidity ~ 1

Figure A.3: Solidity. Solidity calculation in Image J.

$$\textbf{Circularity} = \frac{\boldsymbol{4\pi A}}{\boldsymbol{P}}$$

A: area; P: perimeter

Closer to 1: More circular

Closer to 0: Less circular

Circularity ~ 0.4

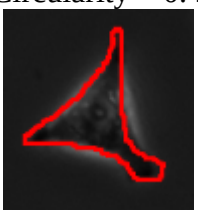

Circularity ~ 1

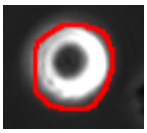

Figure A.4: Circularity. Circularity calculation in Image J.

Appendix B: Migration equations

All calculations were performed in a custom-written Matlab code written by Kimberly M. Stroka and edited by Marina A. Pranda.

Average velocity calculation: [173]

$$v = \frac{\langle d \rangle}{\lambda} \text{ where } \lambda = \text{time step}, \langle d \rangle = \frac{1}{N} \sum_{n=1}^{N} \left| \overrightarrow{d_n} \right| \quad [173]$$

Mean squared displacement calculations (sliding time average): [173]

- Square of x displacement plus square of y displacement
- Averaged over time for each time step λ and for every time step n* λ
- n: ≤ number of total time steps

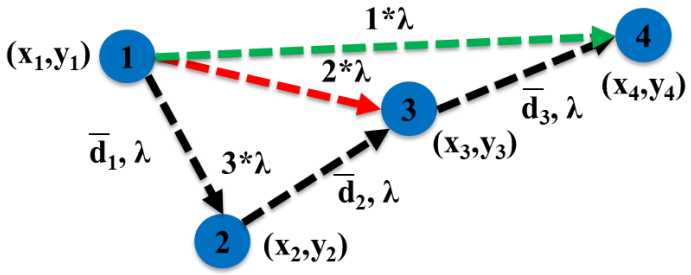

Figure B.1: Migration parameters. (x,y) position of a single cell over 4 time points (3 time steps). Velocity is calculated based on d and λ, mean squared displacement is calculated for every n* λ where n is the number of time steps (n = 1 (green path, positions 1-4), n = 2 (red path, positions 1-3), n = 3 (black path, positions 1-2-3-4).

Non-linear random walk Langevin-like equation (fitted to linear region of mean squared displacement curve): [115], [173], [256]

$$r^2 = 4 D (t - \tau (1 - e^{-\frac{t}{\tau}}) \quad [115], [173], [256]$$

r^2 : two-dimensional mean squared displacement

D : random motility coefficient

t : time

τ : persistence time

Chemotactic index: [108]

$$\text{Chemotactic index} = \frac{Distance_{end-to-end}}{Distance_{total-traveled}}$$

$$= \frac{\sqrt{(x_{end} - x_{start})^2 + (y_{end} - y_{start})^2}}{\sum[(x_{j+1} - x_j)^2 + (y_{j+1} - y_j)^2]}$$

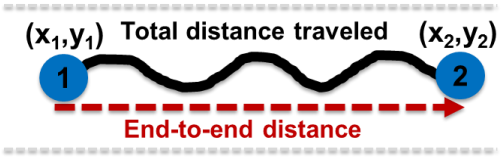

Figure B.2: Chemotactic Index. Chemotactic index calculation illustration for a cell moving from position 1 to position 2.

Appendix C: Effects of confounding variables on the statistical analysis of the migration and morphology of metastatic tumor cells[†]

Appendix C.1 Introduction

Cell migration [72], [257], [258] and morphology [259], [260] are crucial and commonly quantified parameters in studies focusing on cellular physiology and various disease states. For example, in cancer, cell migration speed and their ability to invade tissue, as well as their mesenchymal morphology are key factors in understanding the tumor phenotype, as discussed in Chapter 3 [72]. *In vitro,* there are a variety of different assays that have been developed to study cell migration and morphology, including would healing assays [261], transwell assays [262], microfabricated devices [72], [263], [264], 3D invasion assays in hydrogels [265], as well as 2D chemokinesis assays, as discussed in Chapter 3. These assays provide different types of quantitative and qualitative information; however, it is most common to obtain the information in the form of microscopy images which then have to be further analyzed to quantify cell migration and morphology (Table C.1). Different laboratories and different studies utilize varying methods of cell migration and morphology quantification from image-based data (Table C.1). While some laboratories utilize automated software such as MetaMorph (Table C.1), many labs rely on manual tracking and tracing or tracking plugins in ImageJ (Table C.1). Furthermore, the parameters quantified, data presentation, cell number, and time steps

† This chapter is modified from manuscript in preparation for publication as M.A Pranda*, G.M. Dawson*, T.S. Ornstein, B.J. Murugesan, K.M. Stroka, "Effects of confounding variables on the statistical analysis of the migration and morphology of metastatic tumor cells." All data analyzed by G.M.D with help from T.S.O and B.J.M.

for migration tracking vary from study to study and there are no clear guidelines on the appropriateness of various parameters for a given analysis (Table C.1). However, some aspects also remain consistent, such as the prevalence of speed, velocity, and area quantification, the presentation of data in bar graphs, and the prevalence of pooled data (Table C.1). Here, we explore whether some of the unaddressed variables, or confounding variables, in cell migration and morphology quantification can play a role in the outcome of a study.

Confounding variables, in general, are factors within a study that could be affecting a seemingly cause and effect relationship [266], [267]. Confounding is sometimes referred to as the "mixing effect," referring to the fact that it leads to experimental parameters mixing with additional factors, thereby potentially changing the relationship [267]. For cell migration and morphology analysis, some confounding variables are experimental and can be accounted for by setting up highly controlled studies with well-defined and characterized cell lines, and keeping cell health and passage consistent as well as accounting for any experimental conditions in cell culture and imaging (Figure C.1 A). These parameters are typically reported in the "methods" section of most scholarly papers and it is generally accepted that they have to be controlled for. However, that leaves confounding variables that could be present during image analysis not addressed (Figure C.1 A). One prior study has addressed some confounding in the quantification of cell persistence and presented a computational model for cell persistence quantification that minimizes the effect of confounding [268]. Here, we focus on the effect that the zoom level of an image, the experience level of the person handling the image, and the data sampling has on the

results of migration and morphology analysis of single cells (Figure C.1 B). Furthermore, we investigated how the time interval and type of tracking of cell migration affected the results (Figure C.1 B).

We hypothesize that the consistency of analysis parameters can play an important role in the outcomes of an experimental study, and that inconsistent usage of various parameters can skew the results of a data set. We have found that the zoom level of an image can have a significant effect on the outcome of morphology analysis

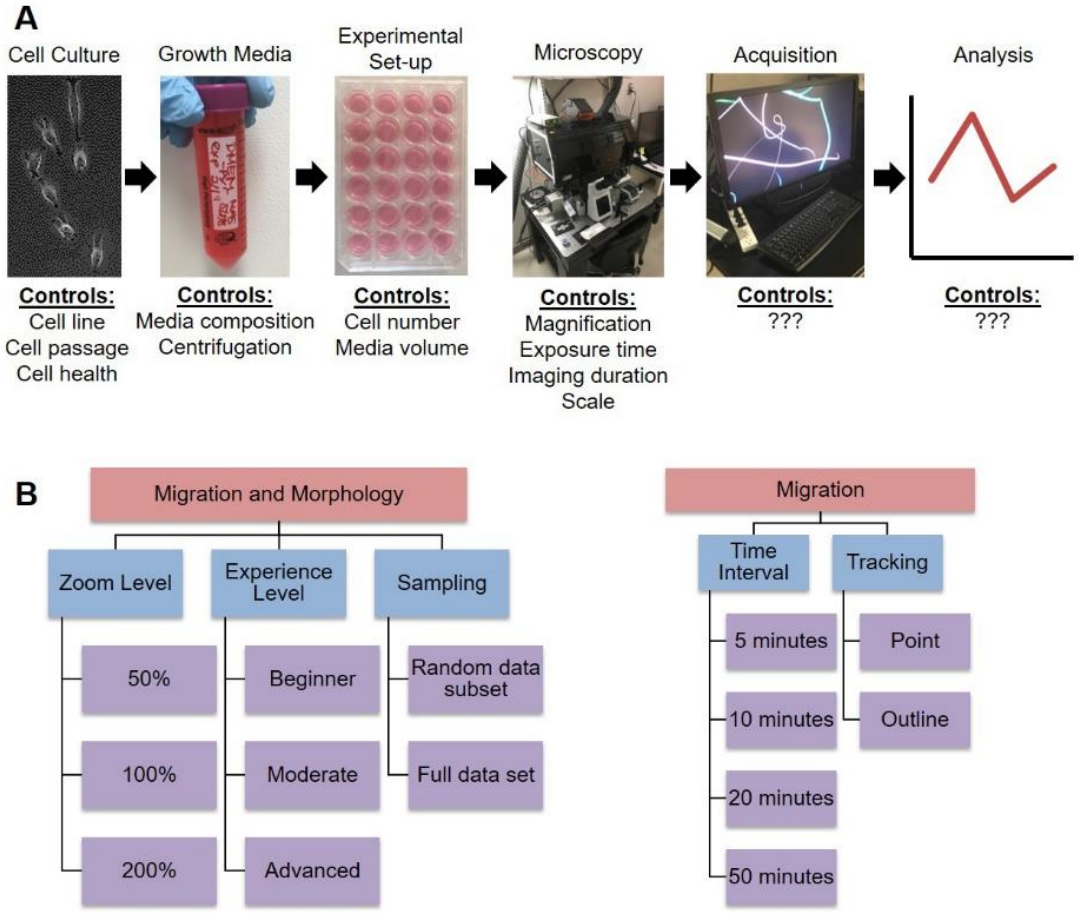

Figure C.1 Schematic of typical data collection and processing. A) Typical workflow in analysis of cell migration and morphology, starting with selection of cells and ending with data analysis and generation of figures. B) Flow charts of manipulations to cell migration and morphology image post-processing methods for data quantification analyzed within this paper. Figure generated by Gregory Dawson.

Table C.1: Literature review of papers with cell migration and morphology quantification. Thea Ornstein assisted with literature review.

Ref.	Method	Parameters		Format	# Cells (N: # trials, n: # cells)	Pool	Δ Time (s, m, h)
[269]	Velocity: not listed. Adhesions: Speckle TrackerJ ImageJ plugin	Cell velocity, % of adhesions, adhesion movement, adhesion lifetime	3D/2D	Velocity: image sequences, box plots, bar graphs. Adhesions: bar & line graphs, scatter plots	Adhesions: >500, ≥6 cells/ condition Migration: N=3, n=48-≥80	Yes	No infor-mation given
[270]	Nuclei tracked using Meta-Morph software	Relative velocity (normalized to control), velocity	2D	bar graphs	30-40 cells/ experiment N=3,4	Yes	5 m for 12–24 h
[271]	Nuclei tracked using Track Point, Meta-Morph. Counted cells in transwell	Velocity, directionality, persistence, lamellae length	2D/3D	bar graphs or migration tracks	N=2-4, n=42-45, 933, 32-34.	Yes	10 or 15 m
[272]	Speed: quantified by computer-assisted cell tracking (Autozell 1.0 software)	Speed, nuclear diameter, % maximum area, elongation, nuclear cross section	3D	Migration: box plots, time-lapse images, line graphs. Morphology: dot plot, bar graphs, line graphs	Morphology: n=21 N=2-3. Migration: n=50-180, N=3-6	Yes	12 m (TCs), 30 s (leuko-cytes) for 19-24 h.
[273]	Morphology: Image J software	Circularity, aspect ratio	3D	bar graphs and heat map	n≥60, N=3	Yes	30 m over 72 h period
[265]	Morphology: OrientationJ, ImageJ plugin to quantify actin organization. Migration: Image J to track the cells centroid over time	Motile fraction, speed (motile: centroid moved>one cell diameter), aspect ratio, fraction of pixels (actin)	3D	bar graphs (motile fraction), box plots (speed), time lapse images, line graph (aspect ratio)	Migration: N=2-3, n > 40. Aspect ratio: n>35	Yes	5 m for 16 h

Ref.	Method	Parameters		Format	# Cells (N: # trials, n: # cells)	Pool	Δ Time (s, m, h)
[274]	2D: either on tissue plastic or wound healing assay. 3D: collagen microtracks	Displacement, distance, step-wise speed, directionality, time to polari-zation & elon-gation, wound closure, area	2D/3D	Bar graphs, migration tracks, pictures of wound healing assays, box-plots, line graphs	40-100 cells	Yes	20 m for 24 h. Wound healing: 1 h for 20 h
[275]	3D collagen I cultures: Displacements and velocities	Displacement, velocity, aspect ratio, persistence	3D	Box plots	Migration: n=17,16; morpholo-gy:n=27,33	Yes	10 m over 12 h
[276]	Durotaxis or chemotaxis. Durotaxis quantified by nucleus tracking with MetaMorph	Velocity, directional persistence	2D	box plots, rose diagrams	n > 7	Yes	Random migration: 5 m for 12 h. Others, vary.
[277]	ImageJ Manual tracking plugin & Chemotaxis tool plugin	Speed, forward migration index	2D/3D	box plots, videos	N > 4 n>200	Yes	5 m for 14 h but vary for some.
[278]	MetaMorph software for imaging, ImageJ for tracking. Transwells were used for chemotaxis.	Velocity, % of control; accumulated distance, % control; chemotaxis, % of control	2D	representative images and bar graphs	N=3, n=60 cells	Yes	1 m for 1 h

Ref.	Method	Parameters		Format	# Cells (N: # trials, n: # cells)	Pool	Δ Time (s, m, h)
[279]	Wound healing: custom Meta-Morph journals, random migration & morphology: ImageJ	Relative velocity, relative wound area, area, circularity	2D	Representative images/videos, bar graphs, line graphs, cell tracks, table of results	Migration: n=25 cells randomly selected from n=70-99 cells, N=3. Area: n=50-100 cells, N=3	Yes	Wound healing: 30 m for 16 h. Random migra-tion:10 m for 14 h
[280]	Migration: centroid of GFP-positive cells tracked with ImageJ. Area: ImageJ	Average directional migration, area	2D	bar graphs, representative images	N≥3	Yes	30 m for 4 h

while the time interval used can significantly affect the outcome of a migration study. Additionally, we have found differences in experimental conclusions based on the type of migration tracking used and variation in migration and morphology when the analysis is conducted by researchers with different experience levels. Overall, we conclude that seemingly minor confounding variables can play a significant role in the conclusions drawn from a study and thus need to be carefully controlled.

Appendix C.2 Materials and Methods

Appendix C.2.1 Cell Culture

MDA-MB-231 (metastatic human breast adenocarcinoma) cells (American Type Culture Collection, Manassas, VA, USA) were cultured in Dulbecco's Modified Eagle's Medium (DMEM) containing high glucose and L-glutamine (ThermoFisher Scientific, Waltham, MA, USA) as previously described in Chapters 3, 4, and 5. The DMEM was supplemented with 1% 10,000 U/ml Penicillin/Streptomycin (Pen/Strep) (ThermoFisher Scientific) and 10% Fetal Bovine Serum (FBS) (ThermoFisher

Scientific). To passage, Phosphate-Buffered Saline (PBS) (VWR, Radnor, PA, USA) was used to wash cells and 0.25% Trypsin-EDTA (ThermoFisher Scientific) was used to detach cells. A climate-controlled incubator at 37°C, with 5% CO_2:95% air and 50% humidity was used to grow up the cells, as previously described in Chapters 3, 4, and 5.

Appendix C.2.2 Preparation of Collagen Substrates

24-well glass bottom plates with 13 mm diameter glass (MatTek, Ashland, MA, USA) were coated with 300 μL of 0.1, 1, 10, 20, and 100 μg/ml type I collagen from rat tail (Sigma Aldrich, St. Louis, MO, USA) dissolved in PBS, for 1 hour at 37°C. 4 wells of each condition were plated. The wells were then washed three times with 1 mL of PBS at 37°C. 1 x 10^4 MDA-MB-231 cells were seeded in each well and left to incubate overnight. On the next day, the media was changed and timelapse imaging was set-up. The procedure was similar to that in Chapter 3, expect with varying concentrations.

Appendix C.2.3 Microscopy

Cells were imaged live, using a 10x phase-contrast objective, overnight with a 5 minute time step using an IX83 microscope (Olympus, Center Valley, PA, USA). Multiple positions were imaged at the same time with a resulting four wells with two positions per each experimental condition. At the end of the time-lapse imaging, the objective was switched to 20x and corresponding stationary images were taking for morphology analysis. The Olympus cellSens Software (Olympus) was used to capture the images. An enclosed chamber surrounding the microscope was maintained at 37°C, 50% humidity, and 5% CO_2:95% air. This procedure was similar to that carried

out in Chapter 3. For image presentation, intensities were adjusted arbitrarily for best visualization, since they were not quantified.

Appendix C.2.4 Data Analysis

Initial data analysis was carried out using ImageJ (https://imagej.nih.gov/ij/). For morphology analysis, cells were manually traced in ImageJ and their area, aspect ratio, circularity, and solidity were calculated as previously described, as previously described in Chapter 3. To calculate cell speed, centroid tracking was carried out using the ImageJ Manual Tracking plug-in, where the centroid of each cell was manually selected across all frames. When outline tracking was used, each cell was manually traced in ImageJ across all frames. The x and y positions of the cell were analyzed by a custom Matlab (MathWorks, Natick, MA, USA), cell speed was calculated, and trajectory plots were generated. Migration tracking was done by tracking cells every 5 minutes for 100 frames. In order to vary the time interval, the Matlab code was simply adjusted to read in only the position values corresponding to the desired time interval: 5, 10, 20, and 50 minutes. Zoom levels were adjusted to 50, 100, and 200% directly in ImageJ during analysis. In order to generate random cell subsets for speed comparison, the Excel (Microsoft, Redmont, WA, USA) "rand" function was used and then sorting of the data with the adjacent data column in ascending order was carried out. Finally, simply the top 10 cells (for speed) and 10, 25, or 50 cells for morphology from the randomly ordered list were selected. In order to obtain the mean square displacement and the diffusion coefficient for a random sample, the "randbetween" function was used to randomly select 10 cells between 1 and the last cells for that experimental group (between 28 and 42 depending upon the

group). The selected data was analyzed by the same Matlab code as the full dataset. This difference in random selection is necessary because the diffusion coefficient and mean square displacement are values calculated for an entire data set, not a single cell. The process was repeated three times to obtain three separate data sets. When comparing different experience levels, three students in the lab were selected who either had never performed cell migration and morphology analysis (beginner), have done it a few times but not frequently (moderate), and a student with vast experience in migration and morphology analysis (advanced).

Appendix C.2.5 Data Analysis

GraphPad Prism 8 (GraphPad, La Jolla, CA, USA) was used to prepare graphs and perform statistical analysis. The non-parametric Kruskal-Wallis ANOVA test with a Dunn's multiple comparison post-hoc test was used for statistical analysis where significance is indicated with stars. Statistical significance was calculated as follows: NS $P > 0.05$, * $P \leq 0.05$, ** $P \leq 0.01$, *** $P \leq 0.001$, **** $P \leq 0.0001$. All errors bars represent standard error of the mean.

Appendix C.3 Results

Appendix C.3.1 Zoom level affects morphological parameters acquired through manual cell tracing

When analyzing visual data using ImageJ or other analysis software, one parameter that is often not controlled for is the zoom level of the images. The default zoom level of an open image can depend on the computer and screen type used, the software version, or even the operating system. Furthermore, different people have different levels of comfort with smaller versus larger objects to analyze and

frequently adjust the zoom based on what is most individually comfortable at any given time. Thus, we examined whether equivalent analysis can yield different results based on zoom levels of the images, with 50%, 100%, and 200% zoom (Figure C.2 A). In fact, we found that morphology parameters such as area, inverse aspect ratio (IAR), circularity, and solidity were different in some of the measurements with changes in zoom level (Figure C.2 B, C, D, E). However, the question remained whether our conclusions about data from several categories would vary depending on the zoom level at which it was analyzed. To test that, we compared the areas of cells grown on 0.1, 1, 10, 20, and 100 μg/ml collagen-1 (Figure C.2 C, D). We found that at 50% zoom, areas of cells grown on 0.1 and 1 μg/ml collagen-1 were significantly different from those grown on 100 μg/ml collagen-1. However, at 100% zoom, only 0.1 and 100 μg/ml collagen-1 conditions were different, and finally at 200% zoom, there were no significant differences (Figure C.2 C, D). Thus, depending on which zoom level was used to for analysis, the conclusions about the data could be quite different. If the zoom levels were mixed and matched during analysis, it would have likely further skewed the data. Interestingly, within each collagen-1 concentration, there were no significant differences among any of the zoom levels (Figure C.2 D). When we compared IAR, circularity, and solidity at different zoom levels, we determined that in while there are no differences between IAR at different zoom levels, circularity and solidity were in fact different between each zoom level (Figure C.2 E). In general, circularity and solidity both decreased with increasing zoom (Figure C.2 E). The differences observed in morphology are potentially caused by the fact that at a higher zoom, cell protrusions are traced more accurately thus resulting in

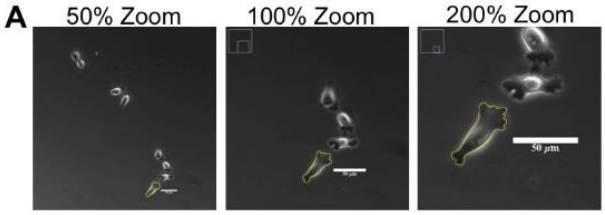

B

Morphology parameters from panel A

	Area (µm²)	IAR	Circularity	Solidity
50%	967.90	0.395	0.543	0.83
100%	758.64	0.330	0.372	0.7
200%	748.46	0.331	0.371	0.678

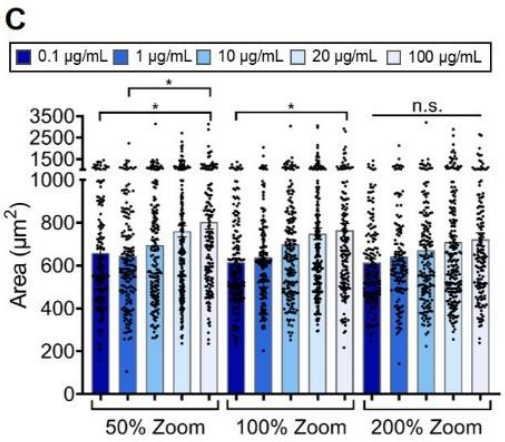

D

Zoom (%)	[Collagen](µg/ml) 0.1	1	10	20	100
50 vs. 100	n.s.	n.s.	n.s.	n.s.	n.s.
50 vs. 200	n.s.	n.s.	n.s.	n.s.	n.s.
100 vs. 200	n.s.	n.s.	n.s.	n.s.	n.s.

[Collagen] (µg/ml)	Zoom (%) 50	100	200
0.1 vs. 1	n.s.	n.s.	n.s.
0.1 vs. 10	n.s.	n.s.	n.s.
0.1 vs. 20	n.s.	n.s.	n.s.
0.1 vs. 100	*	*	n.s.
1 vs. 10	n.s.	n.s.	n.s.
1 vs. 20	n.s.	n.s.	n.s.
1 vs. 100	*	n.s.	n.s.
10 vs. 20	n.s.	n.s.	n.s.
10 vs. 100	n.s.	n.s.	n.s.
20 vs. 100	n.s.	n.s.	n.s.

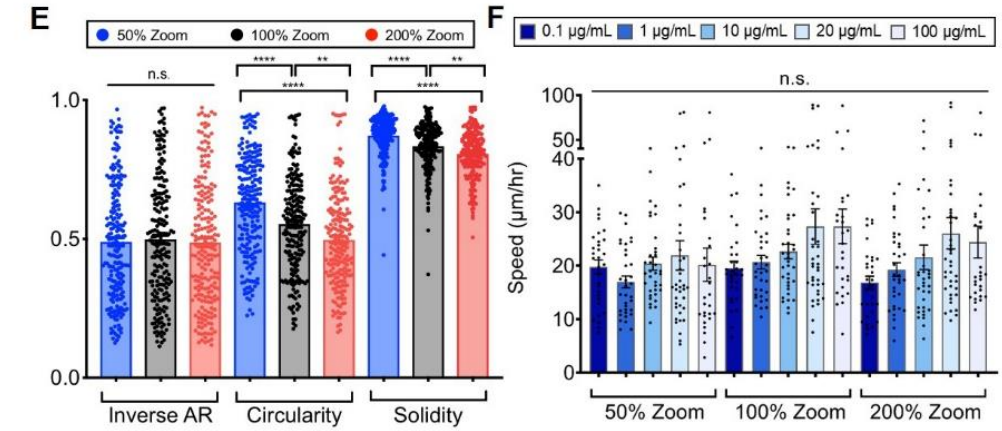

Figure C.2: Analysis of the effect of zoom level on migration and morphology.
(A) Representative images of a typical cell in wells coated with 20 µg/mL collagen-I at 50%, 100% and 200% zoom in ImageJ. Scale bars = 50 µm. (B) Table of individual cell characteristics at different zoom levels from part A. IAR = Inverse Aspect Ratio. (C) Areas of cells on different concentrations of collagen at different zoom levels. Significances are only indicated within each zoom level group, additional statistical significance presented in part D. (D) Charts of significance for experimentally relevant cell area categories at different zoom levels. (E) Morphological characteristics, inverse aspect ratio (AR), circularity, and solidity of cells on 20 µg/mL collagen-I at different zoom levels. (F) Speed of cells on five different concentrations of collagen-I at different zoom levels. Statistical significance was determined by a Kruskal-Wallis nonparametric test with a post-hoc Dunn's multiple comparison test (n.s., $P > 0.05$; *, $P \leq 0.05$; **, $P \leq 0.01$; ***, $P \leq 0.001$; ****, $P \leq 0.0001$). All error bars indicate standard error indicate standard error of the mean and each dot represents an individual cell. Data analyzed by Gregory Dawson.

smaller and more elongated cell measurements. A similar study was repeated by observing cells speeds on 0.1, 1, 10, 20, and 100 μg/ml collagen-1 and there were no significant differences between speeds on any zoom level or between any zoom levels at any given collagen-1 concentration (Figure C.2 F). This could be explained by the fact that speed was measured via centroid tracking and thus it appears that the centroid can be similarly estimated at all zoom levels.

Appendix C.3.2 Random subsets of morphological data can produce altered statistical relationships in data

There are several philosophies on how to select data sets for publication. One philosophy is to pool all the available analyzed cells from all trials together (Table C.1), and report the data for the pooled set. Another philosophy is to conduct multiple trials, test them for consistency, and then report the data for one representative trial. There is also a frequent debate over how many cells need to be analyzed to allow for both a realistic experiment and robust data. Here, we seek to show how the size of a data set randomly selected from a set of pooled data affects the conclusions one would make based on the data set. For this, cell morphology and migration on 0.1, 1, 10, 20, and 100 μg/ml collagen-1 was assessed. For morphology, the full data set contained >152 cells, and the randomly selected subsets contained 50, 25, and 10 cells. Within each set, there were no differences in inverse aspect ratio (Figure C.3 A), circularity (Figure C.3 B), and solidity (Figure C.3 C) between the collagen concentrations or sample sizes, thus showing a consistent trend between all data sets. However, when it came to area, there was a significant difference between the 0.1 and 100 g/ml collagen-1 conditions for the full data set, and not for any of the subsets

(Figure C.3 D). Furthermore, we generated three different randomly selected data sets with 25 cells each and evaluated the inverse aspect ratio across the different collagen-1 concentrations (Figure C.3 E). We found that there were no significant differences between any collagen concentrations or zoom levels among any of the subsets (Figure C.3 E). This suggests that a large enough randomly selected sample could lead to the same conclusions as a different, equally sized data set. When cell speed was observed, the full data set contained >27 cells and a 10 cell random subset was generated. There were no significant differences among the different collagen-1 concentrations or sample sizes in either group (Figure C.3 F). However, when we visually observed the cell trajectories with three different subsets with 10 cells each as well as a full set of 38 cells, one can see that the trajectories are very different, suggesting that the cells chosen do affect the trends observed for a given experiment (Figure C.3 G).

Appendix C.3.3 Time interval affects magnitude of cell migration speed

Time interval during migration tracking is another parameter that is typically chosen arbitrarily. Here, we compared the outcome of migration studies where the same data was analyzed with a 5, 10, 20, and 50 minute time interval. We observed

---

Figure C.3: The effect of sample size on measured migration and morphology. Comparison of (A) inverse aspect ratio (B) circularity, (C) solidity, and (D) area of cells under five different experimental conditions (collagen-I concentrations: 0.1, 1, 10, 20 and 100 μg/) and four different sample sizes (>152, 50, 25, 10 cells). (E) Comparison of inverse aspect ratio of three different randomly generated subsets of data. Sample size of n = 25. (F) Comparison of cell speed with different sample sizes (n > 27, n = 10). A Kruskal-Wallis test with a Dunn's post-hoc multiple comparison test was used to determine statistical significance (n.s., $P > 0.05$; *, $P \leq 0.05$). (G) Trajectory plots of cells on 20 μg/mL collagen-I, showing three different randomly selected subsets of cells along with the original full sample (n = 10 for each data set). All error bars indicate standard error indicate standard error of the mean and each dot represents an individual cell. Only experimentally relevant statistical differences are discussed in-text. Data analyzed by Gregory Dawson.

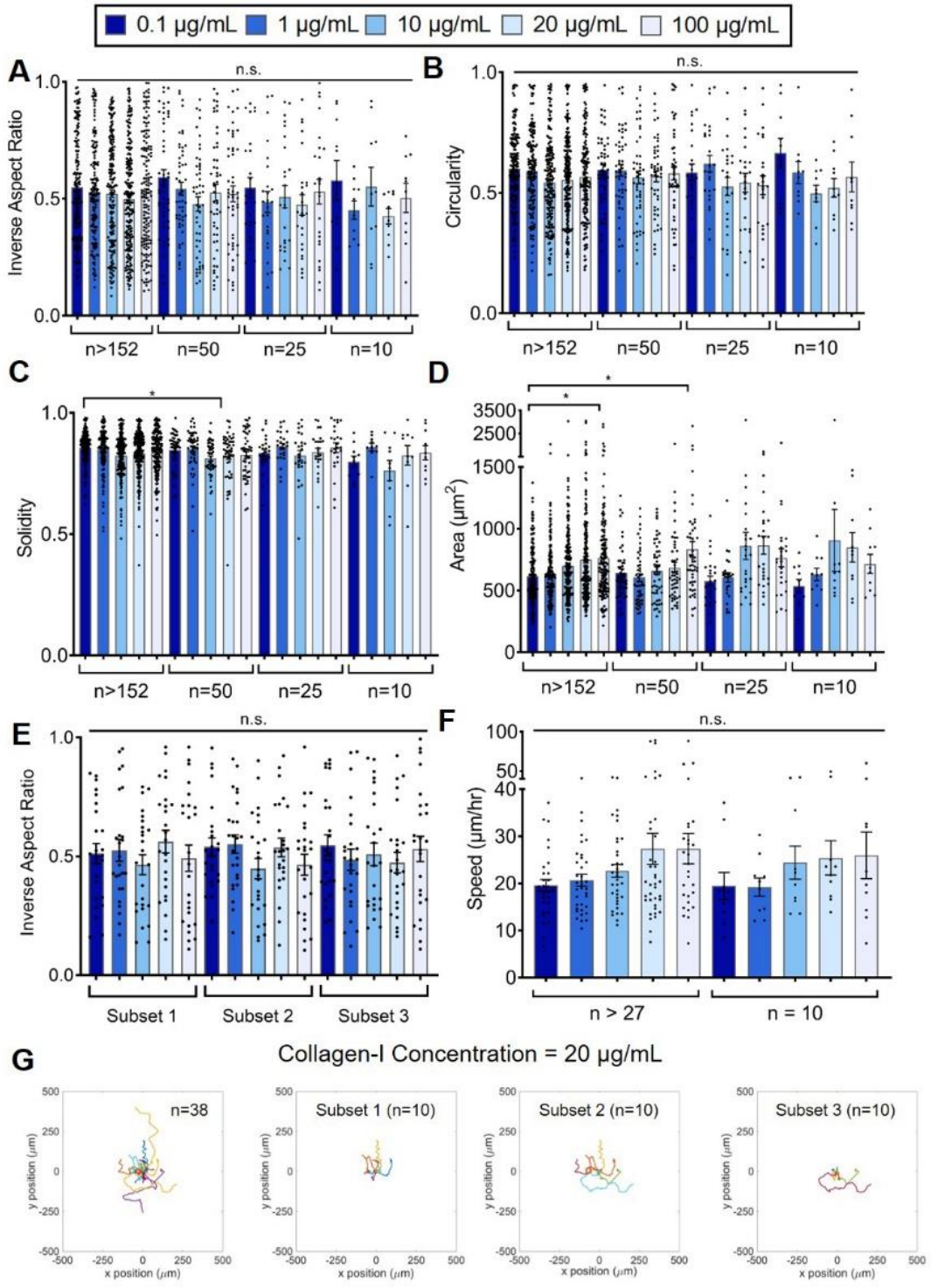
0.1 µg/mL
1 µg/mL
10 µg/mL
20 µg/mL
100 µg/mL
A
Inverse Aspect Ratio
n.s.
n>152
n=50
n=25
n=10
B
Circularity
C
Solidity
D
Area (µm²)
E
Subset 1
Subset 2
Subset 3
F
Speed (µm/hr)
n > 27
n = 10
G
Collagen-I Concentration = 20 µg/mL
n=38
Subset 1 (n=10)
Subset 2 (n=10)
Subset 3 (n=10)
x position (µm)
y position (µm)

that the cell tracks changed slightly with a change in time step (Figure C.4 A). While the general trends remained the same with each time interval, the larger time steps lost some detail and definition in the migration trajectories (Figure C.4 B). The time interval change did not alter the trend between cells speeds on different collagen-1 concentrations, however overall all speed values decreased with increasing time interval (Figure C.4 C). We found that altering the time interval, especially from 5 to 50 minutes and 10 to 50 minutes actually resulted in significant differences in cell speed at the same collagen-1 concentrations (Figure C.4 D). However, we found that changing the time interval did not change the conclusions made about cell speeds on varying collagen-1 concentrations (Figure C.4 D). Together, these results suggest that the time step has a minor effect on the outcome of a migration study.

Appendix C.3.4 Tracking method (point vs. outline) does not affect migration speed

There are several different methods for tracking cell migration. Here, we will examine two common ways, namely the point tracking, where the x and y positions of the centroid of the cell over time are manually selected and recorded, and outline tracking, where each cell is traced manually at each time point and the centroid's x and y positions are calculated in ImageJ, we compared the two analysis techniques to see if they provide different results. Intuitively it seems that outline tracking should provide more accurate data given that it calculates a more precise centroid (Figure C.5 A), and in fact there is a significant difference in the speeds on 20 μg/ml collagen-I between point and outline tracking (Figure C.5 B). However, such a trend is not observed in the speeds on 100 μg/ml collagen-I, despite there being still an

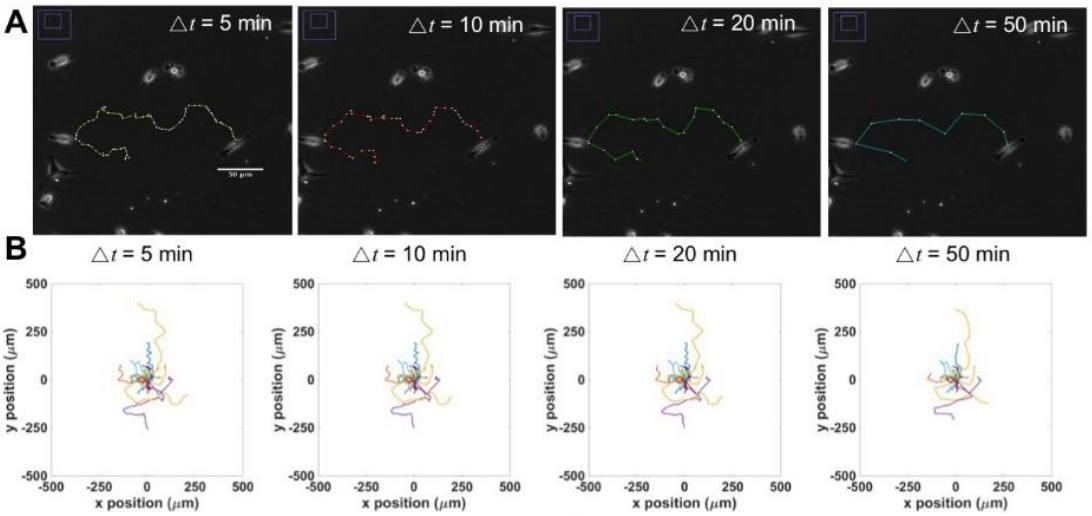

D

Interval (min)	[Collagen] (μg/ml) 0.1	1	10	20	100
5 vs. 10	n.s.	n.s.	n.s.	n.s.	n.s.
5 vs. 20	n.s.	n.s.	n.s.	n.s.	n.s.
5 vs. 50	****	****	****	**	**
10 vs. 20	n.s.	n.s.	n.s.	n.s.	n.s.
10 vs. 50	**	**	***	*	n.s.
20 vs. 50	n.s.	n.s.	n.s.	n.s.	n.s.

[Collagen] (μg/ml)	Interval (min) 5	10	20	50
0.1 vs. 1	n.s.	n.s.	n.s.	n.s.
0.1 vs. 10	n.s.	n.s.	n.s.	n.s.
0.1 vs. 20	n.s.	n.s.	n.s.	n.s.
0.1 vs. 100	n.s.	n.s.	n.s.	n.s.
1 vs. 10	n.s.	n.s.	n.s.	n.s.
1 vs. 20	n.s.	n.s.	n.s.	n.s.
1 vs. 100	n.s.	n.s.	n.s.	n.s.
10 vs. 20	n.s.	n.s.	n.s.	n.s.
10 vs. 100	n.s.	n.s.	n.s.	n.s.
20 vs. 100	n.s.	n.s.	n.s.	n.s.

Figure C.4: The effect of changing time interval on cell migration. (A) Representative tracking path of cells at different time intervals, △t indicates amount of time between each point analyzed. (B) Trajectory plots of cells on 20 μg/mL collagen-I using different time intervals (△t = 5, 10, 20, 50 minutes). (C) Change in apparent cell speeds as a result of changing time interval during speed analysis. Error bars indicate standard error of the mean. (D) Charts of significance for experimentally relevant cell speed categories at different time intervals. A Kruskal-Wallis test with a Dunn's post-hoc multiple comparison test was used to determine statistical significance (n.s., $P > 0.05$; *, $P \leq 0.05$; **, $P \leq 0.01$; ***, $P \leq 0.001$; ****, $P \leq 0.0001$). Data analyzed by Gregory Dawson.

insignificant increase (Figure C.5 B). However, there was no difference in speeds between the two collagen-1 concentrations analyzed with the two different tracking methods (Figure C.5 B). When compared to each other directly for each cell, outline and point tracking speeds on 20 μg/mL collagen-I deviated slightly from each other, with a line of best fit with a slope of 0.7322 (Figure C.5 C). This is consistent with the differences in speed seen prior (Figure C.5 B). The different tracking methods also yielded different trends in mean squared displacement, where for point tracking there was a different between mean squared displacement of cells on 20 vs 100 μg/ml collagen-1, yet that difference was mostly absent with outline tracking (Figure C.5 D). Furthermore, while during point tracking the diffusion coefficient decreased with increased collagen-1 concentration, during outline tracking it increased, showing an opposite trend (Figure C.5 D). Thus, point versus outline tracking can affect the outcome of a migration study and potentially change the conclusions made for some of the parameters.

Appendix C.3.5 Experience level of data analyst affects migration results

We were also interested in determining whether the experience level of the person conducting cell migration and morphology analysis can skew the results of the data. When we compared cell speed on 0.1 and 1 μg/ml collagen-1, we found a significant difference between the beginner and moderate experience analysis on 0.1 μg/ml collagen-1 and a significant difference between the beginner and moderate and advanced level analysis on 1 μg/ml collagen-1 (Figure C.6 A). However, there were minimal differences in mean squared displacement, other than a deviation of the beginner level analysis from the rest after approximately 280 minutes (Figure C.6 B).

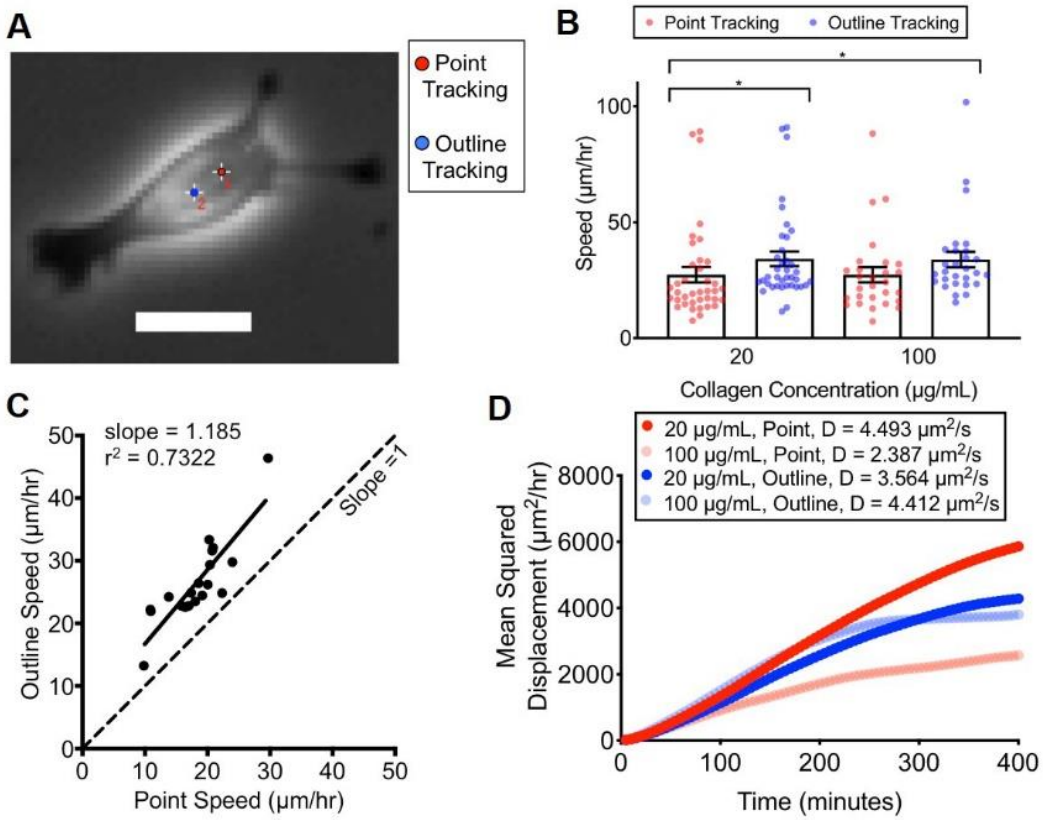

Figure C.5: Centroid vs. Outline tracking of cell speed. (A) Representative image of a cell showing the discrepancy in cell centroid as determined by point tracking (crosshair labeled "1") and centroid as determined by outline tracing (crosshair labeled "2"). Scale bar = 10 μm. (B) Cell speed based on point vs. outline tracking on 20 and 100 μg/mL collagen-I. A Kruskal-Wallis test with a Dunn's post-hoc multiple comparison test was used to determine statistical significance (n.s., $P > 0.05$; *, $P \leq 0.05$). All error bars indicate standard error of the mean and each dot represents an individual cell. (C) Comparison of point tracked speed versus outline tracked speed of cells on 20 μg/mL collagen-I (n = 19). (D) Mean squared displacement of cells on 20 and 100 μg/mL collagen-I based on point vs. outline tracking. "D" represents diffusion coefficient. Only experimentally relevant statistical differences are discussed in-text. Data analyzed by Gregory Dawson.

When the trajectories of cell migration at each experience level were observed, it was evident that there were some differences between all three groups, but especially between beginner and advanced levels, for both 0.1 and 1 μg/ml collagen-1 (Figure C.6 C). Furthermore, when cell speed was observed at different time intervals of tracking for beginner and expert analysis, it was seen that the larger the interval, the more similar the results are between the two levels of analysis (Figure C.6 D), suggesting that increasing the time step could potentially reduce some error of a beginner tracker. The number of cells traced between beginner, moderate, and expert analysis also varied, with beginner tracking resulting in the smallest number of cells tracked (Figure C.6 E). However, there are actually no significant differences in area with different experience levels on 20 μg/ml collagen-1 and only a difference between the beginner and moderate analysis on 100 μg/ml collagen-1 (Figure C.6 F). On 20 μg/ml collagen-1, the inverse aspect ratio did not change at all with experience level, however, circularity significantly increased between the beginner and moderate levels, and solidity changed significantly between beginner and moderate and advanced levels (Figure C.6 G). These results suggest that differences in experience level can affect both migration and morphology outcomes of a study.

Appendix C.4 Discussion

Cell morphology and migration are frequently used as quantitative research metrics and many different assays and techniques exist to quantify them [281]. Among those assays one of the assays that is able to provide the greatest amount of information and is most flexible for different assays is timelapse-based migration imaging [281]. However, imaging requires a substantial amount of post-processing in

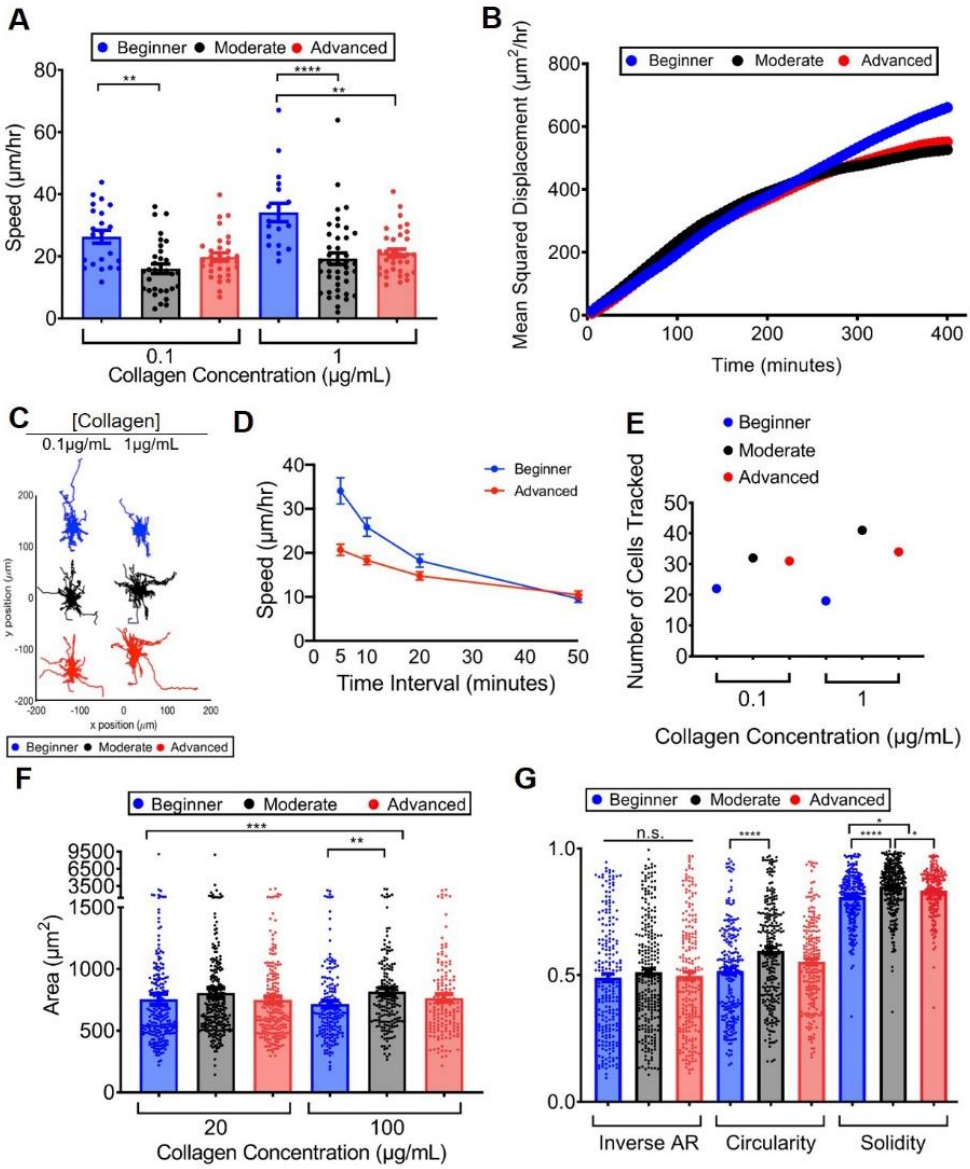

Figure C.6: The effect of experience level on cell migration and morphology. (A) Comparison of speeds as tracked by analysts of different experience levels. (B) Comparison of mean squared displacements as tracked by analysts of different experience levels. (C) Trajectory plots of cell migration as tracked by analysts of different experience levels on 0.1 and 1 µg/mL collagen-1 concentrations. (D) Comparison of cell speed on 1 µg/mL as tracked by beginner and expert level analysts. (E) Comparison of number of cells tracked by analysts of different experience levels. (F) Cell areas as traced by analysts of different experience levels. (G) Morphological characteristics (inverse aspect ratio, circularity, solidity) of cells on 20 µg/mL collagen-1 as tracked by analysts of different experience levels. For panels, A, F, and G, Kruskal-Wallis test with a Dunn's post-hoc multiple comparison test was used to determine statistical significance (n.s, $P > 0.05$; *, $P \leq 0.05$; **, $P \leq 0.01$; ***, $P \leq 0.001$; ****, $P \leq 0.0001$) and each dot represents an individual cell. For all panels, error bars represent standard error of the mean. Only experimentally relevant statistical differences are discussed in-text. Data analyzed by Gregory Dawson.

order to obtain quantitative values for migration and morphology parameters. Multiple studies have reviewed the different available options for cell tracking for primarily migration but in some cases also morphology [282]–[284]. In general, while there is a significant push for the automation of cell tracking due to its time and labor intensiveness, it remains a challenge to carry out automatic cell tracking for phase-contrast images and non-fluorescently stained cells. Thus, manual tracking in open source software such as ImageJ remains the most practical option for many labs. However, both automatic and manual tracking and tracing of cells leaves various confounding variables not controlled for, leaving studies open to potential inconsistencies.

Here, we explored the variation that is introduced into analysis of migration and morphology images tracked manually when zoom levels, cell numbers, time steps, the type of tracking, and the experience level of the person analyzing the data are not held consistent. We have found that changing the zoom level of images being analyzed can lead to different conclusions about morphology data, however the migration results remain minimally affected (Figure C.2). This is potentially because zooming in closer to a cell allows for a more accurate morphology analysis with the inclusion of more protrusions. We have also learned that the number of cells being analyzed ($\geq$ 10 cells) and the subset of a given larger data set, have a minimal impact on morphology and migration of results and conclusions, however they do change the appearance of cell trajectories (Figure C.3). This suggests that above a certain cell number threshold, if the cell population is not highly skewed, the sample size does not to be as large. Furthermore, we have found that altering the time step during

migration analysis does not change the conclusions made about the data, however there are significant differences in absolute speeds between different step sizes (Figure C.4). This could be a result of the fact that increasing the time between recorded positions does skew the general path of the cells, but as long as the same time step is being compared, the changes become normalized for all cells. Additionally, when the same cells are tracked for migration using point and outline tracking, there was a significant difference for one of the collagen concentrations, but not the other suggesting while the conclusions about the data might not change between the analysis types, the exact values do change (Figure C.5). Outline and point tracking do lead to different outcomes for mean squared displacement and diffusion coefficients (Figure C.5). Outline tracking generally estimates the centroid more accurately and thus cell morphology can actually play a role in how the two tracking methods compare (depending on how easy it is to estimate a centroid). It is possible that the mean squared displacement and diffusion coefficient is more sensitive to small changes in centroid position than the speed, which is an average value, leading to more differences in conclusions. Finally, we found that both migration and morphology are sensitive to the experience level of the person doing the analysis (Figure 6). In particular, the beginner level stands apart the most from the other two. Interestingly, the difference in speed between beginner and advanced analysis disappears with increasing time step (Figure C.6). This suggests that potentially beginners are more likely to make mistakes in estimating the centroid, however as the time step increases, small mistakes become less significant among larger migration steps.

Confounding variables in analysis can have a significant impact on both the absolute quantification of migration and morphology as well as the relative outcome between different conditions, changing the outcome of a study. These differences could become more pronounced with more heterogeneous cell populations or with more complex studies. This suggest that researchers should be mindful of these types of confounding variables in their analysis and not limit controls to experiments.

Appendix C.5 Conclusion

In conclusion, we have examined the importance of normalization of cell migration and morphology analysis, which is a frequently overlooked aspect of experimental control. Specifically, we examined the presence of confounding variables in the analysis step of cell migration and morphology analysis such as zoom level, sample size, time interval, different types of tracking, and experience level. We found that it is crucial to examine and normalize these variable parameters in experiments in order to produce the most accurate and repeatable data.

10 Bibliography

[1] C. L. Chaffer and R. A. Weinberg, “A Perspective on Cancer Cell Metastasis,” *Science (80-.).*, vol. 331, no. 6024, pp. 1559–1564, Mar. 2011.

[2] G. P. Gupta and J. Massagué, “Cancer Metastasis: Building a Framework,” *Cell*, vol. 127, no. 4, pp. 679–695, Nov. 2006.

[3] D. X. Nguyen, P. D. Bos, and J. Massagué, “Metastasis: from dissemination to organ-specific colonization,” *Nat. Rev. Cancer*, vol. 9, no. 4, pp. 274–284, 2009.

[4] E. Fokas, R. Engenhart-Cabillic, K. Daniilidis, F. Rose, and H. X. An, “Metastasis: The seed and soil theory gains identity,” *Cancer Metastasis Rev.*, vol. 26, no. 3–4, pp. 705–715, 2007.

[5] I. J. I. . Fidler, “The role of the organ microenvironment in brain metastasis,” *Semin. Cancer Biol.*, vol. 21, no. 2, pp. 107–112, 2011.

[6] I. J. Fidler, “The Biology of Brain Metastasis Challenges for Therapy,” *Cancer J.*, vol. 21, no. 4, pp. 284–293, 2015.

[7] N. J. Abbott, A. A. K. Patabendige, D. E. M. Dolman, S. R. Yusof, and D. J. Begley, “Structure and function of the blood-brain barrier,” *Neurobiol. Dis.*, vol. 37, no. 1, pp. 13–25, 2010.

[8] N. Reymond, B. B. D’Água, and A. J. Ridley, “Crossing the endothelial barrier during metastasis,” *Nat. Rev. Cancer*, vol. 13, no. 12, pp. 858–870, 2013.

[9] J. F. Deeken and W. Löscher, “The blood-brain barrier and cancer: Transporters, treatment, and trojan horses,” *Clin. Cancer Res.*, vol. 13, no. 6, pp. 1663–1674, 2007.

[10] A. J. Engler, S. Sen, H. L. Sweeney, and D. E. Discher, “Matrix elasticity directs stem cell lineage specification,” *Cell*, vol. 126, no. 4, pp. 677–689, 2006.

[11] A. D. Wong, M. Ye, A. F. Levy, J. D. Rothstein, D. E. Bergles, and P. C. Searson, “The blood-brain barrier: an engineering perspective,” *Front. Neuroeng.*, vol. 6, pp. 1–22, Aug. 2013.

[12] N. J. Abbott, L. Roenbaeck, E. Hansson, L. Rönnbäck, and E. Hansson, “Astrocyte-endothelial interactions at the blood-brain barrier,” *Nat. Rev. Neurosci.*, vol. 7, no. 41–53, pp. 41–53, 2006.

[13] B. H. Rath, J. M. Fair, M. Jamal, K. Camphausen, P. J. Tofilon, and M. G. Castro, “Astrocytes Enhance the Invasion Potential of Glioblastoma Stem-Like Cells,” *PLoS One*, vol. 8, no. 1, p. e54752, 2013.

[14] A. L. Placone, A. Quiñones-Hinojosa, and P. C. Searson, “The role of astrocytes in the progression of brain cancer: complicating the picture of the tumor microenvironment,” *Tumor Biol.*, vol. 37, no. 1–69, pp. 61–69, 2016.

[15] M. Valiente *et al.*, “Serpins promote cancer cell survival and vascular co-option in brain metastasis,” *Cell*, vol. 156, no. 5, pp. 1002–1016, 2014.

[16] W. Chen, A. D. Hoffmann, H. Liu, and X. Liu, “Organotropism: new insights into molecular mechanisms of breast cancer metastasis,” *Precis. Oncol.*, vol. 2, no. 1, p. 4, Dec. 2018.

[17] R. L. Siegel, K. D. Miller, and A. Jemal, “Cancer Statistics, 2017,” *CA. Cancer J. Clin.*, vol. 67, no. 1, pp. 7–30, 2017.

[18] “Cancer Facts & Figures 2019,” Atlanta, 2019.

[19] R. L. Siegel, K. D. Miller, and A. Jemal, “Cancer statistics, 2019,” *CA. Cancer J. Clin.*, vol. 69, no. 1, pp. 7–34, Jan. 2019.

[20] J. Massagué and A. C. Obenauf, “Metastatic colonization by circulating tumour cells,” *Nature*, vol. 529, no. 7586, pp. 298–306, 2016.

[21] J. L. Albritton and J. S. Miller, “3D bioprinting: improving in vitro models of metastasis with heterogeneous tumor microenvironments,” *Dis. Model. Mech.*, vol. 10, pp. 3–14, 2017.

[22] L. Nayak, E. Quant Lee, and P. Y. Wen, “Epidemiology of Brain Metastases,” *Curr. Oncol. Rep.*, vol. 14, pp. 48–54, 2012.

[23] N. D. Arvold *et al.*, “Updates in the management of brain metastases,” *Neuro. Oncol.*, vol. 18, no. 8, pp. 1043–1065, 2016.

[24] S. Paget, “The distribution of secondary growths in cancer of the breast,” *Lancet*, vol. 133, no. 3421, pp. 571–573, Mar. 1889.

[25] I. J. Fidler and G. Poste, “The ‘seed and soil’ hypothesis revisited,” *Lancet Oncol.*, vol. 9, p. 808, 2008.

[26] *Metastatic Brain Tumors*. Chicago, 2017.

[27] V. C. Shukla and S. N. Ghadiali, “Substrate Stiffness Modulates Lung Cancer Cell Migration but not Epithelial to Mesenchymal Transition,” *Soc. Biomater.*, no. 614, pp. 1–32, 2016.

[28] A. Haage and I. C. Schneider, “Cellular contractility and extracellular matrix stiffness regulate matrix metalloproteinase activity in pancreatic cancer cells,” *FASEB J.*, vol. 28, no. 8, pp. 3589–3599, 2014.

[29] A. Pathak and S. Kumar, “Independent regulation of tumor cell migration by matrix stiffness and confinement,” *Proc. Natl. Acad. Sci.*, vol. 109, no. 26, pp. 10334–10339, 2012.

[30] A. Pathak and S. Kumar, “Biophysical regulation of tumor cell invasion: moving beyond matrix stiffness,” *Integr. Biol.*, vol. 3, no. 4, p. 267, 2011.

[31] L. Kass, J. T. Erler, M. Dembo, and V. M. Weaver, “Mammary epithelial cell: Influence of extracellular matrix composition and organization during development and tumorigenesis,” *Int. J. Biochem. Cell Biol. 3*, vol. 39, no. 39,

pp. 1987–1994, 2007.

[32] L. E. Barney, L. E. Jansen, S. R. Polio, S. Galarza, M. E. Lynch, and S. R. Peyton, “The predictive link between matrix and metastasis,” *Curr. Opin. Chem. Eng.*, vol. 11, pp. 85–93, 2016.

[33] S. M. Hamilla, K. M. Stroka, and H. Aranda-Espinoza, “VE-Cadherin-independent cancer cell incorporation into the vascular endothelium precedes transmigration,” *PLoS One*, vol. 9, no. 10, p. e109748, Oct. 2014.

[34] D. Wirtz, K. Konstantopoulos, and P. C. Searson, “The physics of cancer: the role of physical interactions and mechanical forces in metastasis,” *Nat. Rev. Cancer*, vol. 11, pp. 512–522, 2011.

[35] P. S. Steeg, “Tumor metastasis: mechanistic insights and clinical challenges,” *Nat. Med.*, vol. 12, no. 8, pp. 895–904, Aug. 2006.

[36] M. J. Paszek *et al.*, “Tensional homeostasis and the malignant phenotype,” *Cancer Cell*, vol. 8, no. 3, pp. 241–254, 2005.

[37] S. Kumar and V. M. Weaver, “Mechanics, malignancy, and metastasis: The force journey of a tumor cell,” *Cancer Metastasis Rev.*, vol. 28, no. 1–2, pp. 113–127, 2009.

[38] K. R. Levental *et al.*, “Matrix Crosslinking Forces Tumor Progression by Enhancing Integrin Signaling,” *Cell*, vol. 139, no. 5, pp. 891–906, 2009.

[39] H. Yu, J. K. Mouw, and V. M. Weaver, “Forcing form and function: biomechanical regulation of tumor evolution,” *Trends Cell Biol.*, vol. 21, pp. 47–56, 2010.

[40] M. Plodinec *et al.*, “The nanomechanical signature of breast cancer,” *Nat. Nanotechnol.*, vol. 7, pp. 757–765, 2012.

[41] W. Xu *et al.*, “Cell Stiffness Is a Biomarker of the Metastatic Potential of Ovarian Cancer Cells,” *PLoS One*, vol. 7, no. 10, 2012.

[42] B. T. Hawkins and T. P. Davis, “The Blood-Brain Barrier/Neurovascular Unit in Health and Disease,” *Pharmacol. Rev.*, vol. 57, no. 2, pp. 173–185, 2005.

[43] L. Xu, A. Nirwane, and Y. Yao, “Basement membrane and blood-brain barrier,” *Stroke Vasc. Neurol.*, p. 198, 2018.

[44] M. S. Thomsen, L. J. Routhe, and T. Moos, “The vascular basement membrane in the healthy and pathological brain,” *J. Cereb. Blood Flow Metab.*, vol. 37, no. 10, pp. 3300–3317, 2017.

[45] B. Ananthanarayanan, Y. Kim, and S. Kumar, “Elucidating the mechanobiology of malignant brain tumors using a brain matrix-mimetic hyaluronic acid hydrogel platform,” *Biomaterials*, vol. 32, no. 31, pp. 7913–7923, Nov. 2011.

[46] N. George and H. M. Geller, “Extracellular matrix and traumatic brain injury,”

J. Neurosci. Res., vol. 96, no. 4, pp. 573–588, 2018.

[47] N. Tominaga *et al.*, "Brain metastatic cancer cells release microRNA-181c-containing extracellular vesicles capable of destructing blood–brain barrier," *Nat. Commun.*, vol. 6, no. 1, pp. 1–12, Dec. 2015.

[48] L. Wang *et al.*, "Astrocytes directly influence tumor cell invasion and metastasis in vivo," *PLoS One*, vol. 8, no. 12, p. e80933, 2013.

[49] Q. Chen *et al.*, "Carcinoma-astrocyte gap junctions promote brain metastasis by cGAMP transfer," *Nature*, vol. 533, no. 7604, pp. 493–498, 2016.

[50] P. Proia *et al.*, "Astrocytes shed extracellular vesicles that contain fibroblast growth factor-2 and vascular endothelial growth factor," *Int. J. Mol. Med.*, vol. 21, no. 1, pp. 63–67, 2008.

[51] Y. Liang, R. A. Brekken, and S. M. Hyder, "Vascular endothelial growth factor induces proliferation of breast cancer cells and inhibits the anti-proliferative activity of anti-hormones," *Endocr. Relat. Cancer*, vol. 13, no. 3, pp. 905–919, 2006.

[52] B. P. He *et al.*, "Differential Rreactions of microglia to brain metastasis of lung cancer," *Mol. Med.*, vol. 12, no. 7–8, pp. 161–170, 2006.

[53] T. Pukrop *et al.*, "Microglia promote colonization of brain tissue by breast cancer cells in a Wnt-dependent way," *Glia*, vol. 58, no. 12, pp. 1477–1489, 2010.

[54] C. Schachtrup *et al.*, "Fibrinogen triggers astrocyte scar formation by promoting the availability of active TGF-β after vascular damage," *J. Neurosci.*, vol. 30, no. 17, pp. 5843–5854, 2010.

[55] M. Pekny, U. Wilhelmsson, and M. Pekna, "The dual role of astrocyte activation and reactive gliosis," *Neurosci. Lett.*, vol. 565, pp. 30–38, 2014.

[56] F. Xing *et al.*, "Reactive astrocytes promote the metastatic growth of breast cancer stem-like cells by activating Notch signalling in brain," *EMBO Mol. Med.*, vol. 5, no. 3, pp. 384–396, 2013.

[57] B. Gril *et al.*, "Reactive astrocytic S1P3 signaling modulates the blood–tumor barrier in brain metastases," *Nat. Commun.*, vol. 9, no. 1, p. 2705, Dec. 2018.

[58] N. Priego *et al.*, "STAT3 labels a subpopulation of reactive astrocytes required for brain metastasis," *Nat. Med.*, vol. 24, no. 7, pp. 1024–1035, Jul. 2018.

[59] H.-B. Wang, M. Dembo, and Y.-L. Wang, "Substrate flexibility regulates growth and apoptosis of normal but not transformed cells," *Am. J. Physiol. - Cell Physiol.*, vol. 279, no. 5, pp. C1345–C1350, 2000.

[60] T. Yeung *et al.*, "Effects of substrate stiffness on cell morphology, cytoskeletal structure, and adhesion," *Cell Motil. Cytoskeleton*, vol. 60, no. 1, pp. 24–34, 2005.

[61] M. Zoeller, “CD44: can a cancer-initiating cell profit from an abundantly expressed molecule?,” *Nat. Cancer Rev.*, vol. 11, pp. 254–267, 2011.

[62] K. M. Flynn, M. Michaud, S. Canosa, and J. A. Madri, “CD44 regulates vascular endothelial barrier integrity via a PECAM-1 dependent mechanism,” *Angiogenesis*, vol. 16, pp. 689–705, 2013.

[63] J. E. E. Draffin, S. McFarlane, A. Hill, P. G. G. Johnston, and D. J. J. J. Waugh, “CD44 Potentiates the Adherence of Metastatic Prostate and Breast Cancer Cells to Bone Marrow Endothelial Cells,” *Cancer Res*, vol. 64, no. 16, pp. 5702–5711, 2004.

[64] C. Rampon *et al.*, “Molecular mechanism of systemic delivery of neural precursor cells to the brain: assembly of brain endothelial apical cups and control of transmigration by CD44.,” *Stem Cells*, vol. 26, no. 7, pp. 1673–1682, 2008.

[65] P. D. Bos *et al.*, “Genes that mediate breast cancer metastasis to the brain,” *Nature*, vol. 459, no. 7249, pp. 1005–1009, Jun. 2009.

[66] C. Conrad *et al.*, “ADAM8 expression in breast cancer derived metastases: Functional implications on MMP-9 expression and transendothelial migration in breast cancer cells,” *Int. J. Cancer*, vol. 142, no. 4, pp. 779–791, Feb. 2017.

[67] J. Molnár *et al.*, “Transmigration characteristics of breast cancer and melanoma cells through the brain endothelium: Role of Rac and PI3K,” *Cell Adh. Migr.*, vol. 10, no. 3, pp. 269–81, 2016.

[68] I. Wilhelm *et al.*, “Role of Rho/ROCK signaling in the interaction of melanoma cells with the blood-brain barrier,” *Pigment Cell Melanoma Res.*, vol. 27, no. 1, pp. 113–123, Jan. 2014.

[69] B. Varga *et al.*, “De-adhesion dynamics of melanoma cells from brain endothelial layer,” *Biochim. Biophys. Acta - Gen. Subj.*, vol. 1862, no. 3, pp. 745–751, Mar. 2018.

[70] H. Herman *et al.*, “Paracellular and transcellular migration of metastatic cells through the cerebral endothelium,” *J. Cell. Mol. Med.*, vol. 23, no. 4, pp. 2619–2631, 2019.

[71] I. A. Krizbai *et al.*, “Endothelial-mesenchymal transition of brain endothelial cells: Possible role during metastatic extravasation,” *PLoS One*, vol. 10, no. 3, pp. 1–19, 2015.

[72] K. M. Stroka and K. Konstantopoulos, “Physical Biology in Cancer. 4. Physical cues guide tumor cell adhesion and migration,” *AJP Cell Physiol.*, vol. 306, no. 2, pp. C98–C109, Jan. 2014.

[73] T. Yoneda, P. J. Williams, T. Hiraga, M. Niewolna, and R. Nishimura, “A bone-seeking clone exhibits different biological properties from the MDA-MB-231 parental human breast cancer cells and a brain-seeking clone in vivo and in vitro,” *J. Bone Miner. Res.*, vol. 16, no. 8, pp. 1486–1495, 2001.

[74] T. Yoneda and T. Hiraga, “Crosstalk between cancer cells and bone microenvironment in bone metastasis,” *Biochem. Biophys. Res. Commun.*, vol. 328, no. 3, pp. 679–687, 2005.

[75] A. Hoshino *et al.*, “Tumour exosome integrins determine organotropic metastasis,” *Nature*, vol. 527, no. 7578, pp. 329–335, Nov. 2015.

[76] M. D. Dun *et al.*, “Proteotranscriptomic Profiling of 231-BR Breast Cancer Cells: Identification of Potential Biomarkers and Therapeutic Targets for Brain Metastasis,” *Mol. Cell. Proteomics*, vol. 14, no. 9, pp. 2316–2330, 2015.

[77] A. Stark, B. Anuszkiewicz, R. Mentlein, T. Yoneda, H. Mehdorn, and J. Held-Feindt, “Differential expression of matrix metalloproteinases in brain- and bone-seeking clones of metastatic MDA-MB-231 breast cancer cells,” *J Neurooncol*, vol. 81, pp. 39–48, 2007.

[78] The American Cancer Society, “Common types of cancer treatment,” *The American Cancer Society*, 2015. [Online]. Available: https://www.cancer.org/treatment/understanding-your-diagnosis/after-diagnosis/common-cancer-treatments.html. [Accessed: 17-Apr-2019].

[79] T. K. Owonikoko *et al.*, “Current approaches to the treatment of metastatic brain tumours,” *Nat. Rev. Clin. Oncol.*, vol. 11, pp. 203–222, 2014.

[80] T. Kobus, I. K. Zervantonakis, Y. Zhang, and N. J. Mcdannold, “Growth inhibition in a brain metastasis model by antibody delivery using focused ultrasound-mediated blood-brain barrier disruption,” *J. Control. Release*, vol. 238, pp. 281–288, 2016.

[81] D. Yan, J. H. Sherman, and M. Keidar, “Cold atmospheric plasma , a novel promising anti-cancer treatment modality,” *Oncotgarget*, no. November, 2016.

[82] M. Keidar, “Plasma for cancer treatment,” *Plasma Sources Sci. Technol.*, vol. 24, no. 3, p. 033001, 2015.

[83] C. Hoffmann, C. Berganza, and J. Zhang, “Cold Atmospheric Plasma: methods of production and application in dentistry and oncology,” *Med. Gas Res.*, vol. 3, no. 1, p. 21, Oct. 2013.

[84] K. Wende *et al.*, “Identification of the biologically active liquid chemistry induced by a nonthermal atmospheric pressure plasma jet,” *Biointerphases*, vol. 10, no. 2, p. 029518, 2015.

[85] A. J. Knoll, P. Luan, A. Pranda, R. L. Bruce, and G. S. Oehrlein, “Polymer etching by atmospheric-pressure plasma jet and surface micro-discharge sources: Activation energy analysis and etching directionality,” *Plasma Process. Polym.*, vol. 15, no. 5, p. 1700217, May 2018.

[86] P. Luan *et al.*, “Decontamination of raw produce by surface microdischarge and the evaluation of its damage to cellular components,” *Plasma Process Polym.*, p. e1800193, 2019.

[87] M. Schuster *et al.*, “Visible tumor surface response to physical plasma and apoptotic cell kill in head and neck cancer,” *J. Cranio-Maxillofacial Surg.*, vol. 44, no. 9, pp. 1445–1452, 2016.

[88] Z. Chen, L. Lin, X. Cheng, E. Gjika, and M. Keidar, “Effects of cold atmospheric plasma generated in DI water on Cancer cells,” no. June, pp. 1–13, 2016.

[89] J.-H. Lee, J.-Y. Om, Y.-H. Kim, K.-N. K.-M. Kim, E.-H. Choi, and K.-N. K.-M. Kim, “Selective Killing Effects of Cold Atmospheric Pressure Plasma with NO Induced Dysfunction of Epidermal Growth Factor Receptor in Oral Squamous Cell Carcinoma,” *PLoS One*, vol. 11, no. 2, p. e0150279, 2016.

[90] X. Xu, X. Dai, L. Xiang, D. Cai, S. Xiao, and K. Ostrikov, “Quantitative assessment of cold atmospheric plasma anti-cancer efficacy in triple-negative breast cancers,” *Plasma Process. Polym.*, vol. 15, no. 8, pp. 1–11, 2018.

[91] D. Trachootham, J. Alexandre, and P. Huang, “Targeting cancer cells by ROS-mediated mechanisms: a radical therapeutic approach?,” *Nat. Rev. Drug Discov.*, vol. 8, no. 7, pp. 579–591, Jul. 2009.

[92] Y. Dayun, A. Talbot, N. Nourmohammadi, J. H. Sherman, X. Cheng, and M. Keidar, “Toward understanding the selective anticancer capacity of cold atmospheric plasma— A model based on aquaporins,” *Biointerphases*, vol. 10, no. 4, p. 040801, 2015.

[93] A. R. Taylor, M. B. Robinson, and C. E. Milligan, “In vitro methods to prepare astrocyte and motoneuron cultures for the investigation of potential in vivo interactions.,” *Nat. Protoc.*, vol. 2, no. 6, pp. 1499–507, 2007.

[94] J. Köritzer *et al.*, “Restoration of Sensitivity in Chemo — Resistant Glioma Cells by Cold Atmospheric Plasma,” *PLoS One*, vol. 8, no. 5, p. e64498, 2013.

[95] K. Priya Arjunan and A. Morss Clyne, “Hydroxyl Radical and Hydrogen Peroxide are Primarily Responsible for Dielectric Barrier Discharge Plasma-Induced Angiogenesis,” *Plasma Process. Polym.*, vol. 8, no. 12, pp. 1154–1164, Dec. 2011.

[96] S. Kalghatgi, G. Friedman, A. Fridman, and A. M. Clyne, “Endothelial Cell Proliferation is Enhanced by Low Dose Non-Thermal Plasma Through Fibroblast Growth Factor-2 Release,” *Ann. Biomed. Eng.*, vol. 38, no. 3, pp. 748–757, 2010.

[97] S. U. Kalghatgi, G. Fridman, A. Fridman, G. Friedman, and A. M. Clyne, “Non-thermal dielectric barrier discharge plasma treatment of endothelial cells,” *2008 30th Annu. Int. Conf. IEEE Eng. Med. Biol. Soc.*, vol. 2, pp. 3578–3581, 2008.

[98] G. Isbary *et al.*, “Cold atmospheric argon plasma treatment may accelerate wound healing in chronic wounds: Results of an open retrospective randomized controlled study in vivo,” *Clin. Plasma Med.*, vol. 1, no. 2, pp. 25–

30, 2013.

[99] I. Witzel, L. Oliveira-Ferrer, K. Pantel, V. Müller, and H. Wikman, “Breast cancer brain metastases: biology and new clinical perspectives,” *Breast Cancer Res.*, vol. 18, no. 1, pp. 8–17, 2016.

[100] F. R. Balkwill, M. Capasso, and T. Hagemann, “The tumor microenvironment at a glance,” *J. Cell Sci.*, vol. 125, no. 23, pp. 5591–5596, 2013.

[101] I. Hohensee *et al.*, “PTEN mediates the cross talk between breast and glial cells in brain metastases leading to rapid disease progression,” vol. 8, no. 4, pp. 6155–6168, 2017.

[102] S. Löffek, O. Schilling, and C.-W. Franzke, “Biological role of matrix metalloproteinases: a critical balance,” *Eur. Respir. J.*, vol. 38, no. 1, 2011.

[103] H. Wang *et al.*, “Chondroitin-4-sulfation negatively regulates axonal guidance and growth,” *J. Cell Sci.*, vol. 15, no. 121, pp. 3083–3091, 2008.

[104] M. Sochocka, B. S. Diniz, and J. Leszek, “Inflammatory Response in the CNS: Friend or Foe?,” *Mol. Neurobiol.*, 2016.

[105] S.-E. Kuzet and C. Gaggioli, “Fibroblast activation in cancer: when seed fertilizes soil,” *Cell Tissue Res.*, vol. 365, no. 3, pp. 607–619, 2016.

[106] S. D. Preston, P. V. Steart, A. Wilkinson, J. A. R. Nicoll, and R. O. Weller, “Capillary and arterial cerebral amyloid angiopathy in Alzheimer’s disease: Defining the perivascular route for the elimination of amyloid β from the human brain,” *Neuropathol. Appl. Neurobiol.*, vol. 29, no. 2, pp. 106–117, 2003.

[107] P. Friedl and S. Alexander, “Cancer invasion and the microenvironment: Plasticity and reciprocity,” *Cell*, vol. 147, no. 5, pp. 992–1009, 2011.

[108] K. M. Stroka *et al.*, “Water permeation drives tumor cell migration in confined microenvironments,” *Cell*, vol. 157, no. 3, pp. 611–623, 2014.

[109] Z. Yu, P. Yu, H. Chen, and H. M. Geller, “Targeted inhibition of KCa3.1 attenuates TGF-β-induced reactive astrogliosis through the Smad2/3 signaling pathway,” *J. Neurochem.*, vol. 130, no. 1, pp. 41–49, 2014.

[110] M. A. Miller *et al.*, “ADAM-10 and -17 regulate endometriotic cell migration via concerted ligand and receptor shedding feedback on kinase signaling,” *Proc. Natl. Acad. Sci.*, vol. 110, no. 22, pp. E2074–E2083, 2013.

[111] N. Nosoudi *et al.*, “Prevention of Abdominal Aortic Aneurysm Progression by Targeted Inhibition of Matrix Metalloproteinase Activity with Batimastat-Loaded Nanoparticles,” *Circ Res. Circ Res.*, vol. 117, no. 11, pp. e80–e89, 2015.

[112] E. M. Balzer *et al.*, “Physical confinement alters tumor cell adhesion and migration phenotypes,” *FASEB J.*, vol. 26, no. 10, pp. 4045–4056, 2012.

[113] Z. Tong, E. M. Balzer, M. R. Dallas, W.-C. Hung, K. J. Stebe, and K. Konstantopoulos, "Chemotaxis of Cell Populations through Confined Spaces at Single-Cell Resolution," *PLoS One*, vol. 7, no. 1, p. e29211, Jan. 2012.

[114] K. M. Stroka *et al.*, "Loss of giant obscurins alters breast epithelial cell mechanosensing of matrix stiffness," *Oncotarget*, vol. 5, 2016.

[115] L. A. Smith, H. Aranda-Espinoza, J. B. Haun, and D. A. Hammer, "Interplay between shear stress and adhesion on neutrophil locomotion," *Biophys. J.*, vol. 92, no. 2, pp. 632–640, Jan. 2007.

[116] A. Kapoor and S. Sen, "Synergistic modulation of cellular contractility by mixed extracellular matrices," *Int. J. Cell Biol.*, 2012.

[117] J. A. Kim, H. N. Kim, S.-K. Im, S. Chung, J. Y. Kang, and N. Choi, "Collagen-based brain microvasculature model in vitro using three-dimensional printed template," *Biomicrofluidics*, vol. 9, no. 101, pp. 024115–1, 2015.

[118] K. Wolf *et al.*, "Collagen-based cell migration models in vitro and in vivo.," *Semin. Cell Dev. Biol.*, vol. 20, no. 8, pp. 931–41, 2009.

[119] X. Xu, Y. Wang, Z. Chen, M. D. Sternlicht, M. Hidalgo, and B. Steffensen, "Matrix metalloproteinase-2 contributes to cancer cell migration on collagen.," *Cancer Res.*, vol. 65, no. 1, pp. 130–6, 2005.

[120] S. A. Liddelow *et al.*, "Neurotoxic reactive astrocytes are induced by activated microglia," *Nature*, vol. 541, no. 7638, pp. 481–487, 2017.

[121] K. C. Flanders, R. F. Ren, and C. F. Lippa, "Transforming Growth Factor-Betas in Neuroegenerative Disease," *Prog. Neurobiol.*, vol. 54, pp. 71–85, 1998.

[122] G. M. Smith and C. Strunz, "Growth factor and cytokine regulation of chondroitin sulfate proteoglycans by astrocytes," *Glia*, vol. 52, no. 3, pp. 209–218, 2005.

[123] K. M. McAndrews, D. J. McGrail, N. Ravikumar, and M. R. Dawson, "Mesenchymal Stem Cells Induce Directional Migration of Invasive Breast Cancer Cells through TGF-β," *Sci. Rep.*, vol. 5, p. 16941, 2015.

[124] M. Egeblad and Z. Werb, "New functions for the matrix metalloproteinases in cancer progression," *Nat Rev Cancer*, vol. 2, pp. 161–174, 2002.

[125] K.-J. Yin *et al.*, "Matrix metalloproteinases expressed by astrocytes mediate extracellular amyloid-beta peptide catabolism," *J. Neurosci.*, vol. 26, no. 43, pp. 10939 –10948, 2006.

[126] H. F. Bigg, A. D. Rowan, M. D. Barker, and T. E. Cawston, "Activity of matrix metalloproteinase-9 against native collagen types I and III," *FEBS J.*, vol. 274, no. 5, pp. 1246–1255, 2007.

[127] R. T. Aimes and J. P. Quigley, "Matrix metalloproteinase-2 is an interstitial collagenase. Inhibitor-free enzyme catalyzes the cleavage of collagen fibrils

and soluble native type I collagen generating the specific 3/4- and 1/4-length fragments," *J. Biol. Chem.*, vol. 270, no. 11, pp. 5872–5876, Mar. 1995.

[128] B. Isaksen and M. K. Fagerhol, "Calprotectin inhibits matrix metalloproteinases by sequestration of zinc," *J. Clin. Pathol. Mol. Pathol.*, vol. 54, pp. 289–292, 2001.

[129] M. Rolli, E. Fransvea, J. Pilch, A. Saven, and B. Felding-habermann, "Activated integrin αvβ3 cooperates with metalloproteinase MMP-9 in regulating migration of metastatic breast cancer cells," *Proc. Natl. Acad. Sci.*, vol. 100, no. 16, pp. 9482–9487, 2003.

[130] R. J. Petrie, H. Koo, and K. M. Yamada, "Generation of compartmentalized pressure by a nuclear piston governs cell motility in a 3D matrix," *Science (80-.).*, vol. 345, no. 6200, pp. 1062–1065, 2014.

[131] C. T. Skau *et al.*, "FMN2 Makes Perinuclear Actin to Protect Nuclei during Confined Migration and Promote Metastasis," *Cell*, vol. 167, no. 6, pp. 1571–1585, 2016.

[132] S. M. Lyons *et al.*, "Changes in cell shape are correlated with metastatic potential in murine and human osteosarcomas," *Biol. Open*, vol. 5, pp. 289–299, 2016.

[133] N. O. Deakin and C. E. Turner, "Distinct roles for paxillin and Hic-5 in regulating breast cancer cell morphology, invasion, and metastasis," *Mol. Biol. Cell*, vol. 22, no. 3, pp. 327–341, 2011.

[134] J. A. Dowell, J. A. Johnson, and L. Li, "Identification of Astrocyte Secreted Proteins with a Combination of Shotgun Proteomics and Bioinformatics," *J. Proteome Res.*, vol. 8, no. 8, pp. 4135–4143, 2009.

[135] H.-L. Hsieh, H.-H. Wang, W.-B. Wu, P.-J. Chu, and C.-M. Yang, "Transforming growth factor-b1 induces matrix metalloproteinase-9 and cell migration in astrocytes: roles of ROS-dependent ERK-and JNK- NF-B pathways," *J. Neuroinflammation*, vol. 7, no. 1, pp. 88–105, 2010.

[136] T. Seike *et al.*, "Interaction between lung cancer cells and astrocytes via specific inflammatory cytokines in the microenvironment of brain metastasis," *Clin. Exp. Metastasis*, vol. 28, pp. 13–25, 2011.

[137] G. Murphy and J. Gavrilovic, "Proteolysis and cell migration: creating a path?," *Curr. Opin. Cell Biol.*, vol. 11, no. 5, pp. 614–621, Oct. 1999.

[138] K. Nabeshima, T. Inoue, Y. Shimao, and T. Sameshima, "Matrix metalloproteinases in tumor invasion: role for cell migration," *Pathol. Int.*, vol. 52, no. 4, pp. 255–64, 2002.

[139] G. Giannelli, J. Falk-Marzillier, O. Schiraldi, W. G. Stetler-Stevenson, and V. Quaranta, "Induction of Cell Migration by Matrix Metalloprotease–2 Cleavage of Laminin-5," *Science (80-.).*, vol. 277, pp. 225–227, 1997.

[140] C. L. Yankaskas *et al.*, “A microfluidic assay for the quantification of the metastatic propensity of breast cancer specimens,” *Nat. Biomed. Eng.*, 2019.

[141] A. S. Achrol *et al.*, “Brain metastases,” *Nat. Rev.*, vol. 5, no. 5, 2019.

[142] F. Arshad, L. Wang, C. Sy, S. Avraham, and H. K. Avraham, “Blood-brain barrier integrity and breast cancer metastasis to the brain,” *Patholog. Res. Int.*, vol. 2011, pp. 1–12, 2010.

[143] Y. Kienast *et al.*, “Real-time imaging reveals the single steps of brain metastasis formation,” *Nat. Med.*, vol. 16, no. 1, pp. 116–122, 2010.

[144] N. J. Abbott and A. Friedman, “Overview and introduction: the blood-brain barrier in health and disease,” *Epilepsia*, vol. 53 Suppl 6, no. 0 6, pp. 1–6, Nov. 2012.

[145] O. Tornavaca *et al.*, “ZO-1 controls endothelial adherens junctions, cell-cell tension, angiogenesis, and barrier formation,” *J. Cell Biol.*, vol. 208, no. 6, pp. 821–838, 2015.

[146] P. Grammas, J. Martinez, and B. Miller, “Cerebral microvascular endothelium and the pathogenesis of neurodegenerative diseases,” *Expert Rev. Mol. Med.*, vol. 13, no. 19, 2011.

[147] T. A. Martin and W. G. Jiang, “Loss of tight junction barrier function and its role in cancer metastasis,” *Biochim. Biophys. Acta - Biomembr.*, vol. 1788, no. 4, pp. 872–891, 2009.

[148] T.-H. Lee, H. Karsenty Avraham, S. Jiang, and S. Avraham, “Vascular endothelial growth factor modulates the transendothelial migration of MDA-MB-231 breast cancer cells through regulation of brain microvascular endothelial cell permeability,” *J. Biol. Chem.*, vol. 278, no. 7, pp. 5277–5284, 2003.

[149] H. K. Avraham, S. Jiang, Y. Fu, H. Nakshatri, H. Ovadia, and S. Avraham, “Angiopoietin-2 mediates blood-brain barrier impairment and colonization of triple-negative breast cancer cells in brain,” *J. Pathol.*, vol. 232, no. 3, pp. 369–381, 2014.

[150] C. Fazakas *et al.*, “Transmigration of melanoma cells through the blood-brain barrier: role of endothelial tight junctions and melanoma-released serine proteases,” *PLoS One*, vol. 6, no. 6, p. e20758, 2011.

[151] J. Fan and B. M. Fu, “Quantification of malignant breast cancer cell MDA-MB-231 transmigration across brain and lung microvascular endothelium,” *Ann. Biomed. Eng.*, vol. 44, no. 7, pp. 2189–2201, 2016.

[152] P. L. Rodriguez, S. Jiang, Y. Fu, S. Avraham, and H. K. Avraham, “The proinflammatory peptide substance P promotes blood-brain barrier breaching by breast cancer cells through changes in microvascular endothelial cell tight junctions,” *Int. J. Cancer*, vol. 134, no. 5, pp. 1034–1044, 2014.

[153] J. Cai, W. G. Jiang, and R. E. Mansel, “Phosphorylation and disorganization of vascular-endothelial cadherin in interaction between breast cancer and vascular endothelial cells.,” *Int. J. Mol. Med.*, vol. 4, no. 2, pp. 191–5, Aug. 1999.

[154] B. Li, W.-D. Zhao, Z.-M. Tan, W.-G. Fang, L. Zhu, and Y.-H. Chen, “Involvement of Rho/ROCK signalling in small cell lung cancer migration through human brain microvascular endothelial cells.,” *FEBS Lett.*, vol. 580, no. 17, pp. 4252–60, 2006.

[155] N. Reymond, P. Riou, and A. J. Ridley, “Rho GTPases and cancer cell transendothelial migration,” *Methods Mol. Biol.*, vol. 827, pp. 123–142, 2012.

[156] M. D. Onken, J. Li, and J. A. Cooper, “Uveal melanoma cells utilize a novel Route for transendothelial migration,” *PLoS One*, vol. 9, no. 12, p. e115472, 2014.

[157] U. Novak and A. H. Kaye, “Extracellular matrix and the brain: components and function,” *J. Clin. Neurosci.*, vol. 7, no. 4, pp. 280–290, 2000.

[158] A. F. Eichler, E. Chung, D. P. Kodack, J. S. Loeffler, D. Fukumura, and R. K. Jain, “The biology of brain metastases-translation to new therapies,” *Nat. Rev. Clin. Oncol.*, vol. 8, no. 6, pp. 344–356, 2011.

[159] J. K. Mouw, G. Ou, and V. M. Weaver, “Extracellular matrix assembly: a multiscale deconstruction,” *Nat. Publ. Gr.*, vol. 15, p. 771, 2014.

[160] J. M. Barnes, L. Przybyla, and V. M. Weaver, “Tissue mechanics regulate brain development, homeostasis and disease,” *J. Cell Sci.*, vol. 130, no. 1, pp. 71–82, 2017.

[161] T. R. Cox and J. T. Erler, “Remodeling and homeostasis of the extracellular matrix: implications for fibrotic diseases and cancer,” *Dis. Model. Mech.*, vol. 4, pp. 165–178, 2011.

[162] G. Akiri *et al.*, “Lysyl oxidase-related protein-1 promotes tumor fibrosis and tumor progression in vivo,” *Cancer Res.*, vol. 63, no. 7, pp. 1657–1666, 2003.

[163] G. D. Prestwich and C. O. N. Spectus, “Evaluating drug efficacy and toxicology in three dimensions: using synthetic extracellular matrices in drug discovery,” *Acc. Chem. Res.*, vol. 41, no. 1, pp. 139–148, 2008.

[164] S. K. Shaw, P. S. Bamba, B. N. Perkins, and F. W. Luscinskas, “Real-time imaging of vascular endothelial-cadherin during leukocyte transmigration across endothelium,” *J. Immunol.*, vol. 167, pp. 2323–2330, 2001.

[165] X. Zheng Shu, Y. Liu, F. S. Palumbo, Y. Luo, and G. D. Prestwich, “In situ crosslinkable hyaluronan hydrogels for tissue engineering,” *Biomaterials*, vol. 25, no. 7–8, pp. 1339–1348, Mar. 2004.

[166] D. Sarrió, S. M. Rodriguez-Pinilla, D. Hardisson, A. Cano, G. Moreno-Bueno, and J. Palacios, “Epithelial-mesenchymal transition in breast cancer relates to the basal-like phenotype,” *Cancer Res.*, vol. 68, no. 4, pp. 989–997, 2008.

[167] Y. Kim and S. Kumar, “CD44-mediated adhesion to hyaluronic acid contributes to mechanosensing and invasive motility,” *Mol. Cancer Res.*, vol. 12, no. 10, pp. 1416–1429, 2014.

[168] P. Zhang, C. Fu, H. Bai, E. Song, and Y. Song, “CD44 variant, but not standard CD44 isoforms, mediate disassembly of endothelial VE-cadherin junction on metastatic melanoma cells,” *FEBS Lett.*, vol. 588, no. 24, pp. 4573–4582, 2014.

[169] A. C. Bellail, S. B. Hunter, D. J. Brat, and E. G. Van Meir, “Microregional extracellular matrix heterogeneity in brain modulates glioma cell invasion,” *Int. J. Biochem. Cell Biol.*, vol. 36, pp. 1046–1069, 2004.

[170] S. McFarlane *et al.*, “CD44 increases the efficiency of distant metastasis of breast cancer.,” *Oncotarget*, vol. 6, no. 13, pp. 11465–76, May 2015.

[171] T. Vallenius, “Actin stress fibre subtypes in mesenchymal-migrating cells,” *Open Biol.*, vol. 3, 2013.

[172] D. E. Discher, P. Janmey, and Y.-L. Wang, “Tissue cells Ffeel and respond to the stiffness of their substrate,” *Science (80-.).*, vol. 310, no. 5751, pp. 1139–1143, 2005.

[173] K. M. Stroka and H. Aranda-Espinoza, “Neutrophils display biphasic relationship between migration and substrate stiffness,” *Cell Motil. Cytoskeleton*, vol. 66, no. 6, pp. 328–341, 2009.

[174] A. A. Narkhede, J. H. Crenshaw, R. M. Manning, and S. S. Rao, “The influence of matrix stiffness on the behavior of brain metastatic breast cancer cells in a biomimetic hyaluronic acid hydrogel platform,” *J. Biomed. Mater. Res. - Part A*, no. February, pp. 1–10, 2018.

[175] K. Pogoda *et al.*, “Soft substrates containing hyaluronan mimic the effects of increased stiffness on morphology, motility, and proliferation of glioma cells,” *Biomacromolecules*, vol. 18, p. 3040−3051, 2017.

[176] S. D. Nath, C. Abueva, B. Kim, and B. T. Lee, “Chitosan–hyaluronic acid polyelectrolyte complex scaffold crosslinked with genipin for immobilization and controlled release of BMP-2,” *Carbohydr. Polym.*, vol. 115, pp. 160–169, Jan. 2015.

[177] M. D. Brigham, A. Bick, E. Lo, A. Bendali, J. A. Burdick, and A. Khademhosseini, “Mechanically Robust and Bioadhesive Collagen and Photocrosslinkable Hyaluronic Acid Semi-Interpenetrating Networks,” *Tissue Eng. Part A*, vol. 15, no. 7, pp. 1645–1653, Jul. 2009.

[178] A. I. Van *et al.*, “Structural and Rheological Properties of Methacrylamide Modified Gelatin Hydrogels,” *Struct. Rheol. Prop. Methacrylamide Modif. Gelatin Hydrogels*, vol. 1, pp. 31–38, 2000.

[179] S. Linder, “The matrix corroded: podosomes and invadopodia in extracellular matrix degradation,” *Trends Cell Biol.*, vol. 17, no. 3, pp. 107–117, Mar. 2007.

[180] L. Ritsma *et al.*, “Intravital Microscopy Through an Abdominal Imaging Window Reveals a Pre-Micrometastasis Stage During Liver Metastasis,” *Sci. Transl. Med.*, vol. 4, no. 158, p. 158ra145, 2012.

[181] K. M. Stroka, H. N. Hayenga, and H. Aranda-Espinoza, “Human neutrophil cytoskeletal dynamics and contractility actively contribute to trans-endothelial migration,” *PLoS One*, vol. 8, no. 4, p. 61377, 2013.

[182] H. S. Leong *et al.*, “Article invadopodia are required for cancer cell extravasation and are a therapeutic target for metastasis,” *Cell Rep.*, vol. 8, pp. 1558–1570, 2014.

[183] C. C. Mader *et al.*, “An EGFR–Src–Arg–cortactin pathway mediates functional maturation of invadopodia and breast cancer cell invasion,” *J. Cancer Res.*, vol. 71, no. 5, pp. OF1–OF12, 2011.

[184] E. J. Hagedorn *et al.*, “The netrin receptor DCC focuses invadopodia-driven basement membrane transmigration in vivo,” *J Cell Biol*, vol. 201, no. 6, pp. 903–913, 2013.

[185] M. Roh-Johnson *et al.*, “Macrophage contact induces RhoA GTPase signaling to trigger tumor cell intravasation,” *Oncogene*, vol. 33, no. 33, pp. 4203–4212, 2014.

[186] R. J. Eddy, M. D. Weidmann, V. P. Sharma, and J. S. Condeelis, “Tumor Cell invadopodia: invasive Protrusions that orchestrate metastasis,” *Trends Cell Biol.*, vol. 27, no. 8, pp. 595–607, 2017.

[187] H. Sibony-Benyamini and H. Gil-Henn, “Invadopodia: The leading force,” *Eur. J. Cell Biol.*, vol. 91, no. 11–12, pp. 896–901, 2012.

[188] C. Arvanitis, S. Khuon, R. Spann, K. M. Ridge, T.-L. Chew, and L. Kreplak, “Structure and biomechanics of the endothelial transcellular circumferential invasion array in tumor invasion,” *PLoS One*, vol. 9, no. 2, 2014.

[189] A. Hielscher, K. Ellis, C. Qiu, J. Porterfield, and S. Gerecht, “Fibronectin deposition participates in extracellular matrix assembly and vascular morphogenesis,” 2016.

[190] K. Y. Lee, Y.-J. Kim, H. Yoo, S. H. Lee, J. B. Park, and H. J. Kim, “Human brain endothelial cell-derived COX-2 facilitates extravasation of breast cancer cells across the blood-brain barrier.,” *Anticancer Res.*, vol. 31, pp. 4307–13, Dec. 2011.

[191] J. J. Jamieson, P. C. Searson, and S. Gerecht, “Engineering the human blood-brain barrier in vitro,” *J. Biol. Eng.*, vol. 11, no. 37, 2017.

[192] J. G. Destefano, J. J. Jamieson, R. M. Linville, and P. C. Searson, “Benchmarking in vitro tissue-engineered blood-brain barrier models,” *Fluids Barriers CNS*, vol. 15, p. 32, 2018.

[193] V. T. Turitto, “Blood viscosity, mass transport, and thrombogenesis.,” *Prog.*

Hemost. Thromb., vol. 6, pp. 139–77, 1982.

[194] N. Baeyens, C. Bandyopadhyay, B. G. Coon, S. Yun, and M. A. Schwartz, "Endothelial fluid shear stress sensing in vascular health and disease," *J. Clin. Invest.*, vol. 126, no. 3, pp. 821–828, Mar. 2016.

[195] J. M. Northcott, I. S. Dean, J. K. Mouw, and V. M. Weaver, "Feeling Stress: The Mechanics of Cancer Progression and Aggression," *Front. Cell Dev. Biol.*, vol. 6, p. 17, Feb. 2018.

[196] H. J. Lee *et al.*, "Fluid shear stress activates YAP1 to promote cancer cell motility," *Nat. Commun.*, vol. 8, no. 14122, 2017.

[197] N. E. Ajami *et al.*, "Systems biology analysis of longitudinal functional response of endothelial cells to shear stress," *Proc. Natl. Acad. Sci.*, vol. 114, no. 41, pp. 10990–10995, 2017.

[198] J. G. DeStefano, Z. S. Xu, A. J. Williams, N. Yimam, and P. C. Searson, "Effect of shear stress on iPSC-derived human brain microvascular endothelial cells (dhBMECs)," *Fluids Barriers CNS*, vol. 14, no. 1, p. 20, Dec. 2017.

[199] M. Ye *et al.*, "Brain microvascular endothelial cells resist elongation due to curvature and shear stress," *Sci. Rep.*, vol. 4, p. 4681, 2014.

[200] L. E. Barney, E. C. Dandley, L. E. Jansen, N. G. Reich, A. M. Mercurio, and S. R. Peyton, "A cell-ECM screening method to predict breast cancer metastasis," *Integr. Biol.*, vol. 7, p. 198, 2015.

[201] K. M. Gray, D. B. Katz, E. G. Brown, and K. M. Stroka, "Quantitative phenotyping of cell-cell junctions to evaluate ZO-1 presentation in brain endothelial cells," *Ann. Biomed. Eng.*, p. Submitted, Apr. 2019.

[202] T. Yoneda, P. J. Williams, T. Hiraga, M. Niewolna, and R. Nishimura, "A bone-seeking clone exhibits different biological properties from the ACHN parental human renal cell carcinoma in vivo and in vitro," *J. BONE Miner. Res.*, vol. 16, no. 8, pp. 1486–1495, 2001.

[203] K. Stoletov *et al.*, "Visualizing extravasation dynamics of metastatic tumor cells.," *J. Cell Sci.*, vol. 123, no. 13, pp. 2332–2341, Jul. 2010.

[204] American Cancer Society, "Cancer Treatment and Survivorship Facts and Figures 2016-2017," Atlanta, 2016.

[205] E. Mehrabian *et al.*, "MicroRNA: A novel target of curcumin in cancer therapy," *J. Cell. Physiol.*, vol. 233, no. 4, pp. 3004–3015, 2017.

[206] R. S. Riley and E. S. Day, "Gold nanoparticle-mediated photothermal therapy: applications and opportunities for multimodal cancer treatment," vol. 9, no. 4, p. e1449, 2017.

[207] F. Papaccio, F. Paino, T. Regad, G. Papaccio, V. Desiderio, and V. Tirino, "Concise Review: Cancer Cells, Cancer Stem Cells, and Mesenchymal Stem Cells: Influence in Cancer Development," *Stem Cells Transl. Med.*, vol. 6, no.

12, pp. 2115–2125, 2017.

[208] M. Wang, B. Holmes, X. Cheng, W. Zhu, M. Keidar, and L. G. Zhang, “Cold Atmospheric Plasma for Selectively Ablating Metastatic Breast Cancer Cells,” *PLoS One*, vol. 8, no. 9, p. e73741, 2013.

[209] D. Yan *et al.*, “The Specific Vulnerabilities of Cancer Cells to the Cold Atmospheric Plasma-Stimulated Solutions,” *Sci. Rep.*, vol. 7, no. 1, p. 4479, 2017.

[210] S. Arndt *et al.*, “Cold Atmospheric Plasma (CAP) Changes Gene Expression of Key Molecules of the Wound Healing Machinery and Improves Wound Healing In Vitro and In Vivo,” *PLoS One*, vol. 8, no. 11, p. e79325, 2013.

[211] H.-R. Metelmann *et al.*, “Scar formation of laser skin lesions after cold atmospheric pressure plasma (CAP) treatment: A clinical long term observation,” *Clin. Plasma Med.*, vol. 1, no. 1, pp. 30–35, 2013.

[212] Z. Chen, X. Cheng, L. Lin, and M. Keidar, “Cold atmospheric plasma discharged in water and its potential use in cancer therapy,” *J. Phys. D. Appl. Phys.*, vol. 50, no. 1, p. 15208, 2017.

[213] Z. Chen, L. Lin, X. Cheng, E. Gjika, and M. Keidar, “Effects of cold atmospheric plasma generated in deionized water in cell cancer therapy,” *Plasma Process. Polym.*, vol. 13, no. 12, pp. 1151–1156, 2016.

[214] Z. Chen, S. Zhang, I. Levchenko, I. . I. I. Beilis, and M. Keidar, “In vitro Demonstration of Cancer Inhibiting Properties from Stratified Self-Organized Plasma-Liquid Interface,” *Sci. Rep.*, vol. 7, no. 1, p. 12163, 2017.

[215] D. Yan *et al.*, “The role of aquaporins in the antiglioblastoma capacity of the cold plasma-stimulated medium,” *J. Phys. D. Appl. Phys.*, vol. 50, p. 055401, 2017.

[216] X. Cheng *et al.*, “Enhancing cold atmospheric plasma treatment of cancer cells by static magnetic field,” *Bioelectromagnetics*, vol. 38, no. 1, pp. 53–62, 2017.

[217] S. Mohades *et al.*, “Moderate plasma activated media suppresses proliferation and migration of MDCK epithelial cells,” *J. Phys. D. Appl. Phys.*, vol. 50, no. 18, p. 185205, 2017.

[218] N. Wada *et al.*, “Effect of plasma-activated medium on the decrease of tumorigenic population in lymphoma,” *Pathol. - Res. Pract.*, vol. 213, no. 7, pp. 773–777, 2017.

[219] A. Shashurin *et al.*, “Influence of Cold Plasma Atmospheric Jet on Surface Integrin Expression of Living Cells,” *Plasma Process. Polym.*, vol. 7, no. 3–4, pp. 294–300, 2010.

[220] D. Guembel *et al.*, “Comparison of Cold Atmospheric Plasma Devices’ Efficacy on Osteosarcoma and Fibroblastic In Vitro Cell Models,” *Anticancer Res.*, vol. 37, no. 10, 2017.

[221] E. A. Ratovitski *et al.*, “Anti-Cancer Therapies of 21st Century: Novel Approach to Treat Human Cancers Using Cold Atmospheric Plasma,” *Plasma Process. Polym.*, vol. 11, no. 12, pp. 1128–1137, Dec. 2014.

[222] D. Koensgen *et al.*, “Cold Atmospheric Plasma (CAP) and CAP-Stimulated Cell Culture Media Suppress Ovarian Cancer Cell Growth – A Putative Treatment Option in Ovarian Cancer Therapy,” *Anticancer Res.*, vol. 37, no. 12, pp. 6739–6744, 2017.

[223] S.-B. Park *et al.*, “Differential Epigenetic Effects of Atmospheric Cold Plasma on MCF-7 and MDA-MB-231 Breast Cancer Cells.,” *PLoS One*, vol. 10, no. 6, p. e0129931, 2015.

[224] H. Tanaka *et al.*, “Plasma-Activated Medium Selectively Kills Glioblastoma Brain Tumor Cells by Down-Regulating a Survival Signaling Molecule, AKT Kinase,” *Plasma Med.*, vol. 1, no. 4, pp. 265–277, 2011.

[225] O. Volotskova, M. A. Stepp, and M. Keidar, “Integrin activation by a cold atmospheric plasma jet,” *New J. Phys.*, vol. 14, no. 5, p. 053019, May 2012.

[226] W. S. Ramsey, W. Hertl, E. D. Nowlan, and N. J. Binkowski, “Surface Treatments and Cell Attachment,” 1984.

[227] A. L. Berrier and K. M. Yamada, “Cell–matrix adhesion,” *J. Cell. Physiol.*, vol. 213, no. 3, pp. 565–573, 2007.

[228] W. Van Gaens, P. J. Bruggeman, and A. Bogaerts, “Numerical analysis of the NO and O generation mechanism in a needle-type plasma jet,” *New J. Phys.*, vol. 16, p. 063054, 2014.

[229] S. Zhang *et al.*, “Spatially resolved ozone densities and gas temperatures in a time modulated RF driven atmospheric pressure plasma jet: an analysis of the production and destruction mechanisms,” *J. Phys. D. Appl. Phys.*, vol. 46, p. 205202, 2013.

[230] P. Luan, A. J. Knoll, P. J. Bruggeman, and G. S. Oehrlein, “Plasma–surface interaction at atmospheric pressure: A case study of polystyrene etching and surface modification by Ar/O2 plasma jet,” *J. Vac. Sci. Technol. A Vacuum, Surfaces, Film.*, vol. 35, no. 5, p. 05C315, Sep. 2017.

[231] P. Luan, A. J. Knoll, H. Wang, V. S. S. K. Kondeti, P. J. Bruggeman, and G. S. Oehrlein, “Model polymer etching and surface modification by a time modulated RF plasma jet: role of atomic oxygen and water vapor,” *J. Phys. D. Appl. Phys.*, vol. 50, no. 3, p. 03LT02, Jan. 2017.

[232] A. J. Knoll, P. Luan, E. A. J. J. Bartis, V. S. S. K. S. K. Kondeti, P. J. Bruggeman, and G. S. Oehrlein, “Cold Atmospheric Pressure Plasma VUV Interactions With Surfaces: Effect of Local Gas Environment and Source Design,” *Plasma Process. Polym.*, vol. 13, no. 11, pp. 1069–1079, Nov. 2016.

[233] S. Hofmann, A. F. H. van Gessel, T. Verreycken, and P. Bruggeman, “Power dissipation, gas temperatures and electron densities of cold atmospheric

pressure helium and argon RF plasma jets," *Plasma Sources Sci. Technol.*, vol. 20, no. 6, p. 065010, 2011.

[234] J. L. Zimmermann, T. Shimizu, H. U. Schmidt, Y. F. Li, G. E. Morfill, and G. Isbary, "Test for bacterial resistance build-up against plasma treatment," *New J. Phys.*, vol. 14, p. 073037, 2012.

[235] P. Luan and G. S. Oehrlein, "Stages of polymer transformation during remote plasma oxidation (RPO) at atmospheric pressure," *J. Phys. D. Appl. Phys.*, vol. 51, no. 13, p. 135201, Apr. 2018.

[236] D. Yan *et al.*, "Principles of using Cold Atmospheric Plasma Stimulated Media for Cancer Treatment.," *Sci. Rep.*, vol. 5, no. November, p. 18339, 2015.

[237] B. Liu, L. Ezeogu, L. Zellmer, B. Yu, N. Xu, and D. Joshua Liao, "Protecting the normal in order to better kill the cancer.," *Cancer Med.*, vol. 4, no. 9, pp. 1394–403, 2015.

[238] Q. Chen, M. S. Kinchln, T. H. LinS, K. Burridge, and R. L. Juliano, "Integrin-mediated Cell Adhesion Activates Mitogen-activated Protein Kinases," *J. Biol. Chem.*, vol. 269, no. 43, pp. 11–25, 1994.

[239] F. Doonan and T. G. Cotter, "Morphological assessment of apoptosis," *Methods*, vol. 44, no. 3, pp. 200–204, Mar. 2008.

[240] M. A. Shumakovich, C. P. Mencio, J. S. Siglin, R. A. Moriarty, H. M. Geller, and K. M. Stroka, "Astrocytes from the Brain Microenvironment Alter Migration and Morphology of Metastatic Breast Cancer Cells," *FASEB J.*, vol. 31, no. 11, pp. 5049–5067, Nov. 2017.

[241] P. J. Bruggeman *et al.*, "Plasma-Liquid Interactions: A Review and Roadmap," *Plasma Sources Sci. Technol.*, vol. 25, p. 053002, 2016.

[242] K. D. Weltmann and T. Von Woedtke, "Plasma medicine - Current state of research and medical application," *Plasma Phys. Control. Fusion*, vol. 59, p. 014031, 2017.

[243] T. Adachi, H. Tanaka, S. Nonomura, H. Hara, S. Kondo, and M. Hori, "Plasma-activated medium induces A549 cell injury via a spiral apoptotic cascade involving the mitochondrial–nuclear network," *Free Radic. Biol. Med.*, vol. 79, pp. 28–44, 2015.

[244] C. Kerksick and D. Willoughby, "The antioxidant role of glutathione and N-acetyl-cysteine supplements and exercise-induced oxidative stress," *J. Int. Soc. Sports Nutr.*, vol. 2, no. 2, pp. 38–44, Dec. 2005.

[245] L. L. Muldoon *et al.*, "Chemotherapy Delivery Issues in Central Nervous System Malignancy: A Reality Check," *J Clin Oncol*, vol. 25, pp. 2295–2305, 2007.

[246] H. Gerhardt and H. Semb, "Pericytes: gatekeepers in tumour cell metastasis?," *J. Mol. Med.*, vol. 86, no. 2, pp. 135–144, Feb. 2008.

[247] R. Daneman, “The blood-brain barrier in health and disease,” *Ann. Neurol.*, vol. 72, no. 5, pp. 648–672, Nov. 2012.

[248] M. A. Matrone *et al.*, “Metastatic breast tumors express increased tau, which promotes microtentacle formation and the reattachment of detached breast tumor cells,” *Oncogene*, vol. 29, pp. 3217–3227, 2010.

[249] E. C. Ory *et al.*, “Extracting microtentacle dynamics of tumor cells in a non-adherent environment,” *Oncotarget*, vol. 8, no. 67, pp. 111567–111580, 2017.

[250] E. S. Lippmann, A. Al-Ahmad, S. P. Palecek, and E. V Shusta, “Modeling the blood-brain barrier using stem cell sources.,” *Fluids Barriers CNS*, vol. 10, no. 1, pp. 1–14, 2013.

[251] E. K. Hollmann, A. K. Bailey, A. V. Potharazu, M. D. Neely, A. B. Bowman, and E. S. Lippmann, “Accelerated differentiation of human induced pluripotent stem cells to blood–brain barrier endothelial cells,” *Fluids Barriers CNS*, vol. 14, no. 1, p. 9, Dec. 2017.

[252] M. Keidar *et al.*, “Cold plasma selectivity and the possibility of a paradigm shift in cancer therapy,” *Br. J. Cancer*, vol. 105, no. 9, pp. 1295–1301, Oct. 2011.

[253] T. Von Woedtke, H. R. Metelmann, and K. D. Weltmann, “Clinical Plasma Medicine: State and Perspectives of in Vivo Application of Cold Atmospheric Plasma,” *Contrib. to Plasma Phys.*, vol. 54, no. 2, pp. 104–117, 2014.

[254] L. Bundscherer *et al.*, “Viability of Human Blood Leukocytes Compared with Their Respective Cell Lines after Plasma Treatment,” *Plasma Med.*, vol. 3, no. 2, pp. 71–80, 2013.

[255] S. Bekeschus *et al.*, “Differential Viability of Eight Human Blood Mononuclear Cell Subpopulations After Plasma Treatment,” *Plasma Med.*, vol. 3, no. 2, pp. 1–13, 2013.

[256] D. A. Lauffenburger and J. Linderman, *Receptors : Models for Binding, Trafficking, and Signaling: Models for Binding, Trafficking, and Signaling*. New York: Oxford University Press, Inc, 1993.

[257] R. J. Petrie and K. M. Yamada, “Fibroblasts Lead the Way: A Unified View of 3D Cell Motility,” *Trends Cell Biol.*, vol. 25, no. 11, pp. 666–674, 2015.

[258] R. J. Petrie and K. M. Yamada, “Multiple mechanisms of 3D migration: The origins of plasticity,” *Curr. Opin. Cell Biol.*, vol. 42, pp. 7–12, 2016.

[259] S. Tatapudy, F. Aloisio, D. Barber, and T. Nystul, “Cell fate decisions: emerging roles for metabolic signals and cell morphology,” *EMBO Rep.*, vol. 18, no. 12, pp. 2105–2118, 2017.

[260] H. Wolfenson, B. Yang, and M. P. Sheetz, “Steps in Mechanotransduction Pathways that Control Cell Morphology,” *Annu. Rev. Physiol.*, vol. 81, pp. 585–605, 2019.

[261] D. B. Patel, K. M. Gray, Y. Santharam, T. N. Lamichhane, K. M. Stroka, and S. M. Jay, "Impact of cell culture parameters on production and vascularization bioactivity of mesenchymal stem cell-derived extracellular vesicles," *Bioeng. Transl. Med.*, vol. 2, no. 2, pp. 170–179, Jun. 2017.

[262] J. Marshall, "Transwell® Invasion Assays," in *Cell Migration. Methods in Molecular Biology (Methods and Protocols)*, 2nd ed., C. Wells and M. Parson, Eds. Humana Press, 2011, pp. 97–110.

[263] M. T. Doolin and K. M. Stroka, "Physical confinement alters cytoskeletal contributions towards human mesenchymal stem cell migration," *Cytoskeleton*, vol. 75, no. 3, pp. 103–117, Mar. 2018.

[264] R. A. Moriarty and K. M. Stroka, "Physical confinement alters sarcoma cell cycle progression and division," *Cell Cycle*, vol. 17, no. 19–20, pp. 2360–2373, Oct. 2018.

[265] S. P. Carey *et al.*, "Comparative mechanisms of cancer cell migration through 3D matrix and physiological microtracks," *Am. J. Physiol. Physiol.*, vol. 308, no. 6, pp. C436–C447, Mar. 2015.

[266] J. H. McDonald, "Confounding variables and random sampling," in *Handbook of Biological Statistics*, 2nd ed., Baltimore: Sparky House Publishing, 2009, pp. 21–23.

[267] A. C. Skelly, J. R. Dettori, and E. D. Brodt, "Assessing bias: the importance of considering confounding," *Evid. Based. Spine. Care. J.*, vol. 3, no. 1, p. 2012, 2012.

[268] R. Gorelik and A. Gautreau, "Quantitative and unbiased analysis of directional persistence in cell migration," *Nat. Protoc.*, vol. 9, no. 8, pp. 1931–1943, Aug. 2014.

[269] A. D. Doyle and K. M. Yamada, "Mechanosensing via cell-matrix adhesions in 3D microenvironments," *Exp. Cell Res.*, vol. 343, no. 1, pp. 60–66, Apr. 2016.

[270] E. E. Joo and K. M. Yamada, "MYPT1 regulates contractility and microtubule acetylation to modulate integrin adhesions and matrix assembly," *Nat. Commun.*, vol. 5, no. 1, p. 3510, Dec. 2014.

[271] R. Pankov *et al.*, "A Rac switch regulates random versus directionally persistent cell migration," *J. Cell Biol.*, vol. 170, no. 5, pp. 793–802, Aug. 2005.

[272] K. Wolf *et al.*, "Physical limits of cell migration: control by ECM space and nuclear deformation and tuning by proteolysis and traction force.," *J. Cell Biol.*, vol. 201, no. 7, pp. 1069–84, Jun. 2013.

[273] F. Bordeleau, B. Chan, M. A. Antonyak, M. C. Lampi, R. A. Cerione, and C. A. Reinhart-King, "Microvesicles released from tumor cells disrupt epithelial cell morphology and contractility," *J. Biomech.*, vol. 49, no. 8, pp. 1272–1279, May 2016.

[274] A. Rahman *et al.*, “Vinculin regulates directionality and cell polarity in two- and three-dimensional matrix and three-dimensional microtrack migration,” *Mol. Biol. Cell*, vol. 27, no. 9, pp. 1431–1441, May 2016.

[275] I. Thievessen *et al.*, “Vinculin is required for cell polarization, migration, and extracellular matrix remodeling in 3D collagen Vinculin is required for cell polarization, migration, and extracellular matrix remod-eling in 3D collagen,” *FASEB J.*, vol. 29, pp. 4555–4567, 2015.

[276] S. V. Plotnikov, A. M. Pasapera, B. Sabass, and C. M. Waterman, “Force Fluctuations within Focal Adhesions Mediate ECM-Rigidity Sensing to Guide Directed Cell Migration,” *Cell*, vol. 151, no. 7, pp. 1513–1527, Dec. 2012.

[277] F. M. Vega, G. Fruhwirth, T. Ng, and A. J. Ridley, “RhoA and RhoC have distinct roles in migration and invasion by acting through different targets.,” *J. Cell Biol.*, vol. 193, no. 4, pp. 655–65, May 2011.

[278] P. J. Bhavsar, E. Infante, A. Khwaja, and A. J. Ridley, “Analysis of Rho GTPase expression in T-ALL identifies RhoU as a target for Notch involved in T-ALL cell migration,” *Oncogene*, vol. 32, no. 2, pp. 198–208, Jan. 2013.

[279] S. Wei Bai *et al.*, “Identification and characterization of a set of conserved and new regulators of cytoskeletal organization, cell morphology and migration,” *BMC Biol.*, vol. 9, no. 54, 2011.

[280] L. E. Goldfinger, C. Ptak, E. D. Jeffery, J. Shabanowitz, D. F. Hunt, and M. H. Ginsberg, “RLIP76 (RalBP1) is an R-Ras effector that mediates adhesion-dependent Rac activation and cell migration,” *J. Cell Biol.*, vol. 174, no. 6, pp. 877–888, Sep. 2006.

[281] N. Kramer *et al.*, “In vitro cell migration and invasion assays,” *Mutat. Res. Mutat. Res.*, pp. 10–24, 2013.

[282] E. Meijering, O. Dzyubachyk, and I. Smal, “Methods for Cell and Particle Tracking,” in *Methods in Enzymology*, vol. 504, Academic Press, 2012, pp. 183–200.

[283] J.-Y. Tinevez *et al.*, “TrackMate: An open and extensible platform for single-particle tracking,” *Methods*, vol. 115, pp. 80–90, Feb. 2017.

[284] A. J. Hand, T. Sun, D. C. Barber, D. R. Hose, and S. Macneil, “Automated tracking of migrating cells in phase-contrast video microscopy sequences using image registration,” *J. Microsc.*, vol. 234, no. 1, pp. 62–79, Apr. 2009.